Development and Characterization of an Irradiation Site for Radiation Damage Studies of the ATLAS ITk Pixel Detector

Dissertation
zur
Erlangung des Doktorgrades (Dr. rer. nat.)
der
Mathematisch-Naturwissenschaftlichen Fakultät
der
Rheinischen Friedrich-Wilhelms-Universität Bonn

von
Pascal Wolf
aus
Köln

Bonn, Februar 2025

Angefertigt mit Genehmigung der Mathematisch-Naturwissenschaftlichen Fakultät der Rheinischen Friedrich-Wilhelms-Universität Bonn

Gutachter/Betreuer:	Prof. Dr. Jochen Dingfelder
Gutachter:	Prof. Dr. Sebastian Neubert
Tag der Promotion:	18.06.2025
Erscheinungsjahr:	2025

Contents

CHAPTER 1

Introduction

Segmented solid state detectors are the tool of choice for high-resolution particle tracking in extreme rate and radiation environments. Specifically pixelated devices are capable of handling occupancies in the order of several tens of MHz cm^{-2} while providing timing and spatial resolutions reaching the sub-ns regime and a few µm, respectively (e.g. [1]). In the field of modern experimental particle physics, silicon detectors constitute the core of tracking systems, located closest to the interaction point (IP) of fixed-target or collider experiments. The need for higher rates and energies in particle physics experiments to validate and explore the Standard Model of particle physics (SM) is the driving force for the continuous development and improvement of pixelated devices. The SM has emerged over the last decades of the 20th century [2] and describes the fundamental building blocks of matter, the elementary particles, and their interactions on a microscopic scale via the *strong*, *weak* and *electromagnetic* forces. Leveraged by powerful particle accelerators such as the Large Hadron Collider (LHC) and large-scale detector systems like ATLAS[1] or CMS[2] at CERN[3], the predictions of the SM have been verified in an enormous amount of observations, making it one of the most successful theories of the modern-day physics. Approximately 50 years after its prediction, the discovery of the *Higgs* boson by the ATLAS [3] and CMS [4] experiments in 2012 constituted the completion of the SM, the most remarkable achievement in particle physics of the 21$^{\text{st}}$ century yet. Since its discovery, experimental data of Higgs events is collected at the large experiments at CERN to probe the Higgs Sector (HS) of particle physics, associated with the study of the underlying Higgs mechanism.
Regardless of its success, the SM fails to explain observable phenomena such as e.g. the existence of dark matter or the asymmetry between baryonic and anti-matter, and hence can only be a subset of more generalized theory. The HS is a promising starting point for the search for Beyond Standard Model (BSM) physics as its theoretical models account for some of the shortcomings of the SM [5]. To explore new physics in the context of the LHC, the number of events, N, of any given process with a production cross-section σ can be expressed as

$$N = \sigma \int \mathcal{L}\, \mathrm{d}t\,, \tag{1.1}$$

[1] A Torodial LHC Apparatus
[2] Compact Muon Solenoid
[3] Conseil Européen pour la Recherche Nucléaire

where $\mathcal{L}$ is the instantaneous and $\mathcal{L}_{\text{int}} = \int \mathcal{L}\, dt$ the integrated luminosity of the collider, a measure for the rate and number of interactions, respectively. With a very small production cross-section of $\sigma_{\text{Higgs}} < 100\,\text{pb}$ over all available processes at the LHC [6], a very high luminosity is required to obtain a sufficient statistical precision to investigate the properties of the Higgs boson (HS).

To extend its discovery potential for rare and BSM physics, the Large Hadron Collider will undergo a substantial upgrade towards the end of this decade, the so-called High-Luminosity Large Hadron Collider (HL-LHC) [7], which will increase the instantaneous luminosity by a factor 5 – 7.5. Within approximately a decade after the HL-LHC upgrade, this will lead to an expected tenfold increase in the integrated luminosity with respect to the initial LHC design value, projected to reach $3\,000 – 4\,000\,\text{fb}^{-1}$.
This poses a challenging environment for the detector systems at the future HL-LHC. Specifically the innermost layers of the tracking systems, consisting of silicon pixel detectors, experience harsh radiation background as they are located only a few cm from the IP. These devices suffer from radiation-induced damage, degrading the detectors performance with number of traversing particles per unit area, the so-called particle fluence Φ. To obtain the number of recorded events N' from Eq. (1.1), the reconstruction efficiency ϵ of the detector system has to be taken into account. As ϵ decreases with degrading detector performance and hence with radiation, the number of correctly reconstructed events N' also decreases.

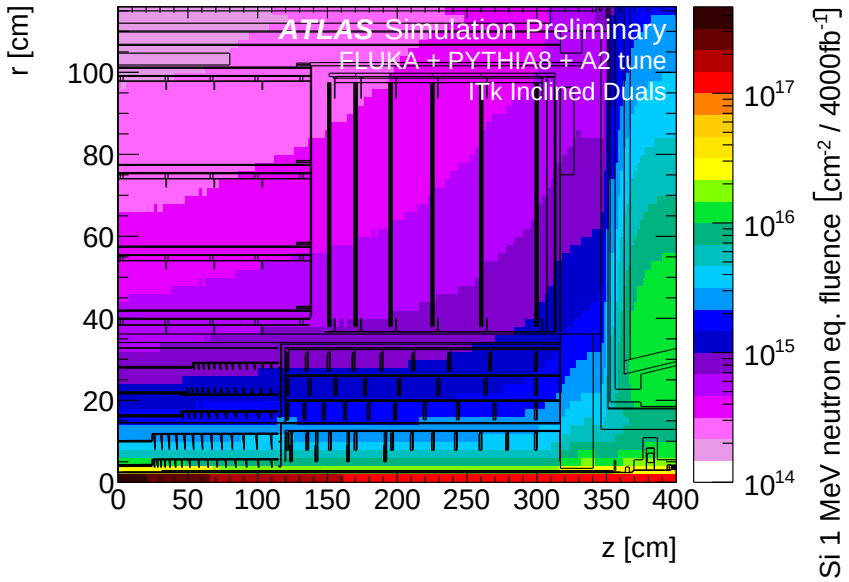

Figure 1.1: Simulation of the 1 MeV neutron equivalent fluence in silicon after an integrated luminosity of $4\,000\,\text{fb}^{-1}$ of proton-proton collisions with a center-of-mass energy of 14 TeV in the ITk, depending on distance from the IP at the origin. An equivalent fluence of $\Phi_{\text{n}_{\text{eq}}} \approx 2 \times 10^{16}\,\text{n}_{\text{eq}}/\text{cm}^2$ will be delivered to the innermost pixel layer. Taken from [8].

To cope with the environment imposed by the HL-LHC, the ATLAS detector will be upgraded accordingly, replacing its tracking system with an all-silicon tracker, the ATLAS Inner Tracker (ITk) [9]. A simulation of the anticipated particle fluence in the ATLAS ITk after the maximum expected

luminosity delivered during the HL-LHC, is shown in Fig. 1.1. The particle fluence is normalized to the damage of 1 MeV neutrons in silicon, the so-called *equivalent fluence* $\Phi_{n_{eq}}$. After an integrated luminosity of 4 000 fb^{-1}, an unprecedented fluence of $\Phi_{n_{eq}} \approx 2 \times 10^{16}\, n_{eq}/cm^2$ is expected for the innermost pixels at approximately 3.5 cm from the IP.
To manage these fluence levels, a new pixel detector readout chip was developed and characterized by the RD53 collaboration [10], the `ITkPix`. To ensure the functionality of the detector throughout its intended operational period in the experiment, radiation hardness studies are crucial. For this reason, irradiation sites are in operation, among others, at CERN [11], Birmingham [12] and Karlsruhe [13], allowing for the application fluence levels equivalent to those expected at the HL-LHC in the order of days.

In this work, a new irradiation site is developed, characterized and commissioned at the University of Bonn, using 14 MeV protons provided by the Bonn Isochronous Cyclotron (BIC). It operates on a novel beam-based irradiation procedure, resulting in highly uniform and precise damage distributions. The developed infrastructure is utilized to perform extended radiation hardness tests of an `ITkPix` pixel detector assembly, consisting of sensor and readout chip, designed for the ATLAS ITk.
The fundamental working principles of semiconductor (silicon) detectors are introduced in Chapter 2. Chapter 3 gives an insight into the layout of the ATLAS experiment at the LHC and briefly describes the ITk upgrade and the corresponding `ITkPix` readout chip. Consequently, the damage mechanisms in the sensitive volume and the chip logic of semiconductor devices as well as the resulting performance degradations are outlined in Chapter 4. In Chapter 5, the irradiation facility at the BIC is presented. A short overview of the accelerator facility is given and the sites' custom beam diagnostics, the beam-based dosimetry approach and the irradiation procedure are explained in detail. Subsequently, the presented infrastructure is thoroughly characterized in Chapter 6. The working principle of the custom beam diagnostics, the irradiation procedure as well as beam-based dosimetry are verified and the hardness factor of the provided protons is determined. In conclusion, a comparison of existing facilities is made. Chapter 7 contains radiation hardness studies of the ATLAS ITk pixel detector assembly, probing the damage to the sensor and readout chip using the available proton beam. The anticipated End-Of-Life (EOL) damage levels are applied at the BIC irradiation site and the detectors' resulting performance is evaluated via a test beam campaign at the DESY II facility [14]. Finally, the findings of this work are summarized and their relevance discussed in Chapter 8.

CHAPTER 2

Principles of Silicon Detectors

Since their introduction into the field of particle physics in the early nineties, solid state pixel detectors have been the workhorse for high resolution particle tracking in high rate environments [15]. Silicon has emerged as the semiconductor of choice for most detector applications, in- and outside of particle physics, as it is abundant, well-studied and exhibits good properties for overall radiation detection. This chapter gives an insight into the functionality and design of silicon detectors, although the principles apply to other semiconductors as well. Section 2.1 introduces the mechanisms of signal generation by interaction of radiation with the detector material. In the following Section 2.2, the properties of intrinsic and doped silicon are treated. The formation of a sensitive volume, the typical readout chain and different sensor layouts are explained. Finally, two design approaches of pixel detectors, namely *hybrid* and *monolithic*, are discussed in Section 2.3. A more detailed treatment of the topics reviewed in this chapter can be found in [16, 17, 18].

2.1 Signal Generation

Particle detection is based on their interaction with the material of a sensitive device. For semiconductor and gaseous tracking detectors alike, the source of signal is the creation of free charge carriers by ionization. Therefore, only charged particles and photons can be registered directly, via their Coulomb interaction. The process of energy loss in matter, resulting in ionization of the material's atoms, is fundamentally different for charged particles and photons and described in the following.

2.1.1 Interaction of Charged Particles with Matter

Charged particles lose energy when traversing matter due to ionization and excitation of the atoms of the medium along their path. The *average energy loss* per path length due to ionization is described by the *Bethe-Bloch formula* as [16]

$$-\left\langle \frac{\mathrm{d}E}{\mathrm{d}x} \right\rangle = K\frac{Z}{A}\rho\frac{z^2}{\beta^2}\left[\frac{1}{2}\ln\left(\frac{2m_e c^2\beta^2\gamma^2 T_{max}}{I^2}\right) - \beta^2 - \frac{\delta(\beta\gamma)}{2} - \frac{C(\beta\gamma, I)}{Z}\right], \tag{2.1}$$

where the quantities are defined as

- $K = 4\pi N_A r_e^2 m_e c^2 = 0.307\,\mathrm{MeV\,cm^2\,mol^{-1}}$ with the classical electron radius $r_e \approx 2.8\,\mathrm{fm}$.
- m_e is the electron mass.
- Z, A are the atomic number and mass of the medium, respectively.
- ρ is the density of the medium.
- z, β, γ are the charge, the velocity and the Lorentz factor of the impinging particle.
- $I \approx 17.7\,\mathrm{eV} \cdot Z^{0.85}$ is the mean excitation energy of the medium.
- T_{max} is the maximum energy transfer per shell electron per collision.

The remaining quantities $\delta(\beta\gamma)$ and $C(\beta\gamma, I)/Z$ are the *density* and *shell* corrections, relevant for the high and low energy regimes, respectively. The negative sign on the left side of Eq. (2.1) is a convention to indicate the loss of energy and is frequently neglected. Furthermore, a normalization to the density of the medium ρ is often performed, resulting in Eq. (2.1) to be given in units of $\mathrm{MeV\,cm^2\,g^{-1}}$. Since the average energy loss results in the slowing down of the particle on its passage through a medium, it is also referred to as *stopping power*, or *mass stopping power* in the density-normalized case. Frequently, both terms are used interchangeably and the latter form of Eq. (2.1) is used. The Bethe-Bloch equation describes the average energy loss due to ionization for heavy particles with masses $M \gg m_e$[1], representing the dominant energy loss mechanism up to extreme energies for which radiative losses start to compete. A collection of stopping power calculations for protons, electrons and alpha particles in various materials and compounds over a wide range of energies can be found in [19]. Figure 2.1 shows the mass stopping power of protons and electrons in silicon in dependence of their energy. Three distinct kinematic regions are visible for the proton data:

$\beta\gamma \leq 1$: The stopping power decreases proportional to $1/\beta^2$ due to the decrease in interaction time between the particle and the atoms of the medium with increasing velocity.

$\beta\gamma = 3 - 4$: A minimum in stopping power of $\left\langle \frac{dE}{dx} \right\rangle \approx 1 - 2\,\mathrm{MeV\,cm^2\,g^{-1}}$ is visible. Particles within this region are referred to as minimum-ionizing particles (MIPs).

$\beta\gamma \geq 10$: The stopping power increases gradually, proportional to $\ln(\gamma)$ as the energy transfer T_{max} increases and relativistic effects, such as extension of the transversal electric field of the projectile, begin to play a role.

The resulting energy loss of a particle is the consequence of many individual interactions, thus it is a stochastic process which is subject to fluctuations in number and amplitude. These variations, commonly known as *Landau fluctuations*, result in a distribution of lost energy with its maximum defining the most probable value (MPV) of energy loss. As this yields the expected signal amplitude in silicon detectors, it is an important concept for device characterization which is done using different sensors for example in [17, 20, 21].
Due to the slow increase in stopping power beyond the minimum, in practice all particles with $\beta\gamma \geq 3$ are considered MIPs. Since the created signal in a detector is proportional to the deposited energy

[1] For electrons and positrons corrections have to be applied, considering, among others, spin, annihilation and scattering processes, see [16].

(see Section 2.2), MIPs define the lower limit of signals available for detection. Therefore, they are often considered when optimizing the detector design.
The characteristic trend of the Bethe-Bloch formula can be used for particle identification (PID) by measurement of the momentum p and $\left\langle \frac{dE}{dx} \right\rangle$ of the incident particle to determine its mass M. For electrons, the course of the energy loss with increasing $\beta\gamma$ exhibits a steep increase for comparatively low energies due to radiative losses becoming dominant. The energy at which the loss by ionization equals the radiative losses is referred to as *critical energy* E_c. An adjusted version of Eq. (2.1) for electrons can be found in [6].

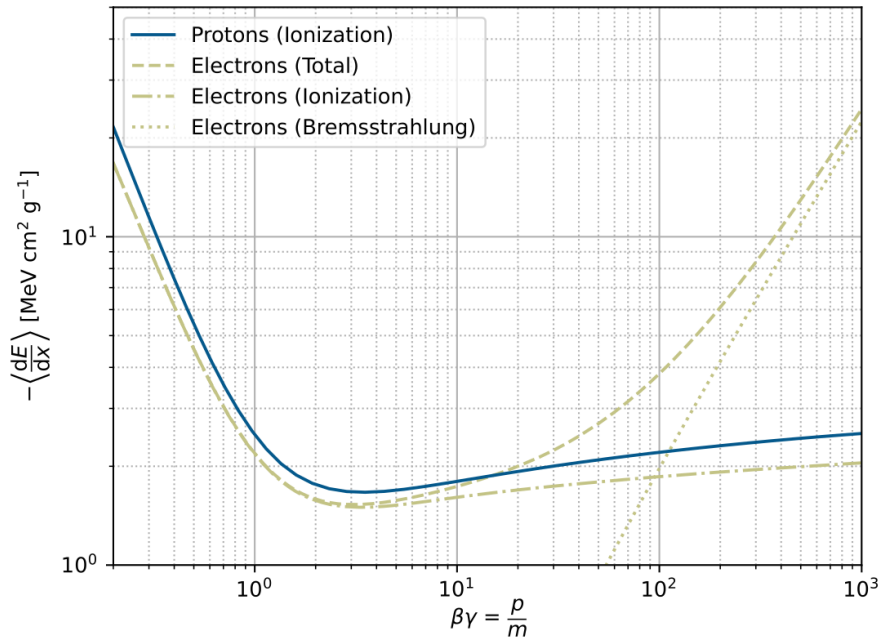

Figure 2.1: *Mass stopping power* of protons and electrons in silicon over four orders of magnitude of $\beta\gamma$. Due to the minimum at $\beta\gamma = 3 - 4$ followed by the relatively slow increase, projectiles with $\beta\gamma \geq 3$ are referred to as MIPs. Taken from [21].

2.1.2 Interaction of Photons with Matter

The interaction of photons with matter differs substantially from the previously discussed interaction mechanism of charged particles. Where the latter undergo a sequence of collisions, each individually contributing to the overall energy loss, photons are either absorbed or scattered off the atoms of the medium. Therefore, charged particles have a fixed *absorption length* λ, depending on their energy, whereas the number of photons N decreases exponentially with depth x as

$$N(x) = N_0 e^{-\mu x} \quad \text{with} \quad \mu = \frac{1}{\lambda} = n\sigma\,, \tag{2.2}$$

where μ is referred to the *absorption coefficient*, N_0 is the number of initial photons, n the target density and σ the cross section. Within the context of particle detectors, three processes[2] contribute to the signal generation via photon interaction:

- **Photoelectric effect**: complete absorption and energy transfer of a photon to the atom with subsequent emission of an electron
- **Compton scattering**: elastic scattering of a photon off a shell electron which is subsequently ejected from the atom
- **Pair production**: conversion of a photon into an electron-positron pair within the electric field of a nucleus

These interaction mechanisms are portrayed schematically in Fig. 2.2. Their individual contributions to the absorption coefficient, i.e. the cross section, in silicon as a function of the photon energy is depicted Fig. 2.3. In the following, the three effects are described in more detail and their dependence on energy and the medium's properties are highlighted.

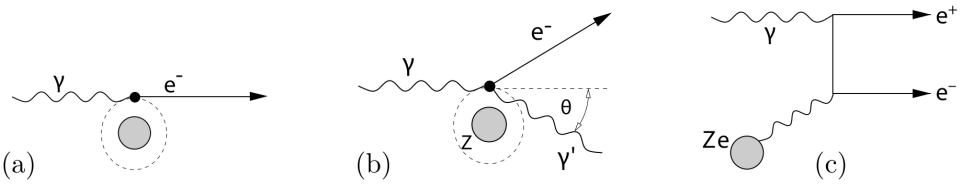

Figure 2.2: Diagrams of the dominant photon interaction mechanisms with matter: the photoelectric effect (a), Compton scattering (b) and pair production (c). From [16].

Photoelectric Effect

The photoelectric effect describes the complete absorption of the incident photon by an atom which releases the transferred energy by emission of an electron. The atom absorbs the recoil momentum and energy of the absorbed photon and ejected electron, respectively, and remains ionized after the reaction. The corresponding diagram is shown in Fig. 2.2 (a). As displayed in Fig. 2.3, the photoelectric effect is the dominant photon interaction mechanism in the energy region between 1 – 100 keV. With the photon energy E_γ required to exceed the binding energy E_B of the electron, the latter is ejected with a kinetic energy of $E_{\text{kin}} = E_\gamma - E_B$ which is, consequently, available for signal generation inside detectors.
The cross section $\sigma_{p.e.}$ for the photoelectric effect is strongly dependent on the photon energy E_γ as well as the atomic number Z of the material. The dependencies can be expressed as

$$\sigma_{p.e.} \propto E_\gamma^{-m} Z^k \quad \text{with} \quad m \lesssim 3.5\,,\, k = 4 - 5\,, \tag{2.3}$$

where, for the energy regime in which the process is prevalent ($E_\gamma \ll m_e c^2$), one finds $m = 3.5\,,\, k = 5$ whereas in the highly relativistic case $m = 1$. In the former, the cross section is dominated by the

[2] Other mechanisms such as *Thomson* and *Rayleigh* scattering transfer energies below the ionization threshold to the atoms, thus they are not relevant for signal generation.

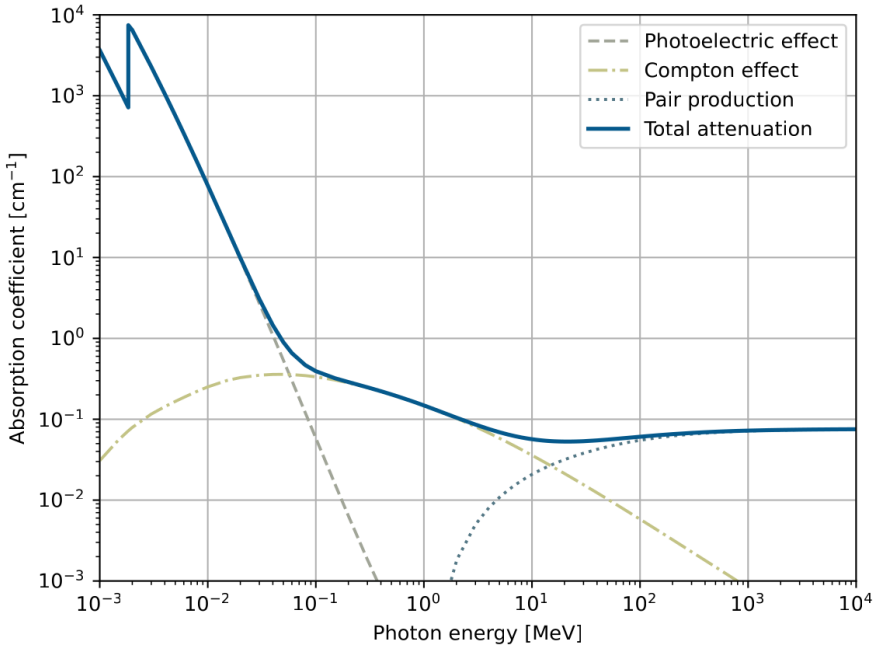

Figure 2.3: Absorption coefficient μ for photons in silicon as a function of energy. The individual contributions of the three relevant photon interaction mechanisms as well as the resulting total are shown. Taken from [21].

ionization of the innermost shell i.e. K-shell electron which produces the characteristic kink in the low energy region of Fig. 2.3. In general, the cross section is highest for the shell with binding energy E_B^i closest to the incident photon E_γ such that $E_\gamma - E_B^i$ is minimal for shell i.
Specifically in X-ray applications, the photoelectric effect accounts for the majority of generated signal in the detector. By utilizing semiconductor compounds with high effective Z, such as cadmium telluride (CdTe, $Z_{\mathrm{Cd}} = 48$, $Z_{\mathrm{Te}} = 52$), a substantial part of the X-ray spectrum can be fully converted to signal using sensors of just 300 µm thickness [16].

Compton Scattering

The Compton effect, also referred to as Compton scattering, is the process of elastic scattering of a photon off a quasi-free electron as schematically portrayed in Fig. 2.2 (b). The term "quasi-free" refers to the condition that the electrons binding energy is small compared to the incoming photons energy $E_B \ll E_\gamma$. As a result, the incoming photon scatters off a shell electron, ejecting it from the atom and carrying away the recoil momentum of the interaction. The incident photon continues to propagate with a reduced energy E'_γ and change in direction at an angle θ_γ with respect to its initial orientation. Using the energy-momentum conservation of the kinematics shown in Fig. 2.2 (b), the energy E'_γ as a function of the angle θ_γ and initial energy E_γ can be derived as [16]

$$E'_\gamma = \frac{E_\gamma}{1 + \tilde{E}\left(1 - \cos(\theta_\gamma)\right)} \quad \text{with} \quad \tilde{E} = \frac{E_\gamma}{m_e c^2} \tag{2.4}$$

With regard to detector applications, the kinetic energy of the emitted electron $E_{\text{kin}} = E_\gamma - E'_\gamma$ contributes to the signal generation inside the sensitive volume. It is also possible for the photon to scatter without ionizing the atom, resulting in negligible energy reduction and directional change. In this case, the entire atom takes the recoil energy and no detectable signal is produced.
The Compton effect is dominant for γ energies between 0.1 – 10 MeV with a broad peak at approximately the middle of this range as shown in Fig. 2.3. For high photon energies $E_\gamma >> m_e c^2$, the Compton scattering (Klein-Nishina) cross section σ_C is inversely proportional to the photon energy

$$\sigma_C \propto \frac{1}{E_\gamma} \quad \text{with} \quad \sigma_C^{\text{atom}} = \sigma_C Z \,. \tag{2.5}$$

Here, σ_C^{atom} is the respective cross section for a single atom which is directly proportional to the atomic number of the medium.

Pair Production

The conversion of a photon into an electron-positron pair within the Coulomb field of a nucleus (or any charged particle) is referred to as pair production. Du to energy and momentum conservation, the charged entity is required to absorb the recoil of the photon in this process. A depiction of the mechanism is given in Fig. 2.2 (c). The photon energy threshold from which pair production in the field of a nucleus[3] is possible is naturally defined in terms of the electron mass as

$$E_\gamma \approx 2 m_e c^2 \,. \tag{2.6}$$

As shown in Fig. 2.3, pair production is the sole contributor to the cross section at high energies $E_\gamma \geq 100\,\text{MeV}$ where it saturates and is independent of E_γ. In this region, the pair production cross section $\sigma_{e^+e^-}$ depends on the atomic number of the medium as follows:

$$\sigma_{e^+e^-} \propto Z^2 \,. \tag{2.7}$$

In this energy regime, the signal inside a sensor is produced by a sequence of recursive pair production events, caused by radiative losses (see also Fig. 2.1), the so-called *Bremsstrahlung*. This process is also referred to as an electromagnetic shower.
For photon detection, the sensor material and readout chain (see Fig. 2.9) are typically adjusted to the expected energy region. For gamma and X-ray applications, high-Z semiconductor materials and compounds such as germanium (Ge), gallium arsenide (GaAs) and the aforementioned CdTe are utilized due to the Z^5 and Z^2 dependency of the absorption coefficient in their respective energy regions. This facilitates the usage of thin sensors, reducing the material budget and power dissipation (see Eq. (2.19)), with absorption efficiencies close to 100 % across the photon energy spectrum. Nevertheless, in the intermediate X-ray regime also silicon provides sufficient absorption capabilities for detector operation.
Photon energies around the 1 MeV mark pose a challenge for detectors as the absorption coefficient in this region is minimal, regardless of the medium. However, the width of the minimum cross section

[3] In case of sufficiently heavy nuclei, their comparatively large mass M constitutes a negligible recoil momentum transfer with regard to double the electron mass. Generally, the threshold energy is a function of the mass M of the charge in whose field the photon converts where it increases with decreasing M [16].

window in energy decreases with increasing Z, once again emphasizing the Z dependence of the sensor material.

2.2 Silicon Detectors

Silicon sensors first appeared in the context of spectroscopy applications in the 1960s, improving the energy resolution compared to the commonly used, gas-based ionization chambers by a large margin [18]. Since then, the dominance of pixelated devices in the field of particle physics has developed due to the need for precise tracking at high occupancies to allow for the study of short-lived (e.g. $\tau \leq 10^{-12}$ s) particles via their decay products.
Silicon surfaced as the semiconductor of choice as, due to the advancements in the electronics industry, it was the most-studied semiconductor material and available in large quantities at low cost. In this section, the properties as well as the formation and principle of radiation-sensitive silicon pixel devices are explained. If not stated otherwise, temperature-dependent quantities such as energies or concentrations are given at the reference temperature of 300 K.

2.2.1 Intrinsic Silicon

If the contribution of impurity atoms in an elemental or compound semiconductor to its electrical conductivity is negligible, the material is considered to be an *intrinsic*, or *pure*, semiconductor. Conversely, if the charge carrier concentration is dominated by (a significant number of) impurities, the semiconductor is referred to as *extrinsic*. The process of adding impurity atoms in a controlled manner is termed *doping*, with the impurities called *dopants*, which is an essential procedure to manufacture semiconductor sensors and treated in the following Section 2.2.2.

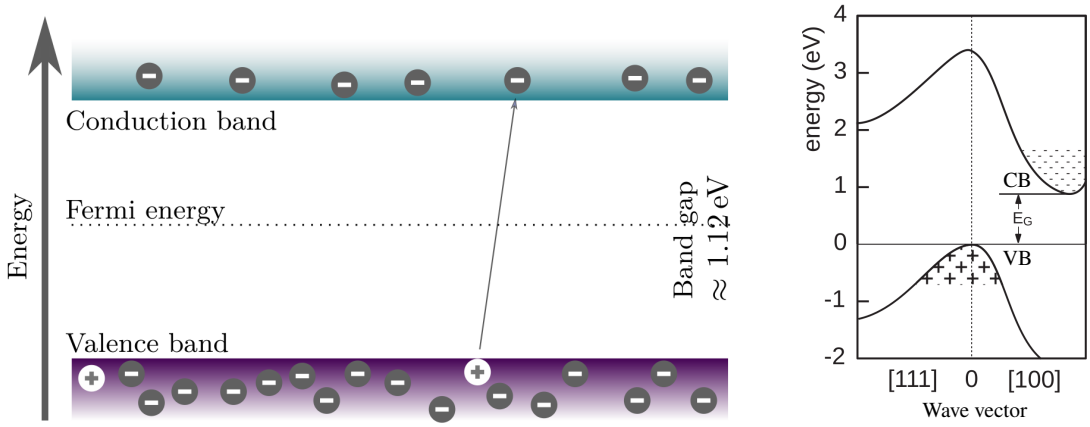

(a) Band model schematic. Taken from [17].

(b) Energy versus crystal momentum. Adapted from [16].

Figure 2.4: Schematic energy band model (Fig. 2.4(a)) and the location of energy extrema with regard to the crystal momentum (Fig. 2.4(b)) in intrinsic silicon. At 300 K, the valence and conduction bands are separated by a gap energy of $E_g = 1.12$ eV. Additionally, a change in crystal momentum is required for a band transition.

As silicon in its solid form has a crystalline structure, its atoms are place on a lattice with constant spacing. This configuration generates a periodic potential among the lattice atoms, resulting in various

energy levels that are occupied by the electrons. Some energy levels are grouped in so-called *bands*, due to their low separation in energy in the order of $O(\text{meV})$ [16]. If bands are separated in energy by a substantial margin or *gap*, the separation is labeled *band gap* and the energy is referred to as *gap energy* E_g. In terms of the electrical characteristics of the material, the two topmost energy bands, with the upper called conduction band (CB) and the lower termed valence band (VB), define its conduction properties. For semiconductors, the gap energy typically lies in the region of 1 eV whereas for insulators the separation is approximately an order of magnitude larger. In silicon, a band gap of $E_g = 1.12\,\text{eV}$ allows for thermal (or external) excitation, resulting in an electron being elevated into the CB from the VB, leaving a hole behind. The configuration is displayed schematically in Fig. 2.4. The electrons in the CB contribute to the electrical conductivity of the semiconductor and facilitate a current flow when an external field is applied. Due to the minimum of the CB and the maximum of the VB being located at different positions in the momentum space of the lattice, silicon is referred to as an *indirect* semiconductor (see Fig. 2.4(b)) and an additional momentum transfer is needed for elevation of a VB electron into the CB. For this reason, the average energy required for electron-hole pair creation in silicon, $\omega_{e\text{–}h}$, is significantly larger than the gap energy:

$$\omega_{e\text{–}h} = 3.65\,\text{eV}\,. \tag{2.8}$$

Considering the energy loss of a MIP in silicon, the most probable number of generated electron-hole pairs per µm of traversed material is approximately 76 *e–h*/µm [16]. In thermal equilibrium, the number of generated free charge carriers follows the *mass action law* [18]

$$n_i^2 = np = N_C N_V \exp\left(-\frac{E_g}{k_B T}\right) = \text{const.}\,, \tag{2.9}$$

where n_i is the intrinsic carrier density, n (p) is the concentration of free electrons (holes) and N_C (N_V) the effective density of states in the conduction (valence) band, for which typical values of 3 $(2.5) \times 10^{19}\text{cm}^{-3}$ are found [16]. Plugging in these values, the thermally generated number of charger carriers in intrinsic silicon is found to be

$$n_i \approx 1 \times 10^{10}\,\text{cm}^{-3}\,. \tag{2.10}$$

Using the electron-hole generation rate of approximately 76 *e–h*/µm in a typical sensor of 300 µm thickness, the number of charge carrier pairs created by a MIP is

$$N_{e\text{–}h} \approx 23\,000\,. \tag{2.11}$$

This signal is many orders of magnitude smaller than the thermally generated background noise from Eq. (2.10), demonstrating that the use of intrinsic silicon as a sensitive volume for particle detection is not applicable.
However, this obstacle can be overcome by the process of doping, resulting in an extrinsic silicon volume free of intrinsic charge carriers which is treated in the following.

2.2.2 Extrinsic Silicon and Sensor Formation

The electrical properties of silicon can be modified by doping, after which the semiconductor is referred to as *extrinsic*. By adding dopants that contribute one additional (*donors D*) or one less

(*acceptors A*) valence electron than silicon to the crystal lattice, the material is termed an n or p-type semiconductor, respectively. Thus, for silicon with four valence electrons, n-type and p-type doping are performed by addition of elements with five and three valence electrons correspondingly. A typical n-type dopant is phosphorus (P) whereas boron (B) is a common element for p-type doping.
In the band model, the additional charge carriers emerging from the doping process are energetically located close to their respective band as depicted in Fig. 2.5. At room temperature, the dopants are effectively completely ionized, resulting in their excess charge carriers being situated inside their respective band. As the typical donor (acceptor) concentration N_D (N_A) is orders of magnitude higher than the number of intrinsic charge carriers from Eq. (2.10), it defines the electrical conductivity of the extrinsic semiconductor. The resistivity $\rho_{n,p}$ of the doped material is expressed as [16]

$$\rho_{n,p} = \frac{1}{e\mu_{e,h}N_{D,A}}\,, \tag{2.12}$$

where $\mu_{e,h}$ is the mobility of electrons and holes, respectively. Thus, the electrical resistivity decreases with increasing concentration.

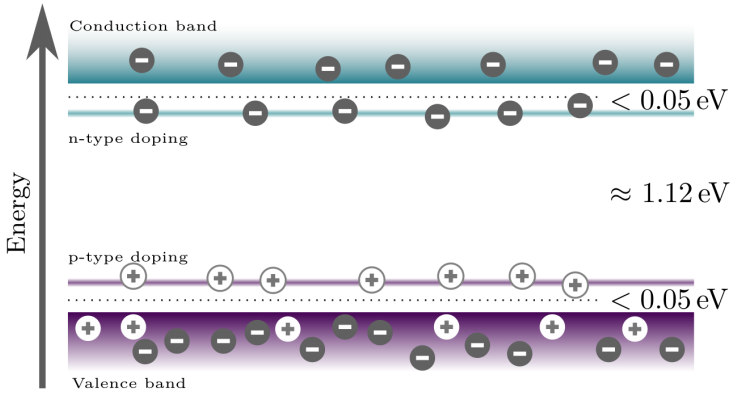

Figure 2.5: Band model as in Fig. 2.4(a) in the presence of n- as well as p-type dopants. Their additional charge carriers are only lightly bound and are located close to their respective band edges. Taken from [17].

The PN Junction

The process of bringing p- and n-type semiconductors into thermal contact results in a structure referred to as *pn junction* or *pn diode*. This configuration is schematically displayed in Fig. 2.6. The (immense) concentration gradient at the boundary, results in a diffusion current I_{diff} of the respective majority carriers from either of the doped regions into the other. As electrons and holes diffuse into the p- and n-doped regions, respectively, they recombine while the ionized atoms remain in place. In this process, a region without free charge carriers is created, the so-called *space charge* or *depletion region*. Its origin is located at the junction and it extends into either side of the doped material. From the stationary charges of the ionized atoms, an electric field E emerges that generates a drift current I_{drift} opposing I_{diff}.
Without external influence, the charges within either space charge region must be equal, giving rise to

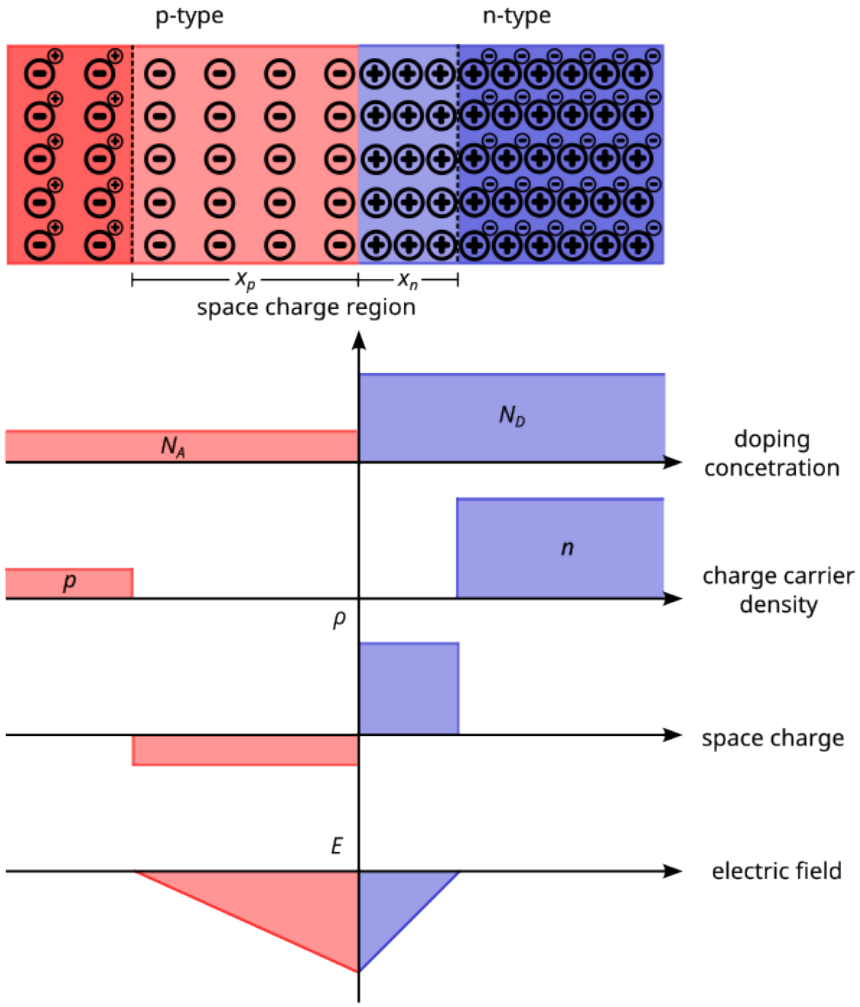

Figure 2.6: Schematic of an abrupt transition of p- to n-type semiconductor, the so-called *pn junction*. The dopants' charge carriers diffuse into the oppositely doped region, resulting in recombination of electrons and holes. This creates a *space charge region* free of charge carriers that extends from the junction into the n-doped (x_n) and p-doped (x_p) material. Adapted from [16].

the so-called *neutrality condition* [16]

$$\frac{x_p}{x_n} = \frac{N_D}{N_A}\,, \tag{2.13}$$

where x_p (x_n) is the extension of the depletion region into the p-doped (n-doped) material. In this constellation, the junction reaches an equilibrium between drift and diffusion of charges, generating the so-called *built-in voltage* V_{bi} that can be written as [17]

$$V_{\text{bi}} = \frac{e}{2\epsilon_{\text{Si}}}\left(N_A x_p^2 + N_D x_n^2\right)\,, \tag{2.14}$$

where $\epsilon_{\mathrm{Si}} = 11.9$ [16] is the relative permittivity of silicon. This allows for a determination of the depletion depth in the respective part of the material as

$$x_p = \sqrt{\frac{2\epsilon_{\mathrm{Si}}}{e}\frac{N_D}{N_A(N_D+N_A)}V_{\mathrm{bi}}}\,, \quad x_n = \sqrt{\frac{2\epsilon_{\mathrm{Si}}}{e}\frac{N_A}{N_D(N_A+N_D)}V_{\mathrm{bi}}}\,. \tag{2.15}$$

With typical doping concentrations in silicon, the built-in voltage lies in the region of $V_{\mathrm{bi}} = 0.4 - 0.8\,\mathrm{V}$. As indicated schematically in Fig. 2.6, the doping concentration in semiconductor detector applications differs between the n- and the p-region, usually by many orders of magnitude. With regard to Eq. (2.13), this results in the depletion zone effectively only growing into the low-doped material.
By application of an external voltage to the pn junction terminals, it is possible to increase the depletion zone beyond the extent arising from the built-in voltage given in Eq. (2.14). This is achieved by connecting the n-type region, or anode, of the diode to a positive potential with regard to the potential present at the p-type side, or cathode, of the structure. This is referred to as *reverse biasing*, with the voltage commonly named *bias voltage* V_{bias} and is the default operation mode of semiconductor detectors. In this state, the junction is not in equilibrium and as the bias increases over the built-in voltage, counteracting I_{diff}, the depletion zone grows.
Due to the depletion zone practically only extending in the weakly doped side of the diode and the bias voltage being at least an order of magnitude larger than the built-in voltage, the depletion width d can be defined as [17]

$$d \approx x_{n,p} \approx \sqrt{\frac{2\epsilon_{\mathrm{Si}}\epsilon_0}{e|N_{\mathrm{eff}}|}(V_{\mathrm{bi}}+V_{\mathrm{bias}})} \overset{V_{\mathrm{bi}} \ll V_{\mathrm{bias}}}{\approx} \sqrt{\frac{2\epsilon_{\mathrm{Si}}\epsilon_0}{e|N_{\mathrm{eff}}|}V_{\mathrm{bias}}}\,, \tag{2.16}$$

where $|N_{\mathrm{eff}}|$ is the absolute *effective doping concentration* of the material into which the space charge region extends and ϵ_0 the vacuum permittivity. This definition is especially relevant after the diode has suffered from radiation damage (see Chapter 4), as radiation-induced effects alter the doping concentration in the depletion region. Conversely, the *full-depletion voltage* V_{dep}, the voltage necessary to extend the depletion region over the full physical width d_{sens} of the sensor, can be calculated as

$$V_{\mathrm{dep}} \approx \frac{e|N_{\mathrm{eff}}|d_{\mathrm{sens}}^2}{2\epsilon_{\mathrm{Si}}\epsilon_0}\,. \tag{2.17}$$

Commonly, silicon detectors are operated *overdepleted*, with a reverse bias voltage larger than V_{dep} applied. As for the example in Section 2.2.1, the free charge carriers generated by a MIP in the depletion region now do not recombine as there are no intrinsic carriers. Instead, they are separated by the external field and collected, generating a measurable signal. This is the concept of semiconductor detectors. The corresponding realization of different sensor implementations is discussed in Section 2.2.3 with the required readout chain briefly introduced in Section 2.2.4.

Diode Electrical Characteristics

The electrical characteristics, namely the Current-Voltage (IV) and Capacitance-Voltage (CV) behaviors, of an ideal pn junction are depicted schematically in Fig. 2.7.
The IV characteristics are shown in Fig. 2.7(a). Without free carriers in the space charge region, the

current originates at the boundaries to the neutral semiconductor. With regard to the external bias voltage V_{bias}, the current exhibits an exponential increase with the temperature T [16]:

$$I = I_S \left(\exp^{\frac{eV_{\text{bias}}}{k_B T}} - 1 \right), . \tag{2.18}$$

Here, I_S is the constant saturation current that is reached for sufficient reverse bias voltages, depending on the geometry and (minority) carrier diffusion characteristics of the diode. Continuously increasing the reverse bias voltage eventually leads to the so-called diode *breakdown* or *breakthrough* after which the current rapidly increases. Due to the high voltage and current, this process can result in permanent damage to the semiconductor material.
In real detector applications, the current flowing when a reverse bias is applied, the so-called *leakage current* I_{leak}, is typically governed by thermal generation of electron-hole pairs in the space charge region and thus proportional to the depleted volume[4] and temperature. The leakage current is an important characteristic and can be defined using the area A of the highly doped implant, named *electrode*, and the depletion depth d as [16]

$$I_{\text{leak}} = eAd\frac{n_i}{\tau_g}\,, \tag{2.19}$$

where τ_g is the lifetime of generated charge carriers. For detector operation, especially its functional dependence on the temperature is an essential quantity. It can be parametrized as [22]

$$I_{\text{leak}} \propto T^2 \exp\left(-\frac{E_{\text{eff}}}{2k_B T}\right) \quad \text{with} \quad E_{\text{eff}} = (1.214 \pm 0.014)\,\text{eV}\,. \tag{2.20}$$

Here, E_{eff} is referred to as the *effective* or *activation energy*. In particular with increasing fluence, the leakage current increases significantly (see Eq. (4.8)) due to the creation of electrically active defects close to the middle of the band gap, so-called deep level defects (see Section 4.3).

The CV behavior of the ideal pn diode is of interest as it allows for the determination of the full depletion voltage V_{dep}. As the space charge region approximately grows only into the low-doped region of the pn junction, the capacitance of the diode can be described by the parallel plate model with a dielectric as

$$C = \frac{\epsilon_{\text{Si}}\epsilon}{d}A\,, \tag{2.21}$$

where A is the diode area and d the depletion width. As d is a function of the bias voltage (cf. Eq. (2.16)), the capacitance of the diode is as well. This CV characteristic is shown in Fig. 2.7(b). Two distinct regions are visible: initially the capacitance decreases with $1/\sqrt{V_{\text{bias}}}$ until full depletion

[4] The leakage current can also have contributions from the surface, caused by the fabrication process or damage conditions from handling of the wafer.

is achieved, from where on the capacitance is constant. This can be described as

$$C = \begin{cases} \sqrt{\frac{e N_{\text{eff}} \epsilon_{\text{Si}} \epsilon_0}{2 V_{\text{bias}}}} A & \text{if } V_{\text{bias}} < V_{\text{dep}} \\ Eq.\ (2.21) & \text{if } V_{\text{bias}} \geq V_{\text{dep}} \end{cases} \tag{2.22}$$

Using a suitable parametrization enables the extraction of V_{dep} from the intersection of two line fits: one to the $C \propto 1/\sqrt{V_{\text{bias}}}$ and one to the C = const. region. As the implementation details of silicon sensors often differ from the ideal assumptions and simplistic geometry of the pn junction, the CV behavior can show deviations from the ideal curve shown in Fig. 2.7(b) (see Section 6.4.2). Nevertheless, the procedure described above to determine the full depletion voltage is sufficient. In contrast, after irradiation the CV behavior starts to depend heavily on the measurement setup (specifically the frequency) as radiation-induced defects, e.g. charge trapping (see Section 4.3.3), play a role. An alternative approach to determine the full depletion voltage of sensors after irradiation is introduced in [23].

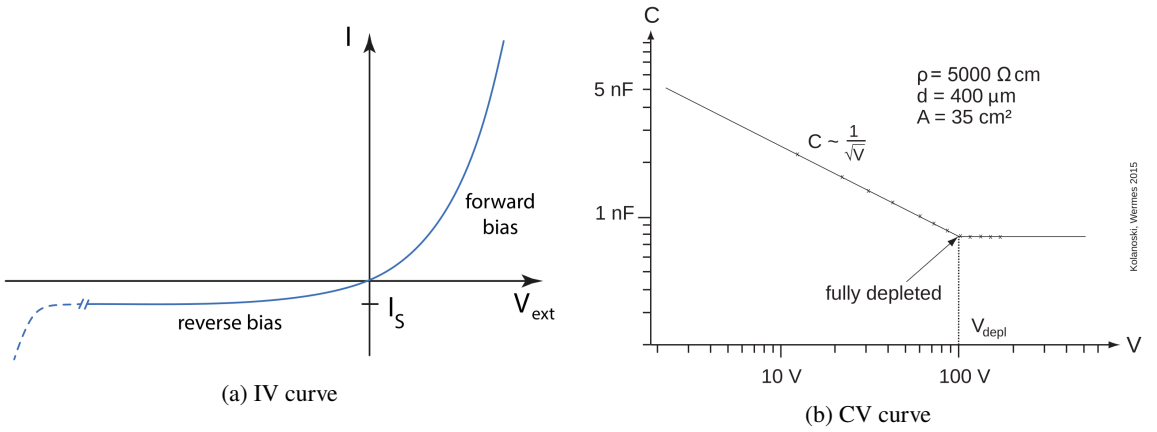

(a) IV curve

(b) CV curve

Figure 2.7: Current-voltage (a) and capacitance-voltage (b) characteristics of an ideal pn diode. Taken from [16].

2.2.3 Pixel Sensor Designs

Due to application-specific requirements, such as fast timing, radiation hardness or low capacitance, the implementation of silicon pixel sensors typically differs from the model of a simple diode shown in Fig. 2.6. The common characteristic among different designs is the realization of a pn junction by a highly doped ($\geq 10^{18}\,\text{cm}^{-3}$) implantation inside a substrate with low doping concentration ($\approx 10^{12}\,\text{cm}^{-3}$). The former is referred to as *collection electrode* and denoted as $\text{n}^{+(+)}$ or $\text{p}^{+(+)}$, depending on the dopant type and concentration. Analogously, the latter is denoted as $\text{n}^{(-)}$ or $\text{p}^{(-)}$ and named *bulk*. Using Eq. (2.12), the high doping concentration of the implantation translates to a low resistivity, facilitating the collection of charge carriers. Conversely, low doping of the bulk results in a high resistivity, allowing for depletion of the substrate (see Eq. (2.16)). Figure 2.8 shows two different geometrical design approaches of silicon (pixel) sensors[5]. The implantation of a shallow

[5] The designs also feature opposite signs of doping of the electrode and bulk (p-in-n in Fig. 2.8(a) and an n-in-p in Fig. 2.8(b)) which have implications on detector operation such as difference in charge collection (electrons versus holes)

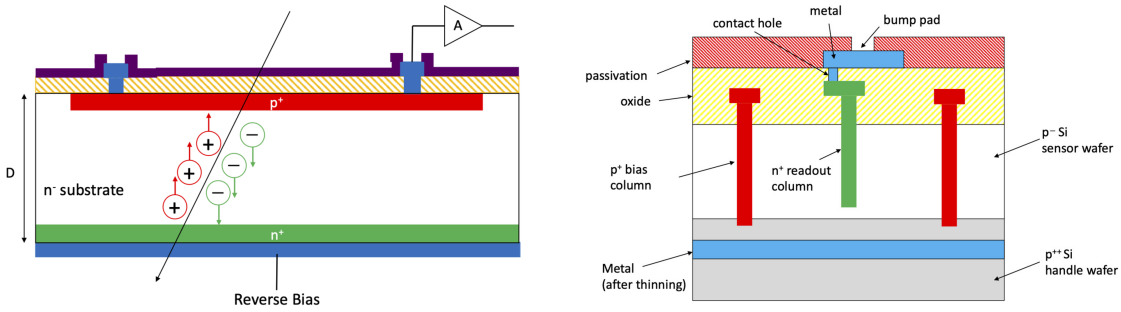

(a) Planar p-in-n pixel

(b) Columnar (3D) n-in-p pixel

Figure 2.8: Two approaches for implementation of semiconductor pixel sensors. The planar (a) sensor features a shallow p^+ collection electrode on an n bulk whereas the 3D sensor (b) implements a junction between columnar n^+ collection and bordering p^+ bias electrodes, all extending perpendicularly to the p substrates surface. In the former case, the depletion zone grows from the collection electrode to the backside, in the latter the bulk is depleted sidewards between the columns. From [24].

collection electrode on the surface of the bulk, extending only a few microns into the substrate, is referred to as a *planar* sensor and depicted in Fig. 2.8(a). In this case, the bulk has a typical thickness of 100 – 300 µm and is depleted from the electrode towards the backside where a highly doped layer of the same doping as the bulk prevents further extension of the space charge region and creates an ohmic contact. This design is applicable for environments with modest radiation hardness and timing requirements, as radiation-induced defects significantly increase the voltage (see Section 4.3.2) to fully deplete the bulk and decrease the signal as a function of drift distance due to trapping (see Section 4.3.3).
The so-called *3D* pixel design improves the performance in these aspects and is portrayed in Fig. 2.8(b). It consist of an arrangement of columnar electrodes, extending perpendicular to the substrate surface into the bulk. The collection electrode is surrounded by multiple bias electrodes, defining the volume of the cell, which is depleted sidewards between the pillars. Due to the spacing between collection and biasing electrodes being significantly smaller than typical bulk thicknesses, the maximum drift distance and the full depletion voltage are substantially lower compared to the planar cell. This enables full depletion of the sensor volume even at extreme fluence levels, facilitating high collection efficiencies. Disadvantages of the 3D design versus the planar approach are the large electrode surface, resulting in a high leakage current and capacitance (see Eqs. (2.19) and (2.21)), relevant properties for potential cooling during detector operation and the interface to readout electronics, respectively.
To realize a complete detector, the latter is required to read out the charge signal that is generated inside a sensitive volume and thus qualitatively discussed in the next section.

2.2.4 Readout Chain

The charge carriers that are generated inside the depletion zone of a semiconductor sensor under reverse bias, are separated by the electric field and begin to move towards the respective implant. The separation and movement induce a signal at the collection electrode which requires analog and

and radiation hardness (dopant removal). In this paragraph, only the difference in geometrical sensor implementation is considered.

subsequent digital processing in order to extract the available information. A typical chain of readout stages of a pixel detector is shown in Fig. 2.9.
Immediately following the sensor, a series of analog processing units is implemented. First, a charge sensitive amplifier (CSA) generates an output voltage that rises with the amount of collected charge. The CSA output is shaped and fed into an a comparator which generates a constant (digital) output voltage if the input signal is greater as a predefined threshold voltage. If the collected charge results in a high output state of the comparator, the digital logic of the detector generates a timestamp and registers a *hit* in the corresponding pixel. If the logic only differentiates between hit and no-hit pixels, the scheme is referred to as *binary*. The amount of time for which the comparator remains in the high state for a given charge, the so-called *time-over-threshold (ToT)*, is directly proportional to the collected charge and typically given in units of clock cycles. Creating a known amount of charge at the input of the CSA (e.g. by a dedicated injection circuitry or by X-ray sources), facilitates a mapping of ToT values to the number of charges, the so-called *charge calibration* which enables an extraction of additional information about the particle.

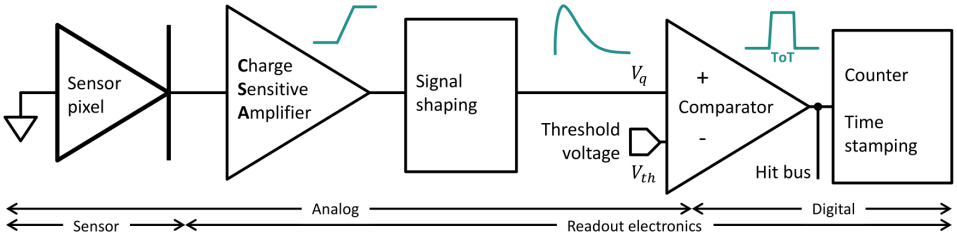

Figure 2.9: Schematic readout chain of a silicon pixel detector. The charge signal, originating in the sensitive volume, undergoes analog amplification, shaping and discrimination, resulting in binary hit information. Digital circuitry facilitates charges measurement using the ToT. From [17].

In modern pixel detectors, the readout chain presented in Fig. 2.9 is typically implemented in each individual basis. Due to variations in the sensor cells as well as analog and digital stages across $O(10^5)$ pixels, dedicated registers provide the possibility to tune the feedback of individual pixels to achieve a uniform response across the entirety of the matrix. This process is generally referred to as *tuning* and is required to adjust the detector for operation at a given threshold, different environmental parameters or increasing radiation levels.

2.3 Pixel Detector Design Approaches

Pixel detectors for High Energy Physics (HEP) applications, consisting of a matrix of sensitive pixel cells with corresponding readout electronics, are primarily realized in two different approaches, which are shown in Fig. 2.10. The state-of-the-art design for harsh radiation environments is the *hybrid* detector (Fig. 2.10(a)), corresponding to the architecture of the current and future ATLAS pixel trackers [25]. In this approach, the sensitive volume and the respective analog and digital readout electronics are fabricated on separate silicon wafers which are connected pixel-by-pixel via a metal bump, a process referred to as bump bonding. Thus, the readout electronics chip, also called front-end (FE) chip, and the sensor have matching geometries. An advantage of this design is the possibility to decouple the development as well as fabrication processes of both parts, allowing for individual optimizations according to the different requirements. This results in unmatched radiation hardness,

retaining hit detection efficiencies of $\geq 97\,\%$ at equivalent fluence levels of $\geq 10^{16}\,\mathrm{n_{eq}/cm^2}$ [26]. As this approach requires the development, production and testing of two dedicated chips, followed by fabrication of a complete detector assembly by bump bonding and re-testing, the manufacturing of hybrid pixel detectors is subject to high cost. Furthermore, as the bump-bonding process requires a certain thickness of both elements to be successful, the material budget of this system has a negative impact on the track reconstruction capabilities due to scattering (see e.g. [20]), especially in low-energy applications.

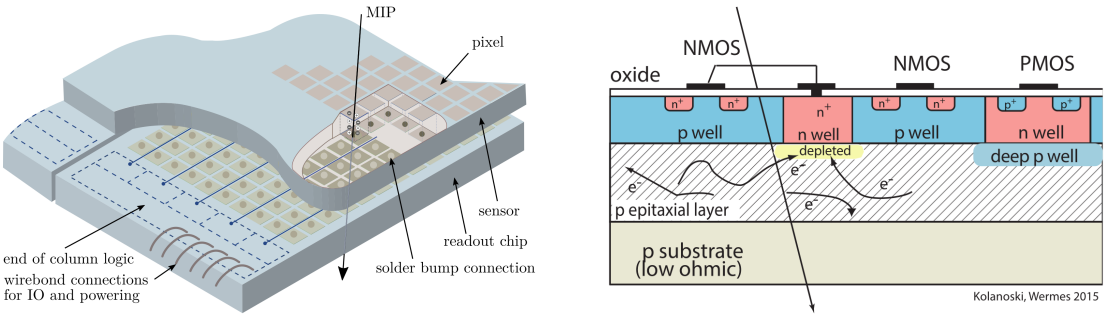

(a) Hybrid pixel matrix. Taken from [17]

(b) MAPS pixel cell. Taken from [16]

Figure 2.10: Schematic of a hybrid pixel detector matrix (a) and a single monolithic MAPS pixel cell (b). The hybrid detector consists of a separate sensor and FE chip, connected through metallic bonds. The monolithic structure implements the required electronics on the surface of the sensitive volume, on the same silicon substrate.

In recent years, the availability of advanced commercial Complementary Metal-Oxide-Semiconductor (CMOS) processes, gave rise to the appearance of *monolithic* devices (Fig. 2.10(b)), so-called Monolithic Active Pixel Sensors (MAPSs), demonstrating radiation hardness that qualifies for many applications in the field of HEP [27, 28]. In this design, the sensitive volume and FE electronics are fabricated on the same silicon substrate. The chip logic is implemented on the substrates' surface, requiring shielding in the form of highly doped *wells*, to prevent the logic nodes from competing with the electrode for charge collection. In the MAPS structure, the depleted volume underneath the electrode reaches only a few microns into the bulk, relying on the diffusion of the generated charges into the space charge region. In this case, only a small fraction of e.g. a MIP signal (see Eq. (2.11)) is detected, requiring a very low noise level of the FE electronics ($\mathcal{O}(100)e^-$) to maintain a reasonable signal-to-noise ratio. In case the MAPS architecture allows for full depletion of its bulk, it is referred to as Depleted Monolothic Active Pixel Sensor (DMAPS) which relies on the availability of high-resistivity processes. The possibility of implementing MAPS structures in commercial CMOS processes, significantly reduces the complexity and cost of the research and development phase of such devices. Furthermore, the material budget can be substantially reduced to only a fraction of the total material budget of a typical hybrid detector.
As monolithic devices are currently entering the HEP field, their suitability for extreme radiation environments, such as the tracking systems at e.g. ATLAS and CMS, needs to be probed carefully. For this reason, radiation hardness studies need to be conducted, making irradiation sites a necessary development infrastructure.

CHAPTER 3

The ATLAS ITk Pixel Detector for the HL-LHC Upgrade

The ATLAS experiment, located at the LHC at CERN, is a general-purpose particle detector, consisting of multiple dedicated sub-systems. Notably in 2012, data recorded using the ATLAS detector enabled the long-awaited discovery of the Higgs boson [3], marking the most impactful achievement in the field of modern particle physics.
To improve its discovery potential, the LHC will undergo an upgrade, the so-called HL-LHC, scheduled to take place between 2026 and 2028, increasing the integrated luminosity by a factor of 10 over the course of the experiment [7]. Especially for the innermost tracking systems of ATLAS, the increase in instantaneous luminosity results in a significantly higher pile-up, i.e. interactions per bunch crossing, from an average of approximately 40 to 200 [29]. To cope with these requirements, the ATLAS tracking detector will be replaced by an all-silicon tracker, the ATLAS ITk [9, 30].
This chapter aims to describe the ATLAS experiment within the context of the HL-LHC. Therefore, the LHC, its high luminosity upgrade and the relevant physics program, i.e. the Higgs phenomenology at the LHC, are briefly treated in Section 3.1. The ATLAS detector and the upgrade of its inner tracking system for the HL-LHC, the ATLAS ITk, are detailed in Section 3.2. Finally, Section 3.3 introduces the novel pixel readout chip for the ITk, the `ITkPix`, designed to cope with the increased occupancy and collision rate and thus, radiation conditions.

3.1 The Large Hadron Collider

The LHC is the largest and most powerful particle accelerator up to date [31, 32]. As it is a so-called *synchrotron* machine, it consists of a storage ring with a circumference of approximately 27 km, located 100 m beneath the ground in the Geneva region in Switzerland and is operated by CERN. A schematic overview of the accelerator facility at CERN is shown in Fig. 3.1. Within the LHC ring, two opposing proton (or heavy ion) beams circulate while being repeatedly accelerated by Radio Frequency (RF) cavities up to a maximum energy of 7 TeV before they are brought to collision in one of the four large experiments: ATLAS, CMS, ALICE[1] or LHCb[2]. At the maximum accelerator

[1] A Large Ion Collider Experiment
[2] Large Hadron Collider beauty

performance, the protons have a velocity $> 99.99\,\%$ of c and a center-of-mass collision energy of $\sqrt{s} = 14\,\text{TeV}$.
The particles inside the LHC are grouped in so-called *bunches*. The accelerator has a capacity of $n_b = 2\,808$ bunches per beam, corresponding to a bunch spacing of $t_b = 25\,\text{ns}$, with a nominal number of protons per bunch $N_p = 1.2 \times 10^{11}$. They revolve with a frequency of approximately $f_{\text{rev}} = 11\,\text{kHz}$ inside the storage ring. Using these parameters, the instantaneous luminosity $\mathcal{L}$ of the machine, as in Eq. (1.1), can be defined as [7]

$$\mathcal{L} = \gamma \frac{n_b N_p^2 f_{\text{rev}}}{4\pi \varepsilon_n \beta^*} R\,, \quad \text{with} \quad R = \frac{1}{\sqrt{1 + \frac{\theta_c \sigma_z}{\sigma}}}\,. \tag{3.1}$$

Here, γ is the relativistic Lorentz factor, ε_n is the normalized transverse beam emittance, a measure of the beam area in phase space, and β^* is the beta function at the point of collision. The factor R constitutes a reduction of the luminosity by geometrical conditions with σ and σ_z being the transverse and longitudinal beam root-mean-square widths, respectively, and θ_c the crossing angle of the colliding bunches. With the nominal values for the operation of the LHC, an instantaneous luminosity of $\mathcal{L} = 1 \times 10^{34}\,\text{cm}^{-2}\,\text{s}^{-1}$ is obtained which translates to a collision rate in the order of of $1 \times 10^9\,\text{Hz}$ and an average pile-up of 30 per bunch crossing. A peak instantaneous luminosity of $\mathcal{L} = 2 \times 10^{34}\,\text{cm}^{-2}\,\text{s}^{-1}$ was reached in 2018, which approximately corresponds to the maximum achievable value with the current configuration of the accelerator [7]. After a total of three data taking runs, the operation of the LHC will have accumulated an integrated luminosity of $\mathcal{L}_{\text{int}} = 350\,\text{fb}^{-1}$, with the final run scheduled to be completed in 2026 [33].

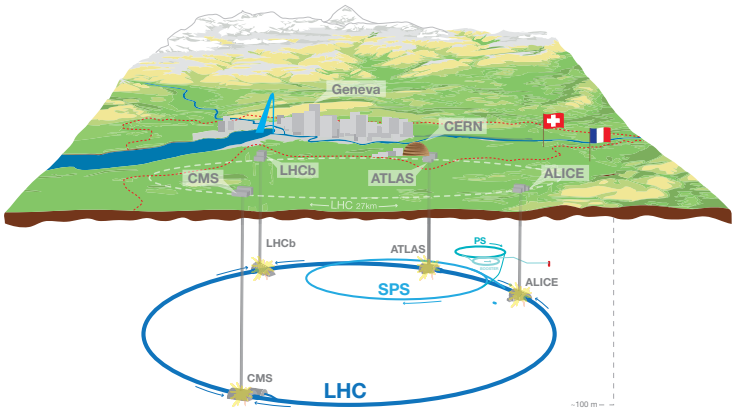

Figure 3.1: Schematic overview of the CERN accelerator complex, showing the LHC ring, its injector stages and the location of the four large experiments: ATLAS, CMS, ALICE and LHCb. From [34]

3.1.1 High-Luminosity LHC Upgrade

The discovery potential at the LHC is primarily determined by the number of recorded events, i.e. Eq. (1.1), and the maximum achievable center-of-mass energy, $\sqrt{s}$, in collisions. With the current technology, the latter can only be substantially increased by increasing the circumference of the accelerator rings. As the former can be increased by upgrading major machine components instead, it corresponds to the upcoming plan to extend the LHC's exploration capability for BSM and rare physics.
The LHC will undergo a major upgrade with the aim to increase its instantaneous luminosity by a factor 5 – 7.5. This HL-LHC upgrade will take place after the final data run as part of a three-year-long machine shutdown, which is currently set to take place from 2026 to 2028. With regard to Eq. (3.1), the improvement in instantaneous luminosity at the HL-LHC will predominantly be achieved by increasing the number of particles per bunch, N_p, while simultaneously reducing the beam emittance, ε_n. Furthermore, as they are closely related, the ratio of the geometric reduction factor and the beta function at the interaction point, R/β^*, is to be adjusted, to result in an overall luminosity gain.
The upgrade is realized by renewal of beamline elements, such as focusing magnets, injections and cooling capabilities, along approximately 1.2 km of the current LHC. After completion, the HL-LHC is expected to accumulate a yearly integrated luminosity in the order of the nominal LHC over its entire runtime.

3.1.2 Higgs Physics at the LHC

Since the discovery of the Higgs boson at the LHC [3, 4] in 2012, the exploration of its properties, such as mass and couplings to other particles and itself, have been a major goal of the HEP community. As an example to motivate the need for complex detector systems and high luminosities, the dominant Higgs production mechanisms at the LHC are depicted in Fig. 3.2. Furthermore, the corresponding production cross sections as a function of $\sqrt{s}$ and subsequent branching ratios, depending on the Higgs mass, are shown in Fig. 3.3.

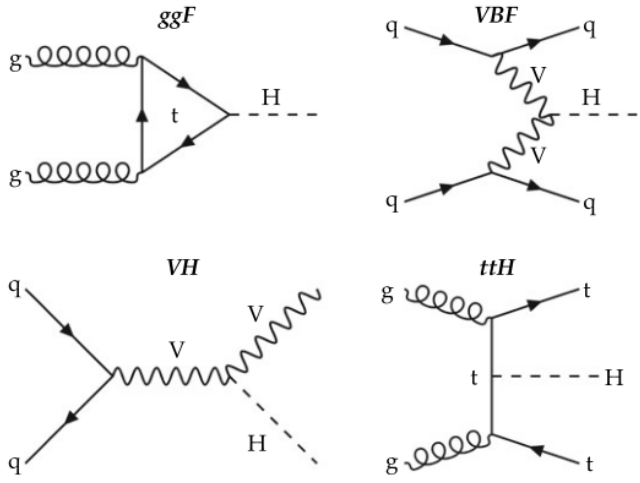

Figure 3.2: Feynman diagrams of dominant Higgs production processes at LHC: gluon-gluon fusion (top-left), vector-boson fusion (top-right), associated production with a vector boson and top quarks (bottom-left and bottom-right respectively). From [35].

For the available center-of-mass energies at the LHC and the SM Higgs mass of $m_H = 125\,\text{GeV}$ [6], the *gluon-gluon fusion* (ggF) is the most dominant process by a margin of almost two orders of magnitude. In descending order, *vector-boson fusion* (VBF), *Higgs-strahlung* off a vector boson (VH) and associated production of Higgs with two top quarks (ttH), are the other contributors to the generation of Higgs bosons at the LHC. Using Fig. 3.3(a) to estimate a cumulative[3] production cross section of $\sigma_H^{\text{LHC}} \approx 55\,\text{pb}$, Eq. (1.1) enables the calculation of the total number of produced Higgs bosons at the LHC to be $N_H^{\text{LHC}} \approx 20 \times 10^6$. In contrast, due to the higher energy of $\sqrt{s} = 14\,\text{TeV}$ and a corresponding larger production cross section $\sigma_H^{\text{HL-LHC}}$ of approximately 70 pb, the number of created Higgs bosons at the HL-LHC will be in the order of $N_H^{\text{HL-LHC}} \approx 260 \times 10^6$, demonstrating its large potential for Higgs precision studies.

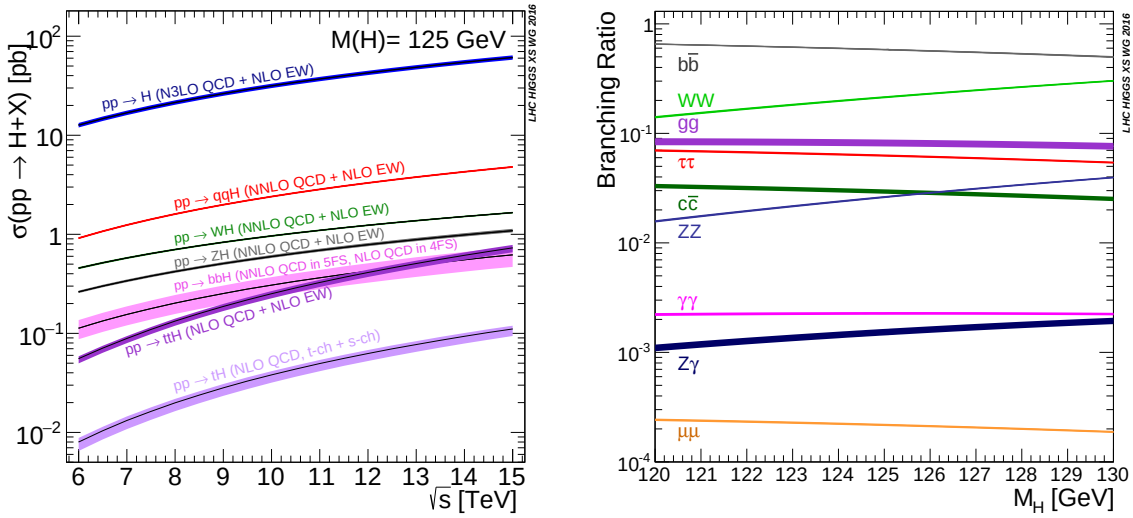

(a) Production cross section versus $\sqrt{s}$

(b) Branching ratios versus m_H

Figure 3.3: Higgs production cross sections in proton-proton collisions at the LHC (a) and branching ratios (b) as a function of the center-of-mass collision energy $\sqrt{s}$ and the Higgs mass m_H, respectively. From [36]

Due to its large decay width [6], the mean lifetime of the Higgs boson is in the order of $10^{-22}\,\text{s}$, making it only detectable via its decay products. Figure 3.3(b) displays the so-called *branching ratios*, i.e. the relative probability for the different decay modes, of the Higgs boson as a function of its mass. At the SM Higgs mass, the dominant decay channels, as well as for example the VBF production in Fig. 3.2, result in final states with a substantial amount of hadronic background from quark pairs or secondary decays, posing a challenge for the detection and identification. As Eq. (1.1) yields the number of produced particles for any given cross section σ, the fraction of correctly reconstructed events, facilitating the characterization of the primary particle, is determined by the capabilities of the detector and subsequent data analysis.

[3] Due to the varying center-of-mass energies between $\sqrt{s} = 7 - 14\,\text{TeV}$ over the three LHC runs, the production cross section also varies (see Fig. 3.3(a)).

3.2 The ATLAS Experiment

The ATLAS experiment is the largest of the two general-purpose detector systems at the LHC. It consist of several detector systems, arranged in a layered barrel structure and endcaps in the forward/backward region, covering nearly the entire solid angle around the IP. With an approximate weight of 7 000 t, a length of 44 m and a diameter of 25 m, it is the largest detector system ever constructed and operated [37]. A labeled schematic of the ATLAS detector for the final LHC data taking run is displayed in Fig. 3.4.

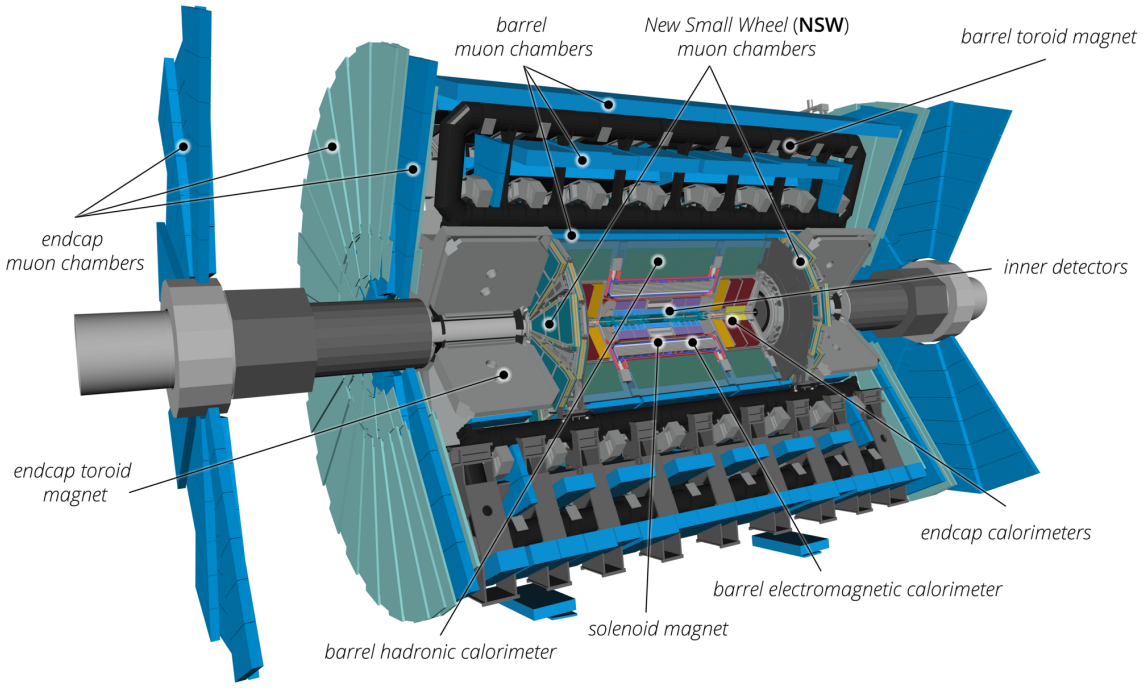

Figure 3.4: Schematic overview of the ATLAS detector configuration for the third and final run of the LHC. From [37].

The main components of ATLAS (from inner- to outermost) are the Inner Detector (ID), responsible for charged particle tracking and vertex reconstruction, the calorimetry system, capable of position and energy measurement of electromagnetically and strongly interacting particles, and the muon spectrometer, tracking emerging muons for event reconstruction, trigger and veto purposes. In the following, the systems are briefly introduced, the information is taken from [9, 37, 38].

Inner Detector As the innermost element of the ATLAS detector, the ID is tasked with vertex and track reconstruction of charged particles, allowing for the determination of their momenta, lifetimes and the location of the IP. It has a radial extension of $r = 31 - 1\,106$ mm from the center and is submerged in a magnetic field of 2 T along the beam axis. Its innermost component is the silicon pixel detector, arranged in four barrel layers encircling the IP parallel to the beam axis and encapsulated by a stack of three disks on both ends perpendicular to the beam axis. The central layer is the so-called Insertable B-Layer (IBL), retroactively installed to improve the

tracking performance, which has a pixel pitch of $(50 \times 250)\,\mu m^2$ whereas the remaining pixels have a pitch of $(50 \times 400)\,\mu m^2$. The configuration has a total of approximately $2\,m^2$ of active area and 10^8 readout channels.
Surrounding the pixels, the SemiConductor Tracker (SCT) is laid out in a similar scheme, using silicon microstrip detectors with a pitch of 80 µm. Analogous to the pixels, they are structured in four barrel layers with a stack of nine discs on both ends. A total active area of $60\,m^2$ is covered via 6×10^6 readout channels.
The outermost part of the ID is the Transition Radiation Tracker (TRT), consisting of 300 000 gas-filled, thin-walled, proportional-mode drift tubes that perform charged particle tracking with approximately 130 µm resolution. As their semiconductor counterparts, the TRT is arranged in barrel layers and stacks of disks. Transition radiation material is interleaved between the tubes of the TRT, providing electron identification alongside its tracking capabilities.

Calorimeters The calorimeter systems of the ATLAS detector are responsible for the position and energy measurement of incoming particles which are fully absorbed in the detector. To allow for measurement of electromagnetically as well as strongly interacting particles, two dedicated calorimeters are installed: a liquid argon electromagnetic and a tile hadronic calorimeter.
The former is arranged around the ID and is composed of multiple sub-structures, covering most of the solid angle. It consists of alternating layers of high Z metals and liquid argon at approximately $-184\,°C$. Via the processes described in Section 2.1.1, charged particles produce secondary electromagnetic showers in the metal whose constituents ionize the liquid argon. The total ionization current measured is proportional to the initial energy, facilitating its determination.
The hadronic calorimeter surrounds the electromagnetic calorimeter and consists of several layers of alternating tiles of steel and scintillators. Particles that have not been absorbed in the liquid argon calorimeter, similarly are converted to hadronic showers inside the steel tiles whose are photons registered in the scintillators. The photons are collected and converted to an electric current, which again, enables the reconstruction of the original energy of the particle.

Muon Spectrometer The outermost element of the ATLAS experiment is the muon system, compromised of a multitude of different tracking detector technologies, encircling the other detector systems. Its main purpose is to track and measure the momenta of muons that emerge from collisions, adding to the information required for event reconstruction and enabling triggering and vetoing mechanisms. Large superconducting air-core toroid magnets in the central region provide the field for deflection of the muon required for momentum determination. Within a time frame of 2.5 µs, fast response detectors of the muon spectrometer provide feedback to the trigger system of ATLAS to allow for event selection for physics analysis.

As described in [37], the majority of the outer detector systems, i.e. the calorimeters as well as the muon system, require very few changes to cope with the substantial increase in instantaneous luminosity expected from the HL-LHC. In contrast, due to the close proximity to the IP, a complete replacement of the ID is necessary to sustain an adequate tracking performance with the increased particle rate, pile-up and radiation background.

3.2.1 The ATLAS Inner Tracker Upgrade

The inner tracking detector of the ATLAS experiment will be completely replaced by an all-silicon tracking system, the ATLAS Inner Tracker (ITk). The initial design of the ITk is described in [9] and its tracking performance is detailed in [29], where most of the quantitative information is taken from. A labeled schematic of the ITk is depicted in Fig. 3.5. It consist of two dedicated silicon semiconductor tracking systems: an inner pixel detector surrounded by an outer microstrip detector.

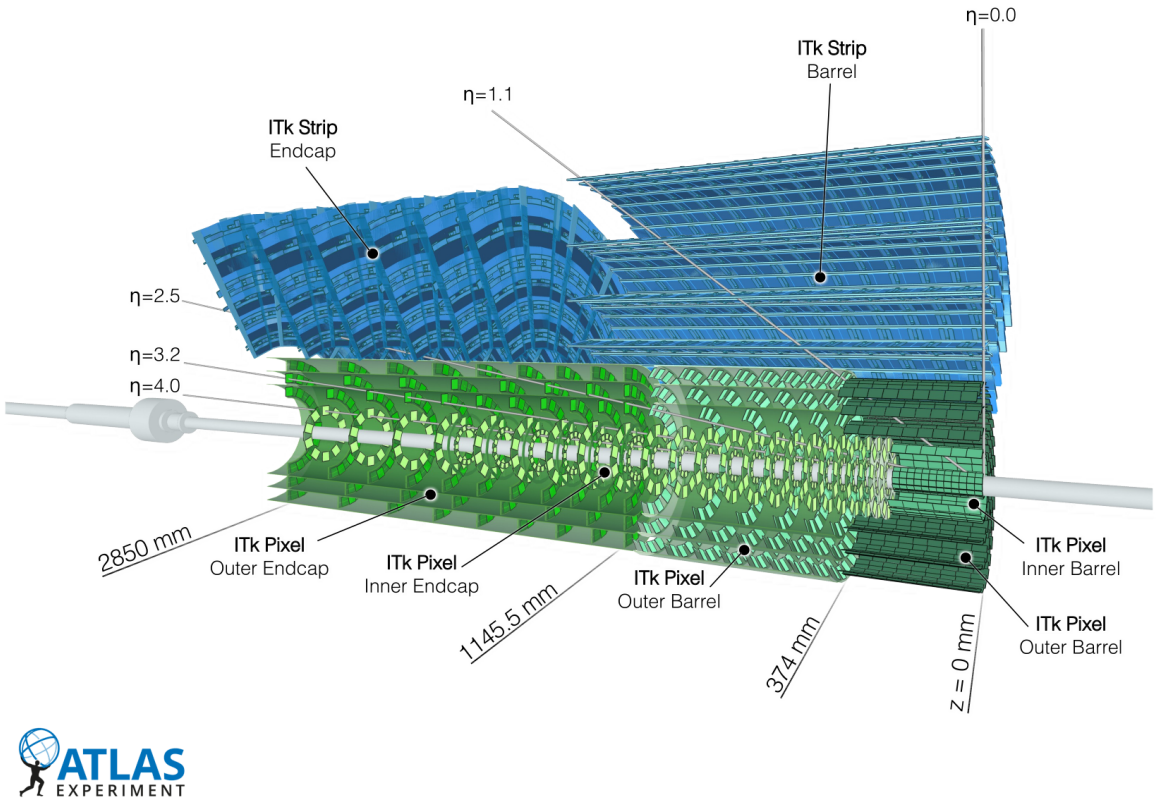

Figure 3.5: Schematic of a section of the ITk for the HL-LHC upgrade. The IP is located at $z = 0$, on the right side of the drawing. From [39]

The pixel system consists of five flat barrel layers, arranged centrally around the IP, and stacks of double-sided endcap rings of different radii located in the forward and backward region. The pixel barrel spans radially from its innermost layer at $r = 34$ mm to its outermost layer at $r = 291$ mm with an extension along the beam axis of $|z| = 0 – 372$ mm ($|z| = 0 – 245$ mm for the innermost two layers). The pixel endcaps are stacked along the beam axis, extending across $|z| = 263 – 2\,850$ mm on either side, with six different radii between $R = 33 – 275$ mm and a varying number of double-sided rings between 6 – 23. The total active pixel area, compromised of a novel hybrid detector, which is the subject of Section 3.3, is approximately 13 m^2. A nominal pitch of $(50 \times 50)\,\mu m^2$ is used for all pixel sensors expect in the central region of the innermost barrel layer, where a pitch of $(25 \times 100)\,\mu m^2$

is utilized. Furthermore, the two innermost layers of the pixel barrel are installed as a separate unit, allowing for their individual replacement which is the current strategy of the ITk to handle the increased radiation levels.
The ITk silicon microstrip detector is located around the pixel detector, exhibiting a similar arrangement. It is explained in detail in [40] and compromised of four barrel layers and stacks of six endcap rings, surrounding the pixel detector. The barrel layers are at radii of $r = 405 - 1\,000$ mm and span symmetrically along the beam axis across $|z| = 0 - 1\,400$ mm. With this setup, the total sensor area is approximately 165 m^2. The inner two barrel layers feature strips with lengths of 24.1 mm whereas for the outer two barrel layers strips of 48.2 mm length are used. Within the endcap rings, the dimension grows with their increasing radius from 19 mm to 60.1 mm. The strip pitch in the barrel section is 75.5 µm whereas in the endcap rings it varies between 69.9 – 80.7 µm.
With this configuration, the newly designed ITk is expected to deliver a tracking performance comparable to the current ID of ATLAS at the much higher instantaneous luminosity of the HL-LHC [29]. As previously outlined in Fig. 1.1, the anticipated equivalent fluence and Total Ionizing Dose (TID) (see Section 4.1.1) levels for the innermost layers of the pixel barrel and endcaps rings after an integrated luminosity of 4 000 fb^{-1} are 2.6×10^{16} n_{eq}/cm^2 and 2 Grad, respectively, where a safety factor of 1.5 is included [9]. To cope with these extreme radiation levels, the inner part of the ITk pixel structure will be replaced after 2 000 fb^{-1}, requiring the pixel detector unit to withstand a corresponding fluence and TID in the order of 1×10^{16} n_{eq}/cm^2 and 1 Grad, respectively.

3.3 The ATLAS ITk Pixel Readout Chip

Especially for the innermost layers of the tracking detector, the increased pile-up at the HL-LHC results in a much higher occupancy, i.e. hits per area and time. This requires a higher granularity, data processing and transmission speeds, and radiation hardness, compared to the current generation of ATLAS pixel chips. Therefore, in a joint development effort of the ATLAS and CMS experiments, the RD53 collaboration [10] was formed in 2013 and tasked with the design of a novel pixel detector chip for the HL-LHC tracking detectors. The chip details are specific to the ATLAS and CMS requirements where the former is named `ITkPix` and the latter `CROC`. A series of three successive iterations of RD53-type chips have emerged: the `RD53A`, `RD53B` and `RD53C`, corresponding to the prototype, pre-production (`ITkPixV1`) and final chip (`ITkPixV2`). An overview of the development process, the principal design and chip characteristics is given in [41]. As radiation hardness studies of the `ITkPix` are the subject of Chapter 7, it is introduced in following. A photograph of this chip, mounted on a dedicated Printed Circuit Board (PCB) for characterization, is depicted in Fig. 3.6.
The ITk pixel detector follows a hybrid approach (see Section 2.3) with the `ITkPix` readout chip manufactured in a 65 nm CMOS process. It features a matrix of 400 × 384 columns and rows, respectively, with a pixel pitch of (50 × 50) μm^2 and a chip area of (20 × 21) mm^2. The chip is capable of handling hit and trigger rates of up to 3.5 GHz cm^{-2} and 1 MHz respectively. The per-pixel analog FE readout chain (see Section 2.2.4) is operated at nominal thresholds between $1 - 1.5\,ke^-$ while providing a signal charge (ToT) measurement with 4 bit resolution. It contains a dedicated charge injection circuitry for probing the threshold settings and calibration purposes. To allow for high particle hit rates, the chip offers a readout rate of up to 5.12 Gbit s^{-1}. Dedicated leakage current compensation circuitry allows for sensor leakage currents of up to 10 nA per pixel and therefore high radiation levels. The digital logic of the `ITkPix` is designed and tested to withstand TIDs of well

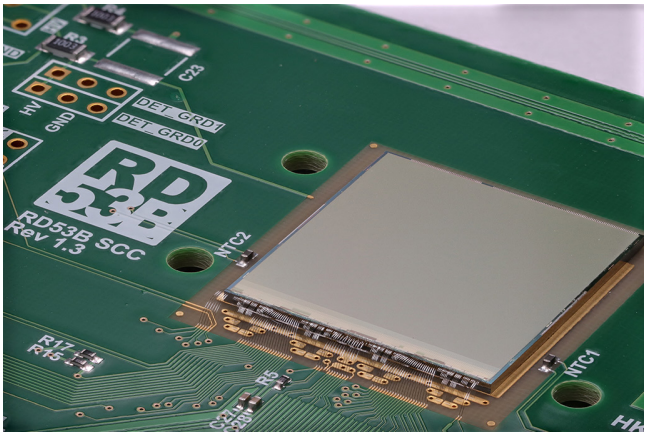

Figure 3.6: Close-up of an `ITkPixV1` situated on a PCB for testing. Thin wire bonds connect the digital chip bottom to traces on the PCB, facilitating powering and communication. From [42].

above 1 Grad (e.g. [35, 43]), translating to 5 – 10 years of HL-LHC operation.
The chip area is separated into the pixel matrix and the digital chip bottom, housing the various logic blocks for receiving commands, sending data, and interfacing registers. Additionally, it contains Analog-to-Digital Converters (ADCs) and Digital-to-Analog Converters (DACs) for biasing, calibration and monitoring purposes as well as temperature and radiation (i.e. TID) sensors.
To form a complete hybrid pixel detector assembly for the ATLAS ITk, also 3D sensors (see Section 2.2.3) with a pixel pitch of $(50 \times 50)\,\mu m^2$ ($(25 \times 100)\,\mu m^2$ in the innermost region) and an active thickness of 150 µm have been developed and characterized [26]. They are tested to operate within ATLAS requirements for tracking performance and power consumption at an equivalent fluence of above $10^{16}\,n_{eq}/cm^2$.

3.3.1 Laboratory Test And Data Acquisition System

To test and characterize the RD53 family of hybrid pixel chips for the HL-LHC upgrades of ATLAS and CMS, the BDAQ53 [44] detector readout system was developed at the University of Bonn. The typical BDAQ53 setup, interfacing an `ITkPix` readout chip, is shown in Fig. 3.7. On the hardware side, the Data Acquisition (DAQ) system consist of the BDAQ53 board, hosting a Field-Programmable Gate Array (FPGA), and a dedicated PCB for characterization, the so-called Single-Chip Card (SCC), on which the chip is situated. Both are connected via a common DisplayPort cable, establishing an interface between the BDAQ53 board and the RD53-type Device Under Test (DUT).
The DUT is connected to the SCC via multiple thin wire bonds, attaching to dedicated pads on the chip bottom (see Fig. 3.6). Various connectors on the SCC facilitate powering, biasing and monitoring of DUT properties. Via the DisplayPort connection to the BDAQ53 board, the chip can be configured and read out. The board itself hosts a commercial FPGA daughter board, constituting the translation layer between the DUT and the DAQ computer. The BDAQ53 system provides the possibility to operate multiple chips simultaneously and connect external trigger inputs from a Trigger Logic Unit (TLU) for synchronization in e.g. test beam measurements (see Section 7.3). The BDAQ53 board connects to the DAQ computer via Ethernet.

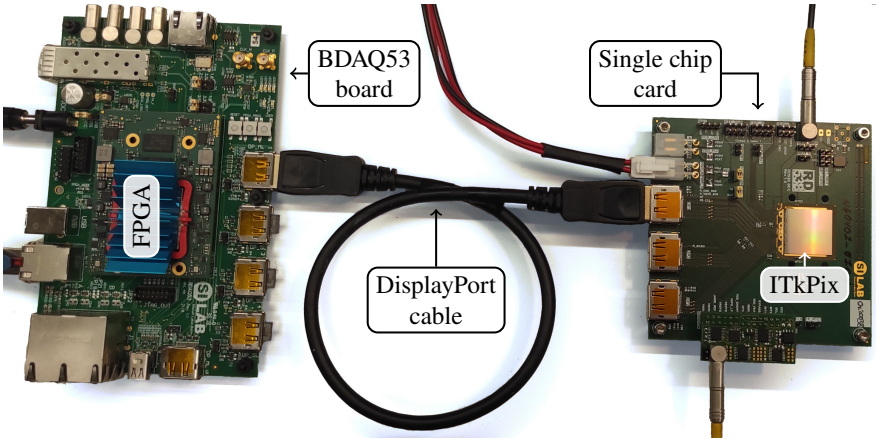

Figure 3.7: Overview of the BDAQ53 pixel detector readout system for RD53-type DUTs. It consists of the BDAQ53 board and a DUT-specific SCC, connected via a DisplayPort cable. Adapted from [43].

On the software side, the BDAQ53 framework consists of a collection of open-source *Python* scripts and *Verilog* firmware modules. The former provide an easy-to-use interface to configure and operate RD53-type chips. Additionally, they contain predefined routines for performing common DUT-related tasks such as identifying and disabling malfunctioning pixels or measuring the threshold distribution of the matrix. The latter are structured in a modular fashion, allowing for easy extension of features as well as integration of new chip types. Due to this versatility of the BDAQ53 platform, it has been adapted to facilitate the readout of other pixel detectors [45, 21].
The minimal hardware and user-friendly software of the BDAQ53 readout system, simplify the readout of RD53-family DUTs in a wide range of applications such as laboratory tests, efficiency studies and irradiation campaigns.

CHAPTER 4

Radiation Damage in Silicon Detectors

Semiconductor devices that are operated in radiation environments, such as in medical, X-ray, space or HEP applications, suffer from radiation-induced defects, that deteriorate their performance. In most scenarios, the damage results in simultaneous degradation of the digital part, i.e. the transistors compromising the logic gates, and the sensitive volume of the detector. Especially the latter has immediate effects on the operational parameters, eventually resulting in the device not meeting its application-specific requirements. Among the various application areas, the current and future HEP experiments represent unprecedented radiation environments for microelectronics, surpassing the tolerance required for e.g. typical space applications by orders of magnitude [41]. To ensure their functionality up to anticipated radiation damage levels, particularly for devices that are not accessible during operation (e.g. detectors in large experiments or space), radiation hardness tests are a necessity. As silicon is the most used material for microelectronics and semiconductor detectors, its radiation hardness is of particular interest. For this purpose, the RD50 collaboration [46] was initiated at CERN, to study radiation-induced damage in silicon devices, consequences for detector applications and mitigation strategies. As the central task of this thesis is the development and characterization of a proton irradiation site for probing the radiation hardness of silicon detectors (see Chapters 5 and 6), this work was largely performed within the context of RD50. Consequently, the radiation-induced defect mechanisms and their implications on silicon devices are treated here[1].

Section 4.1 introduces the damage mechanisms in silicon, namely in the *surface* and *bulk* regions of semiconductor detectors, and their microscopic manifestation inside the crystal lattice. The so-called Non-Ionizing Energy Loss (NIEL) scaling hypothesis, a crucial theory for enabling normalized damage simulations for experiments such as ATLAS and employing particle accelerators for defect studies, is explained in Section 4.2. Section 4.3 describes the damage-induced implications on the operation and performance of the detector, constituting its deterioration. Following, the evolution of the defects over time and temperature, the so-called *annealing*, is treated. It is an important tool for optimizing the operation of irradiated detectors and normalization of damage via NIEL scaling. Lastly, in Section 4.5, a short description of the limitations of NIEL scaling and simulation-based damage prediction tools is given, motivating the need for irradiation facilities.

[1] In principle, the qualitative description of radiation-induced damage in this chapter is also applicable for semiconductor materials other than silicon, where the particular quantities that characterize the deterioration have different values.

An extended discussion and comprehensive overview of recent results on the topics treated in this chapter is given in [47].

4.1 Damage Mechanisms in Silicon Devices

The radiation-induced damage in silicon detectors can be categorized by the affected region of the device in which the defects occur: the silicon *surface*, on which the digital logic of the chip is implemented, and the *bulk* or sensitive volume (cf. Fig. 2.10). The corresponding damage mechanisms are fundamentally different and discussed in the following. As the primary use of the developed irradiation site (see Chapter 5) is the controlled application of damage to the sensor volume of a silicon detector via proton irradiation, this chapter mainly focuses on bulk damage.

4.1.1 Surface Damage

In silicon applications, the radiation-induced deterioration of the shallow Metal-Oxide-Semiconductor (MOS) structures, compromising the logic gates of chip electronics, is referred to as *surface damage*. Specifically, the damage occurs in the oxide insulation layers of typical CMOS arrangements, as shown in Fig. 2.10(b). The oxide layer, commonly silicon dioxide with a thickness of a few nm, insulates the metal gate contact from the silicon substrate below, enabling current flow between the ohmic implants of the transistor by applying voltage to the gate. This results in a high electric field in the thin oxide layer, typically in the order of $O(\mathrm{MV\,cm^{-1}})$.

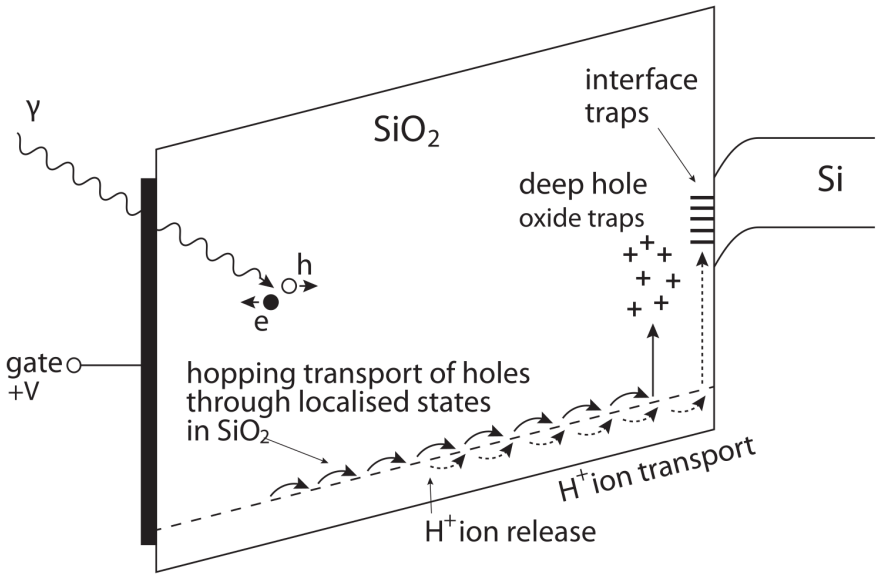

Figure 4.1: Schematic illustration of ionization-induced damage in the gate oxide layer of a MOS transistor. For positive gate voltages, charges of the same sign (holes and hydrogen ions) accumulate close to the SiO_2–Si boundary, where they are trapped. At the interface, ionization directly produces trap states, either charged or uncharged, where the charge sign is a function of the gate voltage sign. These static space charges influence the threshold and leakage characteristic of MOS devices. From [16].

Via the mechanisms introduced in Section 2.1, ionizing radiation produces free electron-hole pairs

inside the oxide layer. Due to the high electric field in combination with the substantial difference in carrier mobility μ_{e-h} ($\mu_e/\mu_h \approx 1 \times 10^6$) in SiO_2 [16], i.e. the ability to propagate through the material, the electron-hole pairs are separated. While the electrons are immediately removed by the field, the holes remain inside the oxide and form quasi-stationary charges. For positive gate voltages, the holes slowly wander towards the SiO_2–Si interface region. Here, due to lattice mismatches between the oxide and substrate as well as diffusion processes, oxygen vacancies in the lattice act as so-called *deep hole oxide traps*, allowing for the accumulation of positive space charge. A schematic depiction of this mechanism is shown in Fig. 4.1.
The holes progress sequentially through the individual lattice locations, known as *hole hopping*. This movement can result in the release of hydrogen ions from impurities in the crystal. The H^+ ions propagate slowly alongside the initial holes, eventually reaching the oxide-substrate boundary where they are capable of forming so-called *interface traps*. These traps are located physically at the SiO_2–Si interface, where they can also directly result from ionization, and energetically within the band level (cf. Fig. 2.5). Therefore, these traps allow for donor- and acceptor-like charge states, either adding to or counteracting the positive space charge in the oxide. The charge state of the trap depends on the applied voltage configuration and thus differs for n- and p-channel devices in CMOS processes where the former primarily results in negative and the latter in positive charges.
Overall, the charge accumulation within the oxide (positive) and interface (device-dependent) region influences the properties of MOS devices, particularly the threshold and leakage current characteristics of transistors. In principal, surface damage effects decrease with decreasing oxide thickness which, in turn, decreases with the feature size. With regard to decreasing transistor sizes, geometric properties start to play a role with for example the gate width and length causing the so-called Radiation-Induced Narrow Channel Effect (RINCE) and Radiation-Induced Short Channel Effect (RISCE) respectively [48].
As modern MOS structures can have complicated oxide configurations, the surface damage effects are consequently more complex than schematically depicted in Fig. 4.1 and the resulting effect on the operational parameters heavily depends on the specific device. A detailed overview of surface damage effects in 65 nm CMOS structures, corresponding to the technology used in the ATLAS `ITkPix` chip (see Section 3.3), is given in [49].
Even though the oxide charges are quasi-static due to their low mobility, they slowly neutralize by means of thermal emission and tunneling of electrons in the oxide. This process is referred to *annealing* (see also Section 4.4) and is a function of temperature and time. As the surface damage is the result of ionization processes, it scales with the so-called Total Ionizing Dose (TID). Therefore, surface damage is also commonly referred to as *TID damage*.

Total Ionizing Dose

The TID is defined as the absorbed dose D, corresponding to energy deposited in a material by ionization, normalized to the its mass m as

$$\mathrm{TID} = \frac{D}{m} \quad \text{with} \quad [\mathrm{TID}] = \mathrm{J\,kg^{-1}} = \mathrm{Gy}\,. \tag{4.1}$$

Instead of the SI unit Gy, the TID is often given in rad where the conversion ratio is 1 Gy = 100 rad. Within the field of HEP, common doses for electronics in pixel detectors are in the order of a few 100 Mrad [50]. For the ATLAS ITk, the TID levels for the innermost pixel layers are expected to be in

the region of 2 Grad over the whole HL-LHC runtime [9].
Using Eq. (2.1), enables a determination of the density-normalized energy loss by ionization of charged particles such as protons. Therefore, knowing the number of protons that penetrate a material facilitates the calculation of the TID, as done in Eq. (5.19).

4.1.2 Bulk Damage

In extreme radiation environments, such as for the ATLAS ITk (see Section 3.2.1), bulk damage currently represents the limiting factor for operation of silicon detectors closest to the IP. Whereas the readout chip performs well within the specifications at the expected EOL TID [35, 43], the sensor characteristics lie close to the upper bounds of the requirements at the corresponding EOL fluence levels [26].

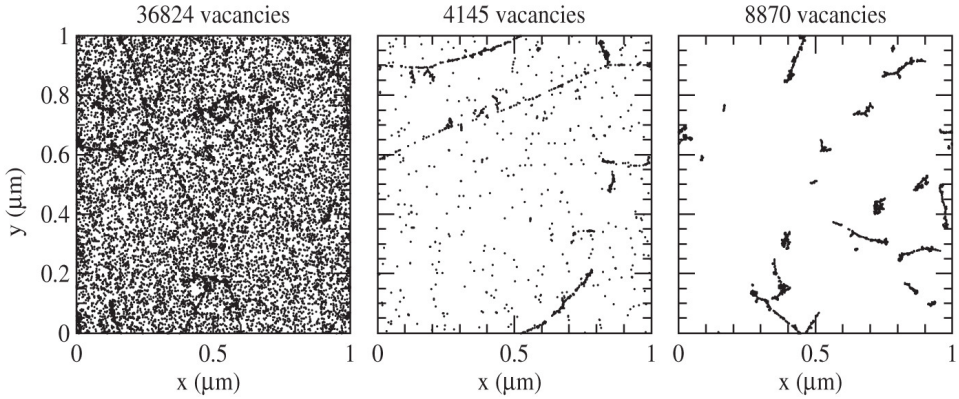

Figure 4.2: Simulation of initial distribution of vacancies in a silicon lattice after irradiation with 10 MeV protons (left), 24 GeV protons (center) and 1 MeV neutrons (right). A projection over a depth of 1 µm and a for particle fluence of 10^{14} cm^{-2} is shown. From [51].

Bulk damage refers to the degradation of the sensitive volume, or bulk (see Section 2.2.3), of detectors due to radiation-related defects in the crystal lattice of the semiconductor material. While the majority of energy deposited in the bulk material by traversing charged particles is via ionization of its atoms, this process is reversible (as opposed to in the surface region, see Section 4.1.1) and does not result in defects. The damage in the sensitive volume is the result of direct collisions and subsequent displacements of silicon (or compound) atoms from their original lattice location, resulting in point- and cluster-like defect formations. The displacements are the result of elastic scattering processes with the nuclei, resulting in a so-called Primary Knock-on Atom (PKA). The energy required to dislocate an atom from the lattice E_d depends on the material where a value of $E_d^{\mathrm{Si}} \approx 25$ eV results in a displacement probability of 50 % for silicon [16]. The maximum energy transfer to a lattice atom for heavy particles, $T_p^{\max}$, and electrons, $T_e^{\max}$, in these scattering mechanisms can be expressed as [16]

$$T_p^{\max} = 4\frac{Mm}{(M+m)^2}T_p \quad \text{and} \quad T_e^{\max} \approx 2\frac{T_e + 2m_e}{M}T_e\,, \tag{4.2}$$

where M is the mass of the lattice atom and $m_{p/e}$ and $T_{p/e}$ are the mass and energy of the particle. The abundance and spatial distribution of lattice defects strongly depends on the recoil energy E_R of

the PKA and therefore on the traversing particle, its scattering cross section and energy transfer in Eq. (4.2). With sufficient E_R, the ejected PKA leaves a vacancy and continues to propagate through the lattice, further ionizing and displacing atoms, before it comes to rest as a so-called *interstitial*. The resulting vacancies and interstitials, in combination with impurity atoms, produce complex defect structures in the silicon lattice. Typical point defects are displayed in Fig. 4.4(a).
Simulated distributions of initial lattice vacancies in silicon from proton (10 MeV, 23 GeV) and neutron (1 MeV) irradiation to a fluence of 10^{14} cm^{-2} are shown in Fig. 4.2. As visible, protons produce points and clusters of vacancies whereas neutrons almost exclusively give rise to cluster arrangements. The low-energy protons (comparable to the energies at the BIC, see Chapter 5) create a factor of 5 – 10 more vacancies compared to the other particles. Therefore, and due to the vast availability of low energy (MeV) proton accelerators for scientific, medical or industrial applications, protons are the ideal candidate for inflicting high bulk damage.
As bulk damage is the result of displacement of lattice atoms from to non-ionizing energy loss, i.e. due to direct collisions with nuclei, it is referred to as *displacement* or *NIEL damage*.

Non-Ionizing Energy Loss

The NIEL describes the energy loss through interactions other than ionization, that is direct collisions with nuclei and lattice vibrations (so-called *phonons*). As the energy is lost almost exclusively due to the former and as phonons do not damage the lattice structure, they are not relevant for bulk damage. The NIEL can be expressed in analogy to the electronic stopping power (see Eq. (2.1)) in units of MeV cm^2 g^{-1} and can be calculated using the so-called *damage function* $D(E)$ as [52]

$$D(E) = \sum_{\nu} \sigma_{\nu}(E) \cdot \int_{E_d}^{E_R^{\max}} f_{\nu}(E, E_R) P(E_R) \mathrm{d}E_R \,. \tag{4.3}$$

Here, the summation index ν runs over all displacement processes available at particle energy E with cross sections $\sigma_{\nu}(E)$ and probability $f_{\nu}(E, E_R)$ to produce a PKA with recoil energy E_R. The integral runs from the minimum energy to achieve displacement within the material, E_d, to the maximum recoil energy of the PKA, $E_R^{\max}$. The partition function $P(E_R)$ yields the fraction of energy which is available for further displacement by the PKA. The damage function can be expressed in terms of the NIEL stopping power, $\frac{\mathrm{d}E}{\mathrm{d}x}\big|_{\mathrm{NIEL}}$, as [52]

$$D(E) = \frac{A}{N_A} \left.\frac{\mathrm{d}E}{\mathrm{d}x}\right|_{\mathrm{NIEL}} , \tag{4.4}$$

where A is the atomic number of the material and N_A Avogadro's constant. $D(E)$ yields the so-called *displacement* or *NIEL damage cross section* in units of MeV mb. The calculated damage function for electrons, neutrons, protons and pions with energy is shown in Fig. 4.3, normalized to the reference damage of 1 MeV neutrons of 95 MeV mb [53, 51]. The normalization is a result of the so-called *NIEL scaling hypothesis* for silicon, introduced in the following.

4.2 Non-Ionizing Energy Loss Scaling Hypothesis

The NIEL scaling hypothesis is an essential tool for measurement and prediction of radiation-induced degradation of silicon sensors, independent of particle species and energy. It is based on the empirical observation that many defect characteristics of the sensitive volume, for example the leakage current increase (see Section 4.3), scale linearly with the NIEL. It makes the assumption that the damage properties approximately only depend on the abundance of the primary point and cluster defects (as depicted in Fig. 4.2) and are independent of their initial distribution in energy and space. Subsequently, the damage inflicted by a variety of particle species with different energies can be scaled by their respective NIEL, i.e. their damage function. This so-called *NIEL scaling* uses the 1 MeV neutron[2] displacement damage cross section $D_{\mathrm{n_{eq}}} = 95\,\mathrm{MeV\,mb}$ as the normalization point, allowing for the expression of any particle's NIEL damage in units of 1 MeV neutron equivalents (1 $\mathrm{n_{eq}}$). Using this, the displacement damage inflicted by exposure to spectrum of different particles with the corresponding energy distribution $\phi(E)$ and damage function $D(E)$ can be normalized to the neutron equivalent damage of the spectrum via [53]

$$\kappa = \frac{\int D(E)\phi(E)\mathrm{d}E}{D_{\mathrm{n_{eq}}} \cdot \int \phi(E)\mathrm{d}E}\,. \tag{4.5}$$

Here, κ is a scaling factor, predominantly referred to as *hardness factor*, yielding the displacement damage of the initial spectrum in $\mathrm{n_{eq}}$ units. Equation (4.5) enables the description of the expected radiation damage in setups exposed to a variety of particle species at different energies, such as the ATLAS experiment, using NIEL as the single metric. Figure 4.3 portrays the scaled NIEL cross sections of various particles, effectively visualizing their hardness factor. In the context of radiation damage studies and irradiation facilities, the neutron equivalent fluence $\Phi_{\mathrm{n_{eq}}}$, that is the number of 1 MeV neutron equivalents per unit area ($\mathrm{n_{eq}/cm^2}$), is used to quantify the displacement damage. It can be calculated from the hardness factor κ via Eq. (4.5) and the individual energy spectrum $\phi(E)$ of the radiation exposure as [53]

$$\Phi_{\mathrm{n_{eq}}} = \kappa \int \phi(E)\mathrm{d}E\,. \tag{4.6}$$

For the deployment of particle accelerators to facilitate controlled displacement damage application via monoenergetic beams of particle species X, Eq. (4.6) simplifies to

$$\Phi_{\mathrm{n_{eq}}} = \kappa_X \Phi_X\,, \tag{4.7}$$

where κ_X and Φ_X are the hardness factor and particle fluence of the species X at the given energy, respectively. This relation provides a straightforward foundation for the implementation of irradiation facilities using particle accelerators to perform displacement damage studies of silicon detectors. Subsequently, the hardness factor of the used particle species needs to be extracted once for a given energy whereas the particle fluence measurement is required on a reoccurring per-irradiation basis.

[2] Due to the rapid fluctuations of the neutron damage function around the 1 MeV mark, as shown in Fig. 4.3, the reference cross section of 95 MeV mb is obtained by averaging over the vicinity of the normalization point. The exact 1 MeV damage cross section is approximately 77 MeV mb [51].

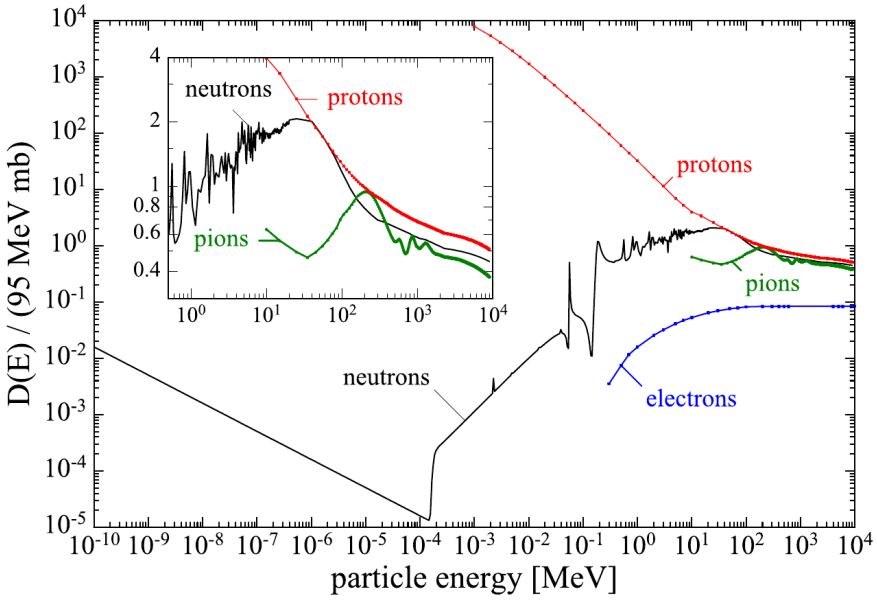

Figure 4.3: Normalized NIEL cross sections, i.e. hardness factors, of various particles as a function of energy. The reference cross section is the 1 MeV neutron equivalent damage of 95 MeV mb. From [47].

While a precise experimental procedure for the determination of the hardness factor of such facilities via the effects described in Section 4.3.1 is presented in [53], a novel approach of beam-based online monitoring of the particle fluence is introduced in Chapter 5 of this work. This new dosimetry procedure allows for low-uncertainty fluence measurements with spatial resolution, enabling to greatly reduce the uncertainty on the aforementioned experimental determination of the hardness factor via Eq. (4.7) versus the standard (cf. [54]) offline dosimetry via metallic foil activation.

4.3 Implications on Detector Operation

The displacements of lattice atoms due to NIEL, resulting in the initial point and cluster vacancy formations as displayed in Fig. 4.2, give rise to macroscopic changes in the operational parameters of silicon devices. Subsequent to the initial vacancies, more complex microscopic structures emerge in the presence of impurity atoms or interstitial Si nuclei. Figure 4.4 gives an an overview of typical point defect formations in the crystal lattice and their corresponding energy levels within the band model in silicon.
Due to the creation of additional energy levels in the band, the electrical behavior of silicon detectors, initially described in Section 2.2, changes with radiation. Qualitatively shown in Fig. 4.4(b), defect levels close to the respective band act as dopants, changing the effective doping concentration, whereas defects near the band gap center contribute to the leakage current generation. Intermediate levels are the cause of charge trapping and therefore a reduction in (in-time) signal registration. An overview of the implications of these defects on the operation of silicon detectors is given in the following.

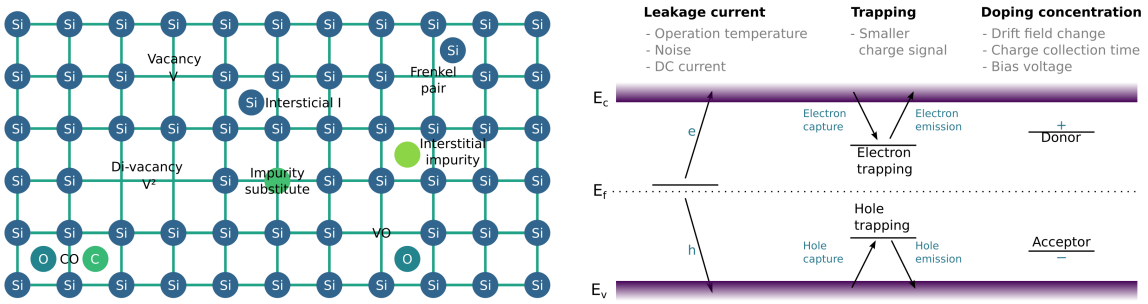

(a) Defect formations

(b) Defect energy levels

Figure 4.4: Formation of various point defects in the lattice (a) and associated energy levels in the band model (b) for silicon. From [17].

4.3.1 Bulk Leakage Current Increase

The leakage current I_{leak} through the sensor bulk in reveres bias, as introduced in Eq. (2.19), increases with displacement damage due to *deep-level* defects, located near the center of the band gap (cf. Fig. 4.4(b)). The leakage current, due to its origin also called *generation current* [47], follows the NIEL scaling hypothesis for silicon devices and is directly proportional to the 1 MeV neutron equivalent fluence $\Phi_{\text{n}_{\text{eq}}}$, independent of the specifics of the silicon (n/p-type, resistivity, fabrication), as demonstrated in Fig. 4.5. Here, for various sensors and irradiation levels, the leakage current increase ΔI before and after irradiation, normalized to the depleted volume V, is projected as a function of $\Phi_{\text{n}_{\text{eq}}}$. The dependency can be expressed as [53]

$$\frac{\Delta I}{V} = \alpha \cdot \Phi \quad \text{with} \quad \Delta I = I^{\Phi}_{\text{leak}} - I^{0}_{\text{leak}}\,, \tag{4.8}$$

where the proportionality factor is α, the so-called *current-related damage rate* or *factor* [47]. The numerical value of α is defined by the annealing procedure (see Section 4.4), the temperature of the current measurement as well as the particle fluence spectrum. Therefore, where applicable, the current-related damage rate is denoted with the annealing procedure as well as particle species X as $\alpha_X^{(t/T)}$, where t is the time in minutes and T the respective temperature in °C.
Using Eqs. (4.7) and (4.8), it follows that the hardness factor of a specific particle species X can be expressed as the ratio of the resulting damage rate α_X and the 1 MeV neutron equivalent rate $\alpha_{\text{n}_{\text{eq}}}$ as

$$\kappa_X = \frac{\alpha_X}{\alpha_{\text{n}_{\text{eq}}}}\,. \tag{4.9}$$

It should be noted, that for the current-related damage factors the same annealing procedures and leakage scaling temperatures must be used for Eq. (4.9) to hold. Consequently, in combination with Eq. (4.8), this provides a method to extract the hardness factor of a given particle spectrum by means of irradiation of silicon sensors to multiple fluences and determination of the α value. This is used in Section 6.4 of this work to measure the proton hardness factor at the BIC.
The leakage current increase ΔI in Eq. (4.8) is commonly dominated by I^{Φ}_{leak} (cf. for example Fig. 6.17), thus $\Delta I \approx I^{\Phi}_{\text{leak}}$ is valid when non-irradiated and irradiated samples are compared.

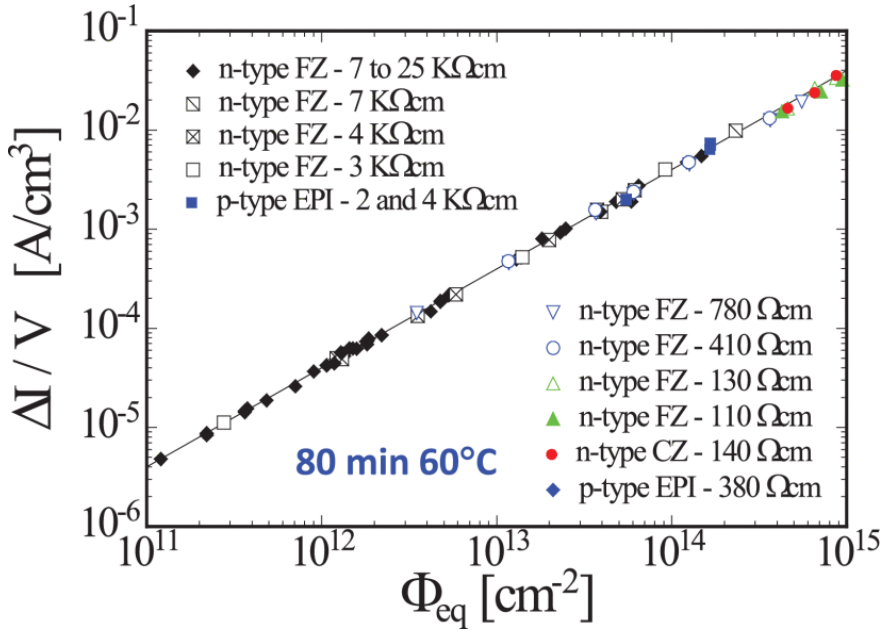

Figure 4.5: Volume-normalized leakage current increase as a function of the 1 MeV neutron equivalent fluence $\Phi_{n_{eq}}$ for various silicon sensors. The data follows a linear trend. The slope is referred to as *current-related damage rate* α and a function of particle species and annealing (see Section 4.4). Here, the sensor data is extracted after annealing for 80 min at 60 °C, corresponding to $\alpha_{n_{eq}}^{80/60} = (3.99 \pm 0.03) \times 10^{-17}\,\mathrm{A\,cm^{-1}}$ [53].

The increase in leakage current with displacement damage in turn causes an increase in detector noise and heat dissipation during operation. As Eq. (2.20) shows a strong temperature dependence of the leakage current, sufficient cooling represents an efficient way to suppress the leakage and power consumption. Due to the space and material restrictions in HEP experiments, detector cooling capabilities are constrained and the leakage often imposes the operational limit. An effective way to decrease the damage-related leakage current is so-called *beneficial annealing* (see Section 4.4).

4.3.2 Effective Doping Concentration Change

The effective doping concentration N_{eff} defines the voltage required to achieve full depletion of a silicon sensor via Eq. (2.17). Radiation-induced defects close to the valence and conduction band levels (cf. Fig. 4.4(b)), introduce additional dopant-like states, resulting in a change in the effective doping concentration. This effect is shown in Fig. 4.6 for an n-type bulk of 300 µm thickness. Due to increasing radiation levels, N_{eff} decreases as predominantly negative space charges are created, compensating for the initial positive space charge of the n-type material [47]. At the so-called point of *type inversion*, the effective space charge flips its sign and the sensor becomes effectively p-type. Further increasing the particle fluence yields in an increase of the effective doping concentration. As the full depletion voltage is proportional to N_{eff}, it grows accordingly. In combination with the increase in leakage current with NIEL (see Eq. (4.8)), a substantial increment in power consumption results. To operate standard (planar) sensors of 300 µm thickness in full depletion after irradiation, bias voltages in the region of 500 – 1 000 V are commonly typically whereas for high fluence levels ($\Phi_{n_{eq}} \geq 5 \times 10^{15}\,\mathrm{n_{eq}/cm^2}$) full depletion is usually not possible anymore [16].

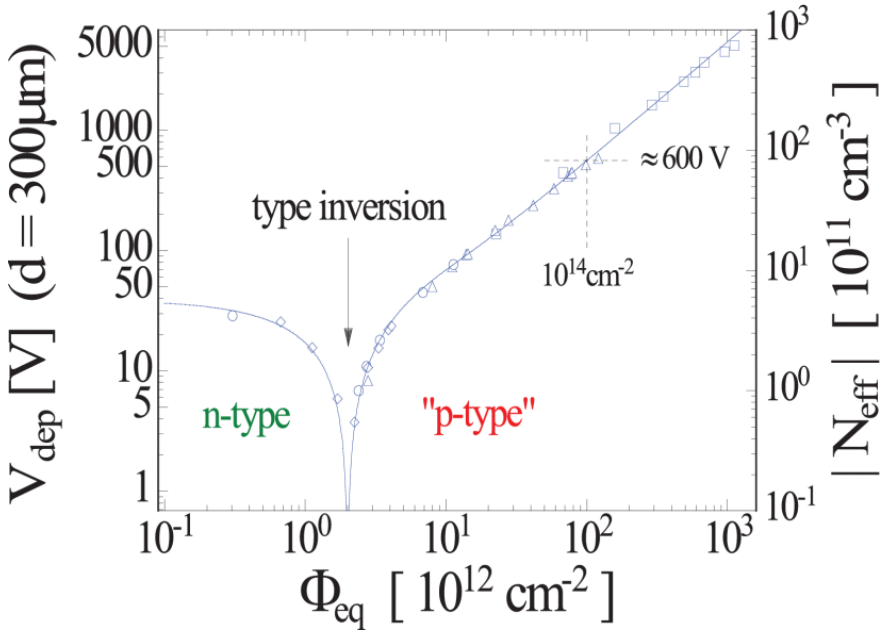

Figure 4.6: Effective doping concentration $|N_{\text{eff}}|$ (right axis) and full depletion voltage V_{dep} (left axis) as a function of the NIEL fluence for a 300 µm n-type silicon sensor. After an equivalent fluence of approximately 2×10^{12} n_{eq}/cm^2, the material effectively changes to p-type due to the creation of primarily negative space charges. Taken from [47].

Due to the behavior shown in Fig. 4.6, the current design of silicon detectors in HEP applications for extreme radiation environments is *n-in-p*, featuring an n-type collection electrode in a p-type bulk. This approach circumvents the type inversion at high fluence levels and maintains a high-resistivity bulk over the time of operation.

4.3.3 Charge Trapping

Radiation-induced charge carrier trapping is the result of the creation of so-called *trapping centers* or *trap levels*, intermediate defect levels located in the band gap (see Fig. 4.4(b)), which can capture and subsequently release charges during their propagation through the bulk. Carrier trapping is the dominant mechanism that deteriorates the collected charge signal after irradiation [16] and thus degrades the (in-time) hit detection efficiency[3]. In the presence of trap levels, the collected charge within a particular time $Q(t)$ can be expressed as [16]

$$Q(t) = Q_0 \exp\left(-\frac{t}{\tau_{\text{eff,e/h}}}\right), \tag{4.10}$$

[3] Typically, the charge collection in a tracking detector is required to be completed within a specific time window (e.g. the bunch-crossing frequency, i.e. 25 ns for LHC/ATLAS).

where Q_0 is the initial charge and $\tau_{\text{eff,e/h}}$ describes the *effective carrier lifetime*:

$$\tau_{\text{eff,e/h}} = \frac{1}{\tau_0} + \beta_{\text{e/h}} \Phi_{\text{n}_{\text{eq}}} \,. \tag{4.11}$$

Here, τ_0 corresponds to the carrier lifetime without the existence of trapping centers and $\beta_{\text{e/h}}$ defines the *effective trapping time* constant, quantifying the charge capture rate for electron and holes, respectively. Equation (4.11) is empirically found to scale linearly with NIEL fluence with the effective trapping time constant varying with the irradiation species (e.g. neutrons, protons, etc.) while depending only little on the measurement temperature. Typical values at $-10\,°\text{C}$ for electrons are $\beta_{\text{e}} \approx 4 - 6 \times 10^{-16}\,\text{cm}^2\,\text{ns}^{-1}$, whereas holes experience slightly stronger trapping with $\beta_{\text{h}} \approx 6 - 8 \times 10^{-16}\,\text{cm}^2\,\text{ns}^{-1}$ [55].

4.4 Annealing

The accumulated defects in irradiated silicon devices, resulting from oxide (TID) as well as lattice (NIEL) damage, are subject to so-called *annealing*: the temperature-induced development of defects over time. Given sufficient thermal stimulation, defect formations can propagate through the crystal lattice, react, dissociate and recombine with other defects, resulting in electrically active damage centers (trap-, generation-, doping-level defects, see Fig. 4.4(b)) becoming inactive. In turn, this corresponds to a change in the observed effects on the detector operation.
As the leakage current increase with fluence, discussed in Section 4.3.1, is of particular interest for this work, the effect of annealing on the current-related damage rate is discussed in the following. The annealing behavior of other damage-impaired properties, such as the effective trapping time $\tau_{\text{eff,e/h}}$ and doping concentration N_{eff}, is described in [47].

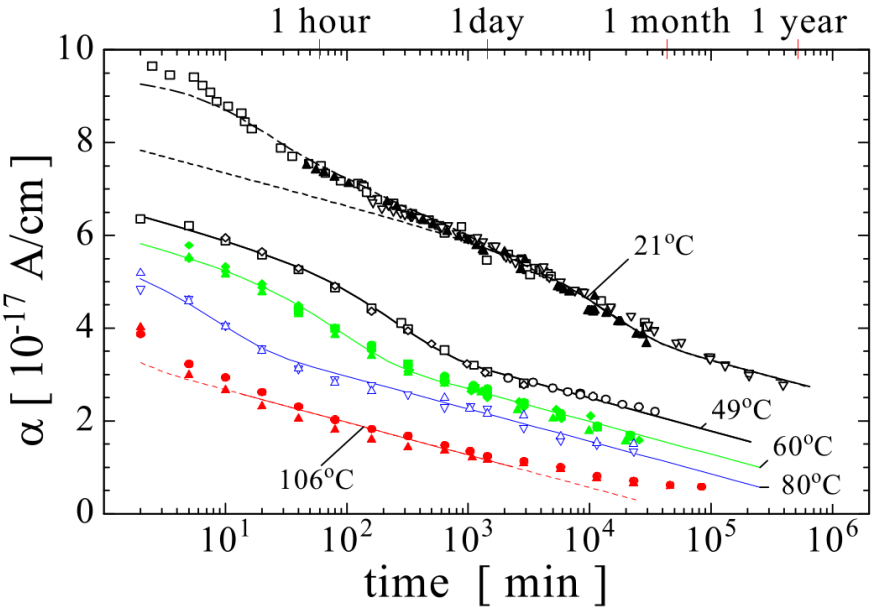

Figure 4.7: Current-related damage rate α over time for different annealing temperatures. The solid lines correspond to fits to the data using Eq. (4.12). From [47].

The annealing curves of the current-related damage factor α over time for different temperatures are shown in Fig. 4.7. The damage rate α decreases with annealing time for all measured temperatures, translating to a proportional decrease in bulk leakage current via Eq. (4.8). Increasing the annealing temperature drastically reduces the starting value of α, allowing one to obtain the same resulting value of α with different annealing procedures, e.g. 20 min at 60 °C and 100 min at 60 °C yielding $\alpha^{20/60} \approx \alpha^{100/49} \approx 5 \times 10^{-17}\,\mathrm{A\,cm^{-1}}$.
To facilitate a meaningful comparison of results, a reference guideline is commonly followed when radiation-induced leakage current measurements are reported: an annealing procedure of 80 min at 60 °C is applied, after which the leakage current is measured at a given temperature and then scaled to 20 °C via Eq. (2.20)[4]. This produces a current-related damage rate of $\alpha_{\mathrm{n_{eq}}}^{80/60} = (3.99 \pm 0.03) \times 10^{-17}\,\mathrm{A\,cm^{-1}}$ after irradiation with 1 MeV neutron equivalents [53] which serves as the reference for determination of hardness factors via Eq. (4.9).
A functional relation for development of the current-related damage rate with time for a given annealing temperature is proposed in [53] as

$$\alpha(t) = \alpha_1 \exp\left(-\frac{t}{\tau_1}\right) + \alpha_0 - \alpha_2 \ln\left(\frac{t}{t_0}\right), \tag{4.12}$$

in which also the physical meaning of the parameters $\alpha_{0/1/2}$, τ_1 and t_0 are discussed. This relation is fitted to the data displayed in Fig. 4.7.
As the bulk leakage current decrease with annealing results in an improvement with regard to power consumption and noise, it is also termed *beneficial annealing* and an essential routine to reduce the impact of radiation damage on the detector operation. It shall be noted that for other quantities, such as the effective doping concentration N_{eff}, a detrimental effect can be observed for long annealing times, the so-called *reverse annealing* [56].
Generally, and as visible in Fig. 4.7, annealing reactions are accelerated with increasing and decelerated with decreasing temperature, where effectively a *freezing* of annealing reactions can be achieved for low temperatures [47] in the order of −10 °C. For this reason, irradiation campaigns and measurements involving irradiated devices are performed at such low temperatures to maintain the initial defect state and prevent uncontrolled annealing, respectively. Furthermore, in (real-world) detector applications, such as the ATLAS tracking system, annealing phases have to be planned accordingly to sustain an overall beneficial annealing contribution.

4.5 NIEL Damage Scaling Limitations

The NIEL scaling hypothesis for silicon devices is an essential tool for prediction and characterization of radiation-induced bulk degradation as it is generally applicable for many key properties of the damage effects. For example, as shown in Fig. 4.5, it accurately scales the leakage current increase with the equivalent fluence, independently of the type of silicon, over many orders of magnitude of $\Phi_{\mathrm{n_{eq}}}$. Nevertheless, the NIEL scaling hypothesis is an empirical model, and thus mostly describes the

[4] Due to the typically high fluences needed for radiation hardness characterization, a measurement at 20 °C is not feasible due to excessive leakage currents and thus high power dissipation, resulting in measurement distortion, uncontrolled annealing and even device damage due to self-heating and thermal runaway, respectively. To avoid these issues, measurements are performed in climate chambers at temperatures around −20 °C (see Section 6.4.2).

resulting macroscopic effects on a qualitative level without resolving the mechanisms on a microscopic level. Subsequently, it has some shortcomings arising from its simplifying assumptions. For example, it does not consider the influence of *annealing* (see Section 4.4) or, by design, does not differentiate between point and cluster defects which is relevant for selected effects e.g. the change in effective doping concentration (see Section 4.3.2) or carrier trap introduction rate [16]. Therefore, exceptions from the assumptions that constitute the NIEL scaling hypothesis have been reported in multiple works for several damage properties such as e.g. a difference in the trapping probability for charged hadron versus neutron irradiation [55] or in the effective doping concentration change in oxygen-enriched silicon [56]. Additionally, there are observations of the leakage current increase deviating from the linear model of Eq. (4.8) (especially for high fluences, cf. [54]).
Other tools for simulating and predicting defect properties in silicon exist in the form of Technology Computer Aided Design (TCAD) models, notably the *Hamburg* and *Perugia* model, with an overview given in [57]. These models are the result of extensive studies (e.g. [56]) and are heavily employed within the RD50 collaboration [46]. However, this simulation-based software commonly requires device-specific input parameters to provide accurate predictions.
Consequently, to understand the effects of radiation-induced displacement damage in a given DUT, irradiation campaigns with subsequent measurements remain the core procedure for reliable radiation hardness tests and device characterization. Particularly in the context of large detectors like ATLAS ITk (see Section 3.2.1), the unprecedented radiation environment requires rigorous hardness studies over multiple generations of chips. This emphasizes the demand for a vast irradiation infrastructure, consisting of well-characterized facilities, allowing for controlled application of NIEL fluence levels with low uncertainty.
The majority of work done within this thesis contributes to the aforementioned infrastructure by development and characterization of a novel proton irradiation site at the HISKP of the University of Bonn which is detailed in Chapters 5 and 6.

CHAPTER 5

Irradiation Facility at the University of Bonn

The development of a proton irradiation site for silicon detectors at the University of Bonn was initiated in mid-2018 [58]. Using a rudimentary setup and procedure, irradiation campaigns of commercial silicon *PiN* diodes were conducted and evaluated. Providing a *proof of concept* measurement, the expected relation between leakage current increase with fluence, given in Eq. (4.8), could be validated. While quantitative results such as the *proton hardness factor* (see Section 4.2) could not be extracted, the suitability of the proton beam provided by the BIC, as well as the irradiation procedure could be verified.

In this work and building upon the findings of [58], the irradiation site at the BIC has been developed into a versatile and well-characterized setup, allowing for flexible irradiation campaigns that result in highly uniform fluence distributions with low uncertainty.

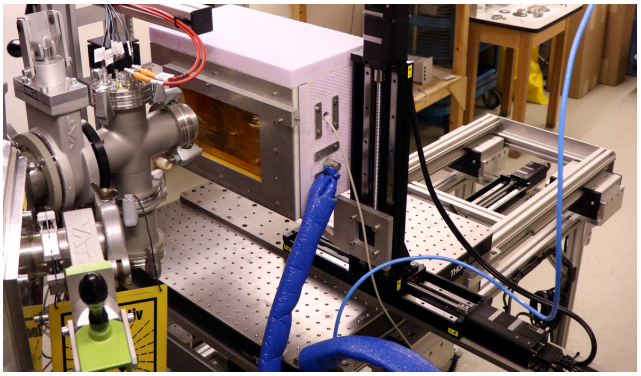

Figure 5.1: Setup in irradiation position in late 2021

In this chapter, the irradiation setup and procedure at the BIC irradiation facility are described. Section 5.1 outlines the BIC accelerator facility, located at the HISKP, as it houses the irradiation site and provides the necessary proton beams. Subsequently, the irradiation site is described in detail in Section 5.2, where an overview of the components, their locations and interconnections is given before the arrangement of individual hardware and typical DUTs is presented. A set of custom-made beam diagnostics, enabling online beam parameter and subsequently fluence monitoring, developed within this work and as part of [59, 60] is explained in Section 5.3. The irradiation procedure is illustrated in Section 5.4. It features an autonomous, beam-driven irradiation routine, accompanied by the purely beam-based, on- and offline dosimetry approach in Section 5.5. Both are enabled by the real-time beam parameter monitoring via the custom beam diagnostics. Finally, the software framework `irrad_control`, developed for DAQ and control of the irradiation site as well as visualization and analysis of the obtained data is introduced in Section 5.6.

Following the description of the irradiation setup and its components, the developed diagnostics, the

irradiation procedure and the dosimetry approach are characterized in Chapter 6.

5.1 The Bonn Isochronous Cyclotron

The BIC is located at the HISKP of the University of Bonn. The accelerator was built by the *Allgemeine Elektricitäts-Gesellschaft (AEG) Beschleunigerbau* on the basis of a pre-existing *synchro-cyclotron*. From 1968 to 1970, it was exclusively operated with an internal ion source and beam for the purpose of radioisotope production. Following the successful conversion to an isochronuous cyclotron in late 1970, multiple efforts were made over the course of a decade to extend the BIC facility. A low-energy injection beamline for connection of external ion sources [61] as well as a beam handling system [62] enabled the extraction of high-energy ion beams from the accelerator towards a multitude of experimental sites. This section aims to give an overview of the operational parameters of the accelerator and the available beam characteristics at the location of the irradiation site. A comprehensive overview of the BIC facility, from which much of the information presented here is taken, can be found on the homepage [63] as well as in [59, 60].

5.1.1 Principle of Operation

A cyclotron operates by repeatedly accelerating positively-charged particles inside dedicated sectors via an alternating electric field. The acceleration sectors are located between multiple electrodes, so-called *dees*, to which an RF voltage is applied. Perpendicular to the plane of the beam, an external magnetic field is applied which forces the ions on an outward-spiraling trajectory. Using the *Lorentz* as well as centripetal force, the *cyclotron resonance frequency* ν_0 for a particle with charge q and mass m can be defined as

$$\nu_0 = \frac{Bq}{2\pi m}\,, \tag{5.1}$$

where B is the magnetic field strength, and ν_0 corresponds to the number of revolutions per second that the particle undergoes inside the accelerator. By operating the cyclotron with an RF frequency ν_{rf} that fulfills the isochronism condition

$$\nu_{\mathrm{rf}} = h \cdot \nu_0\,, \tag{5.2}$$

it is ensured that the particles always arrive on the accelerating phase of the RF voltage. Here, $h \in \mathbb{N}_{>0}$ is the *harmonic number* of the cyclotron's operation mode, corresponding to an integer by which the cyclotron resonance frequency is scaled.
Due to the relativistic increase in momentum, the revolution frequency of the particle decreases over the course of acceleration. To account for this, the magnetic field strength accordingly increases with the radius, subsequently ensuring Eq. (5.2) and defining the characteristic of isochronous cyclotrons.

5.1.2 Accelerator

The BIC consists of a 250 t magnet with a 2 m diameter pole. On the inside, the magnetic field configuration is symmetrically divided into three 120° *hill-and-valley* sections. Each section consists of a 40° *hill* segment with a maximum field strength of 1.9 T and a 80° *valley* segment with 0.7 T,

implementing *strong focusing*. A total of three dees, named *South West*, *South East* and *North* dee after their alignment, are located within the valley portion of each section, incorporating two acceleration gaps, on entering and exiting, per dee. They are coupled to the RF system which operates at frequencies ν_{rf} between 20 and 29 MHz and voltages up to 40 kV. Due to the number of dees, the BIC typically operates with harmonic number $h = 3$ but an operation with $h = 9$, for heavier ions with a charge-to-nucleon ratio of $Q/A \leq 1/3$, is also possible. An image of the cyclotron as well as a schematic are displayed in Fig. 5.2, where also an overview of the parameter space of operation of the BIC is shown.

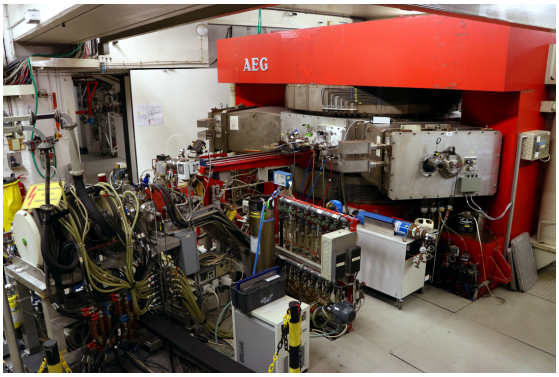

(a) Cyclotron with external Electron Cyclotron Resonance (ECR) ion source in front, from [63]

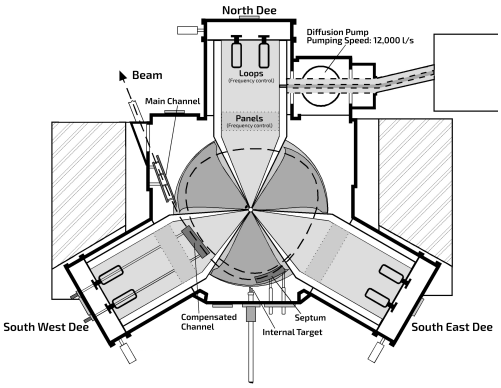

(b) Cyclotron schematic adapted from [63]

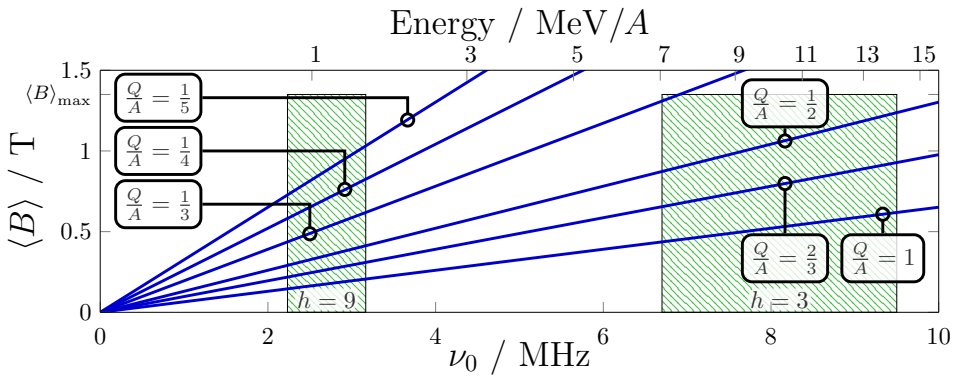

(c) Overview of parameter space of operation, from [59]

Figure 5.2: Overview of the BIC accelerator, its layout and parameter space of operation.

The accelerator is supplied with ions of up to 8 keV from an external ECR source via a low-energy beamline, injecting them centrally from below. After an initial radius of 37 mm, the beam is accelerated over approximately 120 revolutions after which it is extracted at a radius of 900 mm. For the typical operation with $h = 3$ and light ions with $1/2 \leq Q/A \leq 1$, the range of the available RF frequencies translates to energies between 7 – 14 MeV/A, enabling proton beams of maximally 14 MeV. The ion beam is extracted at an intrinsic relative energy resolution of $\Delta E/E = 4 \times 10^{-3}$, which can be further optimized by the beam handling system [62]. The available maximum beam currents immediately after extraction are in the order of 10 µA, where typical currents at the experimental sites are in the region of 1 µA.

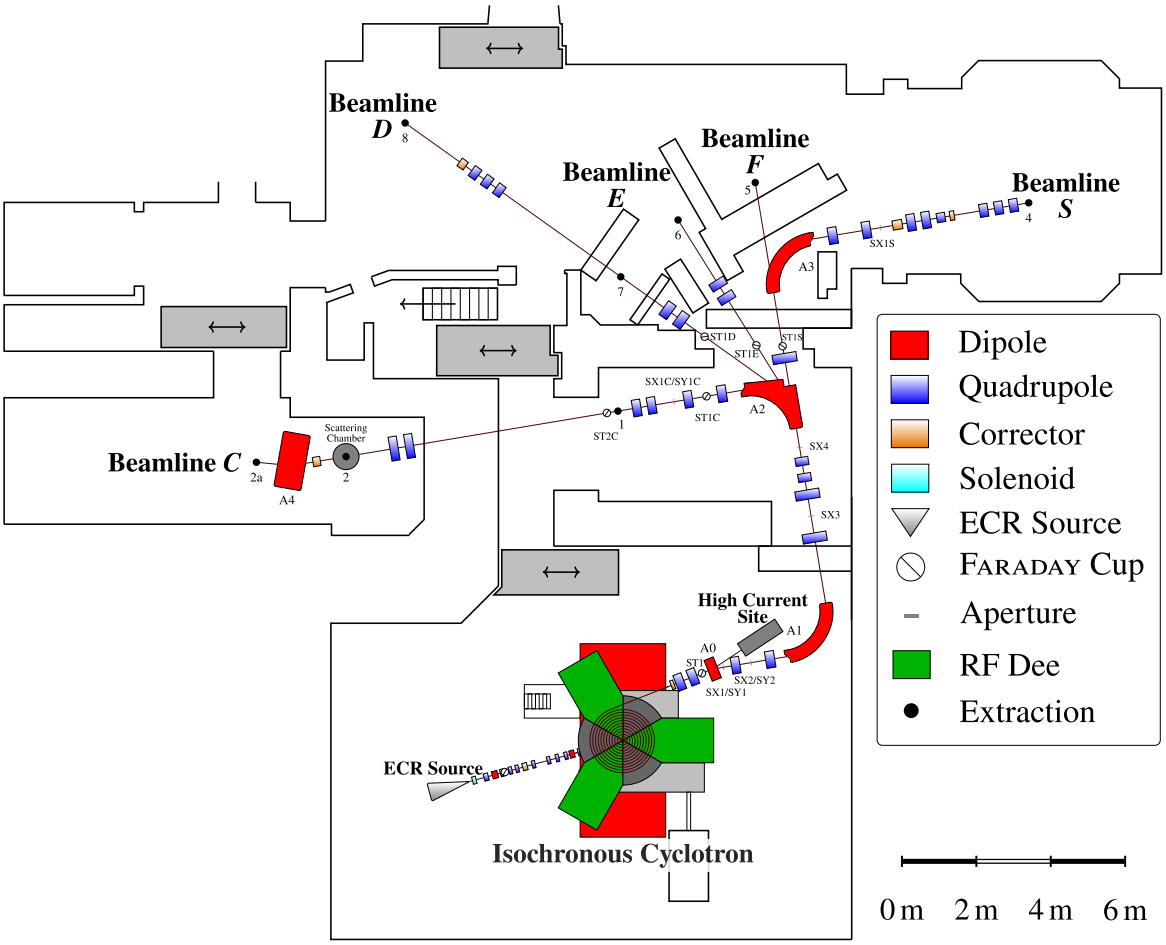

Figure 5.3: Overview of the Bonn Isochronous Cyclotron facility. The accelerator provides beam along the five beamlines *C, D, E, F* and *S*. A total of eight experimental sites as well as a *high-current site*, directly adjacent to the cyclotron, can be supplied. The irradiation site is located inside the *high-current room* at experimental site *2a*, concluding the *C* beamline. Schematic adapted from [59].

The BIC facility accommodates five high-energy beamlines, *C, D, E, F* and *S*, along which the beam is transported to eight dedicated experimental sites. An overview of the facility, beamlines and sites is shown in Fig. 5.3. Here, only the lower level of the facility is depicted, with the upper level housing the control as well as power supply room and a *gallery* area with space for additional setup components. Adjacent to the accelerator, a dedicated *high-current site* is located for the purpose of radioisotope production. Along each of the beamlines, internal beam diagnostics are installed at fixed locations, so-called *stoppers* (prefixed with ST) and *scrapers* (prefixed with S), compromised of Faraday Cups (FCs) and apertures for destructive beam current and position determination, respectively.

5.2 Irradiation Site

The irradiation site at the BIC is located in the *high-current room*, at extraction *2a* which concludes the beamline *C*, as shown in Fig. 5.3. The location exhibits good characteristics with regard to the

requirements for irradiation:

- The beam handling system on the *C* beamline enables high momentum resolution of up to $\frac{p}{\Delta p} = 3 \times 10^4$ [62], allowing for the assumption of a mono-energetic beam being delivered to the site.
- A wide range of proton beam currents between 20 and 1 000 nA is available, facilitating to perform low- as well as high-fluence irradiation campaigns efficiently.
- The high-current room is a dedicated site, isolated from the facility during beam extraction, enabling one to simultaneously carry out irradiations and access the remaining area. This make it possible to situate and operate additional equipment in close proximity (see Fig. A.4).

To minimize the energy loss of the low-energy protons, the setup is installed immediately following the last dipole magnet *A4*, leaving only a few cm of air between it and the exit window of the beamline. A Computer-Aided Design (CAD) render as well as an image of the setup are shown in Fig. 5.4. The site houses several elements which can be divided into setup components and (beam) diagnostics. The setup is described briefly here and in greater detail in the following Section 5.2.2, whereas the diagnostics are covered in Section 5.3.

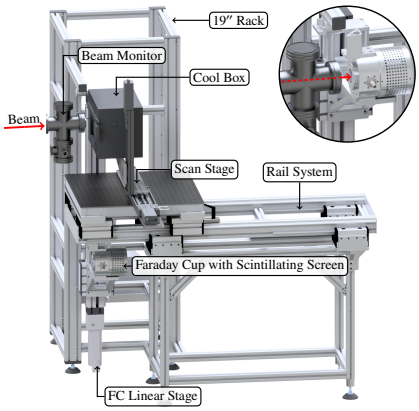

(a) CAD render of irradiation setup, adapted from [60]

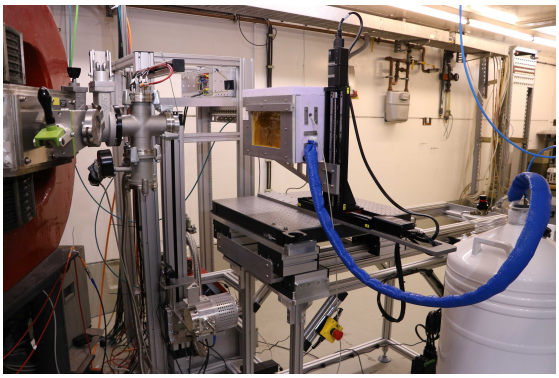

(b) Picture of irradiation setup from October 2021

Figure 5.4: CAD render (a) and picture of the irradiation setup (b), located at the *2a* extraction (see Fig. 5.3). The setup table is retracted using a motorized stage, allowing the on-site FC to be driven in front of the beam monitor. A liquid nitrogen dewar functions a heat exchanger, guiding cool nitrogen gas into the box.

The setup consists of a table which is equipped with a top base plate featuring an optical breadboard. The top plate is mounted on a rail system, adjustable along the beam axis via a motorstage. A two-dimensional scan motorstage is installed on the breadboard, carrying an insulated cool box on an extension arm, movable in the plane perpendicular to the beam. The cool box features an entry window as well as a scintillating screen on the out- and inside for beam-based alignment. Inside the box, a combined shielding and mounting mechanism allows for installation of a variety of DUTs. Adjacent to the table, a 19 " rack is positioned, housing power supplies, vacuum pumps and various connectors, interfacing the irradiation site. Moreover, a vertical motorstage is situated aside the rack, on which a FC with a scintillation screen is placed. In combination with the setup table stage, this

enables to retract the setup and drive the FC into the beam. Lastly, a beam monitor is positioned in front of the setup, housed in a cross-piece, as the final element in the beamline.

5.2.1 Overview

To establish the localities and interfaces of the irradiation site at the BIC facility, a schematic overview is displayed in Fig. 5.5, showing the different setup components and their interconnections. Indicated by the dashed lines, the overview is separated into three main locations; the *high-current room*, the *gallery* and the accelerator *control room*. The high-current room is placed on the accelerators main level, as displayed in Fig. 5.3, whereas the control room and gallery are situated a level above. Each location is connected to the Bonn Isochronous Cyclotron Local Area Network (LAN), allowing integration, control and communication of devices via Ethernet.

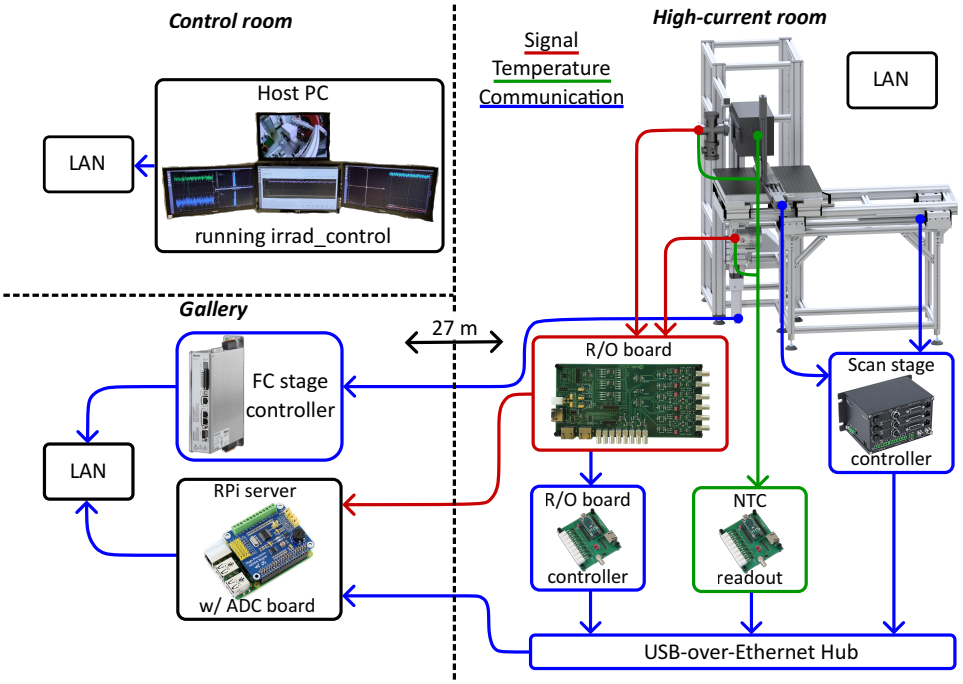

Figure 5.5: Schematic overview of the irradiation site components, their locations and interconnections. It is separated into three localities: the *high-current room*, containing the irradiation setup described in Section 5.2.2, the *gallery*, housing the setup-controlling RPi server and the *control room* with a host computer running the `irrad_control` software.

In the control room of the accelerator, a host computer is running the control software of the irradiation site `irrad_control` (see Section 5.6), facilitating management, DAQ as well as visualization of the irradiation-relevant components and data. Located on the gallery and connected to the host computer via LAN, a dedicated server is running on a Raspberry Pi (RPi) single-board computer. It interfaces the irradiation site via LAN and *USB-over-Ethernet* extenders, facilitating the control of multiple serial devices. Additionally, it is equipped with a commercial ADC expansion board, facilitating DAQ of analog voltage signals transmitted from the readout electronics at the site via approximately 27 m long twisted-pair cables. Using dedicated cables of the same length, the controller for the linear stage of

the on-site FC connects to the irradiation setup. Inside the high-current room, the custom-made beam diagnostics (see Section 5.3) of the irradiation site are read out via an analog readout electronics (R/O electronics) board, placed in a 19" rack, whose output voltages are digitized by the RPi ADC module. Two Arduino-based Nano-Utility-Boards (NUBs) as well as the scan and table stage controller are placed beneath the setup table and are connected to the RPi server. The NUBs are used to control the R/O electronics board settings as well as facilitate the readout of multiple NTC thermistors inside the cool box.
The infrastructure is designed with integration, control and data acquisition of additional hardware in mind, making easy extensions, by e.g. user-specific measurement equipment, possible.

5.2.2 Components

In this section, the individual setup components, shown in the overview in Fig. 5.5, are described in detail. The diagnostics are explained separately, in Section 5.3.

Scan Stage

The scan stage is used to move the cool box in the plane perpendicular to the beam axis, for beam-based alignment and uniform irradiation. It consists of the two commercial linear stages from *Zaber Technologies Inc.* [64] in an XY-configuration. The main specifications of the motor stages are listed in Table 5.1. Each axis has a travel range of 300 mm, allowing for irradiation of the entire cool box area. The axes deliver sufficient position accuracy and velocities of up to $110\,\mathrm{mm\,s^{-1}}$ while providing adequate capacities for installations heavier than the typical cool box plus DUT load. The linear stages feature a stepper motor with integrated encoders as well as drivers and are interfaced via an external motor controller, placed underneath the setup table. This facilitates a placement of the controller with increased distance to the beam plane of up to a few meters, reducing the radiation exposure of the consumer electronics. The *Zaber* motion products are easy to use as they support well-documented ASCII and binary communication protocols with pre-existing software packages for most programming languages.

Model	Step	Travel	Velocity	Accuracy	Load	Thrust	Controller
LRQ300HL	0.2 µm	300 mm	$110\,\mathrm{mm\,s^{-1}}$	55 µm	1 000 N	500 N	X-MCC3

Table 5.1: *Zaber* linear stage specifications for the scan and setup table stages [64]. Maximum values are given for variable quantities.

Setup Table

The in-house designed setup table is constructed using aluminum profiles from *item* [65] as well as an optical breadboard from *Thorlabs* [66], on which the scan stage is mounted (see Fig. 5.4). The breadboard comes with a grid of M6 threads with 25 mm spacing, facilitating easy installation of additional equipment. It is situated on a double rail system, allowing one to move it along the beam axis with a displacement of approximately 1 m in total. An additional *Zaber* linear stage (see Table 5.1) is integrated into the double-rail system, enabling one to remotely displace the breadboard over 0.3 m

within the total range of 1 m. The table is designed to carry loads of up to 100 kg, providing a variety of different setup configurations and additions, and is therefore fixated to the ground.

19" rack & FC stage

Adjacent to the setup table, a 19" rack, also constructed from *item* aluminum profiles, is located (see Fig. 5.4). The rack houses a set of High-Voltage (HV) power supplies, a vacuum pump for the on-site FC and a variety of interfaces to the irradiation site. Here, twisted-pair, coaxial and unshielded cables for e.g instrument interfacing, high-frequency signals and remote power supply, respectively, are available. They connect the irradiation site to a twin rack, located on an upstairs gallery, an area which is accessible during beam extraction.
Additionally, a linear stage from *item* [65] is mounted vertically on the beam-facing side of the rack, on which the on-site FC is installed. The stage has a travel range of 716 mm, in combination with the setup table stage, allowing to drive either the FC or the cool box in front of the beam monitor. The FC stage has a dedicated controller, located off-site on the upstairs gallery.

Cool box

To irradiate DUTs in a cool and dry atmosphere, an insulated cool box has been designed and is shown in Fig. 5.6. It mainly consist of thermally-insulting materials with sufficient rigidity such as *Styrodur* and *Rohacell*. The box features a double entrance window, consisting of two 30 µm *Kapton* layers spaced 1 cm apart, with an area of approximately $(19 \times 11)\,\mathrm{cm}^2$. Using this configuration, beam energy losses are minimized while simultaneously maximizing the thermal insulation. The inner volume of the box is approximately $(19 \times 11 \times 15)\,\mathrm{cm}^3$ with a 1 cm graphite backplate, serving as a beam dump. To avoid condensation, a ventilation bar guides compressed air from top to bottom on the outside of the entrance window. Internal and external scintillation screens are mounted for beam-based alignment of the setup. On the right, a cable feed-through facilitates powering and readout of DUTs during irradiation. The box is cooled by continuous flushing with nitrogen gas which is guided through a copper heat exchanger, submerged in a 60 L liquid nitrogen dewar (see Fig. 5.4(b)). The nitrogen gas is supplied via standard 200 bar cylinders, the temperature is regulated via a flow meter. Here, a single cylinder typically suffices to maintain a temperature less than −20 °C for a full day of irradiation.

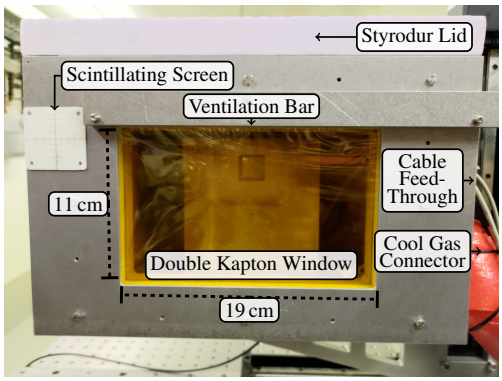

Figure 5.6: Front view of cool box

Data Acquisition & Setup Control

To control the hardware of the irradiation site as well as read out the signals provided by the beam diagnostics, an RPi single-board computer (*3 Model B+*) with an expansion board for Analog-to-Digital/Digital-to-Analog conversion from *Waveshare* [67] is used. The RPi is widely available, cost-efficient, features a variety of interfaces for communication and has a rich software environment

as well as range of extension possibilities which makes it an ideal solution. The *Waveshare* expansion board features a 24 bit, up to 30k samples-per-second ADC with an 8-to-1 input multiplexer, facilitates the measurement of up to eight single-ended input voltage signals within a range of 0 – 5 V. The RPi is situated off-site on the upstairs gallery inside the twin 19" rack that houses the interfaces to the irradiation site. In order to connect to the different devices in the high-current room, the RPi is attached to the BIC LAN that is available across the entire facility, as well as via an USB-over-Ethernet adapter hub, enabling the connection of multiple serial devices. The RPi is configured as a server which is controlled by a central computer, located in the control room of the BIC, via the `irrad_control` [68] software. An overview of the setup is given in Fig. 5.5.

Camera System

The irradiation setup features three cameras installed on-site for visual inspection of the beam spot and alignment on the scintillating screens. A camera, mounted directly on the *A4* dipole magnet, is focused on the internal cool box screen, allowing for a beam-based alignment of the setup. Moreover, a camera is installed on the on-site FC, directed on its screen which is primarily used for visual beam inspection and adjustment when driven into the beam. Lastly, a camera is placed on top of the 19" rack, capturing the entire setup from above through a wide-angle lens. All cameras are connected to a monitor in the BIC control room via a switcher, enabling one to cycle through the different scenes as required.

5.2.3 Devices Under Test

The irradiation site has been developed in parallel to the arrival of the first demonstrator pixel chip `RD53A` (see Section 3.3) with the goal of facilitating radiation hardness tests in Bonn. As the chips are typically mounted on an SCC for testing, the irradiation setup has been optimized to house such and comparable devices. Therefore, in the default operation mode, DUTs are irradiated on a carrier PCB which is placed behind an aluminum shielding. A CAD schematic as well as a front view of this configuration is shown in Fig. 5.7.
The shielding consist of two 6 mm-thick aluminum[1] parts, representing at least six times the projected range of protons in aluminum [19] for the energies available at the BIC. It is separated into a generic as well as a DUT-specific shield with the former providing a rail-based mounting mechanism for the latter as well as the DUT, allowing one to slide both parts into place from the top. The specific shield is manufactured at the irradiation site for each individual DUT, resulting in only the actual DUT cross section[2] being exposed to the beam (see Fig. 5.7(a) top right). A total area of $(6 \times 6)\,\mathrm{cm}^2$ is available to the DUT-specific shield, subsequently limiting the maximum DUT size to the same area for the default operation. The mounting mechanism for typical DUTs, situated on $(10 \times 10)\,\mathrm{cm}^2$ SCC, consists of a set of rails which are installed on the PCB via stand-offs of various length. Within a certain margin, variances of DUT locations between different PCBs can be compensated by mounting the rails on an additional 3D-printed translation layer.
In case the DUT does not reside on an SCC, such as bare sensors, diodes or prototypes on small-scale PCBs, so-called *surfboards*, a dedicated aluminum carrier plate (see Fig. 6.14(c)) is utilized. It features a 1 cm grid on which DUTs are fixated using Kapton tape and subsequently mounted using

[1] To minimize activation of long-lived isotopes, the parts are manufactured from 99.5 % pure aluminum.
[2] A few mm extra are taken into accounted for compensation of misalignments.

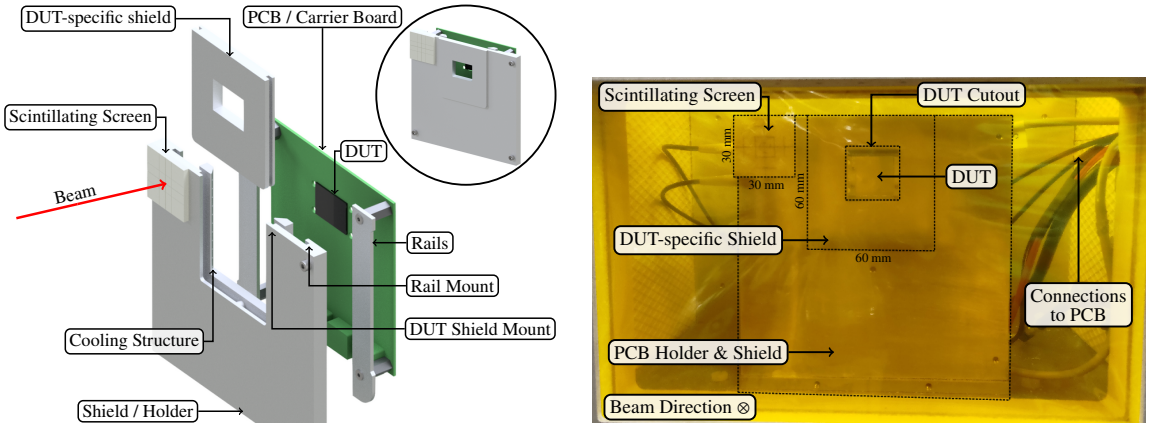

(a) CAD render of default configuration

(b) Front view into cool box with default configuration

Figure 5.7: CAD render and picture of default configuration of DUTs at the BIC irradiation site. Devices are mounted behind a 6 mm aluminum shielding, consisting of a DUT-specific and generic part, using a rail system. Cool nitrogen gas is guided onto the samples via a U-shaped structure.

the standard rail system. For DUTs larger than $(6 \times 6)\,\mathrm{cm}^2$, the default shield can be removed and the full entrance window size of $(19 \times 11)\,\mathrm{cm}^2$ of the cool box becomes available.
In the default configuration, a plastic cooling structure is mounted in between the shielding and the DUTs PCB. It is U-shaped with a connection to the cool nitrogen gas on the bottom and its arms having a perforated surface, angled at approximately 45° towards the carrier PCB. It guides the cool nitrogen into the box and onto the DUT area, situated directly within the gas stream. The structure is fixated to the generic shield via a screw with an integrated NTC thermistor, allowing for a temperature reference measurement during irradiation. If the default configuration is not suitable, the gas can be directed onto the DUT using flexible tubing.
DUTs can be powered and read out during or in between irradiation steps by utilizing a dedicated cable feed-trough within the cool box with a diameter of approximately 2 cm, enabling one to fit multiple cables. As the feed-through can be opened to the top, also large connectors can be used.

5.3 Custom Diagnostics

The BIC features two types of beam diagnostics located at fixed positions along each of the six individual beamlines. FCs, also called *stoppers*, for beam current measurement and apertures, also called *scrapers*, for determination of beam width as well as position within the beam pipe. Their locations are marked in Fig. 5.3, where FCs are encoded using `ST`, followed by an index and the letter of the respective beamline (e.g. `ST1C`) and apertures using `S`, followed by `X/Y` for their orientation and an index (e.g. `SX3`). A more detailed description of the beam handling system can be found in [62].
The available diagnostics determine the beam properties *destructively*, preventing the beam partially (scrapers) or completely (stoppers) from propagating towards the targeted extraction. Furthermore, no diagnostics are located in proximity to the extraction *2a*, where the irradiation setup is situated. The ability to online-monitor the beam properties at the extraction, enables an implementation of a

beam-based irradiation routine as well as a dosimetry approach. These features allow for application of highly uniform fluences with low uncertainty to DUTs as well as obtain spatially resolved information on the fluence distributions. Therefore, a set of custom beam diagnostics has been developed within the scope of this thesis and as part of [59, 60]. They enable a non-destructive, on-site beam parameter monitoring, facilitating a beam-based irradiation procedure as well as dosimetry as described in Sections 5.4 and 5.5. In this section, the fundamentals as well as the individual components are introduced whereas the characterization can be found in Section 6.2.

5.3.1 Fundamentals of Beam Diagnostics

The working principle of the custom beam diagnostics is based on the effect of ion-induced Secondary Electron Emission (SEE) which is fundamentally described in [69]. On penetration of fast ion beams into a given target, Secondary Electron (SE) are emitted from the material's surface. The Secondary Electron Emission Yield (SEY) γ characterizes the process by describing the fraction of emitted electrons per incident ion. If the current of secondary electrons, I_{SEE}, as well as the ion beam current, I_{beam}, are known, γ can be defined as

$$\gamma = \frac{I_{\mathrm{SEE}}}{I_{\mathrm{beam}}} \cdot z_{\mathrm{ion}} \,, \tag{5.3}$$

where z_{ion} is the number of elementary charges q_e carried per ion. As demonstrated in [69, 70], for a given ion X and target material M, the resulting SEE current generally is a function of multiple parameters which can be expressed as

$$I_{\mathrm{SEE}}\left(p, T_{\mathrm{M}}, E_{\mathrm{X}}, A_{\mathrm{X}}, \theta_{\mathrm{X}}, D_{\mathrm{M}}\right) \,, \tag{5.4}$$

where the dependencies are

- the environmental pressure p,
- the target material temperature T_{M},
- the ions kinetic energy E_{X},
- the intensity in ions per unit area A_{X},
- the ions incident angle θ_{X},
- the target material thickness D_{M}.

Furthermore, it is worth to emphasize that SEE is a surface effect and the resulting SEY represents the corresponding conditions on the targets surface. Considering a monoenergetic ion beam with constant intensity penetrating a material perpendicularly inside a vacuum, the fixed parameter space results in a constant γ. For this configuration, a series of measurements of the SEY for graphite and aluminum for a variety of light ions at different energies is shown in Fig. 5.8. Subsequently, Eq. (5.3) can be used to measure the ion beam current as a function of the SEE current:

$$I_{\mathrm{beam}} = \frac{z_{\mathrm{ion}}}{\gamma} \cdot I_{\mathrm{SEE}} = \beta \cdot I_{\mathrm{SEE}} \quad \text{with} \quad \beta = \frac{z_{\mathrm{ion}}}{\gamma} \,. \tag{5.5}$$

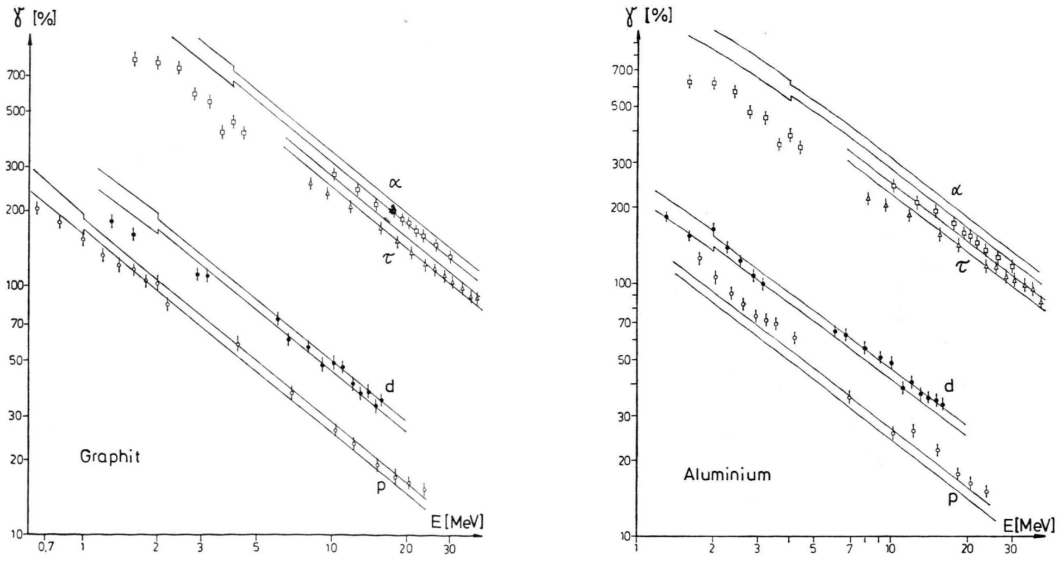

(a) Graphite (b) Aluminum

Figure 5.8: SEY γ for graphite (a) and aluminum (b) for protons (p), deuterons (d), helium-3 (τ) and alpha (α) particles for different energies, from [70]. Here, the beam penetrates the target perpendicularly in a controlled vacuum between 4×10^{-6} and 2.6×10^{-5} mbar. The uncertainty bands include variations due to changes in vacuum pressure.

As γ only varies within a few percent (specifically for thick targets) over multiple orders of magnitude of the ion intensity and target temperature [69], it can be assumed constant in A_X and T_M (see Fig. 6.8). Using the constellation leading to Eq. (5.5), non-destructive, online beam parameter monitoring using a dedicated, custom-made set of diagnostics is realized, introduced in the following Sections 5.3.2 and 5.3.3.

5.3.2 On-Site Faraday Cup

To directly measure the beam current extracted into the cool box of the irradiation setup shown in Fig. 5.4, an on-site FC has been developed. A CAD render as well as a schematic of its working principle are shown in Fig. 5.9. The beam enters the FC through a 30 µm-thick AlMg3 *Lenard* window into a dedicated vacuum at $\leq 1 \times 10^{-6}$ mbar. Subsequently, it propagates through a cylindrical suppressor electrode ring before it is stopped in a conical graphite beam dump. The shape of the beam dump is optimized to prevent SEs to escape from the graphite surface, circumventing erroneous measurement of an increased current. The suppressor electrode is kept at -100 V to further restrict the escape as well as entrance of SEs from the beam dump and *Lenard* window, respectively. Using Computer Simulation Technology (CST) `Studio Suite` [71], simulations of the resulting potentials as well as SEE in equilibrium state for a typical proton beam (see Section 5.4) are displayed in Fig. 5.10.

The produced SEs have a mean energy in the low eV region and are successfully suppressed with a relative SE escape ratio of 7.6×10^{-5} [60]. This corresponds to an intrinsic accuracy of $\geq 99.99\,\%$ for direct measurement of the beam current.
As shown in Fig. 5.4(a), the FC is mounted on a vertical linear stage, enabling one to drive it in and out

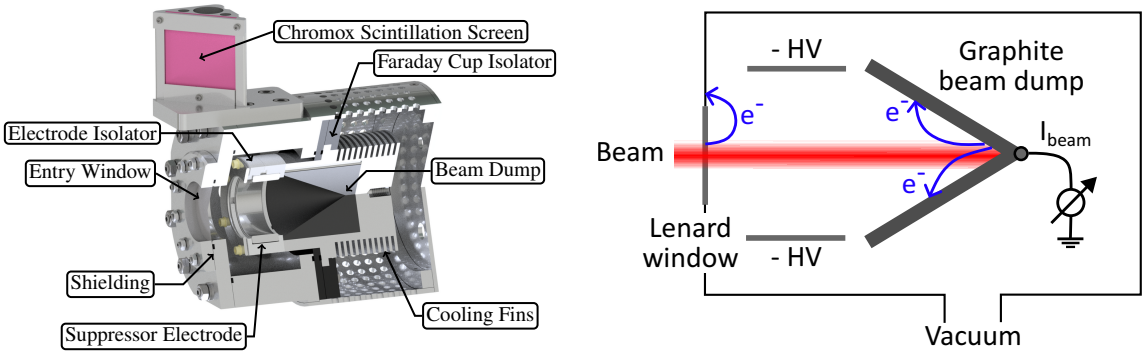

(a) CAD render of on-site FC, from [60]

(b) Schematic function of FC

Figure 5.9: CAD render and schematic of the working principle of the on-site FC at the irradiation site. It consists of a graphite beam dump, a suppressor electrode as well as an entrance window and is mounted on a vertical linear stage (see Fig. 5.4). A scintillation screen is mounted on top allowing for visual beam inspection and adjustment.

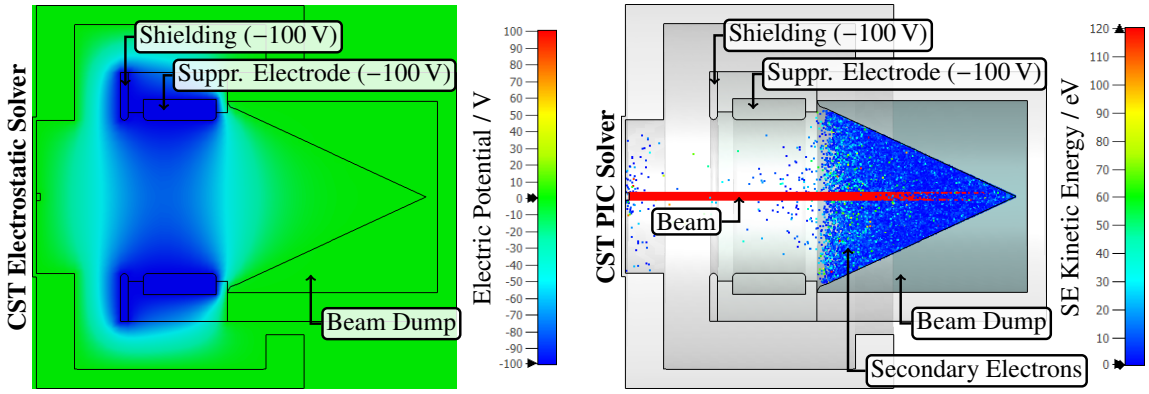

(a) CST simulation of electrostatic potentials

(b) CST Particle in Cell (PIC) simulation of SEE

Figure 5.10: CST [71] simulations of electrostatic potentials and SEE spatial as well as energy distribution of the on-site FC. For a 13.6 MeV proton beam of 1 µA in the equilibrium state, the mean kinetic energy of SEs lies in the low eV regime and the SE escape ratio is 7.6×10^{-5}, resulting in an intrinsic measurement accuracy of $\geq 99.99\,\%$. Results from [60].

of the beam remotely. When moved in the beam, it is situated in front of the beam monitor, replacing the cool box, allowing for measurement of the beam current at the DUT position. This configuration is used to calibrate the beam monitor (see Section 6.2) and is shown in the top right of Fig. 5.4(a). The body of the FC features cooling fins, enabling dissipation of the heat transferred by the beam. The FCs temperature can be monitored via a thermistor, fixed to the cooling fins. Finally, a scintillation screen for visual beam inspection and adjustment is installed on top of the FC.

5.3.3 Calibrated Beam Monitor

The beam monitor allows for a continuous online beam-parameter monitoring directly in front of the DUT and therefore concludes the beamline *C* towards extraction *2a*. It is housed inside a cross

piece. A CAD render and a schematic of its main components are shown in Fig. 5.11. It consists of two main parts, the Secondary Electron Monitor (SEM) and the Beam Loss Monitor (BLM) module. The former provides beam current and position monitoring whereas the latter facilitates beam loss detection. The beam enters the beam monitor traversing the SEM before passing the BLM module, after which it is extracted through a 30 µm-thick AlMg3 *Lenard* window.

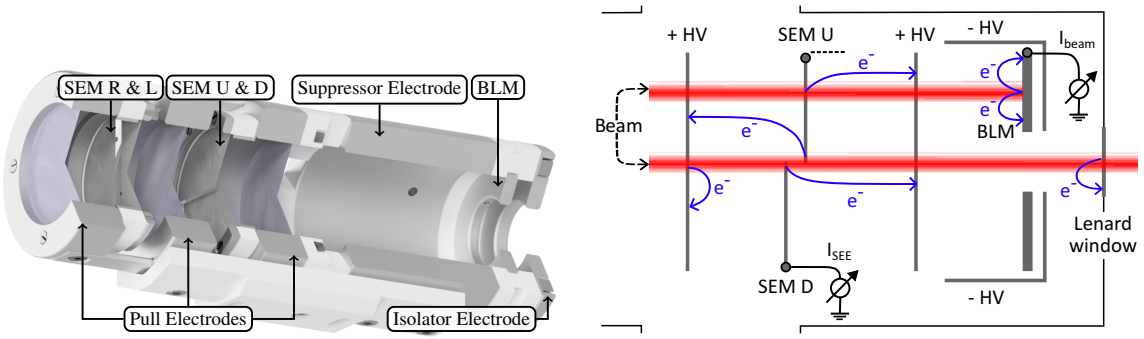

(a) Cut through CAD render of beam monitor from [59]

(b) Schematic working principle

Figure 5.11: CAD render and schematic of working principle of the beam monitor. It consists of a SEM as well as a BLM module for beam current & position and beam loss monitoring respectively. The SEM is composed of two, carbon-coated ($O(100\,\mathrm{nm})$), 4.5 µm aluminum foil pairs, segmented in the vertical and horizontal plane. HV foils are placed in between at 100 V, acting as pull electrodes, removing SEs from the SEM foils.

The SEM module consists of two pairs of horizontally- and vertically-segmented signal foils, each located between two HV foils at 100 V. The foils are each comprised of (half-)circular, 4.5 µm-thick aluminum where the signal foils are additionally coated with carbon of $O(100\,\mathrm{nm})$ to anticipate carbon built-up on the foil surfaces in vacuum under irradiation [72] and the consequent change in SEY. Each signal foil pair represents a dedicated SEM where SEM(L) + SEM(R) compromise the horizontal and SEM(U) + SEM(D) the vertical SEM. When the beam traverses the SEM module centrally, SEs are emitted at the surfaces of each of the signal as well as HV foils. Removing these SEs using the HV foils, results in a positive current flowing onto the signal foils according to Eq. (5.3). The horizontal and vertical SEM expose a total of two foil planes and subsequently four surfaces to the penetrating beam. Here, the resulting SE current I_{SEE} from Eq. (5.3) is obtained by normalizing the sum of the individual SE currents to the number of surfaces

$$I_{\mathrm{SEE}} = \sum_{n} \frac{I_{\mathrm{SEM}}(n)}{4} \quad \text{with} \quad n \in [\mathrm{L}, \mathrm{R}, \mathrm{U}, \mathrm{D}]\,, \tag{5.6}$$

where $I_{\mathrm{SEM}}(n)$ corresponds to the SE current onto the respective SEM foil. To enable the SEM module to monitor the magnitude of beam current for a specific ion, it needs to be calibrated by determination of the respective β in Eq. (5.5). This is realized by utilization of the on-site FC in calibration position (see Fig. 5.4(a), top right) to measure the SEE as well as the beam current simultaneously and extract β via a fit (see Fig. 6.8). The relative position deviation of the mean of the beam distribution to the center of the monitor can be defined via

$$x = \frac{I_{\mathrm{SEM}}(\mathrm{L}) - I_{\mathrm{SEM}}(\mathrm{R})}{I_{\mathrm{SEM}}(\mathrm{L}) + I_{\mathrm{SEM}}(\mathrm{R})}, \qquad y = \frac{I_{\mathrm{SEM}}(\mathrm{U}) - I_{\mathrm{SEM}}(\mathrm{D})}{I_{\mathrm{SEM}}(\mathrm{U}) + I_{\mathrm{SEM}}(\mathrm{D})}, \qquad x, y \in \pm 100\,\%\,, \tag{5.7}$$

where L, R, U, D are the individual signal foils. Here, a position of $(0, 0)$% corresponds to a centrally-aligned beam in the monitor whereas $(-50, 100)$% resembles $1/4$ versus $3/4$ of the beam distribution penetrating SEM(L) and SEM(R), respectively, and 100 % of the beam traversing SEM(U). It is worth to note that this position definition does not translate to the physical position of the mean of the distribution and is independent of the beam Full-Width Half-Maximum (FWHM).

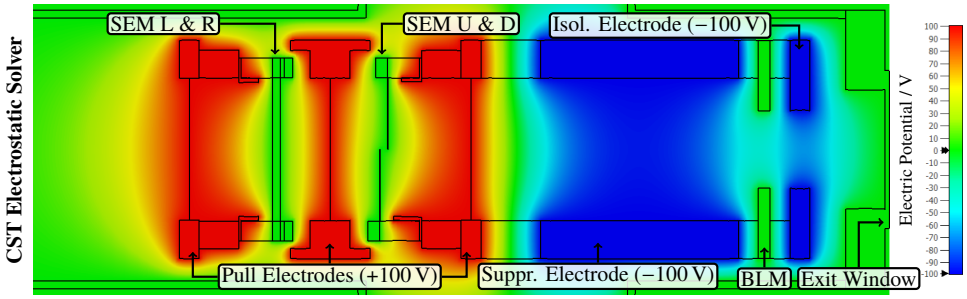

(a) CST simulation of electrostatic potentials

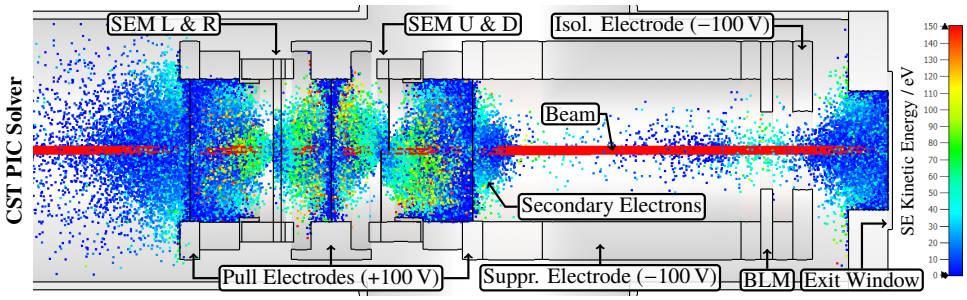

(b) CST PIC simulation of SEE

Figure 5.12: CST [71] simulations of electrostatic potentials and SEE spatial as well as energy distribution of the beam monitor. With the given potential configuration, the SE collection efficiency from the SEM foils is (99.11 ± 0.19) % and (99.77 ± 0.04) % for up- and downstream direction respectively. Results from [59].

The SEM is followed by the BLM module which consists of an 3 mm-thick aluminum aperture, preceded by a suppressor and succeeded by an isolator electrode at −100 V. The aperture has an inner and outer diameter of 20 mm and 40 mm respectively, corresponding to the diameter of the subsequent *Lenard* window, leaving a 10 mm-wide, sensitive iris for beam loss detection. It functions as an internal FC, directly measuring the current of any overlapping fraction of the beam distribution. As in Section 5.3.2, the suppressor electrode aims to prevent SEs to escape the surface of the aperture and therefore avoiding measurement of an erroneous beam current. Likewise, the isolator electrode suppresses SEs emerging from the *Lenard* window to reach the BLM iris. Using the relative position information provided by the SEM module in combination with the BLM module, enables the determination of the direction in which a beam cut-off occurs. Subsequent to the successful calibration of the beam monitor, the current signal of the BLM aperture is used to determine the beam loss I_{loss} and correct the beam current extracted I_{ext} towards the setup

$$I_{\text{ext}} = I_{\text{beam}} - I_{\text{loss}} \,. \tag{5.8}$$

Due to the heat transfer by the beam onto the aperture in conjunction with the limited heat dissipation in vacuum, a thermistor is located on the BLM iris. This facilitates the monitoring of the components' temperature to protect from overheating and damaging e.g. cables.
As in Section 5.3.2, simulations using CST `Studio Suite` [71] have been performed to obtain the potentials as well as SEE spatial and energy distributions within the beam monitor. They are shown in Fig. 5.12. For a typical 13.6 MeV proton beam with 1 µA current (see Section 5.4) the configuration in the equilibrium state again indicates a mean SE energy in the low eV regime. The suppressor and isolator electrode of the BLM module successfully constrain the spatial spread of SEs towards the aperture, preventing erroneous current measurement. Subsequently, the collection efficiency of SEs from the SEM foils is $\geq 99\,\%$ with an uncertainty $\ll 1\,\%$ [59] for the given potentials, allowing for accurate measurement of I_{SEE} and therefore I_{beam} via Eq. (5.5).

5.3.4 Analog Readout Board

The diagnostics introduced in the previous Sections 5.3.2 and 5.3.3 each provide current signals that need to be processed for digitization. For this reason, an analog R/O electronics board has been designed. A picture as well as a schematic of its main circuitry are displayed in Fig. 5.13. It features six inputs, one for each of the SEM module foils as well as one for the BLM and on-site FC. The main functionality is the transimpedance amplification of the current signals to voltages. Here, the transfer function[3] for an input signal I_{in} can be expressed as

$$U_{\mathrm{out}}\left(I_{\mathrm{in}}\right) = \left(-R_{\mathrm{in}} \cdot I_{\mathrm{in}}\right) \cdot \left(-\frac{R_x}{R_c}\right) = \frac{R_{\mathrm{in}} R_x}{R_c} \cdot I_{\mathrm{in}}\,. \tag{5.9}$$

Here, in order to provide accurate amplification also for small input signals, the first amplifier stage is realized by a low-offset operational amplifier `Analog Devices AD8616` [73] with a maximum offset of 65 µV. Introducing the *full-scale input current* I_{FS}, corresponding to an output of ±5 V, the R/O electronics are tuned to fulfill the relation

$$\frac{I_{\mathrm{in}}}{I_{\mathrm{FS}}} = \frac{U_{\mathrm{out}}}{5\,\mathrm{V}} \quad \text{with} \quad I_{\mathrm{FS}} = \frac{R_c}{R_{\mathrm{in}} R_x} 5\,\mathrm{V}\,, \tag{5.10}$$

allowing one to determine the input current I_{in} as a function of U_{out} and the respective I_{FS}. The resistors R_{in} and R_{c} are fixed[4] at 250 kΩ and 1 kΩ, respectively, whereas R_{x} can be adjusted via an 1-to-8 multiplexer, operated by an on-board General-Purpose Input Output (GPIO) extender on an I^2C bus, or manually setting the respective jumpers, effectively defining I_{FS}. The uncertainty on the full-scale input current is dictated by the chosen resistors which typically have a standard deviation of 1 % around their nominal resistance. Subsequently, the relative uncertainty can be expressed as

$$\frac{\Delta I_{\mathrm{FS}}}{I_{\mathrm{FS}}} = \sqrt{\left(\frac{\Delta R_c}{R_c}\right)^2 + \left(\frac{\Delta R_{\mathrm{in}}}{R_{\mathrm{in}}}\right)^2 + \left(\frac{\Delta R_x}{R_x}\right)^2} = \sqrt{3}\%\,, \tag{5.11}$$

where this corresponds to the uncertainty on input current ΔI_{in}. Here, the error represents the variation of I_{in} when utilizing arbitrary input channel and full-scale input current combinations of the R/O

[3] For the expected DC / low-frequency input signals.

[4] R_{in} can be divided by 10 via a jumper, scaling the available I_{FS} selection by 10.

electronics. As indicated in Section 6.2.1, certain pairings of channel and I_{FS} may yield a lower uncertainty due to their well-matched resistor configurations, resulting in an overestimation of the uncertainty for the specific configuration. Nevertheless, the error on the input current is determined using Eq. (5.11) in order to be able to provide an error estimation independent of the R/O electronics setting.

As the typical proton beam current is in the order of 1 µA with an SEE current of approximately

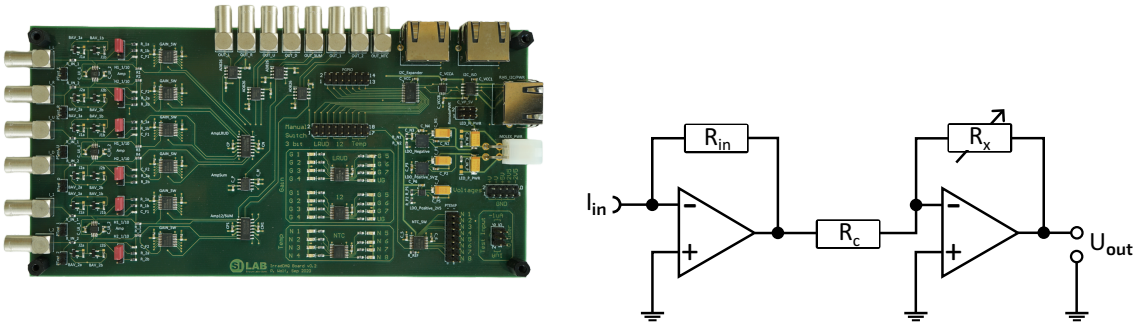

(a) Top view of the R/O electronics board version v0.2

(b) Schematic of amplification circuit

Figure 5.13: Top view of the readout electronics board (a) and schematic of the transimpedence amplification chain (b). The R/O electronics features six inputs, one for each current signal channel of the beam monitor and on-site FC, which are transformed to voltages according to Eq. (5.10) for digitization. The board is configured manually using jumpers or remotely via an I^2C bus.

20 % [70], the I_{FS} default values are chosen as

$$I_{FS} \in [10\,\text{nA}, 50\,\text{nA}, 100\,\text{nA}, 500\,\text{nA}, 1\,\mu\text{A}, 5\,\mu\text{A}, 10\,\mu\text{A}, 20\,\mu\text{A}] \ .$$

The inputs are grouped in SEM and FC inputs, providing a separate I_{FS} per category, to adjust for the possible significant difference between SEE and direct beam signal amplitude. Each input channels' current signal is transformed via Eq. (5.10) to an output voltage, resulting in six outputs. Additionally, Eq. (5.6) is directly implemented in the R/O electronics by analog summation and normalization of the four SEM input signals, providing a further output voltage U_{SEE}. Using this as well as Eq. (5.5), the beam current I_{beam} can be written as

$$I_{beam} = \beta \cdot \frac{U_{SEE}}{5\,\text{V}} \cdot I_{FS} = \lambda \cdot U_{SEE} \cdot I_{FS} \quad \text{with} \quad \lambda = \frac{\beta}{5\,\text{V}} \,, \tag{5.12}$$

where λ is defined as the *calibration constant* of the beam monitor for a given ion and energy (also see Section 6.2) and I_{FS} corresponds to the full-scale input current of the SEM inputs. The uncertainty on the so-obtained beam current is dominated by the one on I_{FC} as defined in Eq. (5.11), as the errors on the calibration constant λ as well as the measured voltage U_{SEE} can generally be neglected.

The R/O electronics also provide eight pin headers for connecting NTC thermistors of nominally 10 kΩ via an additional 1-to-8 multiplexer to one output. The respective NTC can be selected using the I^2C interface or manually setting the respective jumpers, providing the voltage over a 10 kΩ resistor in a voltage divider configuration, allowing for the determination of the resulting NTC temperature via the *Steinhart-Hart-Equation* [74].

The configurations of the selected I_{FS} for each input as well as the NTC header are visualized on the R/O electronics board via a dedicated LED array. In order to test the analog signal processing chain, the R/O electronics features test inputs via pin headers, allowing one to source predefined ±1 µA directly into the respective inputs or adjust the test input current by connecting a voltage source between ±5 V.
The R/O electronics board facilitates the transformation of the current signals obtained from the beam diagnostics into voltages. For any given ion beam, the resulting output voltages of the FC as well as beam monitor channels are positive, yielding a range of 0 – 5 V which can subsequently be digitized using the *Waveshare* ADC expansion board (see Section 5.2.2), enabling digital, real-time data processing of beam-related data.

5.3.5 Arduino-Based Utility Board

The harsh radiation conditions during irradiation in close proximity to the setup, exhibit a difficult environment for digital consumer electronics, possibly resulting in temporary or permanent failure due to transistor damage (see Section 4.1.1). To create a cost-effective and flexible solution to performing a set of on-site tasks related to the irradiation setup, an Arduino-based [75] NUB has been developed within the course of this work. The board and a schematic of its basic functionality is shown in Fig. 5.14, the complete schematics as well as comprehensive documentation can be found in [76]. The board allows for readout of up to eight NTC thermistors, via pin header or Molex MiniFit, in a voltage divider configuration (see Fig. 5.14(b)). Furthermore, the board features an *RJ45* connector allowing to expose the I^2C bus over a twisted pair cable. It is worth to note that the connector pin layout is specifically matched to the one on the R/O electronics board, introduced in the precious section, but offers to feed external signals over the remaining twisted pairs via a pin header. Additionally, the board features a *LEMO* connector, enabling to count logic 5 V pulses. For the board to function properly, it must be configured for the respective task by setting the corresponding jumpers.

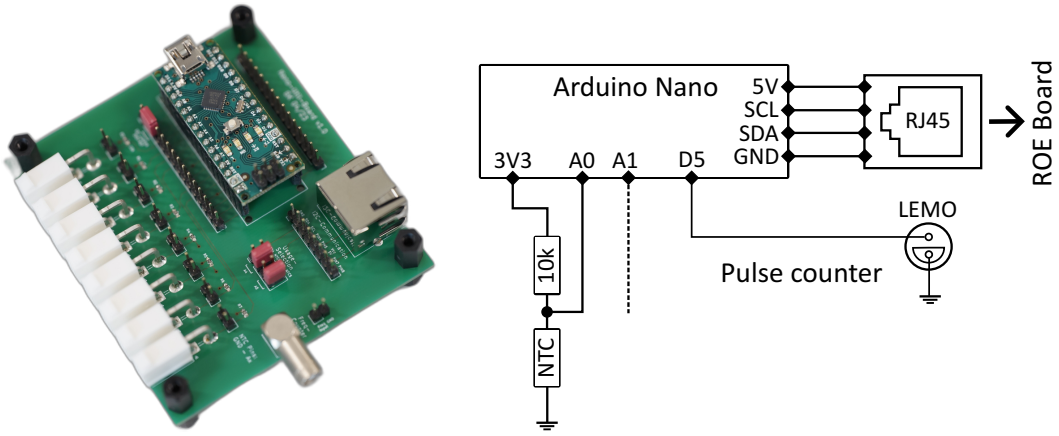

(a) Picture of the NUB version v1.0

(b) Schematic of functions of NUB

Figure 5.14: Top-view of Arduino-based [75] NUB and schematic of its basic functionalities. The board is used to read out up to eight NTC thermistors, control the R/O electronics, introduced in Section 5.3.4, via an I^2C bus and count pre-amplified pulses of a *Geiger* counter.

Within the framework of the irradiation setup, the NUB is used to measure the temperatures of the

BLM aperture (see Section 5.3.3), the on-site FC (see Section 5.3.2) and the DUT as well as ambient temperature inside the cool box during irradiation. If required in a specific setup, also additional NTCs can be connected. Furthermore, using a twisted pair cable, the board is used to interface and configure the R/O electronics, allowing for the adaptation of the input current scale I_{FS} to changing beam conditions on the fly. Lastly, the board is used to count pulses of an on-site *Geiger* tube to monitor radiation conditions close to the setup, especially after irradiation.

5.4 Irradiation Procedure

In this section, the operation of the proton irradiation site at the BIC is described in detail. A significant portion of the procedure is implemented and enabled through the control software of the site, `irrad_control` [68], which is the subject of Section 5.6. In the following Sections 5.4.1 to 5.4.3, the individual steps corresponding to the preparation, irradiation routine, as well as concluding actions for standard DUTs, as showcased in Section 5.2.3, are given.
For irradiation campaigns, the accelerator is typically operated at the upper limit of possible energies, extracting proton beams with an energy of 13.6 MeV, corresponding to 12.3 MeV on the DUT surface, and currents of up to 1 µA to the site. Commonly, the beam spot after extraction into the setup has a FWHM of $\leq$ 10 mm. The temperature inside the cool box, housing the DUT, is maintained at $\leq -20\,^{\circ}\mathrm{C}$.

5.4.1 Prerequisites

Prior to the start of an irradiation, preparatory tasks have to be performed that depend on the specifics of the campaign at hand. These tasks depend on various quantities such DUT type and dimensions, the target fluence as well as beam parameters and are listed in the following.

Irradiation Routine Parameter Estimation

To ensure a homogeneous application of the target fluence via the irradiation routine described in Section 5.4.2, the DUT has to be fully scanned through the beam multiple times. A sufficient number of full scans provides the possibility to level the fluence distribution via corrections. According to the target fluence and DUT area, Eq. (5.13) is used to estimate adequate scan parameters as well as the beam current.

DUT Installation

The DUT as well as its specific shielding are installed inside the cool box, using the rail mounting system. Optionally, if the irradiation campaign requires powering, readout or additional hardware for the DUT, the corresponding connections are set up via the feed-through in the cool box. Subsequently, the cooling system, described in Section 5.2.2, is initiated and the setup is driven into the calibration position, as depicted in the upper right of Fig. 5.4(a), with the setup table retracted along the beam axis and the on-site FC placed in front of the beam monitor.

Beam Preparation

The initial requirement for the irradiation is the adjustment of the beam optics for extraction into the setup. Therefore, the scintillation screen, situated on top of the on-site FC, is centered directly in front of the beam monitor via the linear stage and the beam is extracted. Using the camera system, the beam is visually inspected and adjusted to a well-focused spot, from which a maximum estimation of the beam FWHM is made. Finally, the relative position inside the beam monitor, defined by Eq. (5.7), is utilized to center the prepared beam with the upstream corrector magnets.

On-The-Fly Beam Monitor Calibration

Prior to each irradiation campaign, an on-the-fly beam monitor calibration is conducted to minimize uncertainties on the extracted beam current by run-to-run variations of the beam energy and the environmental parameters. To do so, the on-site FC is driven centrally in front of the beam monitor and the beam is extracted. The resulting SEE (see Eq. (5.6)) as well as the beam current, directly observed in the FC, are recorded and the beam current is varied by ±10 – 20 % around the nominal current, anticipated for the irradiation campaign. Using the analysis capabilities of `irrad_control`, a fit according to Eq. (5.5) is performed from which the calibrated beam current and the calibration constant λ can be determined via Eq. (5.12).

Beam-Based Alignment

To allow for the creation of a relative coordinate system in which the irradiation routine can be executed, a reference position must be defined. Therefore, the on-site FC is driven below the setup table which in turn is moved towards the beam monitor, replacing the FC with the cool box directly in front of the beam monitor. Using the scan stage, the scintillation screen on the shielding inside the cool box (cf. Fig. 5.7) is situated in the approximate center of the beam axis. This configuration corresponds to the setup in irradiation position. The beam is extracted into the cool box, centered in the beam monitor and in combination with the camera system, the beam spot is observed on the scintillation screen. The cool box is consequently moved until the beam spot is located in the screen's center, defining the reference position for the irradiation routine.

5.4.2 Beam-Driven Irradiation Routine

In order to enable a uniform fluence application to the area of a given DUT, it is driven repeatedly through the beam in a dedicated pattern using the scan stage. The process is shown schematically in Fig. 5.15. From the reference position obtained by beam-based alignment of the setup, a pattern of n equidistantly-spaced rows is constructed using the DUT's cross section and relative location. Along the rows, separated by a distance Δ_{row}, the DUT is moved through the stationary beam at the constant velocity v_{scan}. The generated grid incorporates an area larger than the DUT cross section. The excess area includes margins accounting for the beam FWHM in both dimensions, the acceleration distance required to reach v_{scan} as well as misalignments within the relative coordinate system. By selecting a row separation $\Delta_{\text{row}} \ll \text{FWHM}_{\text{beam}}$ and ensuring $v_{\text{scan}} = \texttt{const.}$ while traversing the DUT area, the beam profile is integrated in the vertical and horizontal dimension, respectively. This yields a uniform fluence distribution across the marked area in Fig. 5.15, in which the DUT resides. In contrast, an increased as well as non-uniform fluence distribution accumulates at the peripheries due

to the pattern's turning points. Here, rows of the grid are switched and sufficient beam conditions are awaited (see below), resulting in an increased exposition to the beam. While situated here, the beam is fully located and terminated on the shielding, off the DUT cross-section, therefore not contributing to the target fluence. Sequentially progressing through all n rows of the grid constitutes a *complete scan*, defining the unit by which the delivered fluence is incremented. The procedure is repeated, starting from the last row of the previous scan, until the target fluence is applied to the uniform area in Fig. 5.15.

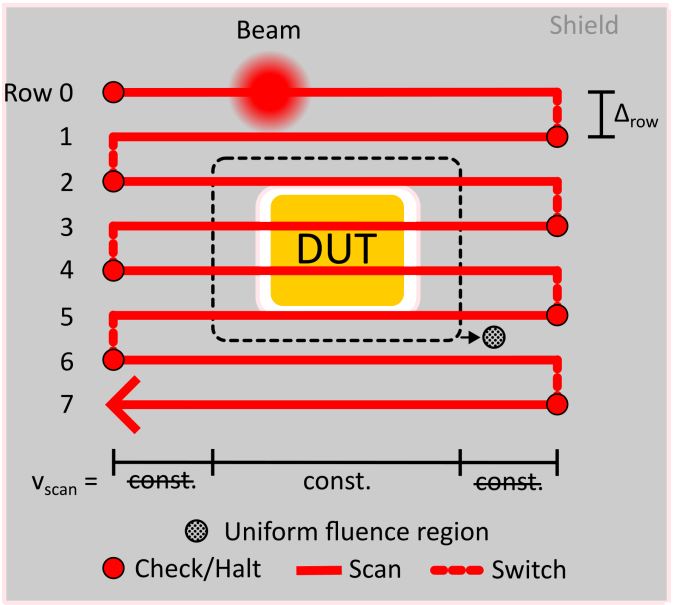

Figure 5.15: Schematic of the beam-driven irradiation routine. A row-based scan grid is constructed on which the DUT is moved through the beam. On turning points, where the beam is located off-DUT, the beam conditions are checked for relevant events (see Section 5.6.3). The target fluence is applied in multiples of *complete scans* of the pattern. Adapted from [77].

Enabled by the custom beam diagnostics, throughout the progression of the irradiation pattern, the beam parameters are online-monitored and recorded at all times with a frequency up to 100 Hz (typically 20 Hz). On the turning points, after switching to the next row as well as prior to scanning it, the status of beam-related (and other) *events* is checked. As explained in Section 5.6.3, events are either *active* or *inactive* and are generated from online data and predominantly indicate deficient irradiation conditions such as beam loss or insufficient current. As long as an event is active, the irradiation routine is halted at the respective turning point until all events become inactive, therefore preventing to expose the DUT to unstable beam conditions. Enabled by the online fluence monitoring (see Section 5.5.1), the event system additionally triggers the automatic termination of the irradiation routine once the target fluence is applied.
The event system enables autonomous reactions of the irradiation setup to varying beam (and setup) conditions, yielding a *beam-driven* routine that produces highly-uniform fluence profiles by ensuring controlled beam parameters when performing irradiations.

Corrections

The beam-driven irradiation routine prevents DUT exposure to unstable beam conditions by performing checks prior to scanning. A defective beam condition occurring during the movement of the DUT through the beam cannot be prevented. Nevertheless, enabled by the online fluence monitoring

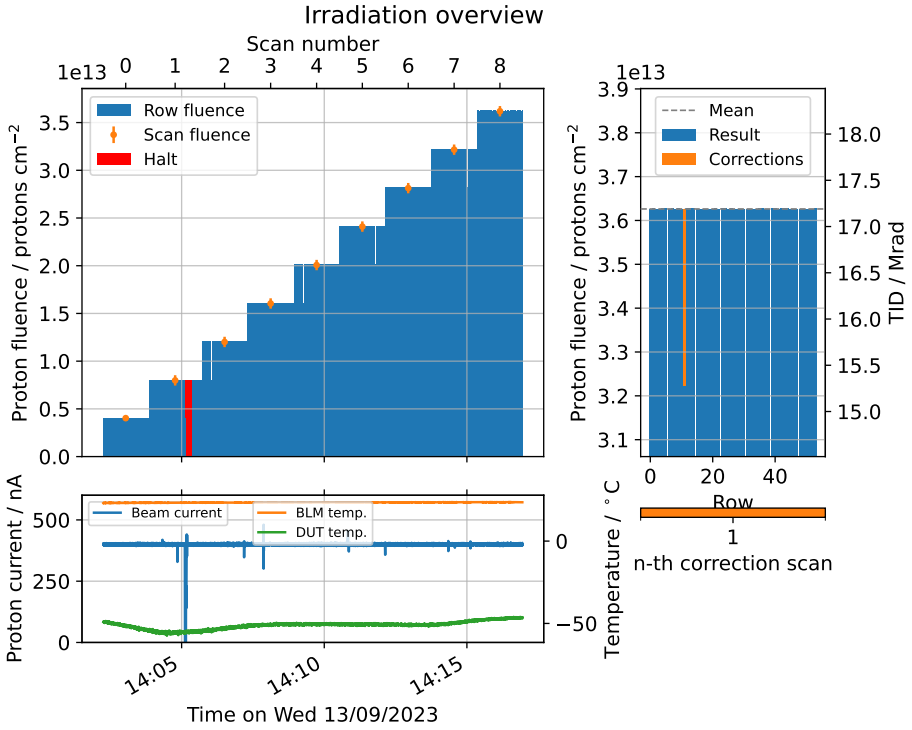

Figure 5.16: Overview of irradiation routine (left), and corresponding beam current and temperatures (bottom), with a correction scan applied to row #11 to the resulting distribution (right). Longer pauses of the irradiation routine due to active events are marked in red (short pauses are not indicated).

(see Section 5.5.1), deficiencies in the applied fluence profile can be identified with row resolution. Implemented within `irrad_control`, such insufficiently irradiated rows can be corrected by re-scanning the respective row(s) with adapted parameters, allowing one to precisely level the resulting distribution. Figure 5.16 shows an overview of an irradiation over a course of approximately 20 min and 9 complete scans, produced by the analysis capabilities of `irrad_control`. Here, the bars correspond to individual fluence contributions within the rows of the scan pattern. As visible in scan number #1, a sudden loss of beam current occurs during movement trough row #11 of the irradiation pattern, resulting in almost no fluence applied in the row wich subsequently halts the routine. This deficit is also visible in all subsequent scan numbers. After termination of the irradiation routine, the respective row is re-scanned, yielding a uniform distribution, as shown on the right of Fig. 5.16.

Custom Fluence Profiles & Irradiation Campaigns

The online fluence monitoring in combination with the ability to apply post-irradiation corrections to the resulting fluence distribution, enables the delivery of custom profiles to the DUT. In the current

configuration, the setup provides the possibility to easily generate a fluence profile as function of the row of the scan pattern in Fig. 5.15, corresponding to the vertical dimension. In a test irradiation, an approximately linear proton fluence distribution is delivered to the DUT, as shown in Fig. 5.17(a). Here, from the upper side of the device, a linear profile with a slope of approximately -5×10^{13} protons/mm is applied by re-scanning the individual rows of the irradiation pattern repeatedly after the base fluence is delivered. Dynamically adapting the velocity v_{scan} of the scan stage while traversing a row of the irradiation pattern, enables the delivery of a custom profile in the horizontal dimension. The application of such profiles can be especially useful for probing detectors that are expected to be exposed to spatially non-uniform fluences.

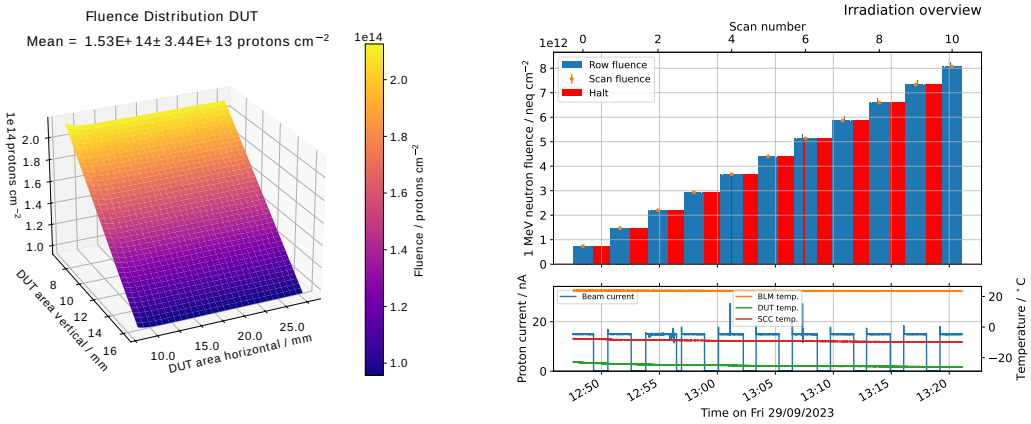

(a) 3D fluence profile approx. linear in vertical dimension

(b) Overview of irradiation with measurement pauses

Figure 5.17: Custom fluence distribution, exhibiting a linear gradient within the vertical DUT dimension, and overview of a custom irradiation campaign, consisting of alternating application of fluence and DUT measurements, during which the beam is not extracted.

Furthermore, custom irradiation campaigns can be conducted, such as performing DUT measurements in between applications of irradiation levels. This is facilitated by the online fluence monitoring capabilities in conjunction with the possibility to power/read out DUTs as well as manually pause the irradiation routine from within `irrad_control` at any time. A campaign where a DUT has been irradiated to a low target fluence is shown Fig. 5.17(b). Here, after each completed scan, the DUT has been powered on and read out. The proton beam is not extracted into the setup during the measurements. This mode of operation allows for determination of radiation-related degradation of the device parameters with fine-grained resolution within a single irradiation campaign.

5.4.3 Post-Irradiation

After the irradiation procedure is completed, the DUT remains situated inside the cool box with the cooling system maintaining adequate temperature, to allow for the decay of short-lived isotopes. After a cool down period of typically between 2 – 3 h, the device is removed and stored in an on-site freezer at a temperature of approximately $-20\,^{\circ}\text{C}$ to prevent annealing. After a few days, depending on the applied fluence, a spectroscopic measurement of the DUT is performed at the gamma spectroscopy center of the HISKP, which is briefly described in Appendix A.5. The created radioisotopes in the DUT due to irradiation are identified and their activities are determined, allowing for an estimation of

the exposure. Following this process, the handling of the device is managed by the radiation protection department of the HISKP.
Within the course of this work, a contribution to this workflow has been made in the form of the `irrad_spectroscopy` package [78] that provides spectroscopic analysis as well as exposure calculation utilities. Table 5.2 gives an overview of the commonly produced isotopes at the proton irradiation site of the BIC. A corresponding gamma spectrum, emitted from an irradiated `ITkPix` detector assembly, is shown in Fig. A.3 in the appendix. At the proton energies of the BIC, all of the isotopes presented in Table 5.2 are produced with the maximum cross section. Especially the exposure as well as the amount of copper within the DUT should be minimized due to the produced ^{65}Zn isotope having a half-life in the order of one year, potentially resulting in large turnaround times due to radio protection.

Isotope production at BIC			Half-life	Potential sources
Isotope	Reaction	Cross section		
^{65}Zn	$^{65}\mathrm{Cu} \xrightarrow{(p,n)} {}^{65}\mathrm{Zn}$	$\approx 600\,\mathrm{mb}$	243.93 days	Lanes/pads (DUT, PCB)
^{48}V	$^{48}\mathrm{Ti} \xrightarrow{(p,n)} {}^{48}\mathrm{V}$	$\approx 550\,\mathrm{mb}$	15.97 days	Wire/bump-bonding
^{79}Kr	$^{79}\mathrm{Br} \xrightarrow{(p,n)} {}^{79}\mathrm{Kr}$	$\approx 650\,\mathrm{mb}$	34.96 hours	Flame retardant (PCB)

Table 5.2: List of common long-lived isotopes, created during proton irradiation of typical DUTs at the BIC. Production reactions and cross sections from [79]. Half-lives taken from [80].

5.5 Dosimetry

Enabled by the extensive beam monitoring capabilities, the dosimetry at the BIC irradiation site is performed on a purely beam-based approach. Facilitated by the custom beam diagnostics (see Section 5.3), the data acquisition of the setup components (cf. Section 5.2) and the `irrad_control` software (see Section 5.6), an on- as well as an offline dosimetry is implemented. Here, both procedures yield the fluence distribution across the area of the irradiation pattern (see Fig. 5.15) where the former provides spatial resolution in one and the latter in two dimensions.

5.5.1 Online Fluence Monitoring

The fluence delivered within one complete scan of the irradiation routine, introduced in Section 5.4.2, can be calculated using the ion beam current I_{beam} as well as the routine's parameters as [81]

$$\Phi = \frac{I_{\mathrm{beam}}}{z_{\mathrm{ion}} \cdot q_e \cdot v_{\mathrm{scan}} \cdot \Delta_{\mathrm{row}}}\,, \tag{5.13}$$

where z_{ion} is the number of the elementary charges q_e carried by the ion. Here, the resulting value corresponds to the fluence applied to the uniform region of the pattern, as indicated in Fig. 5.15, where the DUT is moved through the beam with a constant velocity. In [81], Eq. (5.13) is derived by geometric dissection of the irradiation pattern and the beam spot, the returned fluence is verified to be within 10 % of the measured fluence via isotope activation (see also Section 6.3.1).

Using the online beam current monitoring as well as the row scan start and stop timings provided by the scan stage, Eq. (5.13) is calculated for each row of the scan pattern. Here, the mean value of all beam currents sampled within the scanning of the respective row is taken, thus allowing one to incorporate the beam stability into the uncertainty of the fluence contribution to the complete scan via Eq. (A.2). This approach enables an online monitoring of the fluence contribution per row to each complete scan, effectively yielding the fluence distribuiton with row resolution, as shown on the right side of Fig. 5.16.

5.5.2 Offline Fluence Reconstruction

The extensive beam as well as setup data acquired during the irradiation procedure facilitates the reconstruction of the fluence distribution over the entire scan area, including the periphery, shown in Fig. 5.15. To do so, the area covering the irradiation routine, is abstracted into a two-dimensional map with discrete binning of widths $d_{x/y} \ll \Delta_{\text{row}}$ and indices i, j in the respective dimensions. A schematic of the process is depicted in Fig. 5.18. Using the relative coordinate system in which the scan pattern is constructed, the position of the bin centers are given by $S(i, j) = (x(j), y(i))$. Along the rows of the scan pattern, the beam traverses the map horizontally. The scan stage data provides the scan velocity v_{scan}, acceleration a_{scan} as well as start and stop timestamps for each row. Using this, the center timestamps $T_{\text{row}}(j)$, when the beam is located at the horizontal bin centers, as well as the horizontal bin crossing times $t(j)$ can be determined. Due to the same scan parameters used for every row, $t(j)$ is typically the same for all rows whereas $T_{\text{row}}(j)$ is specific to each row[5]. Caused by de-/acceleration from/to v_{scan}, $t(j)$ is especially not constant in the periphery of the pattern. Utilizing the horizontal bin center timestamps $T_{\text{row}}(j)$ in conjunction with the continuously-monitored beam current, allows for interpolation of the beam currents at the horizontal bin centers $I_{\text{beam}}(T_{\text{row}}(j))$ of each scanned row. These interpolated beam currents corresponds to the points $B_{\text{row}}(j) = (x(j), y_{\text{row}})$, which are located in the horizontal bin centers as well as vertically on the respective row. Given the crossing of a specific bin $k \in j$, the resulting number of ions N_{ion} accumulated during the traversal can be calculated using the bin crossing time $t(k)$ as

$$N_{\text{ion}}(t) = \int_{t(k)} \frac{I_{\text{beam}}(T_{\text{row}}(k))}{z_{\text{ion}} \cdot q_e} dt = \frac{I_{\text{beam}}(T_{\text{row}}(k))}{z_{\text{ion}} \cdot q_e} \cdot t(k) \,. \tag{5.14}$$

Assuming a Gaussian beam profile at the extraction towards the irradiation site, as shown in [82], its distribution $g(x, y)$ and volume G are given by [83]

$$g(x, y) = A \exp\left(-\frac{1}{2}\left(\frac{(x-\mu_x)^2}{\sigma_x^2} + \frac{(y-\mu_y)^2}{\sigma_y^2}\right)\right), \tag{5.15}$$

$$G = \iint_{-\infty}^{\infty} g(x, y) dx dy = 2\pi A \sigma_x \sigma_y \,, \tag{5.16}$$

where A is the amplitude, $\sigma_{x/y}$ the beams widths and $\mu_{x/y}$ the beam's mean position in the respective dimension. Here, the beam widths are extracted from the FWHMs, obtained from visual inspection on the cool box scintillation screen, after beam preparation. Using the number of ions $N_{\text{ion}}(k)$

[5] The bin center timestamps are specific to each actual row that is scanned, not to the row number which keeps repeating in the pattern.

accumulated while traversing bin k, the beam spot is assumed to be stationary, located at $B_{\text{row}}(k)$, for the time of traversal $t(k)$. Using Eqs. (5.14) and (5.16), the amplitude of the Gaussian can be calculated as

$$A(B_{\text{row}}(k)) = \frac{N_{\text{ion}}(k)}{2\pi\sigma_x\sigma_y}\,. \tag{5.17}$$

Consequently, the fraction of fluence delivered to each individual bin, located at $S(i, j)$, by bin k at position $B_{\text{row}}(k)$ is calculated as

$$\Phi(i,j) = \frac{N_{\text{ion}}(k)}{2\pi\sigma_x\sigma_y} \exp\left(-\frac{1}{2}\left(\frac{(x(j)-x(k))^2}{\sigma_x^2} + \frac{(y(i)-y_{\text{row}})^2}{\sigma_y^2}\right)\right)\,. \tag{5.18}$$

By iterating over all bins of the map for every point in $B_{\text{row}}(j)$, a two-dimensional fluence distribution is generated. Additionally, the fluence contribution due to the switching of rows and subsequent checking of the beam conditions via the event system (cf. Section 5.6.3) at the peripheries of the scan pattern is accounted for. Here, prior to scanning each row, the beam is located at $C_{\text{row}} = (x_{\text{start}}, y_{\text{row}})$, at the start of the row to be scanned. Utilizing the duration d_{row} for which the beam remains at C_{row}, the mean of the beam currents sampled during d_{row} and Eq. (5.14), the consequent fluence addition to all bins is calculated via Eq. (5.18). By following this approach, the resulting fluence is given normalized to the unit area of the bins.
Due to the knowledge of the DUT cross section as well as location within the generated fluence distribution, the actually applied fluence on the device can be extracted, allowing for the determination of the mean value as well as the variation of the fluence across the DUT. The two-dimensional fluence distribution over the scan area as well as the device is shown for an example irradiation in Figs. 5.20(a) and 5.20(c).

5.5.3 Total Ionizing Dose Calculation

The TID can be expressed as a function of the primary ion fluence Φ, thus it can be determined analogously, with the same spatial resolution. Given the electronic, density-normalized *stopping power* of the ion, P_{stop}, (compare Eq. (2.1)) in units of MeV cm^2 g^{-1}, the TID, in units of Mrad, can be calculated as

$$\text{TID} = 10^5 \cdot q_e \cdot P_{\text{stop}} \cdot \Phi\,, \tag{5.19}$$

where q_e is the elementary charge. Here, the pre-factor $10^5 \cdot q_e$ converts between MeV g^{-1} and Mrad. A plot of the evolution of the delivered TID, resolved in rows, of an example irradiation is displayed in Fig. 5.20(d).

5.6 `irrad_control`: DAQ, Control and Analysis Software

The proton irradiation site at the BIC was developed around the ability to accurately monitor the beam characteristics at the extraction to the setup, as the respective beamline *C* was recommissioned after years of being inactive. With the custom beam diagnostics, described in Section 5.3, a variety of

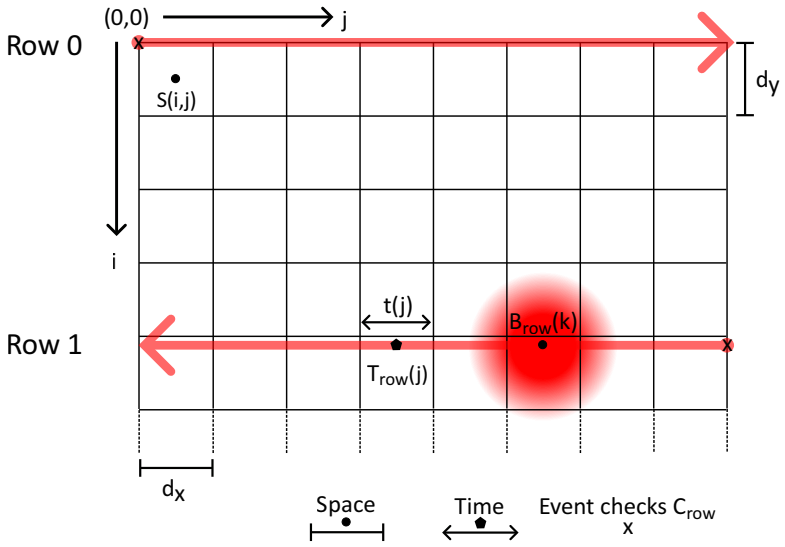

Figure 5.18: Schematic reconstruction of two-dimensional fluence distribution across the area of the scan pattern, shown in Fig. 5.15. The area is dissected into discrete bins within the relative coordinate system of the irradiation scheme.

beam-related signals became available. This required data acquisition, interpretation, storage and, especially relevant during the early stages of development, visualization. To fulfill these requirements, the development of the open-source, *Python*-based `irrad_control` framework [68] was initiated in [58]. During the course of this work, a large effort has been invested to develop `irrad_control` into a versatile framework that enables beam-driven, autonomous irradiation procedures via an event system (see Section 5.6.3), resulting in highly uniform, accurate and customizable fluence distributions. `irrad_control` has been developed with existing proton irradiation sites, such as the ones at Karlsruher Institut für Technologie (KIT) [13] and Birmingham [12], in mind with the goal to easily enable adaptation of the system to other sites with the only required addition being the beam monitor. In this section, the structure as well as the features of `irrad_control` are presented.

5.6.1 Software Structure

At the core, `irrad_control` is designed to run $2 + n$ processes: a GUI, for data visualization and setup control, a converter process, performing online data interpretation as well as storage and n server processes, responsible for data acquisition and hardware control. A schematic overview is shown in Fig. 5.19. The GUI and converter processes run on the irradiation host PC located in the accelerator control room. The server processes run on dedicated RPi[6] servers, interfacing the irradiation-related hardware from the gallery. For the operation of the proton irradiation site at the BIC, a single server is typically sufficient and $n = 1$ is chosen, though tests with $n > 1$ have been successfully carried out. All processes are connected over the LAN, communicating with each other via Transmission Control

[6] The serves can run on any machine but RPis are chosen due to their availability and versatile expansion options.

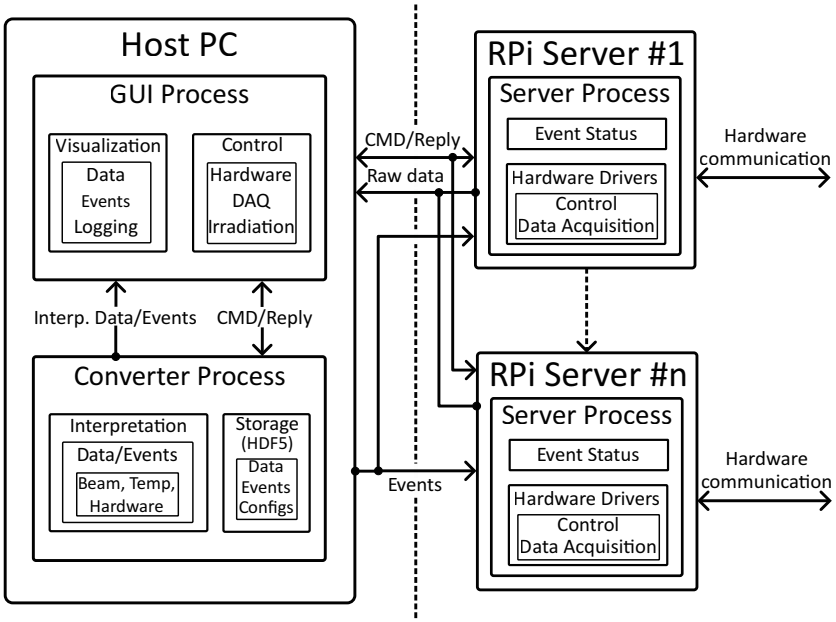

Figure 5.19: Schematic overview of the `irrad_control` software structure. The application runs $2 + n$ processes, a Graphical User Interface (GUI) and a converter process on the host computer, as well as n servers, interfacing the irradiation-related hardware, where $n = 1$ is typically sufficient for running one site.

Protocol (TCP) sockets.
A server process connects to the irradiation setup via the corresponding interface, such as sockets or serial bus systems (USB, SPI, I^2C). It runs the required hardware drivers, included in `irrad_control`, allowing to control each individual device. The server continuously reads out connected DAQ devices, such as ADCs or thermistors, and broadcasts their raw data to the GUI as well as converter processes. On the receiving end, it is connected to the GUI program via a command / reply pattern, allowing one to control the underlying hardware, such as motorstages or the R/O electronics board, from the host PC. Additionally, the servers receive updates on events (see Section 5.6.3) from the converter process.
The main task of the converter process is the interpretation of the acquired data, subsequent storage and redistribution to the other components of `irrad_control`. The converter continuously receives raw data from beam diagnostics, temperature readouts and other irradiation setup components. All incoming data is interpreted to determine the prevalent beam conditions, the fluence & TID levels during irradiation and infer the status of beam- and irradiation-related events. All raw as well as interpreted data and events are stored for later analysis and forwarded to the GUI for visualization and logging.
The GUI process allows for the setup, control and monitoring of the irradiation setup as well as all relevant parameters, from the control room of the BIC. It offers various interfaces, enabling one to prepare the irradiation setup for each individual campaign, setup and steer the irradiation routine, described in Section 5.4.2, and visualize the data acquired during operation. Moreover, the status of events and hardware components is displayed in dedicated logging elements.

5.6.2 Irradiation Data

irrad_control produces two complementary output files for each irradiation campaign: a human-readable configuration record in the *YAML* [84] format and a binary *HDF5* [85] data file. The former contains the initial hardware composition such as connected devices and the diagnostics configuration as well as beam information such as the ion species, energy and damage factor. The latter holds the actual beam-, setup- and irradiation-relevant data which are acquired during operation of the irradiation site. The entries within the data file are classified according to their origin where each distinct entry is assigned a timestamp with 64 bit resolution, allowing one to align them in time. To give an overview of the content of the available data, a selection of relevant fields and their entries are given in Table 5.3.

Field	Description
Raw	Raw voltages of the processed current signals of the beam diagnostics acquired from the ADC expansion board (see Sections 5.2.2 and 5.3)
Beam	Calibrated beam current, loss and relative position, determined by interpretation of the raw data (see Eqs. (5.7), (5.8) and (5.12))
SEE	Secondary Electron Emission currents of the horizontal and vertical SEM as well as the resulting SEY (see Eqs. (5.3) and (5.6))
Scan	Quantities acquired while scanning a row within the beam-driven irradiation routine. Contains current scan & row number, start & stop timestamps & positions, mean beam current, fluence & TID contribution and scan speed & de/acceleration (see Section 5.4.2)
Irrad	Information about irradiation pattern shown in Fig. 5.15. Includes beam-aligned reference position of relative coordinate system, number of rows, row separation, positions defining the scan as well as DUT area, beam widths and target fluence (see Section 5.4.1)
Damage	Accumulated radiation damage per completed scan. Contains scan number, ion fluence and TID (see Eqs. (5.13) and (5.19))
Event	Event name, status and parameters (see Section 5.6.3)

Table 5.3: Data fields and their content as recorded by irrad_control.

The resulting data is available after irradiation and, in conjunction with the included analysis capabilities of irrad_control introduced in Section 5.6.4, allows for an extensive overview of the evolution of the irradiation and applied fluence on the DUT.

5.6.3 Event System

The event system of irrad_control is the core component that enables the beam-driven irradiation routine, described in the preceding Section 5.4.2, to autonomously react to varying conditions. In the context of irrad_control, *events* describe a condition and can either be active or inactive. The main events, their trigger actions and description are listed in Table 5.4.

Event	Trigger	Description
`BeamOff`	$I_{\mathrm{SEE}} < 1\,\%\ I_{\mathrm{FS}}$	No beam signal is measured inside the beam monitor. No other beam-related events are checked if `BeamOff` is active. See Eqs. (5.6) and (5.10)
`BeamLoss`	$I_{\mathrm{loss}} > 2\,\%\ I_{\mathrm{beam}}$	Beam is (partially) cut-off at the extraction to the irradiation site. Measured at the BLM aperture of the beam monitor. See Eq. (5.8)
`BeamJitter`	$\sigma(I_{\mathrm{beam}}) > 5\,\%\ \left[\left\langle I_{\mathrm{beam}}\right\rangle \vee I_{\mathrm{FS}}\right]$	The beam current amplitude is unstable. The standard deviation within a specified time window (10 s) is calculated and compared to the mean and R/O electronics scale. Logial "Or" is applied. See Eqs. (5.10) and (5.12)
`BeamDrift`	$\sqrt{x^2 + y^2} > 50\,\%$	Deviation of beam position from beam-aligned reference. Coordinates measured in the beam monitor. A circle with radius 50 % is defined corresponding to an offset ratio of 1/4 to 3/4 signal in the SEM module. See Eq. (5.7)
`BeamLow`	$I_{\mathrm{beam}} < I_{\mathrm{min}}$	Beam current lower than specified limit I_{min}. Referred to as *minimum scan current*, it is defined per irradiation routine. Ensures sufficient fluence contribution in each row. See Sections 5.4.2 and 5.5.1
`DUTTempHigh`	$T_{\mathrm{DUT}} > -10\,^{\circ}\mathrm{C}$	DUT temperature insufficient. Prevent uncontrolled annealing. See Section 4.4
`Irradiation Complete`	$\Phi_{\mathrm{online}} \geq \Phi_{\mathrm{target}}$	Target fluence is applied. Stops irradiation routine autonomously. Applied fluence detemrmined via online dosimetry. See Eq. (5.13)

Table 5.4: Events generated by `irrad_control` during operation of irradiation site.

Within each interpretation cycle of the converter process, the status of all events is determined, stored and subsequently propagated to the GUI and as well as the server(s). After an event becomes active, its status remains activate for a minimum time, typically in the order of a few seconds, before it can become inactive again. This allows one to e.g. match the rapidly changing beam conditions to the comparatively slow reactivity of the irradiation hardware. Events are categorized into beam-related and non-beam-related ones, facilitating the implementation of customized reactions. The event system is utilized to prevent the DUT to be exposed to faulty conditions during the irradiation procedure but also provides valuable information to the operators to correct or optimize accelerator settings.

The comparative fractions within the trigger conditions are derived empirically over the course of operating the site and reflect the values at the time of writing. As shown in Section 6.2.5, the event system can substantially impact the uniformity of the applied fluence distribution for campaigns with poor beam conditions.

5.6.4 Analysis Capabilities

Based on the contents of the configuration as well as data file generated for each irradiation campaign, `irrad_control` implements a set of predefined analysis procedures to supply comprehensive information and visualization of the progression and results, used frequently within this work. The analysis tools are written in *Python*, using modern libraries such as *NumPy*, *Numba* and *SciPy* [86, 87, 88] enabling fast, efficient data processing, and can be easily integrated into user-specific code. To provide a language-independent interface however, a set of different analysis routines is available via the command line, using the `irrad_analyse` entry point after installation of `irrad_control`:

```
$ irrad_analyse -f INFILE [INFILE ...]
                [-o OUTPDF [OUTPDF ...]]
                [--irradiation | --full]
                [--damage] [--scan] [--beam]
                [--calibration] [--multipart]
```

Here, providing the base name[7] of the output files of `irrad_control` to the `INFILE` argument, allows one to select from four different analysis procedures via the optional flags:

`--damage`
: Determines the applied primary, 1 MeV neutron equivalent and TID damage on the area of the irradiation pattern as well as the DUT area, according to Section 5.5, as shown for an example in Figs. 5.20(a) to 5.20(c). Furthermore, the corresponding error calculations are performed and resolved over the respective area.

`--scan`
: Provides information about the irradiation routines (or *scans*) progression, resolved over time and applied damage, as shown in Figs. 5.20(d) and 5.20(e).

`--beam`
: Extracts the beam parameters, such as current and position, during the irradiation, as displayed in Fig. 5.20(f).

`--calibration`
: Performs a beam monitor calibration (see Section 5.3.3), determining the calibration constant λ from Eq. (5.12), displayed in Fig. 6.8.

The additional flags `--irradiation` and `--full` group the above flags, where the `--irradiation` flag is the default, setting the `--damage` as well as `--scan` flags. In case campaigns are carried out over several separate irradiations, the `--multipart` flag enables to merge their results into one output of the corresponding analysis by supplying all respective input files. Providing multiple input files without setting the `--multipart` flag conducts the selected analysis on each file separately.
This straightforward access to extract meaningful information from irradiation datasets provides a high level of transparency and comprehensibility to users of the site.

[7] Both files share the same base name whereas the file extension is *.yaml* for the configuration and *.h5* for the data file.

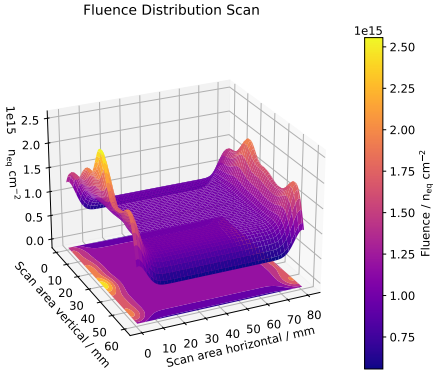

(a) 3D fluence distribution across the scan area

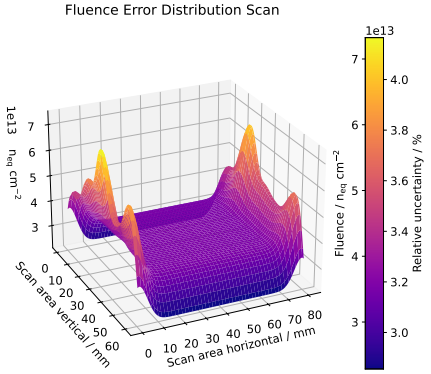

(b) Absolute and relative uncertainties corresponding to Fig. 5.20(a)

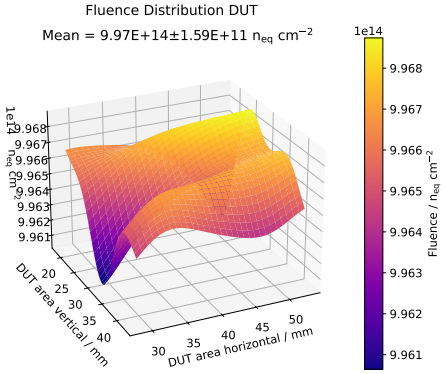

(c) 3D fluence distribution across the DUT area, extracted from Fig. 5.20(a)

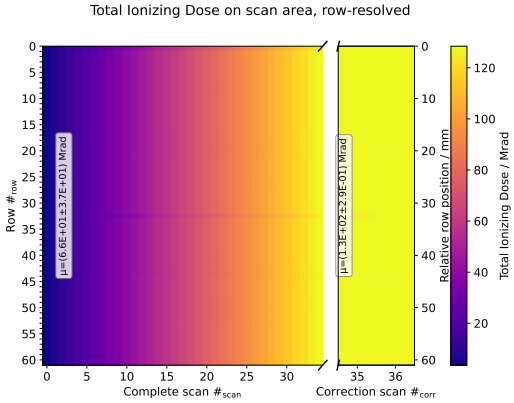

(d) Evolution of TID with scan number in each row

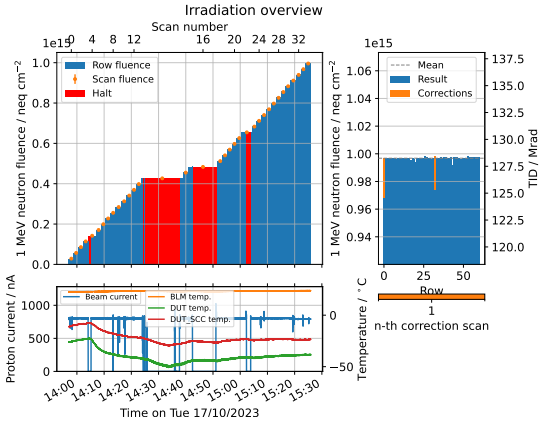

(e) Overview of irradiation routine

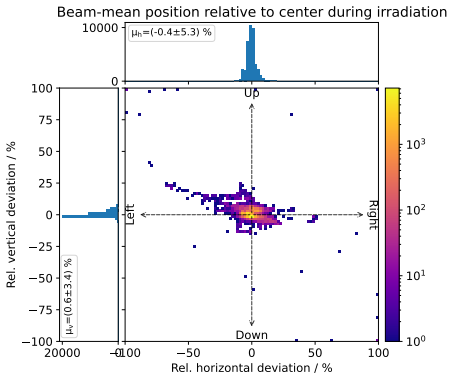

(f) Overview of rel. beam position during irradiation

Figure 5.20: Selection of plots generated from the predefined analysis capabilities included in `irrad_control`

CHAPTER 6

Characterization of the Irradiation Infrastructure

In this chapter, the irradiation facility and the implemented procedures, introduced in Chapter 5, are characterized and their functionality verified. For this purpose, simulations of the energy degradation on transmission to the site of the common, light ions at the BIC are performed in Section 6.1. The signal characteristics of the custom beam diagnostics on beam propagation are examined, the beam monitor calibration verified and the performance of irradiation event system (see Section 5.6.3) probed in Section 6.2. In the following Section 6.3, the irradiation as well as dosimetry procedures, described in Sections 5.4 and 5.5, are tested via irradiation of titanium foils and comparison to dosimetry results via isotope activation in Section 6.3. For the typical operation of the irradiation site with 13.6 MeV protons from the accelerator, the proton hardness factor is determined according to Eq. (4.9) by irradiation of thin silicon sensors in Section 6.4 where additionally the limitations imposed by the low ion energies are discussed. Lastly, an overview of the parameters of established proton irradiation facilities is given in Section 6.5. Here, also a comparison of their specifications and NIEL scaling is presented.

6.1 Ion Energy Simulations

The initial ion energy inside the accelerator degrades on transmission into the irradiation setup. The reduction is due to the beam's penetration of the beam monitor foils as well as the exit window and its propagation outside the vacuum after extraction. As shown in Chapter 4, both, the NIEL as well as the TID damage are functions of the kinetic energy of the respective ion. Especially in the low-energy region for protons in the order of 10 MeV, Fig. 4.3 shows a strong dependence of the hardness factor on the kinetic energy. Therefore, in order to estimate the hardness factor as well as TID at the DUT, *GEANT4* [89] simulations of the energy degradation as well as distributions before and after typical DUTs have been performed for the lightest ions up to α particles where the primary focus is on protons. A cross-section through a CAD rendering of the simulated material configuration is shown in Fig. 6.1, an overview of the individual energy depositions for typical protons is displayed in Table 6.1.

6.1.1 Energy Degradation on Transmission to DUT

The BIC provides light ions in the range between 7 and 14 MeV per nucleon to the irradiation site. In order to obtain accurate TID information and to account for run-to-run variations in beam energy,

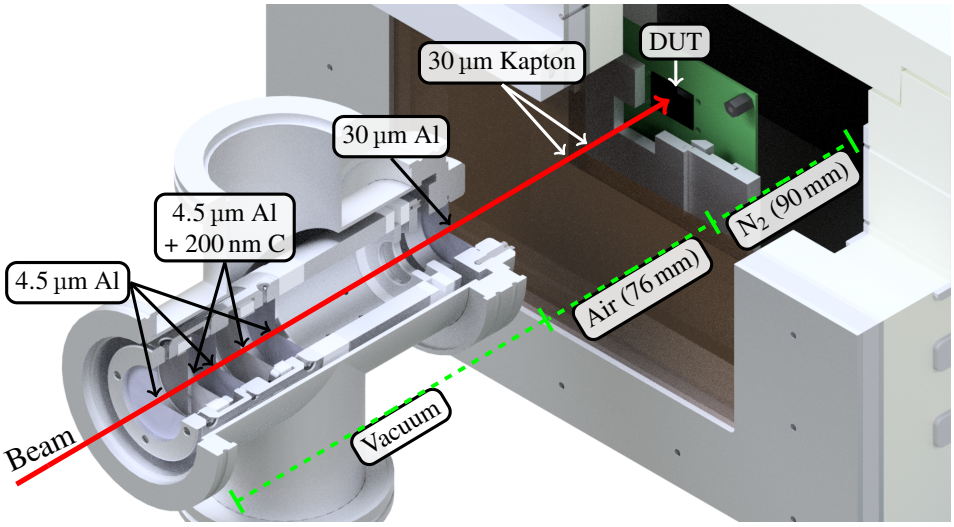

Figure 6.1: Cross-section through CAD schematic of the simulated irradiation configuration. The materials as well as their thicknesses, penetrated by the beam on transmission to the DUT, are indicated and correspond to the values given in Table 6.1. The positioning of the DUT inside the cool box is not to scale.

Material (*GEANT4*)	Thickness	ΔE	Description
Aluminum (G4_Al)	52.5 µm	375.84 keV	SEM & HV foils, exit window
Carbon (G4_C)	400 nm	2.64 keV	SEM foil coating
Air (G4_AIR)	6.6 cm	255.74 keV	Transmission to cool box
Kapton (G4_KAPTON)	30 µm	146.12 keV	1st window cool box
Air (G4_AIR)	1 cm	38.71 keV	Insulation gap window
Kapton (G4_KAPTON)	30 µm	147.83 keV	2nd window cool box
Nitrogen (G4_N)	9 cm	354.92 keV	Transmission to DUT
Silicon (G4_SI)	150/300 µm	1.07/2.22 MeV	DUT

Table 6.1: *GEANT4* simulation of energy loss on transmission of 13.6 MeV protons towards the DUT, housed inside the cool box. A total of 10^8 protons have been simulated for this particular arrangement. The data corresponds to the configuration and distributions shown in Fig. 6.1 and Fig. 6.4.

the *GEANT4* framework is used to carry out simulations of the energy degradation on transmission to the DUT for ions within the available energy range. The simulated configuration is depicted in Fig. 6.1, information on the materials and thicknesses are given in Table 6.1. To extract a statistically reliable result, 10^7 ions[1] are simulated for each energy. The resulting energy at the DUT versus the initial energy in the accelerator for light ions up to alpha particles is shown in Fig. 6.2. The maximum proton energy at the DUT, achievable with the BIC, is approximately 12.6 MeV. By considering the

[1] For the nominal ion energies at the BIC, i.e. 13.6 MeV for protons (see Appendix A.2 for remaining light ions), a total of 10^8 ions are simulated. This applies to all simulations within this Section 6.1.

ion energy degradation, the results allow for a more precise determination of the stopping power and thus the TID at the DUT. Both are shown in Fig. 6.3 where the TID is given in units of particle fluence. Within the irradiation sites control software `irrad_control`, the simulation results are linearly interpolated to determine the stopping power of the light ions at the DUT, providing information on the TID damage according to Eq. (5.19).

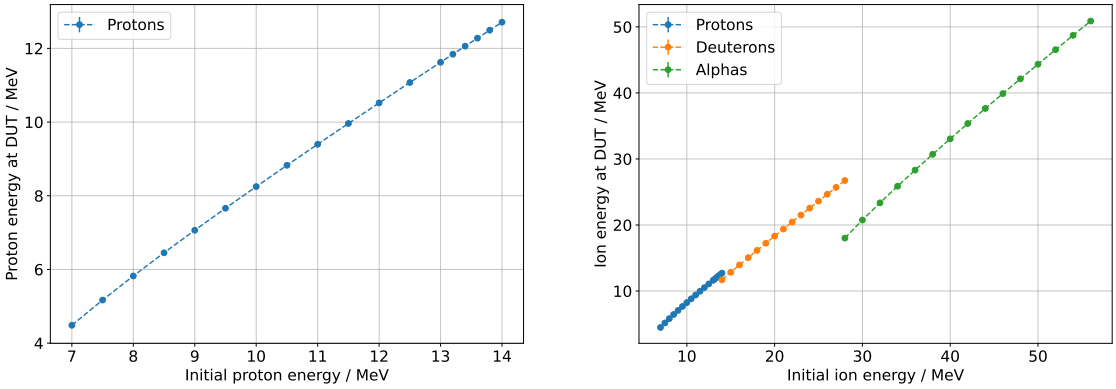

(a) Protons

(b) Light ions

Figure 6.2: *GEANT4* simulation of energy degradation of light ions for the energy ranges of the BIC when extracted to the irradiation site, corresponding to the configuration depicted in Fig. 6.1. Each data point resembles a simulation of 10^7 ions of given initial energy. The uncertainty corresponds to the standard deviation of the simulated distribution. Linear interpolation is used to provide values in between simulated energies.

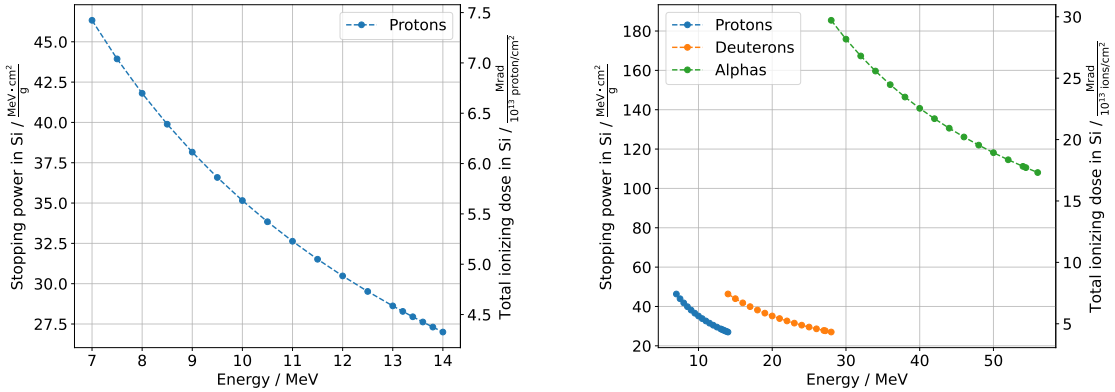

(a) Proton stopping powers & TID

(b) Light ion stopping powers & TID

Figure 6.3: Stopping power and TID per 10^{13}ions/cm^2 of light ions in silicon for the energy ranges of the BIC. The stopping power values for protons and alphas are taken from [19] whereas they are calculated according to Eq. (2.1) for deuterons. Linear interpolation is used to provide values in between simulated energies.

6.1.2 Energy Distributions Pre- and Post-DUT

To estimate the proton hardness factor for the default irradiation operation with 13.6 MeV protons, *GEANT4* simulations of the energy distributions on and after typical DUTs are performed. The results are shown in Fig. 6.4, information on the material, thickness and energy loss is given in Table 6.1. The initial energy distribution is assumed to be a δ-distribution due to the high momentum resolution along the *C* beamline of up to $p/\Delta p = 30000$ [62]. After propagation to the DUT, the proton energy is reduced by approximately 1.32 MeV to (12.28 ± 0.06) MeV. Considering two DUT thicknesses of 150 µm and 300 µm, further energy reduction by 1.07 MeV and 2.22 MeV to (11.21 ± 0.08) MeV and (10.06 ± 0.11) MeV can be observed, respectively. For these energies, a proton hardness factor κ_p in the range of 3.5 – 4 can be estimated from Fig. 4.3, providing an initial estimate for the measurements in Section 6.4. For both DUT thicknesses, the protons are transmitted completely through the silicon, reducing the beam energy by approximately 10 – 20 %. Combining these results with the NIEL damage evolution with energy for protons given in Fig. 4.3, a first indication is given that the energy loss due to ionization within the DUT can notably affect the hardness factor measurement if the variation in NIEL damage between entry and exit is larger than the measurement precision. Consequently, the thinnest devices available are used for determination of the damage factor in Section 6.4. For the sake of completeness, identical simulations are performed for deuterons and alphas. The results can be found in Fig. A.1 in Appendix A.2.

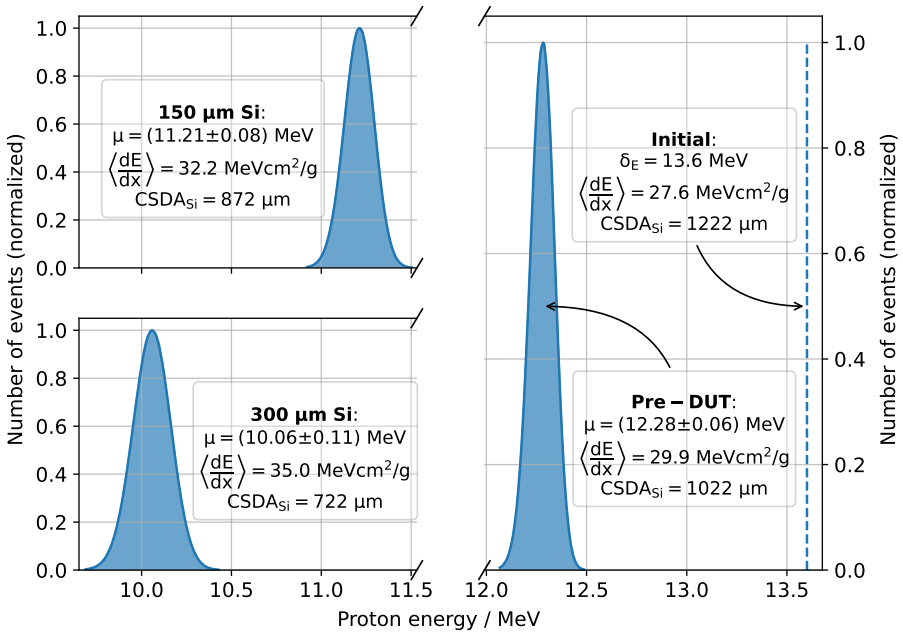

Figure 6.4: *GEANT4* simulation of the energy distributions before and after DUTs of 150 µm and 300 µm thickness for typical protons. The *stopping power* is calculated according to Eq. (2.1), the projected $\mathrm{CSDA}_{\mathrm{Si}}$ range is taken from [19]. The distributions correspond to the transmission from the accelerator through the configuration shown in Fig. 6.1 before and after traversing the DUT. 100 % of the protons are transmitted through the DUT for all simulations.

6.2 Custom Diagnostics

In this section, the custom diagnostics introduced in Section 5.3 are characterized and their intended functionality verified. Unless stated otherwise, all measurements are performed with `irrad_control` and the corresponding readout chain presented in Fig. 5.5. The irradiation setup is operated in calibration position, as shown in the top right of Fig. 5.4(a), and a proton beam is extracted through the beam monitor into the on-site FC. Firstly, the amplification chain of the analog R/O electronics is verified. In the following, the currents obtained from the beam monitor and on-site FC are probed versus the HV applied to the diagnostics electrodes. Subsequently, their signal signature at nominal operating voltage is examined and compared to the expected behavior. The beam monitor calibration procedure is showcased and the stability of the obtained calibration constant is demonstrated over time as well as for the typical run-to-run beam energy variation. Lastly, the irradiation event system, explained in Section 5.6.3, is tested by intentionally creating faulty beam conditions.

6.2.1 Readout Electronics Transimpedance Amplification

The analog R/O electronics, introduced in Section 5.3.4, provide transimpedance amplification for the signals of the beam diagnostics. To verify the current-to-voltage conversion according to Eq. (5.9) and the subsequent utilization of Eq. (5.10) to determine the input current, each channel of the R/O electronics is tested individually. Additionally, the analog circuitry performing Eq. (5.6) is probed. Using two Source Measure Units (SMUs), one feeding in an input current I_{in} and the other reading out the corresponding output voltage U_{out}, each channel is swept across the $\pm I_{\text{FS}}$ range. With the input current I_{SMU}, directly acquired from the SMU, and the calculated current I_{ROE}, determined from U_{out} and I_{FS} via Eq. (5.10), the ratio of $I_{\text{ROE}}/I_{\text{SMU}}$ is used to qualify the accuracy of the reconstructed input current. For all permutations of the six input channels and a selection[2] of full-scale input currents, a histogram of the ratios is displayed in Fig. 6.5.
The resulting distribution is centered around a mean value of 100.31 %, corresponding to a 0.31 % higher mean reconstructed current, with a standard deviation of 1.11 %. The width of the distribution corresponds to the uncertainty of transimpedance amplification which is given in Eq. (5.11), where an error of $\sqrt{3}$ % is expected. The observed width of 1.11 % indicates a slightly better tolerance of the resistors in the amplification chains of the PCB than anticipated, but is generally in agreement with the predicted uncertainty. Outliers occur predominantly close to the sign change of the test input current, i.e. for inputs that are small compared to the respective I_{FS}, emphasizing the need of selecting an adequate full-scale input current. It is worth to note, that for some combinations of input channel and full-scale input current I_{FS} selection, the accuracy of the transimpedence amplification via Eq. (5.10) is better than the anticipated error. In order to account for all possible permutations, the uncertainty of the input current calculated via Eq. (5.10) is determined via Eq. (5.11), possibly leading to an overestimation for specific combinations.
The analog R/O electronics provide transimpedance amplification of the test signals as defined in Eq. (5.10) with an uncertainty according to Eq. (5.11), delivering an analog signal processing stage for the current signals of the custom beam diagnostics that enables subsequent digitization.

[2] Here $I_{\text{FS}} = \{500\,\text{nA}, 1\,\mu\text{A}, 5\,\mu\text{A}, 10\,\mu\text{A}\}$ are used, corresponding to common values.

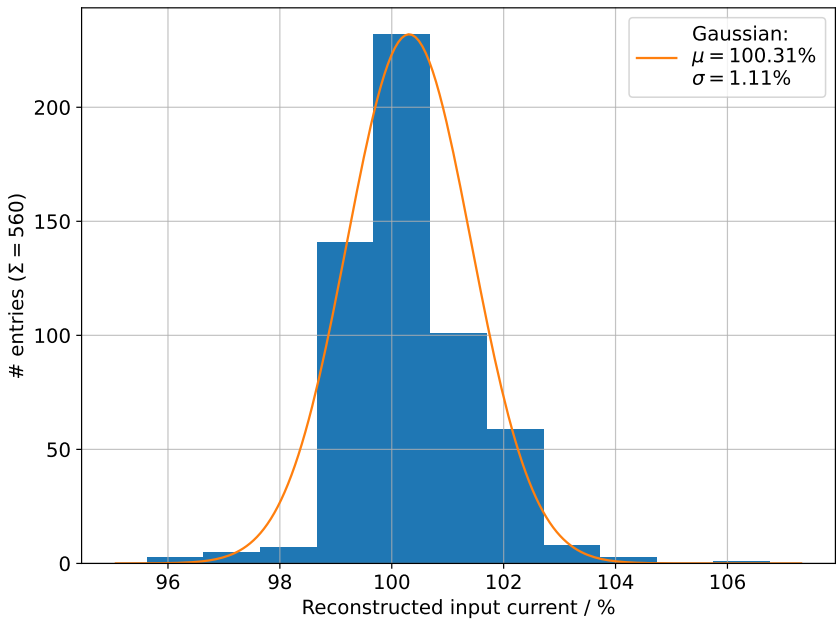

Figure 6.5: Histogram of the ratio of reconstructed (via Eq. (5.10)) and sourced (via SMU) input current $I_{\mathrm{ROE}}/I_{\mathrm{SMU}}$ and corresponding normal distribution over all six input channels and $I_{\mathrm{FS}} = \{500\,\mathrm{nA}, 1\,\mu\mathrm{A}, 5\,\mu\mathrm{A}, 10\,\mu\mathrm{A}\}$. The mean of the distribution lies at approximately 100 % with a standard deviation corresponding to Eq. (5.11).

6.2.2 HV Behavior of Beam Diagnostics

To verify the expected behavior from Sections 5.3.2 and 5.3.3 and estimate optimal operational parameters, the signal variation as a function of the applied HV of the beam diagnostics electrodes is measured. Therefore, a proton beam of 13.64 MeV and approximately 80 nA is extracted through the beam monitor into the on-site FC. The signals are measured using the readout chain, consisting of custom R/O electronics board and an ADC, where the respective current is determined using Eq. (5.10). Two SMUs are utilized to supply HV to the electrodes of to the diagnostics where the FC as well as BLM are supplied collectively by one and the SEM by the other SMU. The HV for each of the electrodes is swept in adaptive steps, resulting in an increased measurement density in critical regions. Each voltage is applied for 10 s (3 s for the BLM sweep to prevent excessive heat-up) and the corresponding current signal is measured. The results are shown in Fig. 6.6. The data points and uncertainties represent the mean value and standard deviation of the signal over the measurement time. The signal is normalized to the level present in the saturation region of operation.
As described in Section 5.3, the BLM and on-site FC both operate on the same functional principle. Consequently, their HV behavior follows the same general profile. When providing a positive voltage, their suppressor electrodes invert their functionality and remove SEs emerging from the surface under beam penetration, effectively increasing the signal. Removing all SEs results in a saturation of the signal which can be observed for the BLM and FC at approximately 10 V and 20 V, respectively. Here, the velocity with which saturation is achieved is significantly higher for the BLM, supporting the geometrically optimized design of the FC to reduce the escape of SEs. In contrast, when providing

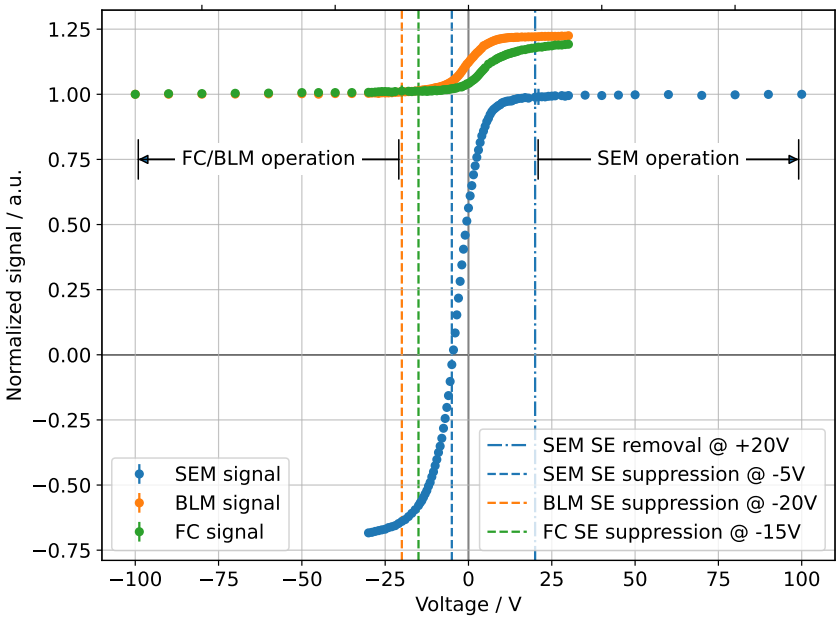

Figure 6.6: Current signal, normalized to signal at nominal HV, from the beam diagnostics introduced in Section 5.3 versus the applied HV. For each voltage, the signal is measured over 10 s (3 s for the BLM to omit heat-up) using the R/O electronics board (see Eq. (5.10)) in combination with an ADC. The data points corresponds to the mean, the uncertainties to the standard deviation of the recorded signal over time, where the uncertainties are too small to be visible.

a negative voltage to their electrodes, the intended functionality is restored, fully suppressing the escape of SEs at approximately −20 V and −15 V for the BLM and on-site FC, respectively. Again, the optimized design of the FC results in a lower SE suppression voltage. Above these voltages, the electrodes function according to their intended design and the signal saturates. A comparison of the fully suppressed SE signal amplitude with the one at full SE removal provides an estimate of the SEY of the respective material. Here, the SEY for the graphite beam dump of the FC, γ_{FC}, and for the aluminum aperture of the BLM, γ_{BLM}, are extracted as

$$\gamma_{\mathrm{FC}} = (19.21 \pm 0.56)\,\% \quad \text{and} \quad \gamma_{\mathrm{BLM}} = (22.49 \pm 0.16)\,\% \,.$$

The values are generally in agreement with measurements and uncertainties presented in Fig. 5.8, with the graphite SEY located at the lower end of the expectations. This indicates that, due to the optimized design, the applied positive HV is not sufficient to fully collect the SEs for the FC. The results show that for both, the BLM and FC, the SE suppression saturates within −20 V. Therefore, the operational voltage is set to −100 V for both diagnostics to ensure full SE suppression.
The SEM modules HV behavior is analyzed by measuring the SEE current, as defined in Eq. (5.6). When providing an increasingly negative voltage to the SEM electrode foils, SEs emerging from the signal foils are suppressed, resulting in a decrease in signal. Providing a negative voltage that yields no current from the SEM foils, allows for estimation of the kinetic energy distribution of SEs reaching the electrodes. Here, applying approximately −5 V produces a full suppression of the signal,

indicating a kinetic SE energy distribution with a maximum of 5 eV which is compatible with the simulations portrayed in Fig. 5.12. Further decreasing the voltage reverses the SEM foil configuration: the signal foils act as HV foils, removing the SEs, whereas the HV foils provide the signal. This is observed by an increasingly negative signal, measuring the actual SE current in electrons, at the signal foils. Applying a positive voltage to the HV foils corresponds to the intended operation mode. An increase in the signal can be observed with increasing positive voltage, representing the SE current removed from the signal foils. From approximately 20 V onward, the current saturates, corresponding to the complete removal of SEs and the operating mode of the SEM module. Consequently, ensuring to run in full saturation, an operational voltage of 100 V is applied to the HV foils of the SEM module. The results given in Fig. 6.6 show the intended behavior of the beam diagnostics with their applied HV and are in line with the simulations performed in Section 5.3, verifying their general functionality.

6.2.3 Beam Diagnostics Signal Signature

Operating the diagnostics at their nominal HVs of 100 V for the SEM and −100 V for the on-site FC and BLM, a proton beam of approximately 100 nA is extracted and its position in the plane perpendicular to the beam pipe is varied, using corrector magnets placed along beamline *C*. Here, the corresponding signals of the diagnostics were recorded in order to verify the expected signal signature which is shown over time in Fig. 6.7.

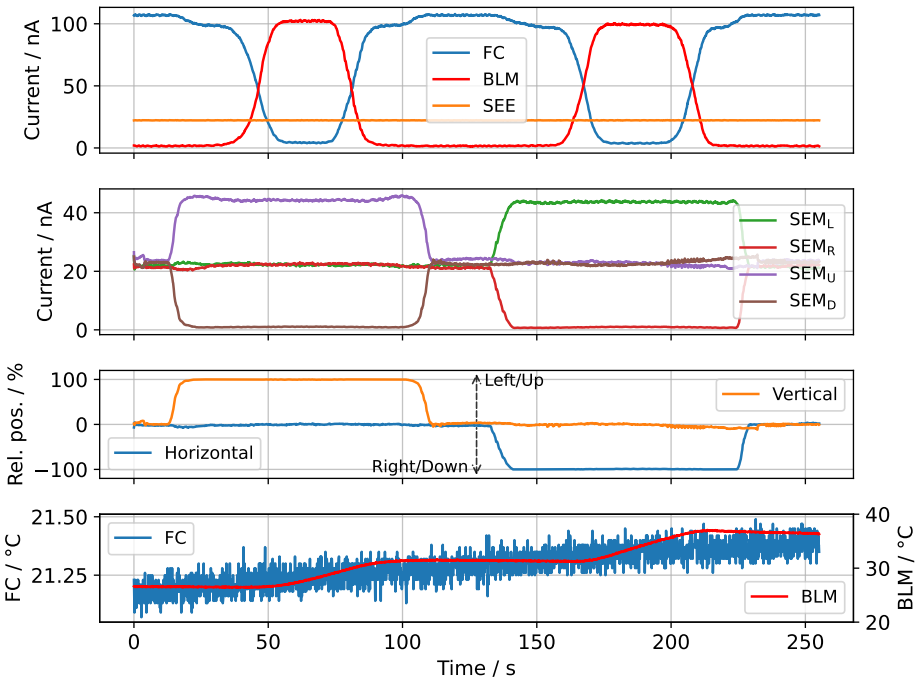

Figure 6.7: Signal signature of diagnostics during beam extraction. From top to bottom: current signals of the beam diagnostics, relative position deviation from the beam monitor center (see Eq. (5.7)) and temperature measurements. During extraction, the beam position is shifted off center using corrector magnets along the beamline *C*. A "shoulder" and signal remnants in the FC, and the latter also in the BLM, are visible due to non-optimal beam optics that result in a measurable beam halo.

Initially, the beam is centered inside the beam monitor, yielding an approximate signal equilibrium of 25 nA between all of the SEM foils and the beam is fully extracted into the on-site FC, resulting in no beam loss being registered at the BLM. Subsequently, the beam is displaced completely to only penetrate the upper foil of the vertical SEM while maintaining a central position in the horizontal plane. Accordingly, the current signal $I_{\mathrm{SEM}}(\mathrm{U})$ doubles whereas $I_{\mathrm{SEM}}(\mathrm{D})$ approaches zero. Further displacement of the beam towards the upper SEM foil eventually leads to the anticipated beam loss, detected at the BLM. Accordingly, a decrease in signal is registered at the FC, eventually approaching zero, due to the beam being fully positioned on the BLM aperture. Performing the same variation in beam position in the horizontal plane produces the equivalent signal signature whereas re-centering the beam restores the initial conditions. Independent of the beam position, the beam constantly traverses the SEM foils which results in a constant normalized SEE current I_{SEE}, according to Eq. (5.6). This verifies the expected, position-independent beam current measuring capabilities of the beam monitor. The NTC thermistors situated on the on-site FC as well as BLM show the anticipated temperature increase due to the beam's heat transfer. The FC is designed with a large heat capacity and dedicated cooling fins to enable high-current measurements over long time periods. The resulting increase of approximately 0.5 °C over the measurement period confirms an effective heat dissipation. In contrast, the BLM temperature rapidly increases with the passages being visible where the beam is fully stopped on the aperture. The temperature over the measurement increases by approximately 10 °C and remains constant after no beam is cut off due to the low heat dissipation capabilities inside the vacuum. Both diagnostics show the anticipated temperature behavior.
When precisely inspecting the signal course of the on-site FC and BLM over this particular measurement, an atypical "shoulder" in the FC current is observed when re-/de-centering the beam. Additionally, a small signal remainder can be observed at the BLM, when the beam is centered and fully extracted into the FC, and for the FC when it is fully resting on the BLM aperture. This is due to a non-optimal configuration of the accelerator and the beam optics along the respective beamline, resulting in a wide beam *halo* that carries a small fraction of the current. Using the signal signature of the beam diagnostics, this misadjustment can be identified and corrected.
At their respective operational voltages, the beam diagnostics provide signals, corresponding to the anticipated course for a given beam scenario. Subsequently, the monitor enables the detection of faulty beam configurations as well as online beam monitoring at the irradiation site.

6.2.4 Beam Monitor Calibration

The beam monitor is designed to perform non-destructive online beam parameter monitoring close to the irradiation site. To do so, it requires a calibration which is realized by simultaneous measurement of the SEE current I_{SEE} and the respective ion beam current using the on-site FC. By variation of the extracted beam amplitude, the *calibration constant* λ can be determined from a linear regression according to Eq. (5.12). An example of a calibration measurement is shown in Fig. 6.8. Here, a 13.483 MeV proton beam is extracted into the irradiation setup and its magnitude altered between 200 and 900 nA.
The SEM input of the R/O electronics is configured with a full-scale input current of $I_{\mathrm{FS}} = 500\,\mathrm{nA}$ whereas the FC inputs were set to $I_{\mathrm{FS}} = 1\,\mu\mathrm{A}$. A linear fit according to Eq. (5.5) is performed, allowing for the extraction of the SEY γ for the carbon-coated signal foils of the SEM module and consequently

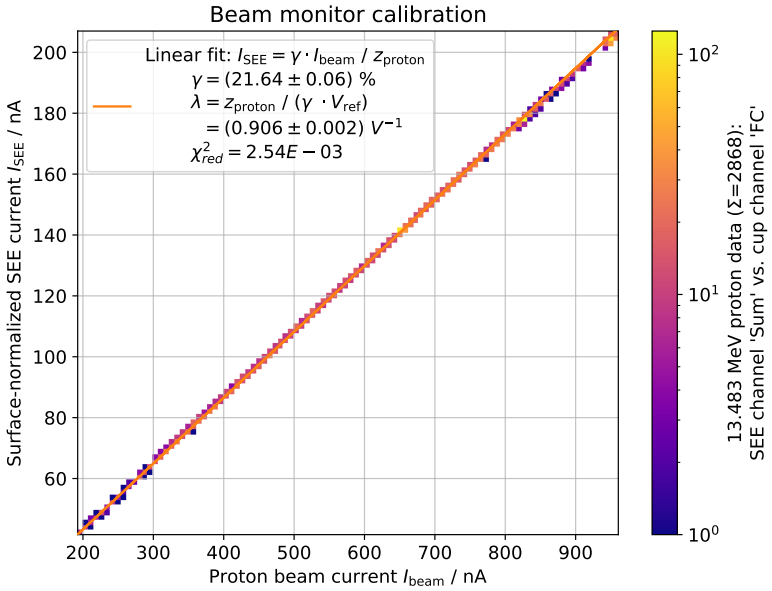

Figure 6.8: Histogram of beam monitor calibration for 13.483 MeV protons. Using the setup depicted in the top right of Fig. 5.4 and the R/O electronics, the beam current I_{beam} is measured destructively using the on-site FC and the SEE current I_{SEE} via Eq. (5.6). Using Eq. (5.5), a fit is performed to extract the SEY of $\gamma = (21.64 \pm 0.06)$ % for the SEM foils. Here, Eq. (5.5) is valid over approximately one order of magnitude.

the calibration constant λ. The resulting values are

$$\gamma = (21.64 \pm 0.06)\ \% \quad \overset{\text{Eqs. (5.5) and (5.12)}}{\Rightarrow} \quad \lambda = (0.906 \pm 0.002)\ \text{V}^{-1}\,,$$

where the SEY is in good agreement with the data provided in Fig. 5.8. The low reduced χ^2 of 2.5×10^{-3} is due to an overestimation of the input current errors as the corresponding channel I_{FS} combination of both signals is close to the mean in Fig. 6.5. As postulated in Section 5.3.1 for the beam monitor configuration and environment, the obtained calibration is valid over a large dynamic range of beam current of approximately one order of magnitude, allowing one to non-destructively measure the extracted beam current over the same range.

In order to probe the repeatability of calibration results in between irradiation campaigns, several measurements for protons are performed and resolved in energy and time. All measurements correspond to proton beams tuned for irradiation to a target energy of 13.6 MeV, allowing to estimate the change introduced by run-to-run variations of the beam energy. The resulting calibration constants λ and corresponding SEYs γ are shown in Fig. 6.9. For proton energies of 13.434 – 13.627 MeV, with a mean of (13.495 ± 0.043) MeV, the distribution indicates no dependency of the calibration constant λ on the proton energy within the uncertainties. As shown in Fig. 5.8, an energy dependency of the SEY and therefore λ is expected, suggesting that here, the change due to energy variation is smaller than the measurement uncertainty. Subsequently, run-to-run energy fluctuations do not significantly affect the beam monitor calibration.

Over a period of approximately 1.5 years, including a 9 month accelerator maintenance window, the

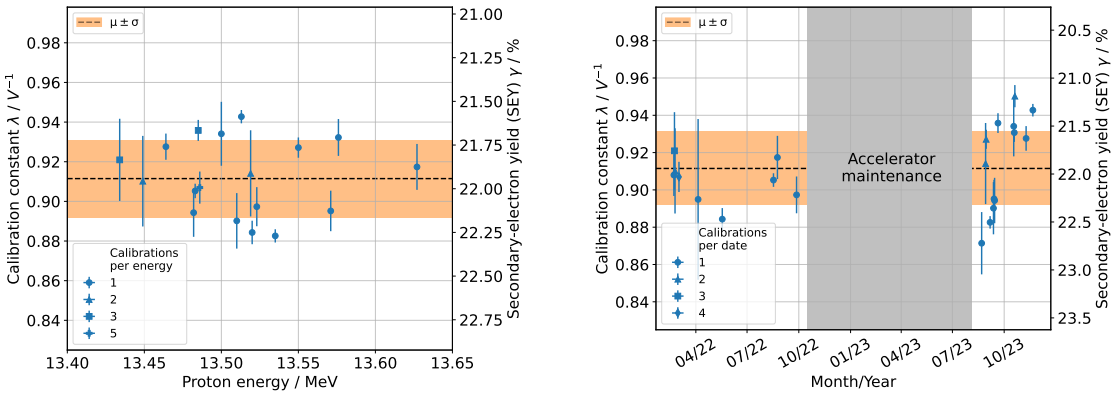

(a) Energy

(b) Time

Figure 6.9: Beam monitor calibration constants and corresponding SEYs according to Eq. (5.12) for proton beams adjusted for irradiation, resolved in energy and time. The resulting mean and its standard deviation of the distribution are shown. Multiple calibration measurements are performed per energy and date as indicated in the legends. The difference in uncertainties is due to accelerator performance for the respective measurement.

observed λ values appear clustered in time, following no functional trend. Taking into account the dependencies of the SEE current from Eq. (5.4), the expected cause for these variations over time are fluctuations in pressure close to the extraction *2a*, possibly caused by changes affecting the vacuum system.
For the mean proton energy of (13.495 ± 0.043) MeV for the calibration measurements, a value of $\gamma = (22.57 \pm 1.35)$ % for graphite can be extracted from the literature values displayed in Fig. 5.8. The mean and standard deviation of the distribution of all measurements is indicated in Fig. 6.9:

$$\gamma_{\text{mean}} = (21.94 \pm 0.47)\ \% \quad \overset{\text{Eqs. (5.5) and (5.12)}}{\Rightarrow} \quad \lambda_{\text{mean}} = (0.912 \pm 0.020)\ \text{V}^{-1}$$

which is in good agreement with the expected value within the uncertainties. The relative standard deviation of 2.2 % supports a consistent beam monitor calibration result over time and energy. It is composed of the uncertainties of the transimpedance amplification process as well as the changes in environmental conditions, primarily due to vacuum pressure fluctuations. In order to provide accurate beam monitoring, a monitor calibration, as shown in Fig. 6.8, is performed prior to each irradiation campaign, using the procedure described in Section 5.4.1. The uncertainty on the obtained beam current via Eq. (5.12) is defined by the error on the calibration and the full-scale input current I_{FS}. Generally, ΔI_{FS} dominates as the calibration constant for individual runs can be determined with a much lower relative uncertainty, as shown in Fig. 6.8.

6.2.5 Beam-based Irradiation Events

As introduced in Section 5.6.3, `irrad_control` provides an event system to improve the uniformity of the applied fluence by preventing exposition of the DUT to faulty beam conditions. Analyzing the data of an example proton irradiation (output from `irrad_control`) the event system is showcased by probing recorded events against the corresponding beam monitor signals which is shown in Fig. 6.10.

The relative beam position as defined in Eq. (5.7), the beam loss and calibrated current according to Eq. (5.12) as well as the corresponding events and their duration are displayed. Over the course of the example irradiation, three sections are selected that represent typical characteristics of faulty beam conditions which regularly appear during operation.

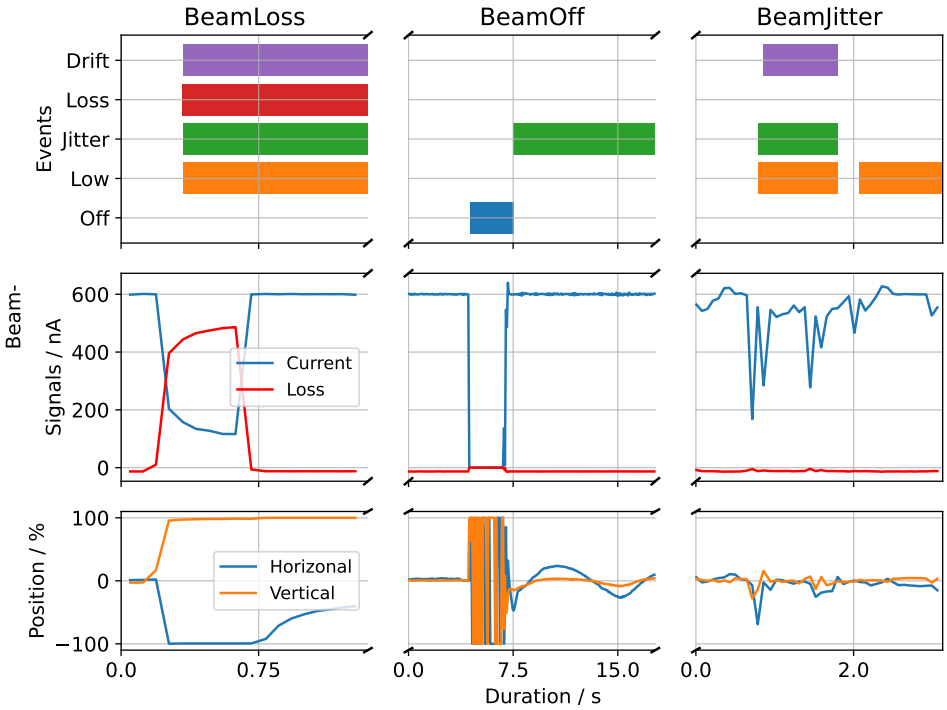

Figure 6.10: Beam-based events and their signal signature within the beam monitor for three primary events. Each initial event results in one or more secondaries. Due to the difference in cooldown time, the duration of the events differs.

The first section shows a `BeamLoss` event due to the beam handling system of the BIC undergoing an upset in the beam position control unit. As a result, the beam at the extraction moves up and right, causing approximately 2/3 of the beam current to be registered on the BLM and extracting only 1/3 to the DUT. After 0.5 s, the control unit partially restores the position and the extracted beam current is recovered without beam loss. The position of the beam remains off-center, as the beam is still positioned fully on the upper SEM foil. Accordingly, the event system correctly recognizes the respective events. Due to the sub-second duration of this defect, some events are active longer than the beam fault due to their cooldown of $\geq$ 1 s.
The subsequent section displays a `BeamOff` event caused by an upset of the ion source, resulting in no ions being transmitted into the accelerator for 3 s. During the `BeamOff` event, no other beam events are checked for, yielding no activation of other events. After recovery of the ion source, the beam current returns to its previous amplitude and the `BeamOff` event is deactivated. A `BeamJitter` event becomes and remains active due to the sudden as well as significant change in signal amplitude.
The last section visualizes a typical `BeamJitter` and consequent `BeamLow` as well as `BeamDrift` events, caused by fluctuations of the ions transferred from the source into the cyclotron. The extracted beam current fluctuates over the course of approximately 1 s, falling below the *minimum scan current*

(see Section 5.4.2). Additionally, the fluctuations cause a brief offset in beam position to the lower right which is quickly restored.
While any event is active, the irradiation routine is halted with the beam located on the shielding and off the DUT. In this case, the beam is stopped, preventing it from introducing irregularities into the applied fluence distribution on the DUT.

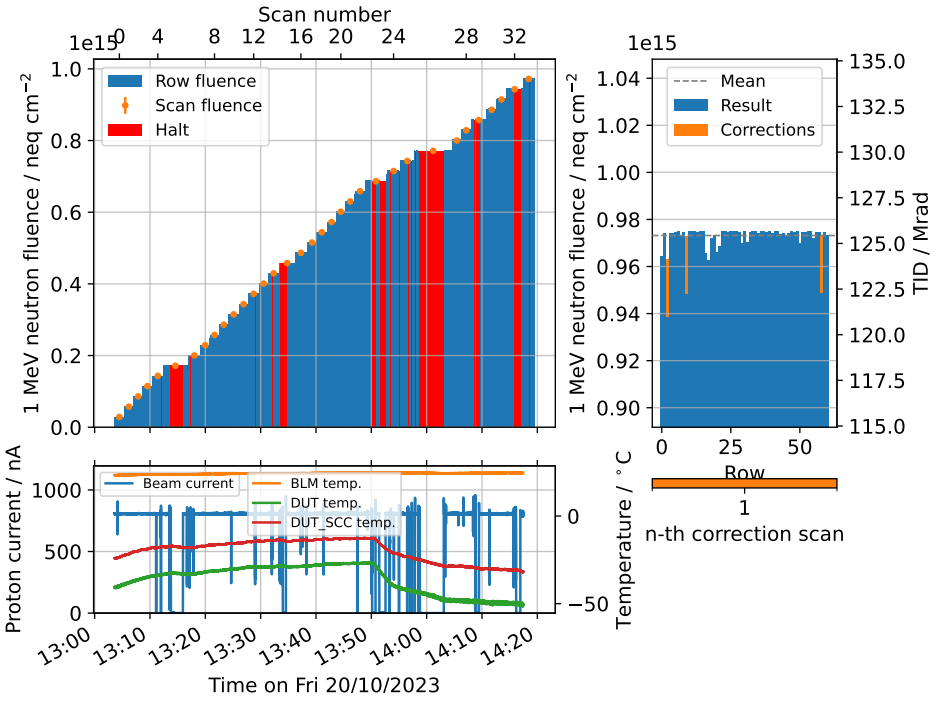

Figure 6.11: Overview of irradiation campaign performed under unstable beam conditions. The beam current (bottom) and the applied equivalent fluence (top) over time are shown as well as the resulting distribution (right). The beam current fluctuates frequently over the course of the irradiation, resulting in pauses of the irradiation routine due to the corresponding events. Plot generated by `irrad_control` after each irradiation.

To indicate the impact of the beam-based event system on an irradiation campaign and resulting fluence uniformity, an overview of an irradiation with unstable beam conditions is shown in Fig. 6.11. The extracted proton beam current as well as multiple temperatures over time are displayed on the bottom. Moreover, the evolution of the applied fluence, resolved over row and scan number of the irradiation pattern, is depicted on top whereas the resulting distribution is illustrated on the right. Over the duration of the irradiation campaign of approximately 80 min, a variety of erroneous beam conditions can be seen. The ones yielding a halt in the irradiation routine of $\geq$ 10 s are indicated. Due to the event system, the routine avoids to scan the DUT during multiple phases without beam as well as unstable beam conditions. This results in a mean beam current during scanning the DUT of (805 ± 39) nA, yielding not only a uniform fluence distribution but also ensuring to apply the specified target fluence of 10^{15} n_{eq}/cm^2.
Indicating the limitations of the event system, multiple deficits in the resulting distribution are caused by events triggered during the scanning of the DUT. Due to the online fluence monitoring capabilities of `irrad_control`, the fluence distribution is leveled by re-irradiation of insufficient rows with

adapted parameters (see Eq. (5.13)) after completion of the irradiation routine.
The event system introduced in Section 5.6.3 enables the irradiation procedure to omit unstable beam conditions, resulting in improved uniformity of the applied fluence distribution while ensuring to deliver the specified target fluence, contributing to a well-controlled irradiation system.

6.3 Irradiation Procedure and Dosimetry

The knowledge of the primary particle fluence is an essential requirement for the quantitative characterization of the radiation damage delivered at the irradiation site. It facilitates the application of NIEL-scaling according to Eq. (4.7) in order to determine the 1 MeV neutron equivalent fluence $\Phi_{n_{eq}}$ and the extraction of the administered TID via Eq. (5.19). Consequently, a fundamental prerequisite for verifying the functionality of the site is that the irradiation procedure, described in Section 5.4, applies the specified particle fluence to the area of a given DUT. Accordingly, it is imperative that the actual fluence delivered to the DUT is accurately extracted by the available dosimetry.
To verify these requirements, a series of dedicated irradiations are carried out in which the proton fluence is determined using both the de facto standard [81, 90, 54] of foil (isotope) activation and the beam-based dosimetry methods. Subsequently, the general approach of fluence measurement via isotope activation is introduced. Finally, an overview of the proton irradiation configuration for seven titanium foils is given for which the dosimetry results via foil activation and beam-based methods are compared.

6.3.1 Fluence Measurement via Isotope Activation

The determination of the applied primary particle fluence is conventionally performed by irradiation of a thin metallic foil sample alongside the DUT. The foil is placed within the area of uniform fluence distribution as shown in Fig. 5.15. Considering a metal M and a corresponding radioisotope X which is produced due to proton irradiation according to the process $M\,(p,x) \rightarrow X$, the mean proton fluence Φ_p can be derived from the resulting isotope activity after irradiation [91]

$$\Phi_p = 10^{27} \cdot \frac{A_X}{\Omega_X} \cdot \frac{m_X^{\text{mol}}}{m^{\text{foil}} \cdot N_A} \cdot \frac{1}{\lambda_X} \cdot \exp\left(\lambda_X \cdot t\right) \quad \text{with} \quad \lambda_X = \frac{\ln(2)}{T_{1/2}}\,. \tag{6.1}$$

Here, A_X is the isotope activity in kBq, Ω_X the production cross section in mb, m_X^{mol} the isotopes molar mass in $\mathrm{g\,mol^{-1}}$, m^{foil} the foil mass in mg, $N_A = 6.022 \times 10^{23}\ \mathrm{mol^{-1}}$ the Avogadro constant, λ_X the decay constant of the isotope in Hz and finally t the duration between irradiation and activity measurement in seconds.
In order to reliably measure the resulting activity, the isotope must have a sufficiently large production cross section Ω_X and half-life $T_{1/2}$ as well as γ-line intensity. Furthermore, the production cross section Ω_X typically depends strongly on the ion energy, requiring knowledge of the energy at the foil and a thin foil to reduce the change in cross section due to energy loss during propagation. The uncertainty on the result obtained by Eq. (6.1) is mainly composed of the uncertainty on the production cross section $\Delta\Omega_X$, the measured activity ΔA_X and the foil weight Δm^{foil} which typically yields a relative uncertainty in the order of 15 % [13].
For the proton irradiation sites in Karlsruhe [13] and Birmingham [12], operating in the mid-20 MeV

region, nickel foils are used. The PS IRRAD facility [11] at CERN uses aluminum foils for 23 GeV protons [54]. For the proton energies at the BIC, titanium foils are best suited [92]. Using natural titanium, the vanadium isotope ^{48}V is produced according to $^{\text{nat}}$Ti (p, x) $\rightarrow^{48}$ V. With a half-life of $T_{1/2}$ = 383.424 h, two high-intensity γ-lines at 983.5 keV (99.99 %) and 1 312.05 keV (97.49 %) and a broad maximum in the production cross section around 11 MeV, it exhibits ideal properties for determining the proton fluence at the BIC irradiation site via foil activation.

6.3.2 Irradiation of Titanium Foils

To obtain reference dosimetry measurements via the isotope activation approach, seven 99.6 % titanium foils of 25 µm thickness and approximately 1 cm^2 area are irradiated as DUTs, using the procedure explained in Section 5.4. Simultaneously, the results of the beam-based dosimetry are recorded for all irradiations. The foils are irradiated to proton fluences ranging from 7×10^{13} to 12×10^{14} p/cm^2 with the target fluence is applied using the online fluence monitoring capabilities of `irrad_control`. An image of a typical foil cutout is shown in Fig. 6.12. Prior to irradiation, each foil is weighed using an analytical scale. Subsequently, the foils are situated on the generic DUT carrier plate using Kapton tape. To avoid additional energy loss, the Ti foils are glued on the Kapton tape so that they face the beam first. Utilizing the 1 cm grid on the carrier, the position of the foil relative to the scintillation screen inside the cool box is extracted and fed into `irrad_control` to construct the scan grid.

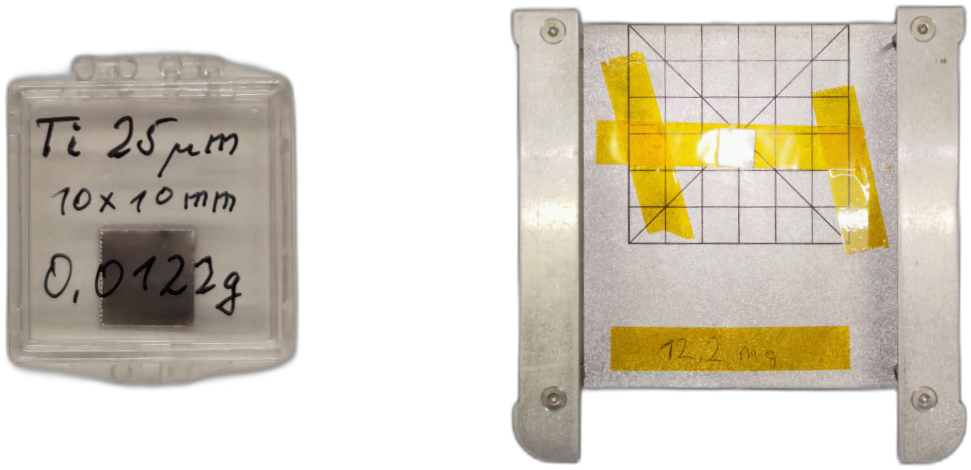

(a) Thickness, area and weight

(b) Mounted on carrier board

Figure 6.12: Titanium foil, cut to an approximate square of 1 cm^2, with specifications on a plastic casing and mounted on the carrier board via Kapton tape for irradiation.

To probe the independence of the resulting fluence on the irradiation parameters used in Eq. (5.13), the nominal beam current, the row separation as well as the scan velocity are varied between irradiations. An extensive overview of parameters, dosimetry results obtained using the beam-based approach and general information on each irradiation can be found in Table A.1. Post irradiation, the gamma spectrum of each foil is measured at the spectroscopy center of the HISKP and the recorded data is analyzed with `irrad_spectroscopy` [78] to determine the activity of the vanadium isotope ^{48}V in

each foil. The production cross section for the process ^{nat}Ti (p, x) $\rightarrow^{48}$ V is taken from [92, p.52, Tab.2], where a value of (412 ± 47) mb is stated for protons of (12.5 ± 0.2) MeV. This corresponds approximately to the proton energy at the foils over all irradiations of (12.22 ± 0.05) MeV with reasonable uncertainty. The foil weight, isotope activity as well as the resulting proton fluence via Eq. (6.1) for each irradiation are shown in Table 6.2.

Fluence / 10^{14} protons/cm^2		Foil weight / mg	^{48}V activity / kBq
Target	Calculated		
0.7	0.73 ± 0.10	12.00 ± 0.36	2.17 ± 0.12
1	1.03 ± 0.13	11.80 ± 0.36	2.90 ± 0.16
3	3.20 ± 0.41	11.70 ± 0.36	9.3 ± 0.5
5	4.99 ± 0.64	11.00 ± 0.36	13.0 ± 0.7
8	7.99 ± 1.03	12.20 ± 0.36	22.9 ± 1.2
10	9.46 ± 1.22	11.50 ± 0.36	26.8 ± 1.4
12	13.86 ± 1.78	11.80 ± 0.36	39.1 ± 2.0

Table 6.2: Dosimetry via proton irradiation of seven titanium foils and subsequent activation of the vanadium isotope ^{48}V. Shown are the measurements that are input to Eq. (6.1), yielding the mean proton fluence. The uncertainty on the activity is composed of the statistical uncertainty and an estimated 5 % relative uncertainty on the measurement. The uncertainty on the measured weight of the foils is given by the scales repeatability and linearity.

The mean proton fluence determined via isotope activation agrees with the target value within the uncertainties for all irradiation campaigns, with the exception of the 12×10^{14} p/cm^2 target, where the relative deviation of ≤ 1 % is marginal after exhaustion of the error margins. In conclusion, the general agreement between target and resulting fluence values verifies that the irradiation procedure, introduced in Section 5.4, applies the target proton fluence as anticipated, independent of the irradiation parameters going into Eq. (5.13). Moreover, the agreement indicates an adequate prediction of the proton energy degradation towards the site from the simulations shown in Fig. 6.2. These findings qualify the irradiation procedure used at the BIC irradiation site to predict and deliver a specified proton target fluence to a DUT. In the following, these results are used to evaluate whether the beam-based dosimetry provides equivalent results.

6.3.3 Comparison of Dosimetry Methods

The beam-based dosimetry used at the BIC irradiation site provides a set of advantages compared to the standard fluence determination via foil activation:

- Online fluence monitoring with resolution in the row dimension of the scan pattern (see Fig. 5.15) of the irradiation routine
- Dynamic correction of the uniformity of the applied fluence profile post irradiation
- Application of user-specific fluence profiles and measurements at predefined fluence levels

- Two-dimensional offline reconstruction of the fluence profile over the scan pattern and extraction of the DUT-specific distribution

Overall, the beam-based methods deliver spatial distributions, providing additional information compared to the scalar mean fluence value obtained from the dosimetry via isotope activation. Furthermore, time and resources can be saved as foil irradiation and subsequent spectroscopy are no longer necessary.

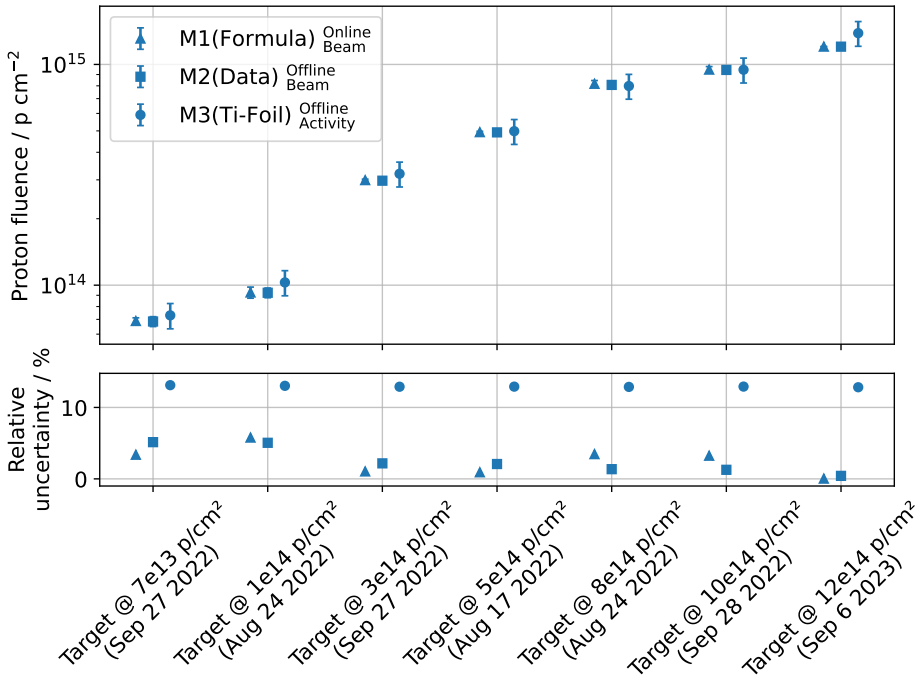

Figure 6.13: Proton fluence measurement by the beam-based online monitoring via Eq. (5.13) (*M1*), offline irradiation data analysis using Eq. (5.18) (*M2*) and isotope activation via Eq. (6.1) (*M3*) for seven irradiations of titanium foils. Additionally, the relative uncertainties on the fluences for each method are shown.

To validate that they yield comparable values, the dosimetry for the irradiations of titanium foils is now carried out with the beam-based methods. The corresponding analysis is included in the `irrad_control` software, enabling one to extract the results and compare them to the findings of the previous Section 6.3.2. Consequently, the three different methods are categorized as follows:

M1 : Online fluence monitoring described in Section 5.5.1
M2 : Offline fluence reconstruction via irradiation data as explained in Section 5.5.2
M3 : Offline dosimetry via isotope activation as introduced in Section 6.3.1

The fluences as well as their relative uncertainties for all irradiations, determined via each method, are shown in Fig. 6.13. Additional details can be found in Table A.1. To obtain comparable values for the beam-based dosimetry, the fluences correspond to the mean value and the uncertainties to the mean error in conjunction with the standard deviation of the respective distribution (see Eq. (A.2)). The determined proton fluences are in agreement across all methods and irradiations, verifying that the

beam-based and isotope activation dosimetry approaches result in comparable mean fluences within their uncertainties. Moreover, the beam-based dosimetry consistently yields relative uncertainties of $\leq 5\,\%$ with typical values around $2\,\%$, whereas the isotope activation method resides around the anticipated $\geq 10\,\%$. It is worth to note that method *M1* is utilized to measure the damage levels during the irradiation routine, e.g. to determine when the target damage is applied. Method *M2* produces the final reference value for each irradiation as it delivers a more accurate result, including the uncertainties and variations across the whole DUT area.
In conclusion, the beam-based dosimetry approach is validated to provide comparable results to the fluence measurement via isotope activation, whereas the former yields lower uncertainties and additional spatial information. This meets the prerequisite for an accurate conversion of the proton to NIEL fluence via Eq. (4.7) at the BIC.

6.4 Proton Hardness Factor

As introduced in Section 4.2, the hardness factor κ expresses the NIEL damage of a given particle in units of 1 MeV neutron equivalent n_{eq} , corresponding to 95 mb MeV (see Fig. 4.3). It enables the determination of the NIEL fluence Φ_{eq} from the primary particle fluence via Eq. (4.7) and therefore a comparison of the damage induced to silicon devices by different particle species. Consequently, it is an integral quantity for the characterization and operation of an irradiation facility for silicon detectors. The simulation results in Figs. 4.3 and 6.4 allow one to initially estimate a proton hardness factor of $\kappa_p \approx 4$ for the energies at the BIC. Using Eqs. (4.8) and (4.9), the proton hardness factor can be determined by irradiation of silicon sensors to different fluences and subsequent measurement of the volume-normalized leakage current increase.
Therefore, six silicon sensors are irradiated and electrically characterized. The sensors are briefly described and an overview of the irradiation campaign is given. Moreover, the electrical characterization, namely the IV and CV behavior, is performed pre and post irradiation. With these results, the current-related damage rate of the BIC protons is extracted which is used to determine the hardness factor. At last, a brief description of the limitations of the obtained NIEL scaling is given.

6.4.1 Irradiation of Silicon Sensors

To extract the proton hardness factor at the irradiation site in Bonn, six passive CMOS n-in-p sensors, manufactured by LFoundry (LF), are irradiated to different proton fluences. The 150 µm-thick sensors have 400×192 pixels with a pitch of (50×50) µm^2 or (25×100) µm^2, which corresponds to an area of approximately (2×1) cm^2. The pixel electrodes are either connected to the bias grid via a resistor (DC coupling) or additionally to a series capacitor (AC coupling). The bias voltage to deplete the sensor can be applied between the bias grid and the backside contact. The development and characterization of these sensors has been the main subject of [20]. Furthermore, their CV behavior is documented in [93]. Here, they exhibit good IV and CV characteristics for determination of the quantities required in Eq. (4.8).
Six of these sensors, situated on and wire-bonded to generic PCBs (so-called *surfboards*), are irradiated with protons of initially ≈ 13.6 MeV, corresponding to ≈ 12.3 MeV at the irradiation site. The resulting proton fluences range from 5×10^{12} to 16×10^{13} p/cm^2. An image of the simplified pixel cross section, a sensor on the surfboard as well as the surfboard mounted to the carrier plate for irradiation are

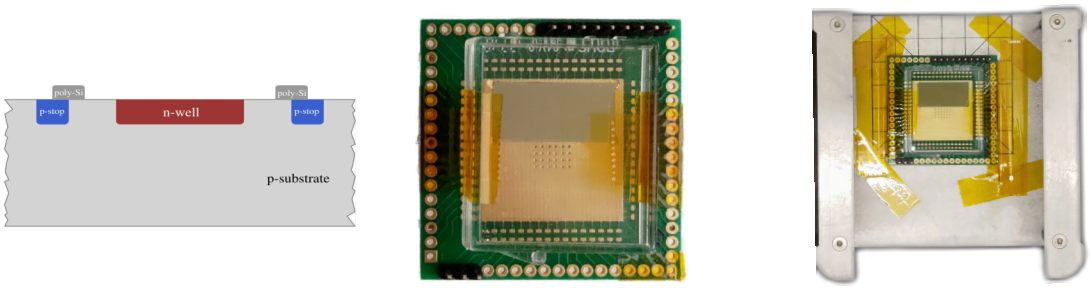

(a) Pixel cross section, from [20] (b) Sensor on surfboard (c) Surfboard on carrier board

Figure 6.14: Simplified pixel cross section (a) and images of an LF sensor, glued and wire-bonded to a surfboard (b) and mounted on the carrier board for irradiation (c). The metallization of the backside is omitted in the schematic.

shown in Fig. 6.14. In order to distinguish the sensors, they are assigned a unique identifier. The results of the sensor irradiations are given in Table 6.3, an extensive overview, containing information on irradiation parameters, is displayed in Table A.2.

Sensor	Proton		Pixel	
identifier	fluence / p/cm^2	energy at DUT / MeV	pitch / µm^2	coupling
S11	$(4.83 \pm 0.54) \times 10^{12}$	12.18	25×100	DC
S1	$(9.67 \pm 0.77) \times 10^{12}$	12.17	50×50	DC
S7	$(2.00 \pm 0.10) \times 10^{13}$	12.25	50×50	DC
S8	$(4.01 \pm 0.17) \times 10^{13}$	12.25	50×50	DC
S9	$(7.62 \pm 0.23) \times 10^{13}$	12.15	50×50	DC
S10	$(1.60 \pm 0.05) \times 10^{14}$	12.15	50×50	AC

Table 6.3: Proton fluence levels and energies at the DUT, according to Fig. 6.2, for the irradiation of six sensors. The pixel pitches and couplings to the bias grid are also stated.

As an example, Fig. 6.15 shows the irradiation overview and the resulting proton fluence distribution on the DUT, as provided by the `irrad_control` analysis functions, for sensor S11. The irradiation to approximately 5×10^{12} p/cm^2 is performed within 5 min and 5 scans. Due to the low fluence level, the irradiation site is operated at the lower end of its nominal parameters, resulting in a low number of scans which limits uniformity of the applied fluence distribution. The equivalent portrayal for all remaining sensors can be found in the appendix in Fig. A.2.
Following the standard convention for probing the NIEL scaling via Eq. (4.8), all sensors are annealed for 80 min at 60 °C, as shown in Fig. 4.7, for which the reference 1 MeV neutron equivalent current-related damage rate is $\alpha_{n_{eq}} = (3.99 \pm 0.03) \times 10^{-17}\,\mathrm{A\,cm^{-1}}$ [53].

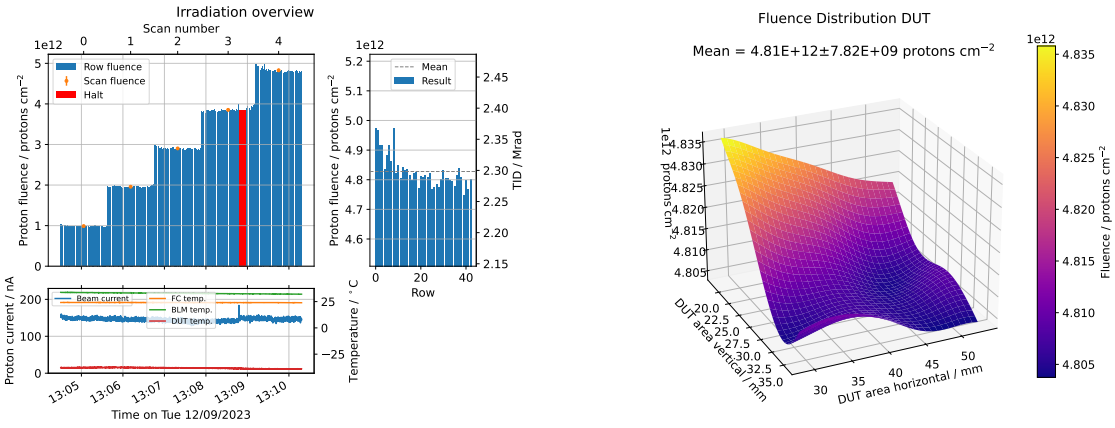

(a) Irradiation overview

(b) Resulting proton fluence distribution

Figure 6.15: Irradiation overview and resulting proton fluence distribution on the LF sensor S11, generated by `irrad_control`.

6.4.2 Electrical Characterization

The electrical characterization, i.e. the measurement of the IV and CV behavior, allows for determination of the volume-normalized leakage current increase due to irradiation according to Eq. (4.8). A measurement of the IV characteristics provides information of the nominal leakage current, arising from the fraction of the depleted bulk for a given bias voltage. Additionally, the CV behavior allows for an extraction of the full-depletion voltage V_{dep}. In conjunction with the active area and thickness of the senor, both measurements yield the volume-normalized leakage current.
Firstly, the measurement setup is introduced, followed by the measurements for all sensors before and after irradiation.

Measurement Setup

To record the IV curves, the bias grid, connected to the collection electrodes of the pixels, is set to ground potential whereas the backside is connected to negative HV, effectively operating the sensors in reverse bias. For the CV curves, a preexisting setup, developed and characterized in [93], is used. It consists of an *HP 4284A* LCR meter as well as a custom DUT box, shown in Fig. 6.16(a). Additionally, to enable sufficient bias application after irradiation, an external SMU is used via a bias box, connecting both the SMU and the LCR measuring device to the DUT box. The LCR meter is operated at a frequency of 1 kHz for the measurement of the unirradiated sensors.
After irradiation, all measurements are performed in a climate chamber at stable temperatures $\leq -10\,^{\circ}\text{C}$ to reduce the nominal leakage current and therefore prevent damage and measurement distortion due to self-heating or thermal runaway. An image of the bias box inside the climate chamber is displayed in Fig. 6.16(b). Additionally, to ensure a stable temperature when measuring the IV curves after irradiation, the sensors are thermally coupled to a copper block via a thermal pad, as portrayed in Fig. 6.16(c). Here, a *Sensirion SHT85* temperature sensor is mounted on the same thermal pad to provide accurate temperature readings for each bias voltage, allowing for the leakage current to be scaled via Eq. (2.20).
For each bias voltage, each quantity is measured five times, using the standard deviation of these

measurements as an uncertainty estimate. For the temperature scaling, an uncertainty of 1 °C is assumed.

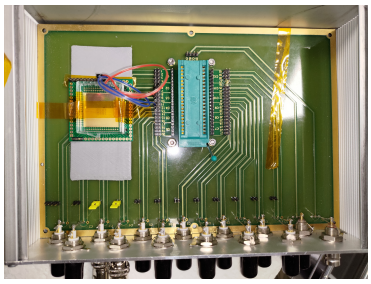

(a) Sensor in DUT box

(b) DUT box in climate chamber

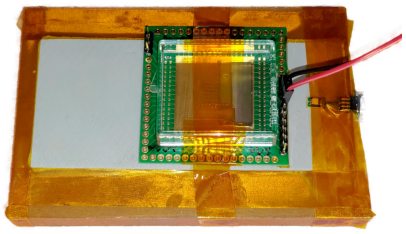

(c) Sensor and SHT85 on copper block, coupled via a thermal pad

Figure 6.16: Setup for electrical characterization of LF sensors. After irradiation, all measurements are performed inside a climate chamber to reduce the nominal leakage current and prevent annealing.

IV curves

The IV curves, scaled to 20 °C using Eq. (2.20), of the sensors before and after irradiation are shown in Fig. 6.17. Before irradiation, the curves of all sensors follow the anticipated trend with a kink around the expected full-depletion voltage region, following a nominal leakage current in the low range of $\leq 10\,\text{nA}$ up to around 200 V. Above this voltage, the sensors start to break down, as indicated by the rapid increase in leakage current which is limited by the SMU to a maximum of 500 nA. The sensor S11, featuring an asymmetric pixel pitch, breaks down earlier than the other sensors which share the same symmetric pitch.
After irradiation, the IV curves show the expected leakage current increase with fluence, dominated by the generation current in the bulk from deep-level defects (see Section 4.3.1). The shift of the sensor breakdown to higher voltages is explained by the change in the effective doping concentration and thus the depletion depth (see Sections 2.2.2 and 4.3.2). The sensor S11, irradiated to the lowest fluence, exhibits an increase to the breakdown voltage of $\approx 40\,\text{V}$ whereas for the highest fluences no clear breakdown is visible up to approximately 400 V.
The observed IV curves before and after the irradiation display the expected behavior, in agreement with the characterization in [20]. Consequently, this supports further use of the results in conjunction with the CV behaviour to extract the leakage current at full depletion. A collection of information extracted from IV curves can be found in Table 6.4.

CV curves

The CV curves of the unirradiated sensors can be seen in Fig. 6.18. Here, $1/C^2$ is plotted versus the applied bias voltage. This allows for the identification of the full-depletion voltage V_{dep} from the properties of Eq. (2.22), where a linear increase of the data with the bias voltage can be expected, followed by a plateau indicating full depletion. The transition corresponds to a kink in the graph, enabling to determine V_{dep} via a fit to the region of linear increase and the plateau region where V_{dep} is extracted from their intersection [94].

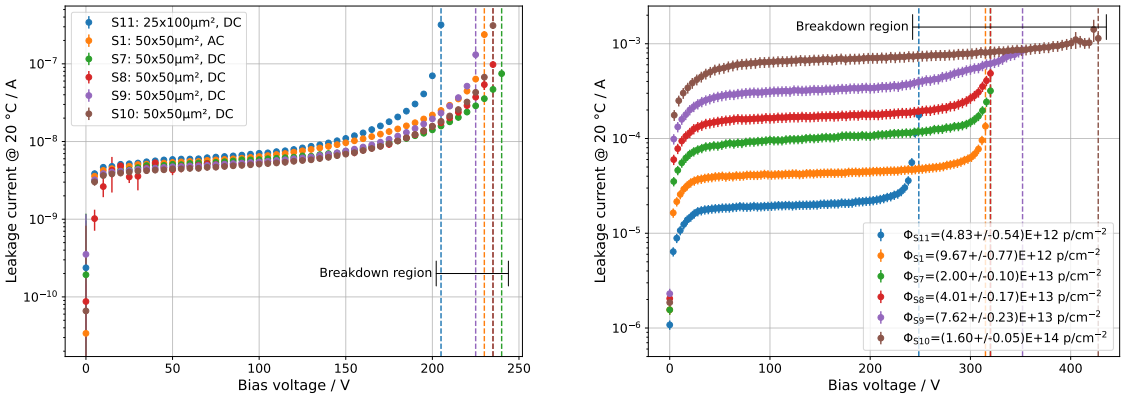

(a) Unirradiated

(b) Irradiated

Figure 6.17: IV characteristics of LF sensors before (a) and after (b) irradiation. In both cases, Eq. (2.20) is used to scale the results to 20 °C for further comparison. Measurement uncertainties are mostly too small to be visible in the unirradiated case.

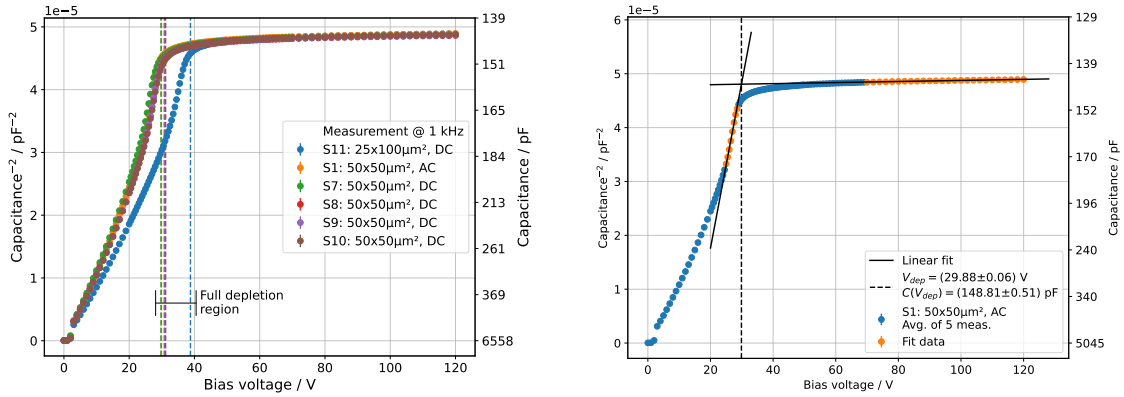

(a) CV curves of all sensors

(b) Extraction of full-depletion voltage from CV curve of S1

Figure 6.18: CV characteristics of unirradiated LF sensors, measured at 1 kHz. Measurement uncertainties are too small to be visible.

As visible in Fig. 6.18(a), the CV curves of all sensors exhibit the characteristic kink at approximately 30 V for the (50×50) µm^2 pixel pitch sensors and approximately 40 V for the (100×25) µm^2 pitch sensor. The data deviates slightly from the model in Eq. (2.22) as the region of linear increase actually exhibits two sections with different slopes. This indicates that more complex structures, such as pixelated sensors, are not fully described by the simple parallel-plate model. Nevertheless, using the slope closest to the kink, the characteristic trend of the measurements allows for the extraction of the full-depletion voltage as per the aforementioned approach which is shown as an example for sensor S1 in Fig. 6.18(b). A full-depletion voltage of $V_{\text{dep}} = (29.88 \pm 0.06)$ V with a capacitance of

(148.81 ± 0.51) pF can be derived[3]. This procedure is applied for all sensors and an overview of the results is shown in Table 6.4. In the unirradiated case, the measured capacitance is independent of the used LCR meter frequency [23], where 1 kHz is used.

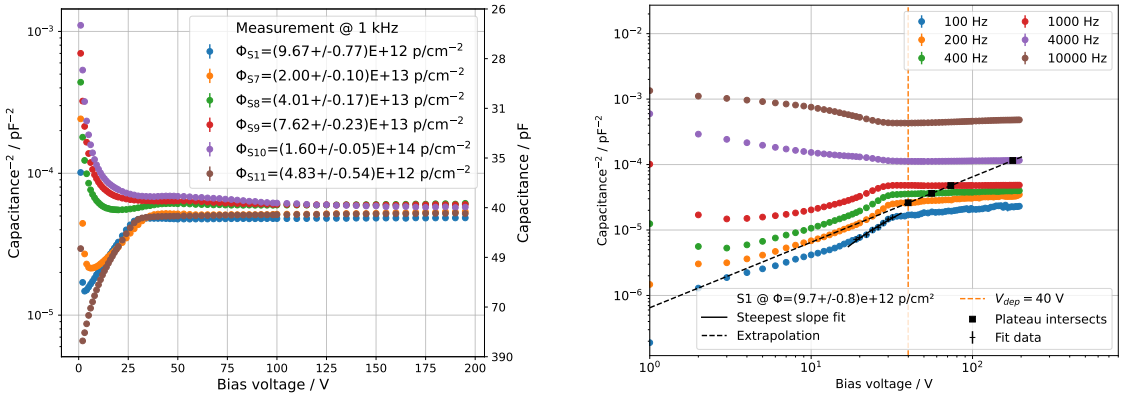

(a) CV curves for all sensors after irradiation, measured at 10 kHz

(b) CV curves for sensor S1 after irradiation, measured at multiple frequencies

Figure 6.19: CV characteristics of irradiated LF sensors for measurements at 1 kHz for all sensors (a) as well as a variety of frequencies for a single sensor (b) to demonstrate the determination of V_{dep} via [23]. Measurement uncertainties are too small to be visible. Systematic uncertainties are not accounted for in the stated depletion voltages and capacitance values.

After irradiation, the CV curves of all sensors are shown in Fig. 6.19. These measurements are also performed at a frequency of 1 kHz and show significant deviation from the expected trend. Due to the introduction of radiation-induced defects, such as charge carrier trapping (see Section 4.3.3), the resulting capacitance is strongly dependent on the measurement frequency and the extraction of the full-depletion voltage via two linear fits yields insufficient results.
An attempt to describe and model the CV behavior of silicon sensors after irradiation is made in [23]. In this paper, an alternative approach for determining the full-depletion voltage is given, which is shown in Fig. 6.19(b) as an example for sensor S1. For each sensor, several CV curves are measured at different frequencies and the steepest slope in the linear region of the $1/C^2$ data is extracted. Using this, a straight line through the origin is constructed whose first intersection with the plateau region of one of the CV curves yields a good estimate of V_{dep}. By following this procedure, the full-depletion voltage after irradiation is determined for each of the sensors.
The results of the CV characterization allow for a determination of the full-depletion voltage before and after irradiation. In combination with the IV curves, the leakage current increase for the fully depleted sensor volume can be obtained.

[3] The systematic uncertainty due to the double-slope increase and selection of which region to fit is not accounted for in the stated result. As the IV properties are evaluated at $V_{\text{dep}} + 50$ V, the contribution of the systematic error can be neglected here.

Results

Table 6.4 contains the important quantities for the hardness factor measurement, extracted from the electrical characterization of the LF sensors before and after irradiation. Utilizing the aforementioned approach to determine the full-depletion voltage after irradiation, the resulting V_{dep} values generally increase with fluence, although no distinction can be made for some adjacent fluence levels[4]. In general, an uncertainty of 10 % is assumed for this method. Finally, in order to ensure full depletion of the sensors, the IV curves are evaluated at $V_{\text{dep}} + 50\,\text{V}$. The uncertainties are estimated by evaluating the IV curves at the error margins of $V_{\text{dep}} + 50\,\text{V}$ and constructing the mean value of the upper and lower limits. These findings are used in the following Section 6.4.3 to determine the proton hardness factor at the BIC.

Sensor	Proton fluence / p/cm^2	Full depletion voltage V_{dep} / V	Sensor leakage current (scaled to 20 °C) at $V_{\text{dep}} + 50\,\text{V}$ / A
S11	0	38.8 ± 0.1	$(6.66 \pm 1.15) \times 10^{-9}$
	$(4.83 \pm 0.54) \times 10^{12}$	33 ± 3	$(1.90 \pm 0.22) \times 10^{-5}$
S1	0	29.9 ± 0.1	$(5.88 \pm 1.02) \times 10^{-9}$
	$(9.67 \pm 0.77) \times 10^{12}$	40 ± 4	$(4.10 \pm 0.51) \times 10^{-5}$
S7	0	29.8 ± 0.1	$(5.50 \pm 0.95) \times 10^{-9}$
	$(2.00 \pm 0.10) \times 10^{13}$	74 ± 7	$(9.70 \pm 1.15) \times 10^{-5}$
S8	0	30.8 ± 0.1	$(5.10 \pm 0.90) \times 10^{-9}$
	$(4.01 \pm 0.17) \times 10^{13}$	71 ± 7	$(1.67 \pm 0.22) \times 10^{-4}$
S9	0	30.9 ± 0.1	$(5.14 \pm 0.89) \times 10^{-9}$
	$(7.62 \pm 0.23) \times 10^{12}$	94 ± 9	$(3.51 \pm 0.66) \times 10^{-4}$
S10	0	31.2 ± 0.1	$(4.81 \pm 0.83) \times 10^{-9}$
	$(1.60 \pm 0.05) \times 10^{14}$	94 ± 9	$(6.68 \pm 0.96) \times 10^{-4}$

Table 6.4: Results of electrical characterization of LF sensors before and after irradiation. Leakage currents are scaled to 20 °C via Eq. (2.20) and evaluated at $V_{\text{dep}} + 50\,\text{V}$ to ensure full depletion.

6.4.3 Extraction of Hardness Factor

Using the results of the electrical characterization of the sensors, as presented in Table 6.4, the proton hardness factor can be extracted via Eqs. (4.8) and (4.9). The leakage currents before, I_0, and after, I_Φ, irradiation are evaluated at $V_{\text{dep}} + 50\,\text{V}$, ensuring full depletion of the sensors. Consequently, the depleted volume can be obtained from the sensor geometry as

$$V = n_{\text{col}} \cdot x_{\text{pitch}} \cdot n_{\text{row}} \cdot y_{\text{pitch}} \cdot d = 2.88 \times 10^{-2}\,\text{cm}^3\,,$$

[4] For sensor S9, the method produced an indistinct result, a factor of two larger than for the highest fluence sensor S10. After confirming via visual inspection of the data, it is estimated that this is due to large errors within the low frequency data sets. The full-depletion voltage of sensor S10 is subsequently also estimated for S9.

where $n_{\text{col/row}}$ is the number of columns/rows, x/y_{pitch} is the pixel pitch in the respective dimension and d is the sensor thickness. Here, the values from Section 6.4.1 are used. To account for variances in the fabrication process, an uncertainty of 10 µm on the sensor thickness is assumed. For each irradiation, $\Delta I = I_\Phi - I_0$ over V is plotted versus the proton fluence Φ_p, which is displayed in Fig. 6.20. Additionally, a linear fit according to Eq. (4.8) is performed, using an orthogonal distance regression

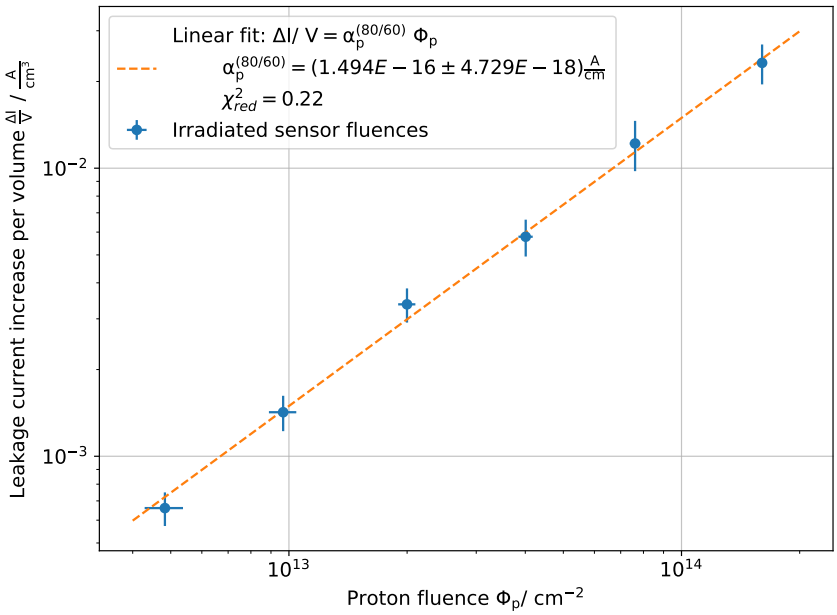

Figure 6.20: Determination of the current-related damage rate α_p of the protons at the BIC. Shown is the volume-normalized bulk leakage current versus the proton fluence for six sensor irradiations. The data follows the relation given in Eq. (4.8).

algorithm [88], to extract the current-related damage rate $\alpha_p^{80/60}$ for the protons after the corresponding annealing procedure. As visible, the data is in excellent agreement with the linear model with a reduced χ^2 of 0.22, indicating that the data follows the model more accurately than the uncertainties suggest. The resulting current-related damage rate, extracted from the fit, is

$$\alpha_p^{80/60} = (1.49 \pm 0.05) \times 10^{-16}\,\text{A}\,\text{cm}^{-1}\,.$$

This allows for a calculation of the proton hardness factor κ_p via Eq. (4.9). Using the reference value for 1 MeV neutrons, $\alpha_{\text{n}_{\text{eq}}}^{80/60} = (3.99 \pm 0.03) \times 10^{-17}\,\text{A}\,\text{cm}^{-1}$ [53], the proton hardness factor at the BIC is

$$\kappa_p = 3.75 \pm 0.12\,.$$

This result is in good agreement with the expectations for protons with a mean energy of (12.19 ± 0.04) MeV (see Table 6.3), for which a hardness factor of ≈ 3.65 can be extracted from Fig. 4.3. The relative uncertainty of κ_p of approximately 3 % in conjunction with the comparable relative uncertainty on the proton fluence measurement via beam-based dosimetry (see Section 6.2), result in an equivalent

fluence determination via Eq. (4.7) with a relative uncertainty of typically $\leq 5\,\%$. In comparison, the resulting proton hardness factor at the BIC provides the highest NIEL scaling with the lowest relative uncertainty among to the values reported for the irradiation facilities in [54].

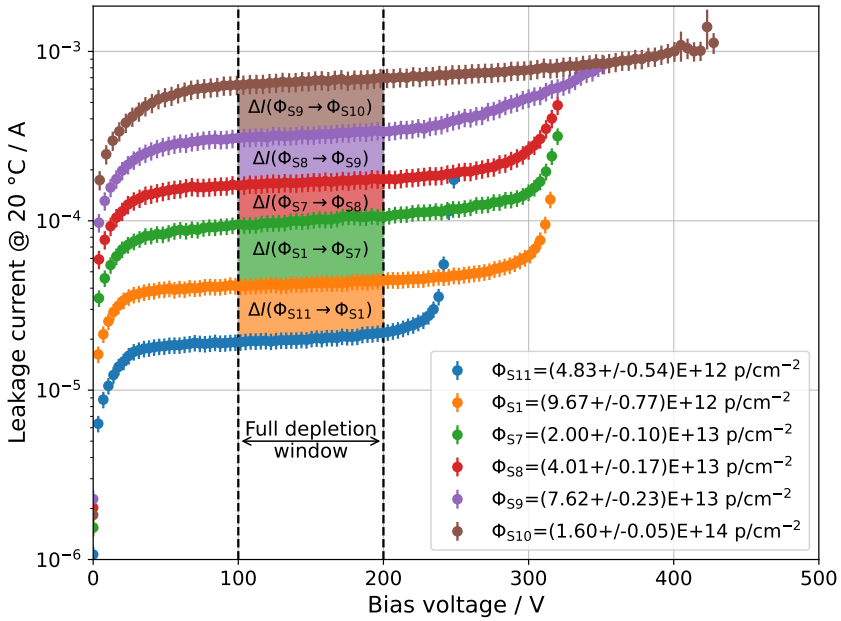

Figure 6.21: IV curves, scaled to 20 °C, of LF sensors post irradiation. Indicated is the leakage current within a 100 V bias window, for which full depletion is achieved for every sensor. Moreover, the leakage current difference ΔI between data sets for adjacent fluence levels is marked. The data is the same as shown in Fig. 6.17(b).

An additional approach to obtain the proton hardness factor from the data gathered during the electrical characterization in Section 6.4.2 is made to validate the previously determined value of $\kappa_p = 3.75 \pm 0.12$. This process aims to minimize the dependence of the result on the selected bias voltage, above full depletion, at which the IV characteristics are evaluated and to maximize the use of information contained in the measurements. The former is relevant because the leakage current above V_{dep} is theoretically constant, as the contributing volume does not change with increasing voltage. In reality, a slow but steady increase of the leakage current above V_{dep} is observed in many cases, as in Fig. 6.17(b), for which a possible explanation is the sensor self-heating with increasing power dissipation [22]. This is realized by evaluation of the IV data within a bias window, as opposed to a single voltage, in which full depletion is achieved for all fluences. Looking at Table 6.4, this is the case for all sensors above 100 V. Simultaneously considering Fig. 6.17, none of the sensors exhibit a breakdown (behavior) below 200 V. Therefore, all data within a window of 100 – 200 V is selected, as indicated in Fig. 6.21. The mean leakage current increase in Eq. (4.8) for two different proton fluences Φ_a and Φ_b can be defined as the mean value of all absolute differences in the given bias window:

$$\langle \Delta I \rangle_{\text{a,b}} = \frac{1}{N} \sum_{V_i = 100\,\text{V}}^{200\,\text{V}} \left| I_{\Phi_\text{a}}(V_i) - I_{\Phi_\text{b}}(V_i) \right| .$$

Here, N is the number of bias voltages for which current measurements are performed and I_{Φ_a} and I_{Φ_b} the corresponding leakage currents. The uncertainty is calculated as the resulting uncertainty on the mean value in conjunction with the standard deviation of all differences in the sum (see Eq. (A.2)).

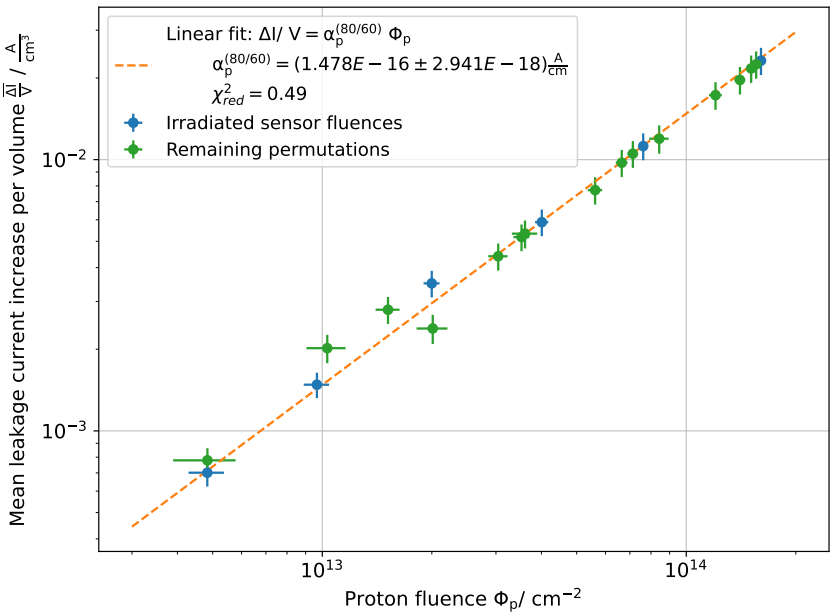

Figure 6.22: Additional determination of the current-related damage rate α_p of the protons at the BIC. Shown is the mean, volume-normalized bulk leakage current versus the proton fluence for all permutations of the IV data from six sensors. The data follows the relation given in Eq. (4.8).

Furthermore, to fully process the information contained in the measurements, apart from the applied proton fluences, Eq. (4.8) is also determined for all remaining permutations of fluence differences between the data sets as

$$\frac{\langle \Delta I \rangle_{\mathrm{a,b}}}{V} = \alpha \cdot \left| \Phi_{\mathrm{a}} - \Phi_{\mathrm{b}} \right| .$$

Disregarding the combinations with the unirradiated data sets, an additional 15 permutations remain to be entered into the fit to contribute to the result. The difference in leakage current between data sets of adjacent fluence levels is indicated in Fig. 6.21. Applying these steps leads to a volume-normalized mean leakage current increase $\langle \Delta I \rangle / V$ in dependence of all possible permutations of the proton fluence, as depicted in Fig. 6.22. As shown in Fig. 6.20, the data points follow the anticipated linear trend. A fit according to Eq. (4.8) is performed and the current-related damage rate extracted. With this result and analogously to the previous findings, the proton hardness factor is determined via Eq. (4.9) and the reference value $\alpha_{\mathrm{n_{eq}}}^{80/60} = (3.99 \pm 0.03) \times 10^{-17}\,\mathrm{A\,cm^{-1}}$ [53]. The obtained values are

$$\alpha_p^{80/60} = (1.48 \pm 0.03) \times 10^{-16}\,\mathrm{A\,cm^{-1}} \quad \Rightarrow \quad \kappa_p = 3.70 \pm 0.08\,.$$

This is in good agreement with the previously determined value of 3.75 ± 0.12 with a comparable reduced χ^2 of 0.49, indicating a good description of the data by the model. Consequently, this indicates the reliability of the standard measurement procedure where the IV data is evaluated at a single bias voltage above full depletion and show that the steady leakage current increase after reaching full depletion does not affect the result within the uncertainties.
The determined hardness factor is valid within the error margins for the typical operation of the irradiation site with a proton beam of initially 13.6 MeV and thin DUTs. A more detailed examination of the proton energy corresponding to the measured hardness factor and the limitations of accurate NIEL scaling via Eq. (4.7) at the BIC are discussed in the following Section 6.4.4.

6.4.4 NIEL Scaling Limitations at the BIC

The determination of the 1 MeV neutron equivalent fluence $\Phi_{n_{eq}}$ via Eq. (4.7) considers the proton hardness factor κ_p to be a constant irrespective of the penetration depth into the DUT. This is the case if the energy loss on transmission through the device does not result in a (measurable) change in the hardness factor, i.e. translates to a constant damage profile with depth. For high-energy ions ($E_{\text{kin}} \geq 1$ GeV), this is mostly the case, as the energy loss is negligible and no change in hardness factor is observed. In some cases, this allows for stacking of two or more devices along the beam axis (see e.g. [11]).
Considering Fig. 4.3, the damage function for low-energy protons starts to strongly depend on the energy below $\approx$ 10 MeV. As an example, a hardness factor of $\kappa_p = 2.49$ can be determined for 27 MeV protons. After a DUT of 300 µm thickness, these protons have approximately 26 MeV (using National Institute of Standards and Technology (NIST) *PSTAR* [19]), for which a hardness factor of 2.56 is shown in Fig. 4.3. This difference is negligible compared to the uncertainty on the hardness factor measurement, which is currently in the order of 20 % for facilities in this energy range [54].
In contrast, the low uncertainty on the hardness factor in combination with the low proton energy at the BIC allow for circumstances in which the energy loss in the DUT is not negligible. For instance, a hardness factor of $\kappa_p = 3.65$ for 12.3 MeV protons can be obtained from Fig. 4.3. Using Fig. 6.4, an energy decrease to 10.1 MeV is observed after passage of a typical 300 µm silicon DUT for which a hardness factor of $\kappa_p = 3.95$ can be extracted from Fig. 4.3. This corresponds to an increase of approximately 10 %. Given the relative uncertainty on the proton hardness factor of approximately 3 % determined in Section 6.4.3, for these energies the hardness factor increase due to energy loss in the silicon is substantially larger than its error margin.
To showcase these limitations, an additional proton hardness factor measurement is discussed in the following. In this case, commercial silicon *PiN* diodes of type *BPW34F* are irradiated at the BIC with 13.6 MeV protons to five different fluences. These particular diodes are characterized and tested in [95] for their suitability to monitor high-level 1 MeV neutron equivalent fluences. Subsequently, they are used in a multitude of works for the purpose of fluence monitoring [96, 97] and hardness factor measurements of various irradiation facilities [54]. The diodes feature a sensitive area of 2.65 mm × 2.65 mm [98] with an active thickness of 300 µm [95]. Additionally, they are contained inside a packaging, that serves as an optical filter, resulting in a 500 µm-thick layer of epoxy in front of the silicon.
A total of 15 diodes, resulting in three devices per fluence, are irradiated and annealed for 80 min at

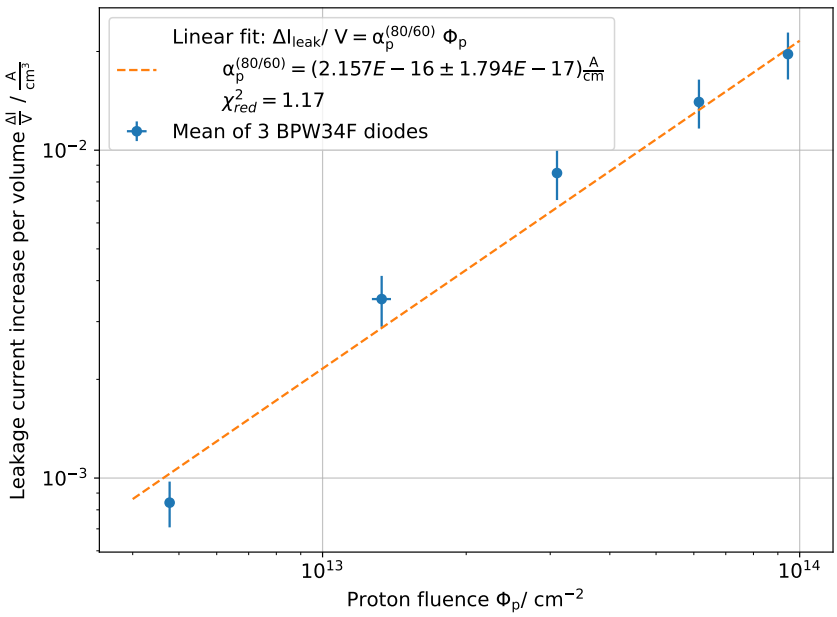

Figure 6.23: Current-related damage rate for protons at the BIC, extracted via irradiation of commercial *BPW34F* diodes. The additional 500 µm epoxy packaging in front of the 300 µm thick silicon causes an increase in α_p as compared to Fig. 6.20. Nevertheless, the data follows the relation given in Eq. (4.8).

60 °C. Their IV characteristics are recorded, in analogy to the process described in Section 6.4.2.[5]. The resulting leakage current increase per volume versus the applied proton fluence, as per Eq. (4.8), is shown in Fig. 6.23. In general, the data follows the linear trend as expected. The extracted current-related damage rate and proton hardness factor are

$$\alpha_p^{80/60} = (2.16 \pm 0.18) \times 10^{-16}\,\mathrm{A\,cm^{-1}} \quad \Rightarrow \quad \kappa_p = 5.41 \pm 0.45\,.$$

This is significantly larger than the expectation from Fig. 4.3 for the corresponding energy of ≈ 12.3 MeV on the DUT. This is caused by the additional 500 µm of epoxy material in front of the silicon. Considering polyethylene, data available in *PSTAR* [19] yields an additional energy loss of approximately 2 MeV inside the epoxy, yielding ≈ 10.3 MeV on the silicon where another 2.4 MeV is lost on transmission. This leaves the protons with an energy of ≈ 8 MeV, allowing for the estimation of a hardness factor of $\kappa_p = 5$ from Fig. 4.3.
This result emphasizes that such devices are not suitable for determination of the proton hardness factor at the BIC as the additional energy loss inside the packaging significantly increases the NIEL damage between entering and exiting the device. To avoid this issue, 150 µm thin sensors are selected for the hardness factor measurement (see Section 6.4.1), where the expected increase of κ_p due to the energy loss inside the silicon is in the same order of magnitude as the measurement uncertainty.
Subsequently, the proton energy, corresponding to the hardness factor measured in Section 6.4.3, is

[5] The full-depletion voltage is estimated from the characteristic plateau region after full depletion in the IV curves.

calculated as the mean value before and after the DUT from Fig. 6.4:

$$\kappa_p\,[(11.75 \pm 0.08)\,\text{MeV}] = 3.75 \pm 0.12\,,$$

which is valid for DUTs with a thickness of $d_{\text{DUT}} \leq 150\,\mu\text{m}$ within the uncertainties. For larger DUT thicknesses, the hardness factor is expected to increase by up to 10 % from Fig. 4.3 for $d_{\text{DUT}} \leq 300\,\mu\text{m}$. To prevent underestimation of the damage, a proton hardness factor of

$$\kappa_p = 4.0 \pm 0.4\,, \quad \text{if } 150\,\mu\text{m} < d_{\text{DUT}} \leq 300\,\mu\text{m}$$

is assumed with an increased uncertainty that reflects the anticipated growth in the hardness factor with penetration depth. For devices $\gg 300\,\mu\text{m}$ thickness, the increase of the damage with penetration depth is considered to be significant. In this case, the conversion of the primary fluence to the NIEL fluence via Eq. (4.7) does not yield meaningful results as the hardness factor is not constant over the device.
In conclusion, the irradiation site at the Bonn Isochronous Cyclotron is suitable for thin silicon DUTs with a maximum active thickness in the order of 300 µm.

6.5 Comparison of Facilities

To give an overview and a comparison of the available proton irradiation facilities, their characteristics are briefly given and their 1 MeV neutron equivalent scaling is compared. The measurements of their proton hardness factors are the main subject of [54], from which the majority of information is taken. In this paper, the irradiation facilities at the MC40 Cyclotron in Birmingham [12], operating at 24 MeV, the cyclotron of the *Zyklotron AG* at KIT [13], using 23 MeV protons, and the PS IRRAD facility [11], running with 23 GeV, are covered, where the proton energies are given on the DUT. Selected parameters are listed in Table 6.5 with typical values stated where feasible. Further information on the facilities is taken from [90, 99].

Facility	Bonn	CERN	KIT	Birmingham
Energy at DUT	12.3 MeV	23 GeV	23 MeV	24 MeV
Hardness factor κ_p	3.75 ± 0.12	0.62 ± 0.04	2.20 ± 0.43	2.11 ± 0.49
TID per 10^{16} n_{eq}/cm^2	1.2 Grad	500 Mrad	1.3 Grad	1.3 Grad
Typical intensity	20 – 1 000 nA	10^{14} protons/h	0.1 – 20 µA	100 – 500 nA
Available area / cm^2	18×11	20×20	44×17	15×15
Beam spot / mm^2	$\leq 10 \times 10$	5×5 to 20×20	$\leq 8 \times 8$	10×10
Temperatures	$\leq -20\,^\circ$C	$-25\,^\circ$C	$-30\,^\circ$C	$\leq -25\,^\circ$C

Table 6.5: Comparison of characteristic properties for various proton irradiation facilities. The TID per 10^{16} n_{eq}/cm^2 is calculated with Eq. (5.19) using stopping powers from [19]. Entries for proton hardness factors and energies other than for Bonn are taken from [54]. Further information is acquired from [90, 99].

When comparing the parameters of the irradiation facilities, the (site at the) BIC provides protons

with the highest NIEL damage, allowing for delivery of approximately twice the equivalent fluence per time with regard to the sites at KIT and Birmingham where equivalent irradiation procedures (i.e. as in Section 5.4) are used. Approximately six times the equivalent fluence per time can be delivered compared to the site at CERN. Regarding the TID damage per fluence, the sites at KIT and Birmingham both apply approximately 1.2 Grad per 10^{16} n_{eq}/cm^2 (using Eq. (5.19)) whereas the PS IRRAD at CERN yields ≅ 500 Mrad for the same fluence. The irradition facilities in Bonn, Birmingham and KIT are operated with a continuous proton beam whereas the CERN site uses spills of 5×10^{11} proton/spill over 400 ms [11]. All sites offer the possibility to scan devices through the beam using a scan motorstage system, resulting in a uniform fluence application on the sample. Compared to the other facilities, the setup in Bonn houses smaller devices of up to typically (60×60) mm^2 with the possibility to extend the area to the full entrance window size of the cool box (see Section 5.2.2). The setup has the smallest volume and load capacity of all sites. The facilities altogether feature a cooling system, allowing for irradiation at temperatures $\leq -20\,^{\circ}C$ to prevent annealing, whereas at CERN a cryogenic setup is also available [11].

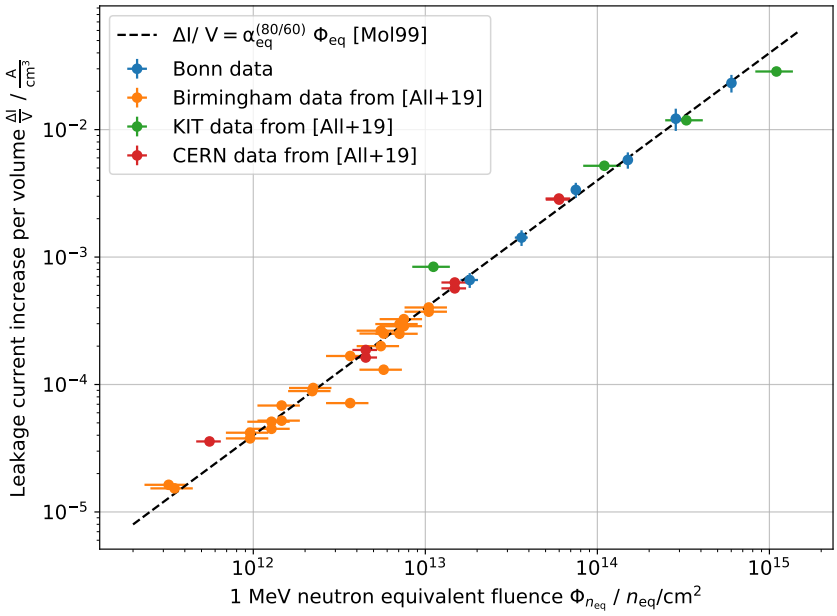

Figure 6.24: Comparison between leakage current increase per volume versus 1 MeV neutron equivalent fluence, according to Eq. (4.8), for the irradiation facilities in Birmingham, at CERN, at KIT and in Bonn. The entries for Bonn correspond to the results from Section 6.4.3. Measurements for the other sites are taken from [54].

In order to validate that the NIEL scaling of the proton fluence via Eq. (4.7), using the proton hardness factors in Table 6.5, yields comparable results, the data sets obtained in [54] are used. In this case, the leakage current increase measurements after proton irradiation of *BPW34F* [98] diodes are taken and normalized to the devices' full-depletion volume (compare Section 6.4.4). Moreover, the corresponding proton fluence is converted to the 1 MeV neutron equivalent fluence via Eq. (4.7) with the respective hardness factor. Accordingly, this is performed for the data of the hardness factor measurement obtained in Bonn (see Section 6.4). The resulting leakage current

increases per depleted volume are plotted versus the equivalent fluence $\Phi_{n_{eq}}$ altogether[6], shown in Fig. 6.24. Additionally, the literature scaling according to Eq. (4.8) with the current-related damage rate $\alpha^{80/60}_{n_{eq}} = (3.99 \pm 0.03) \times 10^{-17}\,\mathrm{A\,cm^{-1}}$ [53] is displayed. As visible, the data of all irradiation facilities follows the anticipated linear trend over an equivalent fluence range of over three orders of magnitude, from 3×10^{12} to 1×10^{15} n_{eq}/cm^2. The majority of measurements are in agreement with the literature reference within their uncertainties, except for a few outliers. In particular, the data from Bonn, which is the same as in Fig. 6.20, is in very good agreement with the expected literature value, showing no outliers within the uncertainties.
Within the precision of the measurements presented in [54] and in this work, the overall agreement of the data points with the reference line validates the NIEL scaling between the four irradiation facilities. This confirms that independently of the particular parameters such as beam current, proton energy or irradiation procedure, the damage can be normalized to the corresponding NIEL damage via the hardness factor over three orders of magnitude of fluence. This result is generally expected and is crucial for the operation of irradiation sites and subsequently for radiation damage studies of silicon detectors.

[6] The original uncertainties on the measurements from [54] are not transferred individually, instead a relative error of 15 % on the proton fluence and 10 % on the leakage current measurement are assumed, which approximately corresponds to the reported uncertainties. Furthermore, the uncertainty on the hardness factors is considered.

CHAPTER 7

Radiation Damage Tests of the ATLAS ITk Pixel Detector

The irradiation infrastructure, introduced and characterized in Chapters 5 and 6, is utilized to perform radiation hardness tests of an `ITkPix` pixel detector assembly, designed for ATLAS ITk upgrade. The goal of the studies presented in this chapter is to demonstrate the capabilities of the irradiation site at the BIC and compare the effects (see Section 4.3) of NIEL as well TID damage to reference works [26, 35]. Ultimately, the aim is to verify the radiation hardness of the readout chip and corresponding sensor up to the EOL damage levels anticipated for the HL-LHC operation.
Therefore, a brief description of the Device Under Test and its relevant characteristics before the irradiation tests is given first, in Section 7.1. Section 7.2 contains an overview of the performed irradiations, split into two campaigns to investigate TID and NIEL degradation separately. The resulting damage characteristics of the readout chip and sensor are investigated and compared. To probe the intended functionality of the detector after irradiation, a test beam study was performed at DESY, which is presented in Section 7.3. Finally, the findings are compared to existing studies of the TID response of the readout chip as well as the deterioration due to NIEL damage of the sensor.

7.1 Device Under Test

In this chapter, the radiation tolerance of an `ITkPix` pixel detector assembly is tested for the requirements of the ATLAS ITk. The assembly is composed of an `ITkPixV1.1` readout chip to which a 3D-silicon sensor (cf. Section 2.2.3) is bump-bonded. The specifications of readout chip are given in Section 3.3.
The sensor is fabricated by *SINTEF* for use in the innermost layers of the ITk and characterized with respect to its radiation performance in [26]. It features a pixel pitch of $(50 \times 50)\,\mu m^2$ and an active thickness of 150 µm. After exposure to $10^{16}\,n_{eq}/cm^2$ of NIEL fluence, the sensor is tested to reach hit detection efficiencies of $\geq 97\,\%$ while remaining within the operating specifications of the ATLAS ITk.
A photograph of the Single-Chip Card (SCC), hosting the `ITkPix` assembly, is shown in Fig. 7.1. For the purpose of identification, the chip is given a unique chip identifier, or *chip ID*, which is typically reported in results for the sake of completeness. The assembly used here has the chip ID 0x17172.

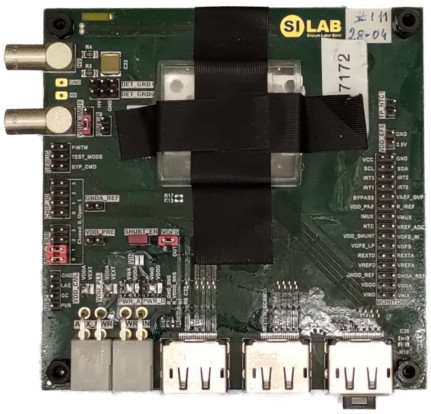

Figure 7.1: ITkPix assembly 0x17172 on SCC. The detector is seated centrally, in the upper half of the PCB (also compare Fig. 3.6), protected using a plastic lid. To prevent accidental illumination of the sensor, the lid is covered in black tape. The BDAQ53 system interfaces the readout chip via one of the DisplayPort connectors.

7.1.1 Data Acquisition System

The BDAQ53 DAQ system, as introduced in Section 3.3.1, is used to configure and readout the ITkPix assembly in the studies presented in this chapter. The minimal hardware setup, displayed in Fig. 3.7, is ideal for deployment at the BIC irradiation site and DESY test beam facility due to its compact size and minimal hardware configuration.
As described in Section 3.3.1, BDAQ53 provides the functionality to tune the chip to operate at a specified threshold, test the digital/analog pixel components (cf. Fig. 2.9) and read out on-chip/SCC temperature sensors. If not stated otherwise, the detector is configured, read out and the obtained data is visualized utilizing the predefined routines contained in the BDAQ53 framework.

7.1.2 Pre-Irradiation Characteristics

To quantitatively evaluate the radiation-induced degradation of the readout chip and sensor performance, as discussed in Section 4.1.1 and Section 4.3, respectively, the initial characteristics of either detector component have to be recorded. For measuring the effect of surface damage on the readout chip logic, the dedicated TID monitoring circuitry, consisting of a series of so-called *Ring Oscillators (ROs)*, requires calibration. For determination of the displacement damage, the sensors IV behavior (cf. Section 2.2.2) is recorded.

Ring Oscillators

All RD53-type chips contain a set of ROs for monitoring the TID effect on the logic cells, located in the digital chip bottom [100]. The ROs consist of different logic cell drivers, such as gates (NAND/NOR), inverters (INV) or clocks (CLK), which oscillate at a given frequency ν_{RO} that depends on the digital supply voltage V_{DDD} as well as temperature. When exposed to ionizing radiation, the ring oscillator frequency decreases as a result of damage-induced defects in the oxide layers, translating to an decrease in transistor switching speed, also termed *effective gate delay*. For a constant V_{DDD} and temperature, the effective gate delay is approximately linear with TID, enabling to express the dose as a function of ν_{RO} after calibration via, for example, an X-ray tube with known dose rate. It shall be noted, that the effective gate delay has been shown to depend strongly on the dose rate for the CMOS process

used in the ITkPix, in particular in the low dose-rate regime below 100 krad/h, whereas for dose rates exceeding 4 Mrad/h the dependence begins to saturate [35]. This complicates the calibration process and measurements should be conducted at the same dose rate for comparison where possible.
As an increase in effective gate delay also impairs the functionality of the digital logic, it allows for the definition of a limit up to which the logic remains operational. Here, simulations in [101] indicate that an effective gate delay of 200 % for the RD53 family of chips still maintains correct digital timing, therefore chosen as the upper limit for ensuring the chip functionality.
Furthermore, to differentiate the effective gate delay for different feature sizes, the ROs logic cells are fabricated in two different gate sizes, labeled 0 and 4, corresponding to the physical gate dimension. They are also referred to as gate *strengths*, i.e. str. 0/4, where str.-4 gates most closely resemble the chip's logic cells [35].
The ROs are located in so-called *banks*, i.e. arrangements of multiple ROs grouped together, in the chip bottom with two banks (*bank A* and *bank B*) present in RD53B and later chips. Bank A contains eight different RO types and is found across all RD53 readout chips. Thus, only bank A ROs are considered within the scope of this work, facilitating comparison between all chip iterations.

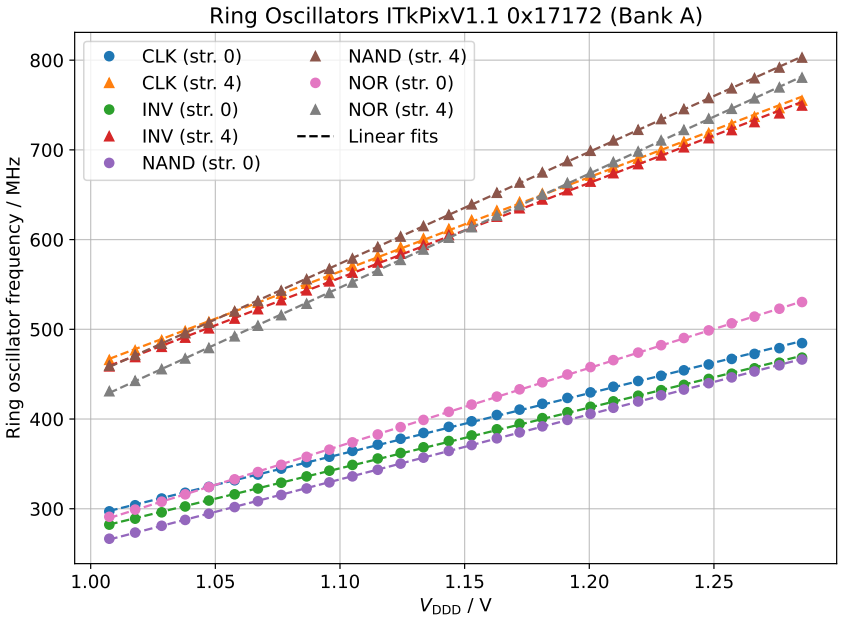

Figure 7.2: RO frequency ν_{RO} versus digital supply voltage V_{DDD} for all bank A ROs of the ITkPix at room temperature. Linear relations are fitted to each data set, showing very good agreement.

The frequency ν_{RO} depends strongly and linearly on the digital supply voltage, with variations of up to $\approx 100\,\%$ over the typical region of operation [35]. In contrast, the change with temperature is $\leq 10\,\%$ over approximately the whole specified operational range. To enable quantitative analysis of the data, the variation due to these parameters must be considered. Due to strong dependency on V_{DDD}, the sigificantly lower influence of temperature and the fact, that measurements are mostly performed at similar temperatures, only a V_{DDD} calibration of the ring oscillator frequency is performed[1]. This

[1] As the dependence on temperature is neglected, it is accounted for in the uncertainty discussion instead, where applicable.

allows for compensation of variations in V_{DDD} over the course of the irradiation studies and is shown for all eight ROs of bank A of the `ITkPix` chip in Fig. 7.2. For each RO a linear relation is fitted to the data, showing a good agreement, and is used in the following for correction of V_{DDD} changes during RO measurements.

Sensor IV

The electrical characteristics of the used *SINTEF* and similar 3D sensors, fabricated by other foundries for the ITk upgrade, are treated in [26]. Here, a hit detection efficiency of up to 97 % is reported after a NIEL fluence of $10^{16}\,\mathrm{n_{eq}/cm^2}$, highlighting the performance improvement of the 3D design over planar sensors (see Sections 2.2.3 and 4.3.3). This comes at the expense of an increase of detector noise due to a higher pixel capacitance as well as leakage current (see Section 2.2.2), resulting in higher minimum thresholds, all compared to the planar design.
Before irradiation, these sensors are fully depleted at approximately $V_{\mathrm{dep}} \leq 10\,\mathrm{V}$. A higher operational voltage V_{op} of $V_{\mathrm{op}} = V_{\mathrm{dep}} + 20\,\mathrm{V}$ is targeted to ensure operation at full depletion for which a leakage current limit of $2.5\,\mu\mathrm{m\,cm^{-2}}$ is imposed [26]. The sensors leakage current characteristic before irradiation is shown in Fig. 7.3. The leakage is measured at room temperature for bias voltages up to V_{op} using a SMU. As the reference temperature for operation of the ITk is −25 °C [9], the current is scaled accordingly via Eq. (2.20) an normalized to the detector area. As visible, the sensor leakage stays well below the anticipated limit up to the target of $V_{\mathrm{op}} = 30\,\mathrm{V}$, fulfilling the requirement.

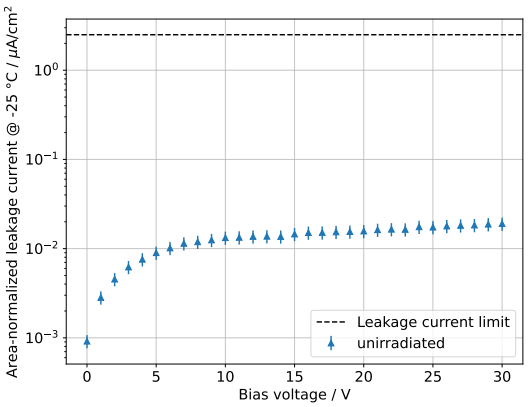

Figure 7.3: IV behavior, scaled to −25 °C, of *SINTEF* 3D sensor before irradiation. The leakage current is measured five times per bias voltage. The corresponding mean is the stated value, the standard deviation is displayed as the uncertainty.

Chip Tuning

The chip requires configuration to ensure a uniform detector response across the entire pixel matrix at a given operational threshold. In this work, this is achieved by a pipeline of routines or *scans*, included in the BDAQ53 framework, that adjust local (in-pixel) and global threshold settings using of a dedicated injection circuitry.
The threshold is defined as the signal charge for which 50 % occupancy of the matrix is measured. The chip's internal circuitry discharges a known capacitance via an adjustable injection voltage called ΔV_{CAL}, to generate a charge at the input of the analog pixel. The translation of ΔV_{CAL} to the generated charge in electrons can be obtained by a calibration using e.g. X-ray sources, which yields a value of approximately $5\,e^{-}/\Delta V_{\mathrm{cal}}$ [102] for the `ITkPixV1` in the range of operational parameters. This allows for the conversion of the injection voltage into charge in units of electrons, enabling one to relate the

threshold level to a known signal charge of, for example, a MIPs.
In the following, the individual scans required to bring the chip to an operational state are briefly explained. The list of adjustments constitute a so-called *threshold tuning*:

Global Threshold Scan The global threshold is set and a charge injection sweep is started. The pixel response of the matrix is registered.

Local Threshold Scan Each pixel has a local threshold setting, facilitating the correction of e.g. fabrication-related differences in response. The charge injection is swept around the target threshold and the local setting is adjusted to minimize the deviation.

Noisy/Stuck-Pixel Scan Identification of pixels that either have increased hit registration rates compared to their surroundings (noisy) or always/never register a hit (stuck), independent of the threshold setting. These pixels are masked and excluded from further measurements.

The reference threshold tuning is performed to a target of $300\,\Delta V_{\mathrm{CAL}}$, corresponding to approximately $1.4\,\mathrm{k}e^-$, within the scope of this study. During the tuning routine, the sensor is supplied with bias voltage to achieve depletion and reduce noise. The resulting threshold distribution of all pixels is shown Fig. 7.4. It follows a normal distribution with the mean at the target value of $300\,\Delta V_{\mathrm{CAL}}$ and the standard deviation corresponding to the *threshold dispersion* of approximately $6\,\Delta V_{\mathrm{CAL}}$. In the following, this tuning serves as a reference for the unirradiated state.
In this work, the procedure is repeated in between measurements to account for changes due to radiation-induced damage. The target threshold for all measurements is between 1 000 and $2\,000\,\mathrm{k}e^-$, corresponding to the anticipated range for operation of the ATLAS ITk [9].

7.2 Irradiation Campaign

A proton irradiation campaign was conducted at the BIC site between September and October of 2023. The goal is the simultaneous application and distinct characterization of NIEL damage to the sensor as well as the TID damage to the chip logic, using 14 MeV protons.
The surface damage to the 65 nm CMOS transistor technology used in the `ITkPix` design, has a strong dose-rate dependence which is the topic of [101]. To establish a baseline for comparison of the degradation of the chip's digital logic with TID from X-ray and proton irradiations, the studies are separated into two parts: a low- and a high-dose-rate irradiation campaign. In the former, the resulting dose rate is in the order of a few Mrad/h, similar to high-intensity X-ray studies [103], allowing for a more appropriate comparison of the effects between proton and X-ray irradiation. During the low dose-rate campaign, a few Mrad and negligible NIEL damage are applied to the `ITkPix` assembly.
In the high dose-rate campaign, the anticipated EOL damage levels for the operation of the innermost ITk layer of approximately $10^{16}\,\mathrm{n_{eq}/cm^2}$ and 1 Grad [9] are applied to the detector.

7.2.1 Setup

The irradiation setup, used throughout all campaigns, is shown in Fig. 7.5. The SCC is mounted inside the cool box, behind a dedicated shielding, using the rail system (see Section 5.2.3). Two SMUs are connected to the SCC, providing bias voltage to the sensor and reading a multiplexer output, allowing one to obtain the digital and analog supply voltages. The chip is powered in Shunt-LDO (SLDO) mode

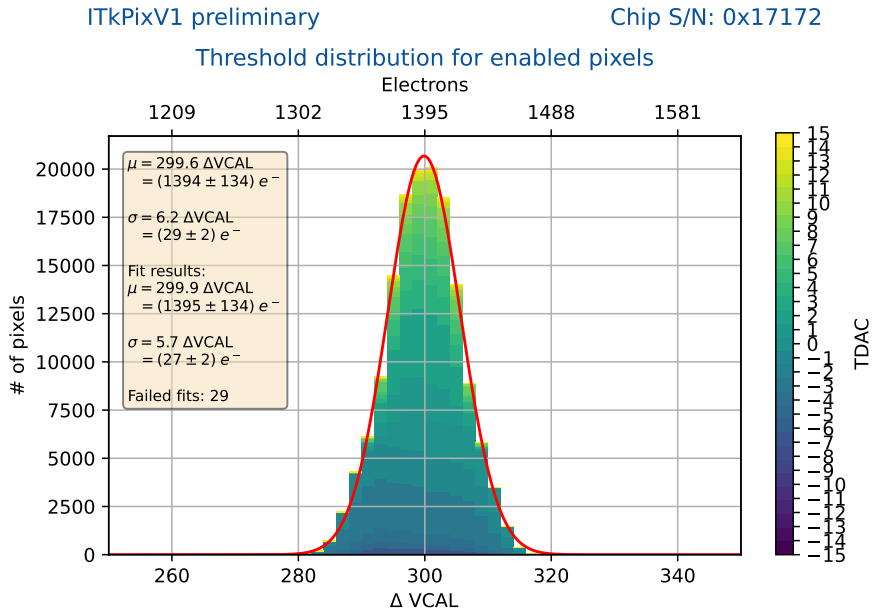

Figure 7.4: Threshold distribution before irradiation after performing tuning a routine with BDAQ53 to 300 ΔV_{CAL} (DAC units), or approximately 1.4 ke^{-}. The color coding corresponds to the 5-bit values of the local (in-pixel) threshold setting.

with the supply voltages $V_{\mathrm{DDD/A}}$ set to 1.2 V and connected to the BDAQ53 board via a DisplayPort cable. In addition to the on-board thermistors, an NTC is mounted on the top side of the single-chip card and read out using `irrad_control`.
During irradiations, the SMUs, power supply, DAQ hardware and computer are located directly outside the *high-current room* (cf. Figs. 5.3 and A.4), connecting to the setup via approximately 8 m long cables.

7.2.2 Irradiations

This section gives an overview of the two dedicated parts of the irradiation campaign. As the severity of the TID damage to the transistors is a function of the applied gate voltage [50], the chip is powered throughout each individual irradiation step, supplying the ROs logic chain with bias at all times. After each irradiation step, the IV characteristic of the *SINTEF* sensor is measured while the DUT resides in the cooled irradiation setup. Additionally, the chip is re-tuned to a threshold of 300 ΔV_{CAL}, as detailed in Section 7.1.2, and the threshold drift versus the pre-irradiation state is recorded.

Low-Dose-(Rate) Campaign

The low-dose-rate irradiation was conducted on September 29, 2023. The goal is to resemble the irradiation conditions, such as dose and dose rate of typical TID damage tests using X-ray setups, enabling a more quantitative comparison of results. Therefore, where possible, the parameters of the

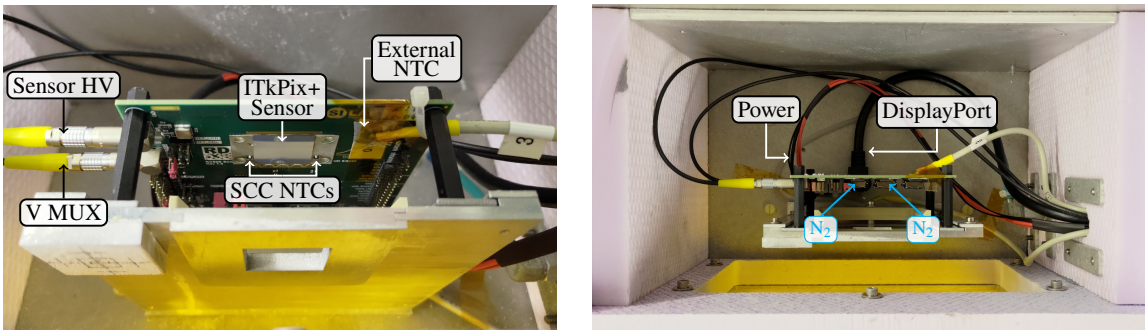

(a) DUT front view

(b) DUT top view

Figure 7.5: The `ITkPix` SCC, mounted behind a dedicated shield, inside the cool box of the irradiation setup. The power, HV and readout-related cables, as well as the DisplayPort interface that connects the DUT to the BDAQ53 system are routed into the setup via a feed-through. The on-SCC NTC thermistors as well as the chip itself are located directly in a stream of cool N_2 gas.

proton irradiation campaign are selected according to [103], in which the typical quantities for X-ray studies of `RD53B` chips are described.

Beam current / nA	Damage per scan		Resulting damage	
	TID / Mrad	NIEL / n_{eq}/cm^2	TID / Mrad	NIEL / n_{eq}/cm^2
15 – 20	0.105	8.25×10^{11}	6.29 ± 0.23	$(4.89 \pm 0.16) \times 10^{13}$

Table 7.1: Parameters and results of the low-dose irradiation campaign of the `ITkPixV1.1` assembly. The irradiation site was operated at the lower limit of possible proton beam currents.

An overview of the campaign's characteristics is given in Table 7.1, the irradiation overview, as generated by `irrad_control`, is shown in Fig. 7.6. Operating at the low end of possible currents at the BIC, the DUT is irradiated with proton beam currents between 15 and 20 nA and an energy of 13.50 MeV, corresponding to 12.17 MeV on the assembly. As shown in Fig. 7.6, the irradiation is partitioned into 60 *complete scans* (cf. Section 5.4.2), each applying an average of 105 krad to the chip. After completion of a scan, the irradiation procedure is halted, the beam extraction stopped and the relevant parameters, such as RO frequencies, V_{DDD} and temperatures, are read out. This is in accordance with [103], stating an RO frequency read at least every 0.1 Mrad. To obtain statistical information, the RO frequencies as well as all other data is read out ten times per irradiation step. With the average scan duration being 85 s, the dose rate normalized per complete scan is approximately 4.4 Mrad/h[2] which is comparable to typical dose of rates of 1 – 5 Mrad/h for X-ray studies [103]. After completion of the irradiation campaign within approximately 3.5 h, a TID of (6.29 ± 0.23) Mrad as well as a NIEL fluence of $(4.89 \pm 0.16) \times 10^{13}$ n_{eq}/cm^2 is applied and the assembly is annealed at room temperature (see Section 7.2.3).

[2] Still the instantaneous dose rate on the area of the RO banks is orders of magnitude higher, as in the used routine the damage is applied on a per-scan basis as opposed to a continuous dose rate.

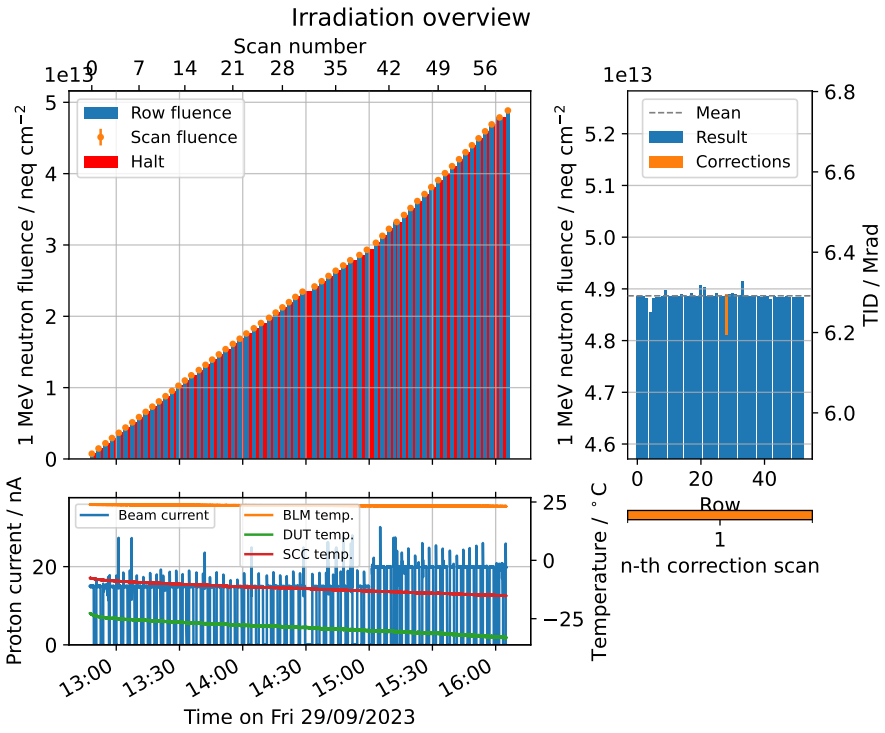

Figure 7.6: Overview of damage applied in the low-dose campaign, resolved in scans and rows of the irradiation pattern, as well as beam currents and temperatures. The frequent routine halts and corresponding stops of beam current extraction between increasing damage levels indicate the dedicated measurement pauses. For further explanation see Sections 5.4.2 and 5.6.

High-Dose-(Rate) Campaign

From October 17 – 20, 2023, the high-dose irradiation campaign was performed. The irradiation site is operated at its nominal parameters (see Section 5.4) with the aim of simultaneous application of the approximate surface and displacement EOL damage to the `ITkPix` DUT. The target equivalent fluence and dose of 10^{16} n_{eq}/cm^2 and 1 Grad, respectively [9], are applied over ten irradiation steps and four days. In each step, a fluence of 10^{15} n_{eq}/cm^2 and a dose of 128 Mrad are delivered over approximately 34 complete scans of the device. After completing a step, the relevant parameters, such as RO frequencies, V_{DDD} and temperatures, are read out ten times in succession to obtain information on the statistical fluctuation. The irradiation-relevant properties are shown in Table 7.2, a listing of the parameters of each individual irradiation step is given in Table A.3 in the appendix.

Beam current / nA	Damage per scan		Resulting damage	
	TID / Mrad	NIEL / n_{eq}/cm^2	TID /Mrad	NIEL / n_{eq}/cm^2
800	3.66	2.86×10^{13}	$1\,283 \pm 38$	$(9.96 \pm 0.03) \times 10^{15}$

Table 7.2: Parameters and results of the high-dose irradiation campaign of the `ITkPixV1.1` assembly. The site was operated at the nominal parameters for proton irradiation.

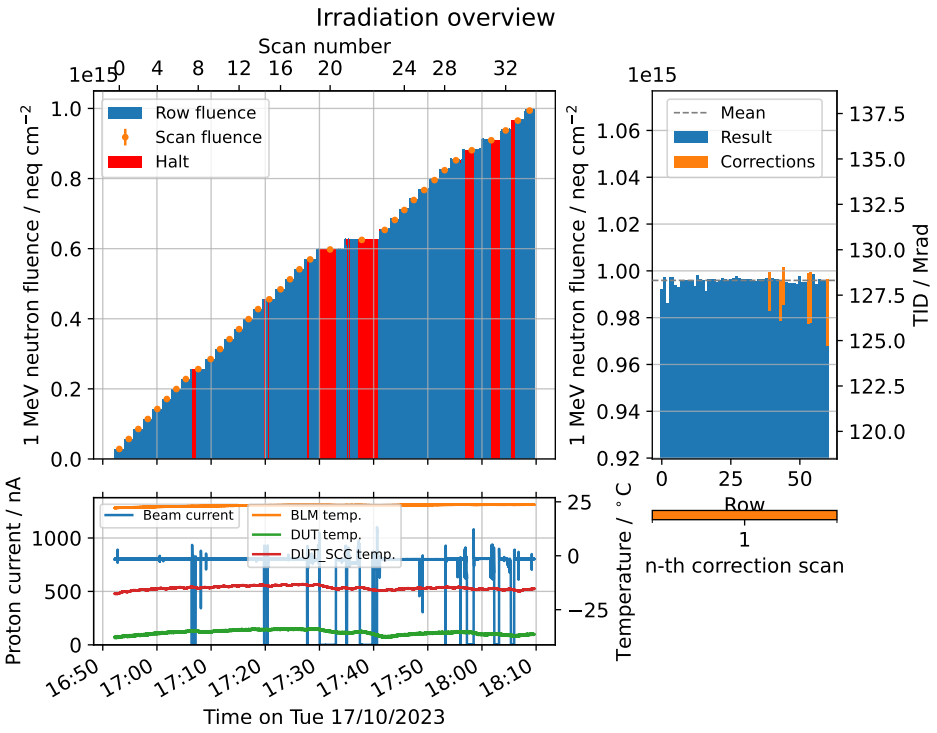

Figure 7.7: Overview of scan, rows and beam currents as well as temperatures of an exemplary high-dose irradiation step. In this particular example, insufficient beam conditions result in multiple halts of the scan routine which are corrected for post-irradiation.

Utilizing a proton beam with an average energy of 13.50 MeV (12.16 MeV on the DUT) and 800 nA beam current, averaging over all irradiation steps, the damage of an individual step is applied within approximately 1.3 h and 35 complete scans. An overview of an exemplary step is depicted in Fig. 7.7. Here, a dose of 3.66 Mrad is applied per scan. Using the same approach as before, the dose rate, normalized per scan, is approximately 156 Mrad/h where the same considerations (see footnote on Page 115) apply. The halts in Fig. 7.7 indicate faulty beam conditions during irradiation which are corrected for in the resulting fluence distribution. With up to three steps per day, the sensor IV curve is measured after every step, whereas controlled annealing is performed over night and at the start of each irradiation day (see Section 7.2.3 below). After ten steps with similar characteristics, as displayed in Fig. 7.7, the resulting damage levels are $(9.96 \pm 0.03) \times 10^{15}$ n_{eq}/cm^2 and (1 283 ± 38) Mrad which, in combination with the low dose levels, correspond to the anticipated EOL radiation damage [9].

7.2.3 Annealing

To reduce the radiation-induced leakage current increase between irradiations and allow for a quantitative analysis with respect to NIEL, controlled annealing procedures are performed throughout the campaign. Their relevant quantities, such as accumulated fluence, temperature and duration are listed in Table 7.3.
Following all irradiation steps, room temperature annealing is performed during which the DUT resides in the irradiation setup without active cooling. Additionally, the reference annealing procedure

Fluence step / n_{eq}/cm^2	Annealing		Cumulative damage
	Temperature / °C	Time / min	rate α_{cum} / 10^{-17} A cm^{-1}
5×10^{13}	21	4800	5.08
2×10^{15}	21	800	3.99
	60	80	
5×10^{15}	21	750	3.80
	60	80	
8×10^{15}	21	800	3.63
	60	80	
1×10^{16}	21	1200	3.45
	60	80	

Table 7.3: `ITkPix` annealing procedures, performed after specific steps of the irradiation campaign. The DUT remained inside the setup at room temperature between irradiation days. The reference annealing procedure (see Section 4.4) is applied at the beginning of each following day. The cumulative, *current-related damage rate* α_{cum} is calculated according to Eq. (7.1).

(see Section 4.4) for probing sensor NIEL degradation is conducted each campaign day, prior to initiating the irradiation steps. Using Fig. 4.7, the *cumulative*, current-related damage rate α_{cum}, resulting from a series of irradiations to fluences Φ_i and corresponding annealing procedures at temperature T and duration t can be defined as

$$\alpha_{cum} = \frac{1}{\Phi_{tot}} \sum_i \Phi_i \alpha_i^{t/T} \,. \tag{7.1}$$

Figure 4.7 is used to determine the respective, current-related damage rate $\alpha_i^{t/T}$ after each individual irradiation and annealing step where the 21 °C curve is used for room temperature. Using the proportionality in Eq. (4.8), the leakage current increase after two different annealing procedures α^{t_a/T_a} and α^{t_b/T_b} for the identical fluence and depleted volume, follows the relation

$$\frac{\Delta I^a_{leak}}{\alpha^{t_a/T_a}} = \frac{\Delta I^b_{leak}}{\alpha^{t_b/T_b}} \,. \tag{7.2}$$

This allows one to determine the theoretical leakage current increase $I^{n_{eq}}_{leak}$ after the reference annealing procedure that yields the current-related damage rate $\alpha^{80/60}_{n_{eq}} = (3.99 \pm 0.03) \times 10^{-17}\,\mathrm{A\,cm^{-1}}$ by measurement of the leakage current increase ΔI^{cum}_{leak}, corresponding to α_{cum}. Subsequently, the leakage current measurements after controlled annealing procedures enable the re-evaluation of the proton hardness factor from the `ITkPix` irradiations. To further support the value determined in Section 6.4, this analysis is performed in Section 7.2.5.

7.2.4 Ring Oscillator Frequency Delay

The performance degradation of the chip logic of the `ITkPixV1` with increasing levels of TID is extensively discussed in [35]. In this reference, different irradiation campaigns are performed, using X-ray setups and radioactive sources, applying TID at varying dose rates to levels exceeding 1 Grad. Additionally, `ITkPixV1` assemblies with 3D sensors are irradiated with protons at the Birmingham MC40 cyclotron (see Section 6.5) up to a fluence of 5×10^{15} n_{eq}/cm^2 and TID of 500 Mrad[3]. Subsequently, it serves as an excellent reference for comparison of results obtained in the course of this work.
An overview of the results, according to the specifications in [103], obtained over the course of all irradiation steps, is shown in Fig. 7.8. The bank A RO frequencies, corrected for V_{DDD} variations via Fig. 7.2, are displayed versus the increasing TID. Additionally, the chips digital supply voltage V_{DDD} as well as the temperature are depicted for all measurements.

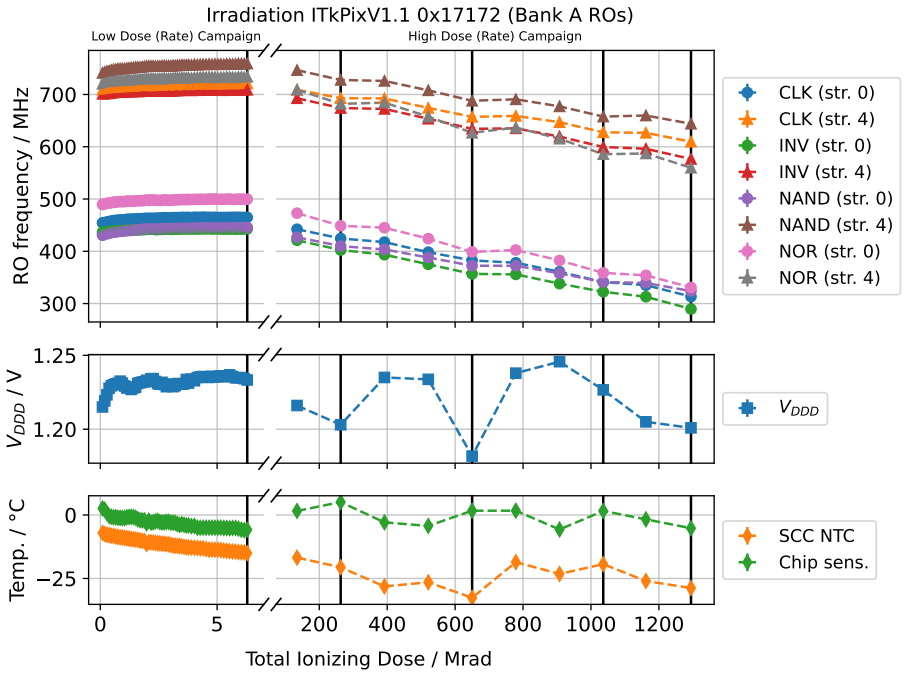

Figure 7.8: Evolution of RO bank A frequencies of the course of all irradiations. As per recommendation in [103], the frequencies are normalized to changes in V_{DDD}. The solid black lines indicate the damage levels at which controlled annealing is performed (cf. Table 7.3). The entries correspond to the mean of ten measurements, the errors are the respective standard deviations which are too small to be visible. In between entries, linear interpolations are shown.

Generally, the course of all RO frequencies versus the applied TID follows the same trend where only the absolute values differ. During the first few Mrad, the RO frequencies increase slightly and saturate from approximately 4 Mrad onward for the remaining TID applied within low dose campaign. As anticipated, over the course of application of the total dose of approximately 1.2 Grad, the frequencies

[3] As calculated according to Eq. (5.19), corresponding to the Bethe-Bloch model (cf. Eq. (2.1)).

of all ROs decrease with TID following a linear trend. At the maximum dose, the average difference for the strength-0 gates is approximately 140 MHz whereas for the strength-4 gates, 120 MHz are observed. This agrees with the expectation, that the transistors with narrow physical channels experience larger TID damage, as a larger fraction of the channel is influenced by radiation-induced, stationary charges in the oxide (see Section 4.1.1). As visible at the damage levels at which annealing procedures are performed, the rate of frequency decrease of the ROs is reduced after annealing, indicating a beneficial effect as discussed in Section 4.4. Over the two dedicated irradiation campaigns, the temperatures on-chip as well as on-PCB only vary by a few degrees Celsius within the respective campaign. The difference in temperature readings of the two sensors most likely arises from the positioning of the SCC NTCs directly within the cool gas stream of the cooling setup (see. Fig. 7.5). The on-chip temperature sensors are exposed to the digital chip bottom's heat dissipation [100].

As introduced in Section 7.1.2, an alternative representation of the data is the relative gate delay which must stay below 200 % to maintain the chip's digital timings [101]. The relative gate delay versus the applied TID is visualized for all ROs in Fig. 7.9. After receiving a dose of approximately 1.2 Grad from proton irradiation at the BIC, the delay for strength-0 and -4 gates remains below 35 % and 20 %, respectively, residing well below the limit of 200 %.

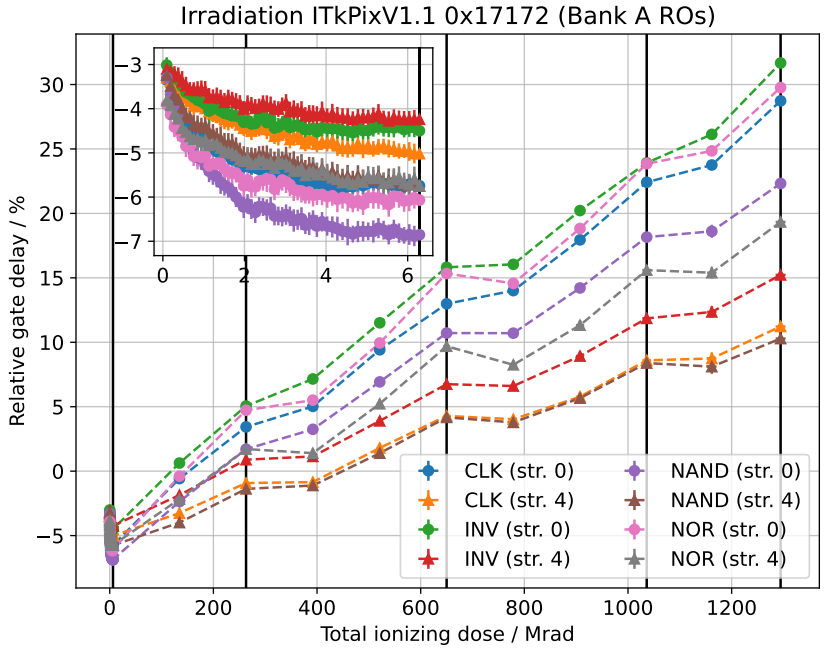

Figure 7.9: Relative gate delay of bank A ROs as a function of TID. The zoomed-in inset plot corresponds to the measurements of the dedicated low-dose campaign in Fig. 7.6. The solid black lines indicate the damage levels at which controlled annealing is performed (cf. Table 7.3). The entries correspond to the mean of ten measurements, the errors are the respective standard deviations, which are too small to be visible. In between entries, linear interpolations are shown.

Focusing on the initial course of the gate delay, occurring within the first few Mrad, the results are

generally comparable with the ones reported in [35]. As the gate delay decreases, no distinct minimum is visible within 6 Mrad, which is likely due to substantially higher dose rates. While the reported delay minimum in this region is approximately -2 %, it is up to -7 % in this work (see Fig. 7.9). This most likely originates from the temperature dependence of the RO frequency, that was not considered for this analysis. The reference was measured at room temperature, possibly resulting in an offset of a few percent.
The results from X-rays with high (4 Mrad/h) dose rates from [35] show relative gate delays in the order of 70 % and 30 % for strength-0 and -4 gates, respectively, at a TID of 1 Grad. Compared to this, the relative gate delays resulting from proton irradiation in this work are substantially lower, approximately half of the values from X-rays in [35]. Especially when considering low dose-rate results in [35], the delays introduced due to TID by protons within this work are substantially lower. On examination of the proton TID studies performed in [35], a similar trend is observed. The resulting gate delays are approximately halved for proton compared with high-rate X-ray irradiation, normalized to the dose received. Now comparing between the proton-induced delays, at a dose of 600 Mrad values of approximately 15 – 20 % in [35] and 12 % in this work are found for the CLK 0 drivers. The observed difference in RO response among proton irradiations is likely a combination of several components, all potentially yielding a decreased gate delay with dose:

- A factor two higher dose rate at the BIC compared to the Birmingham MC40 cyclotron[4]
- Annealing procedures carried out between irradiation steps
- Neglecting the temperature dependence of the RO frequency

However, the level of contribution of the effects cannot be resolved. Considering the dose-rate dependencies reported in [35], the recorded gate delay increase in %/Mrad, irrespective of the gate type and strength, appears to become only weakly dependent on the dose rate for sufficiently high rates. Subsequently, due to the many orders of magnitude higher dose rate for protons as compared to X-rays, the difference between the proton irradiation results is possibly caused by the annealing procedures and neglected temperature scaling of RO frequencies.
The measurements performed within this work indicate, that the damage to the digital logic of the chip, as measured by the relative gate delay, after proton irradiation up to a dose of 1.2 Grad is safely below the upper limit of 200 %. The results agree with the ones reported in [35], where a dose of 500 Mrad is delivered via protons. Therefore, it can be generally estimated, that the dose applied during proton irradiation results in less damage effect to the chip logic than the equivalent dose from X-ray irradiation. The difference potentially lies within the large discrepancy in dose rates, which are several orders of magnitude larger for proton irradiation.

7.2.5 Sensor Leakage Current Increase

As anticipated from Eq. (4.8), the sensors IV behavior degrades, manifesting in an increase of leakage current with fluence. The evolution of IV characteristics over the course of the irradiation campaign, including the controlled annealing procedures (see Section 7.2.3), are presented in Fig. 7.10. The data is recorded using an SMU and normalized to the sensor area. To prevent damage to the sensor, a conservative leakage current limit was enforced during the measurements, limiting the

[4] Proton stopping power in silicon of 30 MeV cm^2 g^{-1} in Bonn versus 18 MeV cm^2 g^{-1} in Birmingham, see Table 6.5.

maximum reverse bias voltage to approximately 150 V, which is expected to result in full depletion according to the results reported in [26]. Using Eq. (2.20), the leakage currents are scaled to −25 °C, corresponding to the benchmark temperature for the 3D sensors after irradiation [26]. The SCC NTCs, as depicted in Fig. 7.5, are used as a temperature reference during the IV measurements. For further remarks regarding the determination of the DUT temperature during the irradiation campaigns, see Appendix A.7.

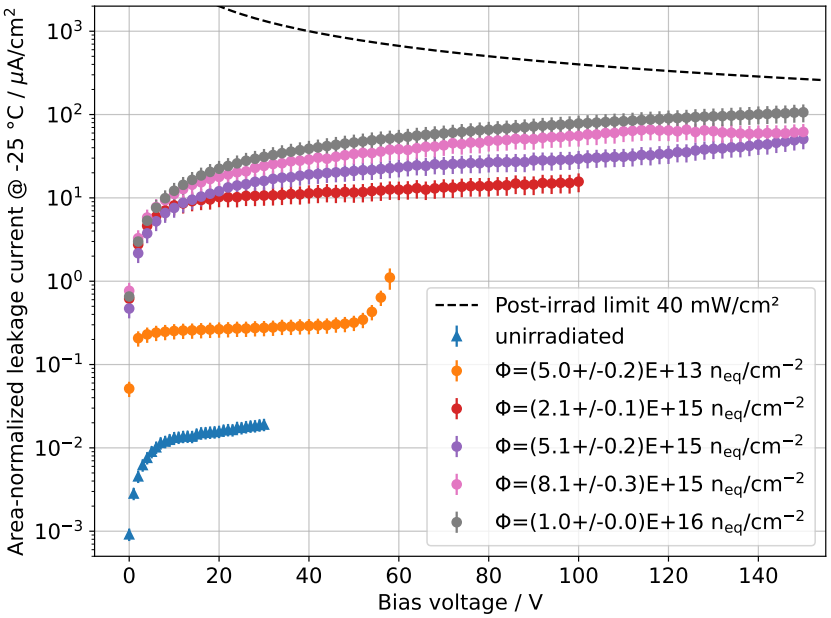

Figure 7.10: Area-normalized IV curves of the *SINTEF* 3D sensor at different fluence levels, after annealing (cf. Section 7.2.3). Each entry of each dataset corresponds to the mean of five measurements, the error to the standard deviation. An uncertainty of 2 °C was taken into account when scaling the results to −25 °C via Eq. (2.20). The power limit of 40 mW cm^{-2} throughout the operation in the ATLAS ITk [26] is indicated.

In addition to the IV curves, the imposed power limit of 40 mW cm^{-2} [26] for the 3D sensors of the ITk innermost layers at the reference temperature is displayed. As visible for the highest fluence level of 1×10^{16} n_{eq}/cm^2, the leakage current is approximately a factor of three below the limit. This leaves headroom up to 3×10^{16} n_{eq}/cm^2 at the same bias, supporting the sensor operability up to the anticipated levels. It is worth to note that these findings have been obtained after reduction of the leakage current due to the performed annealing procedures.

NIEL Scaling Verification

The sensor IV data obtained during the `ITkPix` irradiation campaign can furthermore be utilized to verify the accuracy of the NIEL scaling according to Eq. (4.7) at the BIC. This can be achieved by confirming that Eq. (4.8) yields the current-related damage rate $\alpha_{n_{eq}} = (3.99 \pm 0.03) \times 10^{-17}$ A cm^{-1} [53] for 1 MeV equivalent fluences after the reference annealing routine (cf. Section 4.4). Therefore, analogously to the procedure in Section 6.4, the leakage current is scaled to 20 °C and the IV curves

are shown in Fig. 7.11(a). The leakage levels after the reference annealing are determined by Eq. (7.2) in conjunction with the cumulative damage rates in Table 7.3. This allows for the calculation of the leakage current increase observed after every fluence level as if the reference instead of the cumulative annealing had been applied. Finally, the full-depletion voltage at each fluence level is estimated by visual inspection, as depicted in Fig. 7.11(a). With an active thickness of the sensor of 150 µm, the depleted volume can be calculated. Considering the uncertainties, estimations are made similar to Section 6.4.3: an error of 10 % on the active thickness, accounting for process variations as well as full-depletion voltage estimates, is taken and an uncertainty of 2 °C during temperature scaling. The resulting leakage current increase per depleted volume versus the equivalent fluence is portrayed in Fig. 7.11(b).

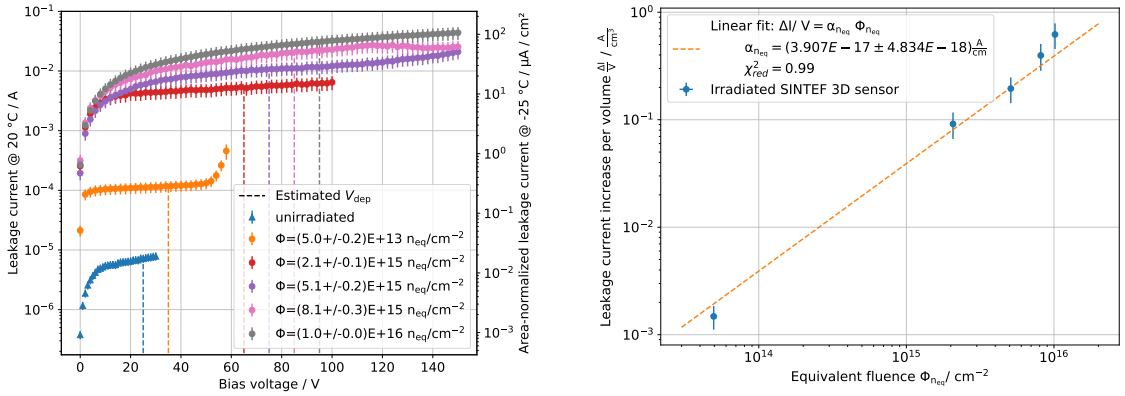

(a) IV curves at 20 °C

(b) Leakage current increase with fluence

Figure 7.11: IV behavior at room temperature (a), scaled via Eq. (2.20), and leakage current increase with 1 MeV neutron equivalent fluence (b) of the *SINTEF* 3D sensor of the `ITkPix` assembly. The data shown in Fig. 7.11(a) is equivalent to Fig. 7.10 where the temperature scaling is different and the IV curves are area-normalized.

The data follows the expected linear increase with the equivalent fluence. A linear fit, according to Eq. (4.8), is performed, verifying the overall good agreement of the obtained data within its uncertainties and the model with a reduced χ^2 of 0.99. The current-related damage rate extracted from the fit corresponds to $\alpha_{n_{eq}}^{meas} = (3.91 \pm 0.48) \times 10^{-17}\,A\,cm^{-1}$. Comparison to the reference value from [53] yields

$$\frac{\alpha_{n_{eq}}^{meas}}{\alpha_{n_{eq}}^{[53]}} = \frac{(3.91 \pm 0.48) \times 10^{-17}\,A\,cm^{-1}}{(3.99 \pm 0.03) \times 10^{-17}\,A\,cm^{-1}} = 0.98 \pm 0.12\,,$$

which validates the NIEL scaling at the BIC via Eq. (4.7), using the proton hardness factor determined in Section 6.4. Within the accuracy of the utilized method, the expected linear course of the leakage current increase with equivalent fluence is visible over a range of more than two orders of magnitude.

7.2.6 Effects on Detector Operation

The threshold and noise distributions after irradiation are investigated to probe the effect of radiation damage on the detector functionality. After all irradiation steps throughout the low- as well as

high-dose (rate) campaigns, the chip is re-tuned to a target threshold of 300 ΔV_{CAL}, or approximately 1.4 ke^-, with the routine described in Section 7.1.2. The threshold tuning is performed inside the setup, immediately following the irradiation, at temperatures between −20 and −30 °C using the BDAQ53 system. The corresponding threshold and noise distributions for the low- and high-dose campaign are

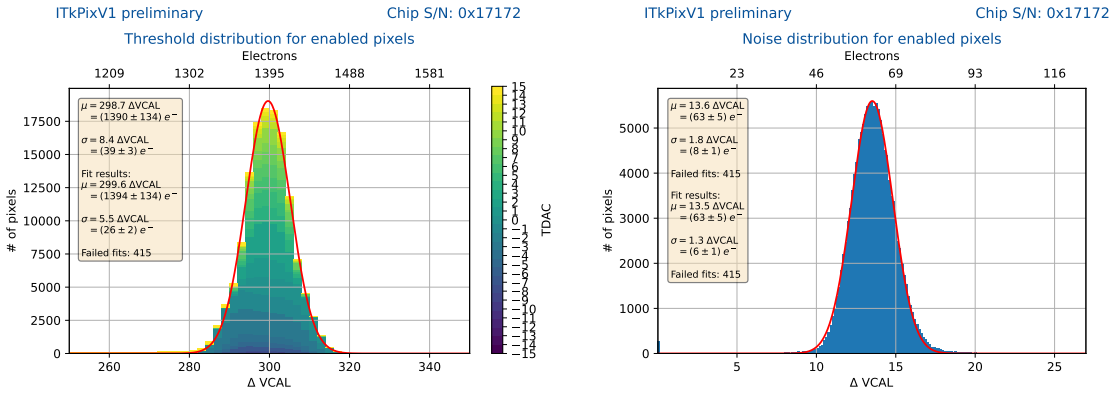

(a) Low dose (rate) irradiation campaign

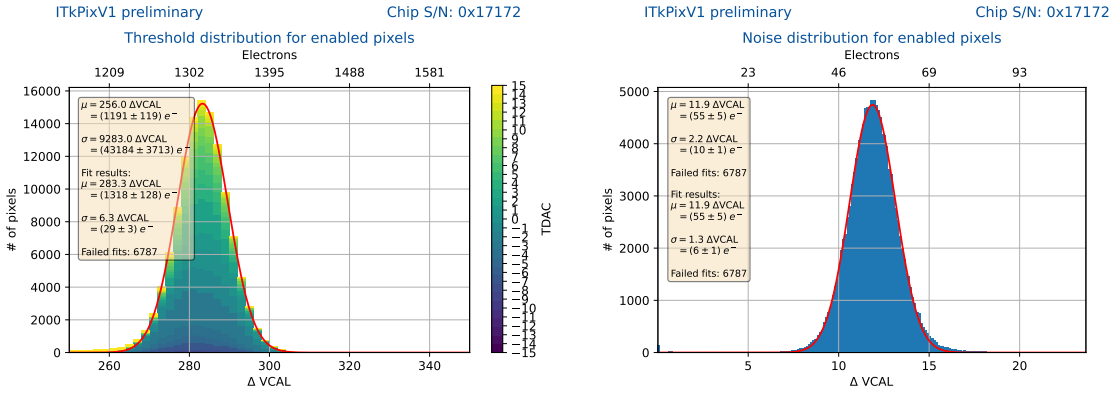

(b) High dose (rate) irradiation campaign

Figure 7.12: Threshold (left) and noise (right) distributions after the doses delivered during the low (a) and high (b) dose campaign.

displayed in Figs. 7.12(a) and 7.12(b), respectively. The threshold dispersions show comparable values after the low- and high-dose campaign with (26 ± 2) e^- and (29 ± 3) e^-, respectively, indicating that local in-pixel tuning is possible up to the applied TID. However, after receiving a dose of 1.2 Grad, the resulting threshold is 1.3 ke^-, slightly lower than the anticipated target. This is assumed to originate from faulty enabled pixels and yields a shift of the plotted distribution to lower values.
The mean values of the noise distributions after both campaigns are comparable with (63 ± 5) e^- after 6 Mrad and (55 ± 5) e^- after 1 200 Mrad, respectively. They lie within 1 standard deviation of the distributions. The difference in mean value is possibly due to slightly different measurement parameters such as temperature, applied sensor bias and enabled pixel.
Figure 7.13 shows the threshold dispersion, noise and degradation versus total ionizing dose. In this context, the threshold dispersion corresponds to 1 σ of the distribution after re-tuning the chip. The

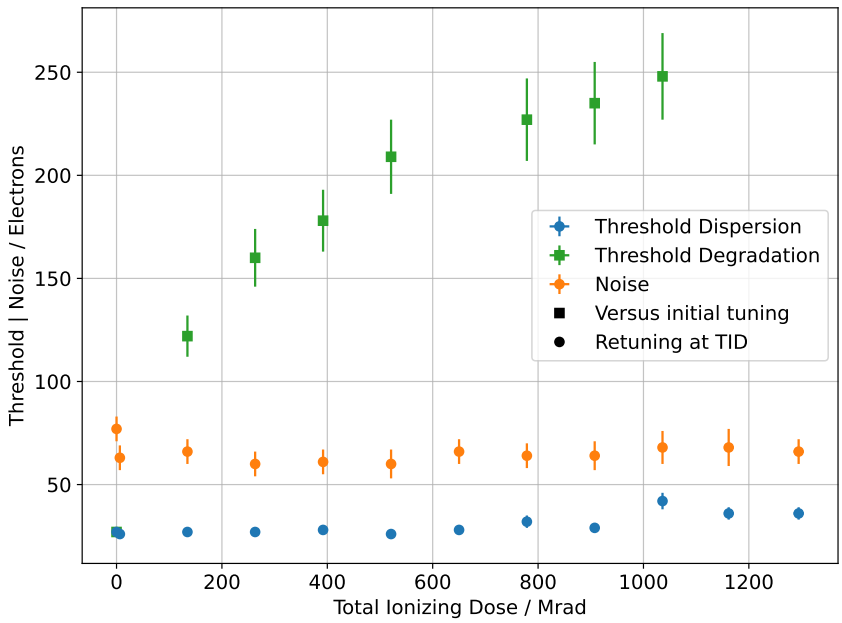

Figure 7.13: Threshold and noise levels over the course of TID of the ITkPix assembly. Additionally, the threshold degradation (see text) is depicted. The measurements are taken inside the setup of the irradiation site at $\leq -20\,^{\circ}\mathrm{C}$ with the BDAQ53 DAQ system. Circular and square markers indicate comparisons with and without re-tuning, respectively.

threshold degradation describes the same quantity without re-tuning after irradiation. The threshold degradation grows significantly with dose, reaching approximately $250\,e^-$ at 1 Grad. The relative change appears greater in the lower dose region whereas an approximate saturation appears for higher doses. In contrast, the threshold dispersion and noise remain approximately constant when retuning the chip. This is observed over the entire measurement with only marginal deviations and a slight increase in threshold dispersion at high dose.
These findings indicate that the detector can be operated successfully up to 1.2 Grad after retuning with only small variations in noise as well as threshold dispersion compared to the unirradiated case. This agrees with the results obtained using X-rays in [35, 43]. With regard to Section 7.2.4, these results have to be taken with care as the dose rates during proton irradiation are orders of magnitude higher than for typical X-rays. The latter yields significantly higher TID-related damage, measured in RO delay (see Fig. 7.9), at the same dose.

7.3 Test Beam Campaign

Following the irradiation campaign to simultaneous TID and NIEL EOL levels at the BIC and subsequent verification of the detector functionality in the laboratory, the performance of ITkPix assembly was studied at the DESY test beam facility [14] in the second half of October 2023. Here, the primary goal is the determination of the hit detection efficiency of the detector after irradiation to $10^{16}\,\mathrm{n_{eq}/cm^2}$ as well as 1.2 Grad and comparison to results of previous studies, featuring the same

sensors at comparable fluence levels [26]. The DESY II test beam facility offers continuous (up to a few kHz) electron as well as positron beams with energies of up to 6 GeV. The test beams are available at the three different areas TB21, TB22 and TB24, where two preinstalled, EUDET-type beam telescope setups (see Section 7.3.1), *DATURA* and *DURANTA*, are available.
The test beam studies within this work are performed at the TB24 area, utilizing the *DURANTA* telescope setup (cf. Fig. 7.15), where an electron beam between 3.8 and 5 GeV is extracted. First, an overview of the telescope setup is given. Subsequently, the measurement procedure is introduced and the hit detection efficiency studies are presented.

7.3.1 Telescope Setup

A pixel detector telescope setup facilitates hit detection efficiency studies of arbitrary DUTs by providing a reference system which allows for particle track reconstruction. Integration of the DUT into the setup and subsequent track extrapolation onto its area enables calculation of the hit detection efficiency (see Section 7.3.4). A schematic depiction of a pixel detector telescope setup is shown in Fig. 7.14. The actual *DURANTA* setup at the TB24 area is portrayed in Fig. 7.15. It consists of six

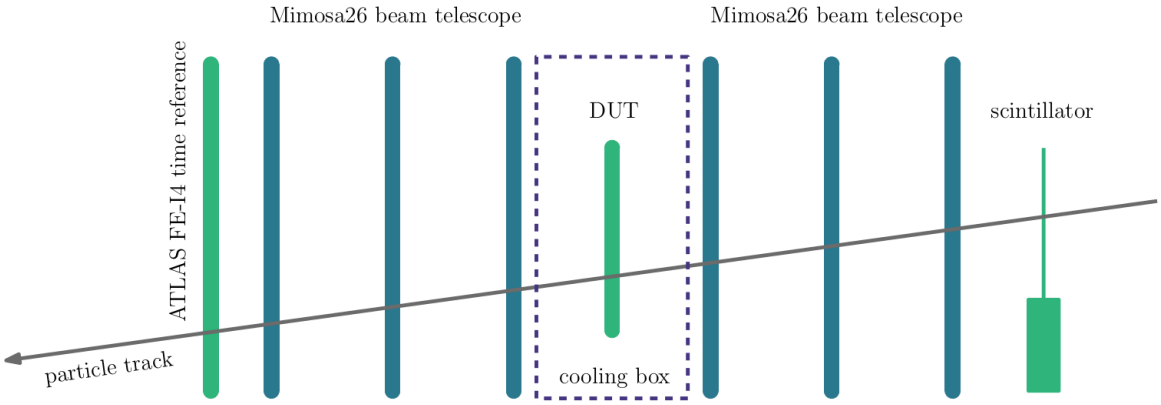

Figure 7.14: Schematic of a pixel detector telescope, from [20]. It consists of a scintillator for triggering, six `Mimosa26` telescope planes for spatial and an ATLAS `FE-I4` for temporal track reconstruction. The DUT is placed within this reference system, allowing for hit detection comparison. The telescope plane numbers increases downstream, from right to left.

`Mimosa26` [104] MAPS planes (cf. Section 2.3), providing excellent spatial resolution, an ATLAS `FE-I4` hybrid pixel detector [105] plane, yielding necessary time information, and two scintillators for triggering. The `Mimosa26` sensors cover an area of $(21.1 \times 10.6)\,\mathrm{mm}^2$, divided into 1152 columns and 576 rows with a quadratic pitch of $(18.4 \times 18.4)\,\mu\mathrm{m}^2$. Within a telescope setup, these MAPS yield an excellent spatial resolution of below 2 µm [104]. The `FE-I4` time reference covers an area of $(20.0 \times 16.8)\,\mathrm{mm}^2$, divided into 80 columns and 336 rows with a pixel pitch of $(250 \times 50)\,\mu\mathrm{m}^2$. It operates with a nominal clock of 25 ns, providing the required time stamping capabilities to the reconstructed tracks.
The `Mimosa26` telescope planes are installed on a rail system, allowing one to freely position them along the beam axis. They are separated into two stacks of three planes, surrounding the test beam cool box [106] that houses the irradiated `ITkPix`.The inside of the cool box is shown in Fig. 7.15(c). Here, the DUT's SCC is mounted on a frame, allowing for preliminary alignment of the closed container

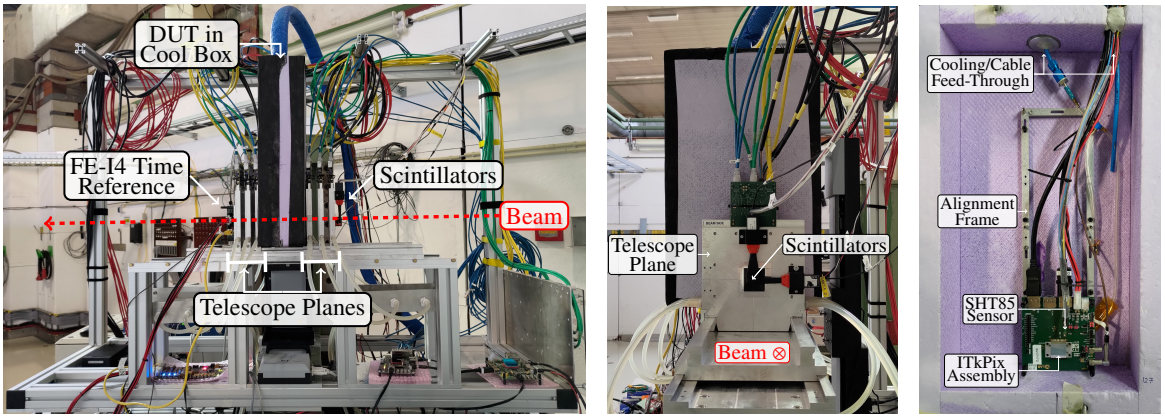

(a) Side view, beam right to left (b) Front view, beam into plane (c) `ITkPix` in cool box

Figure 7.15: *DURANTA* beam telescope setup, installed at the TB24 area during the October 2023 test beam at the DESY II facility [14]. The `ITkPix` assembly is mounted inside the DUT cool box, developed for the test beam infrastructure [106].

within the telescope, and connected to the readout system via a cable feed-through. In close vicinity of the chip, a *Sensirion SHT85* temperature and humidity sensor is placed, used for the automated atmosphere control system of the cooling setup as well as for temperature reference. The cooling system is described in [106] and enables continuous operation at temperatures below −20 °C over periods of up to 1 d.
The telescope infrastructure is read out and configured with Python-based DAQ software and dedicated readout boards developed at Bonn. The `Mimosa26` planes are operated using the Multi-Module-Card 3 (MMC3) and the *pymosa* [107] readout software. The `FE-I4` is operated using the Multi-IO 3 (MIO3) board and *pyBAR* [108], the Bonn ATLAS Readout in Python. The `ITkPix` is interfaced utilizing the BDAQ53 [44] DAQ system. The scintillator pulses are processed by the TLU, which is operated via the *pyTLU* [109] package.

7.3.2 Telescope Alignment

To allow for reconstruction of tracks from the data that is obtained during beam measurements, the telescope needs to be aligned. This is achieved by adjusting the position-sensitive detectors inside the telescope until the beam spot is located on the pixel matrix and a correlation between the x- and y-coordinates of hits is observed among the planes. Typically, the preinstalled telescope setups such as *DURANTA* are already well aligned due to their mounting frame. The cool box, in which the irradiated `ITkPix` DUT resides, does not feature a mounting mechanism for the alignment. Instead, it is placed between the two stacks of `Mimosa26` planes and the initial alignment is performed using markings on the outside of the box, indicating the DUT position. The final alignment is found by iterative adjustment of the DUT position, subsequent beam extraction and calculation of the hit correlation until the hits among all planes of the telescope are correlated, indicated by a sharp hit occupancy diagonal on the matrix.
An exemplary correlation of hits, indicating the successful alignment of the setup, is shown in Fig. 7.16. The correlation of the hit x-coordinates between the first (w.r.t. beam direction, see Fig. 7.15(a)) plane

(Mimosa26) and the central DUT is shown in Fig. 7.16(a) whereas the hit correlation of y-coordinates between the DUT and the last telescope plane FE-I4 is displayed in Fig. 7.16(b). The occupancy diagonal, roughly intersecting with the coordinate origin, indicates an approximately centrally-aligned telescope with the majority of the beam spot covering the detector's sensitive area. As this alignment is found between the extremities and central plane of the telescope, also an alignment of the remaining detectors can be assumed.
The final alignment parameters, particularly the positions along the beam axis, are an important for the track reconstruction. For all telescope measurements in this work the data can be found in Table A.4.

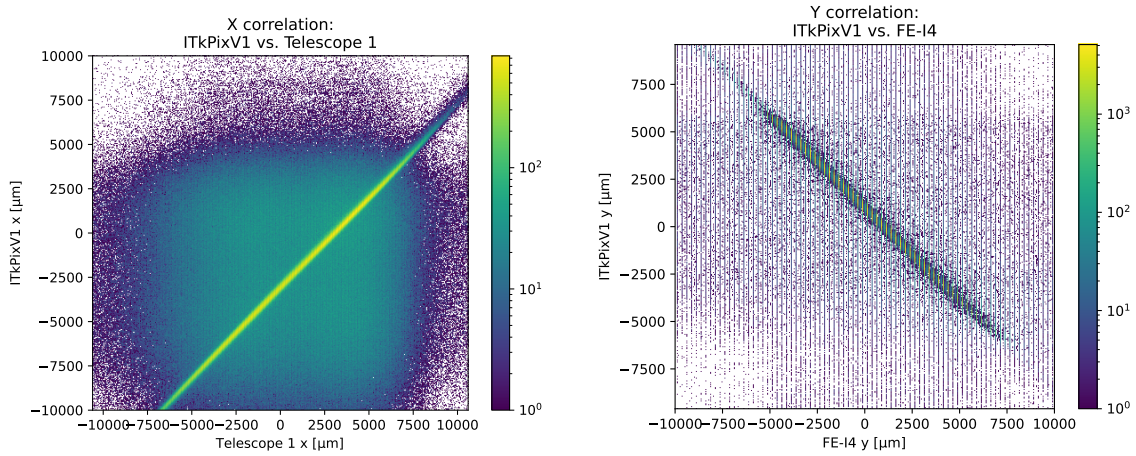

(a) Horizontal (X) correlation between Mimosa26 plane 1 and ITkPix

(b) Vertical (Y) correlation between ITkPix and FE-I4

Figure 7.16: Hit correlation of selected telescope planes and the DUT inside the *DURANTA* setup at DESY during the 2023 test beam. Shown are the horizontal correlation between the first telescope and the DUT plane (a) and the vertical correlation between the DUT and the time reference plane (b), which is the last plane in the setup.

7.3.3 Bias Runs

Using the aligned telescope, multiple beam measurements at different sensor bias voltages are performed to obtain the hit detection efficiency as a function of the bias voltage. For these so-called *bias runs*, a 3.8 GeV electron beam with a rate of approximately 2 kHz is extracted trough the telescope setup and each detector is read out. Several runs are recorded with varying bias voltages applied to the *SINTEF* 3D sensor of the ITkix assembly. Each run contains approximately 2×10^6 triggers, distributed by the TLU. An SMU is used to supply bias voltage to the DUT and measure the corresponding sensor leakage current. For each run, the DUT is tuned to a threshold of approximately $300\,\Delta V_{\mathrm{CAL}}$, comparable to Fig. 7.12(a).
A total of 13 runs with increasing bias voltages between 20 and 95 V are recorded. As an example, the resulting maps of registered hits by the DUT as well as reconstructed track and their extrapolation onto the ITkPix are visualized in Fig. 7.17 for the lowest bias run at 20 V. A comparison of the approximate number of hits in the DUT and tracks intersecting with it, gives an estimated hit detection efficiency for the selected bias voltage of roughly 20 %. This is a direct consequence of the radiation-induced

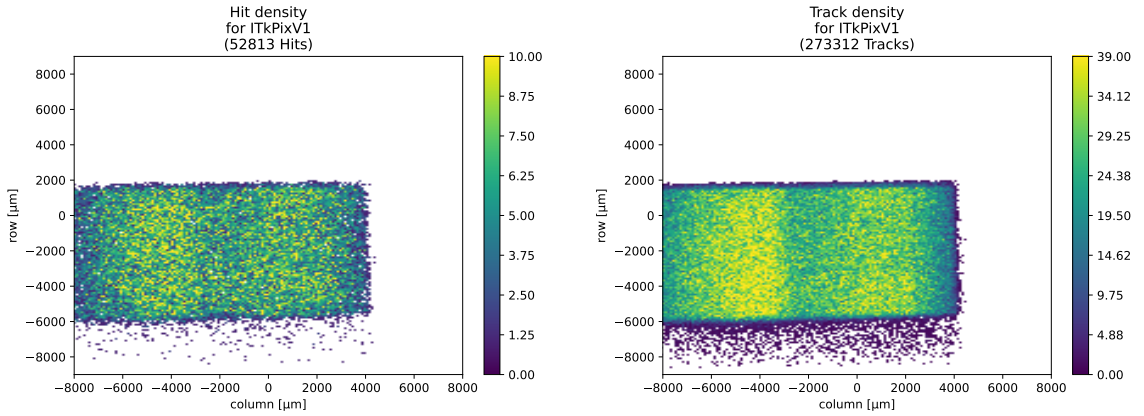

(a) Hit map

(b) Track map

Figure 7.17: Map of hits registered by the `ITkPix` DUT (a) and map of reconstructed tracks (b), extrapolated onto the `ITkPix` for a single bias run at 20 V. Comparing the approximate numbers of hits and tracks of 50×10^3 and 270×10^3, respectively, facilitates a rough estimation of the efficiency in the order of 20 %.

damage to the detector. As a result, an increasing voltage is required for depletion of the sensor while the signal-to-noise ratio decreases due to charge trapping and leakage current increase (compare Section 4.3).
After performing additional IV measurements inside the test beam setup, the chip could not be configured to maintain a stable threshold at voltages ≥ 100 V; after tuning and immediately reading back the threshold, shifts larger than the previous dispersion were observed. Repeating measurements at lower bias voltages produced inconsistent results. Several attempts to resolve the issue by different chip configurations, including activation of the Leakage Current Compensation (LCC), did not succeed. Due to time constraints, it was not possible to identify the underlying problem and continue the bias run measurements for higher voltages. Therefore, only the runs up to 95 V are considered in the following hit detection efficiency studies for which the reference measurements in [26] already show efficiencies meeting the ATLAS requirement of ≥ 97 % [9] over the lifetime of the detector for some sensors.

7.3.4 Hit Detection Efficiency

The hit detection efficiency ϵ is an essential property of a detector and the main characteristic of the sensor. Especially after irradiation, the effects of radiation-induced damage (discussed in Section 4.3) result in an overall decrease of the signal-to-noise ratio, reducing the so-called *Charge Collection Efficiency (CCE)*. Using a pixel detector telescope setup as described in Section 7.3.1, the hit detection efficiency can be defined as [20]

$$\epsilon = \frac{N_{\text{tracks}}^{\text{DUT}}}{N_{\text{tracks}}^{\text{total}}} \quad \text{with} \quad \epsilon \in [0, 1] \ , \tag{7.3}$$

where $N_{\text{tracks}}^{\text{total}}$ and $N_{\text{tracks}}^{\text{DUT}}$ are the total number of reconstructed tracks in the beam telescope setup and the number of hits registered by the DUT that correspond to a track, respectively.

The required information to extract ϵ can be obtained from the recorded data of each detector plane in the telescope setup trough a variety of sequential analysis steps, as listed in detail in chapter 5 of [20]. A software package that provides the necessary utilities is Beam Telescope Analysis (BTA) [110], an analysis toolset for processing telescope-based detector data. It is written in *Python* and *C++*, resulting in an easy-to-use as well as performant software, and consists of a series of independent utilities that altogether yield a full analysis and track reconstruction. Parts of its implementation details are described in [20] as well and, within this work, it is used to determine the hit detection efficiency of the irradiated `ITkPix` assembly for different sensor bias voltages. The uncertainty on ϵ is usually dominated by the systematic error introduced in the analysis procedure and is $\Delta\epsilon \ll 1\,\%$ [21] for the statistics contained in typical test beam measurements.

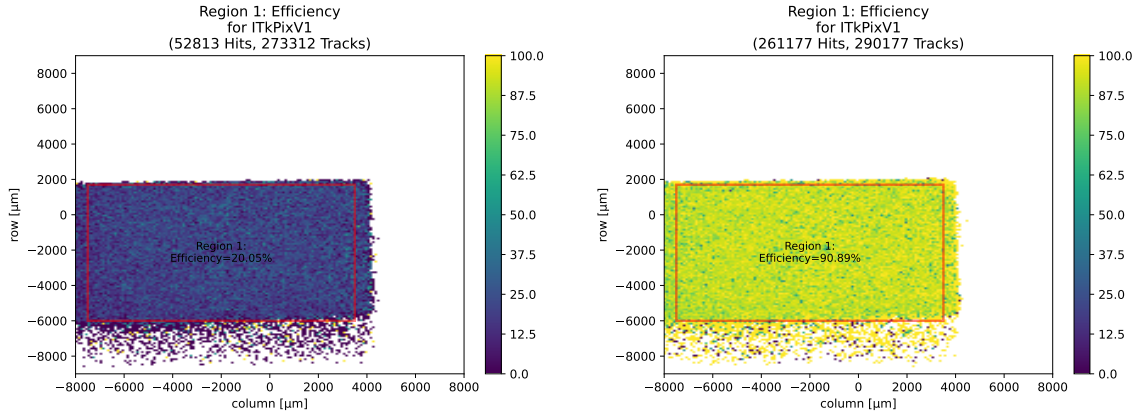

(a) 20 V bias

(b) 95 V bias

Figure 7.18: Efficiency maps of the *SINTEF* 3D sensor at low and high bias voltages of 20 V and 95 V, resulting in efficiencies of 20.05 % and 90.89 %, respectively.

The resulting efficiency maps for the irradiated DUT at the lowest and highest bias voltage of 20 V and 95 V are shown in Figs. 7.18(a) and 7.18(b), respectively. For both runs, an approximate 300 k tracks have been reconstructed using the *DURANTA* telescope data and BTA analysis routines. For the low-bias run an efficiency of $\epsilon_{\text{low}} = 20.05\,\%$ is determined whereas $\epsilon_{\text{high}} = 90.89\,\%$ is found for the highest bias voltage, both resulting in a uniform response across the illuminated detector area. As previously stated, the uncertainties are estimated to be $\Delta\epsilon \ll 1\,\%$ for all measurements and are therefore not explicitly given. The efficiency as a function of the bias voltage is displayed in Fig. 7.19. A steep increase of ϵ with bias voltage is visible within the first 60 V with an asymptotic trend towards higher bias voltages. Additionally, the sensor leakage current, normalized to the area and scaled to −25 °C via Eq. (2.20), is shown. With regard to the requirements of ATLAS, the highest efficiency of $\epsilon_{\text{high}} = 90.89\,\%$, extracted from the measurements performed at DESY, do not meet the anticipated criteria of $\epsilon \geq 97\,\%$ [9] over the entire detector lifetime.
Considering the obtained efficiencies for the same sensors after $10^{16}\,\text{n}_{\text{eq}}/\text{cm}^2$ from [26], a value of $\epsilon \geq 96\,\%$ was extracted for bias voltages in the range of 80 – 150 V with thresholds of $\approx 1\,\text{k}e^-$. Specifically, at 95 V bias, the *SINTEF* 3D sensor is 97 % efficient in [26] whereas for a similar configuration a value of approximately 91 % was determined within this work. This significant difference is unlikely to be the result of just the marginally-higher threshold in this work. A collection

of additional factors are the mitigated TID effects on the RD53A chip due to it not being powered during irradiation [50, 49] and the higher beam energies at the CERN as well as DESY test beam facilities of 120 GeV pions and 5 GeV electrons, respectively. Moreover, the usage of three different front-ends of the RD53A, as compared to the single, differential front-end in RD53B, or a more careful configuration of the chip registers and its matrix with regard to noisy or disconnected pixels, could yield a difference in efficiency.

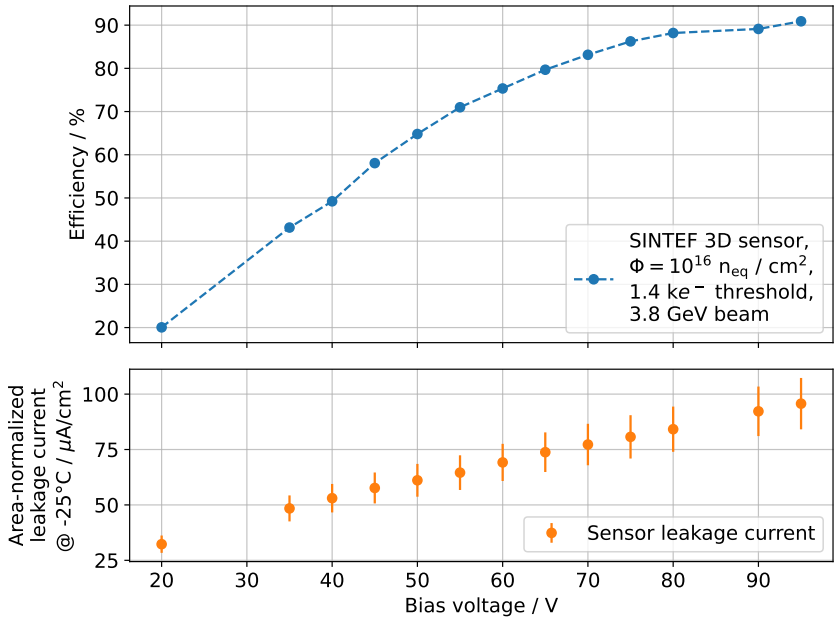

Figure 7.19: Efficiency versus bias voltage of irradiated *SINTEF* 3D sensor of the ITkPixV1.1 assembly. The efficiencies are determined with the BTA software [110]. Each run contains an approximate 300 k tracks in the telescope (cf. Fig. 7.15).

Nevertheless, the resulting efficiency of 90 % for bias voltages $\geq$ 90 V provides a solid indication that the requirements can be met after a combined 10^{16} n_{eq}/cm^2 and 1.2 Grad via proton irradiation, using the ITkPixV1.1 chip. The resulting power dissipation at 95 V corresponds to approximately 10 mW cm^{-2}, which is below the upper limit for the ATLAS ITk of 40 mW cm^{-2} [26]. In combination with the upper limit for the operational bias voltage after irradiation of 250 V [26] and the leakage levels observed up to 150 V in Fig. 7.10, it appears plausible that an efficiency of $\geq$ 97 % can be achieved with the ITkPix assembly employed in this work.

CHAPTER 8

Conclusion

Radiation hardness tests of pixel detectors are a necessity for research, development and verification of prototype devices for high-energy physics experiments. The upcoming High-Luminosity Large Hadron Collider will set a new frontier for the radiation hardness requirements of the innermost layers of the tracking detectors, with anticipated radiation levels of approximately $10^{16}\,\mathrm{n_{eq}/cm^2}$ and 1 Grad for the ATLAS Inner Tracker. In this work, an irradiation site for radiation hardness tests of silicon pixel detectors has been developed, characterized and commissioned at the BIC, contributing to the research and development of novel generations of silicon tracking detectors at the University of Bonn.

At the irradiation site, DUTs are irradiated with nominally 14 MeV protons with a beam current of approximately 1 µA while situated inside a thermally-insulated cool box. To achieve a uniform damage distribution on the device, the box is mounted on a motorized 2D-linear stage and moved through the beam on a row-based scan pattern. During irradiation, the cool box is continuously flushed with cool nitrogen gas, maintaining temperatures of $\leq -20\,^{\circ}\mathrm{C}$, to prevent uncontrolled annealing and provide a dry atmosphere, avoiding condensation. A set of custom-made on-site diagnostics, compromised of a beam monitor, a Faraday Cup and an analog readout electronics, enables non-destructive beam parameter monitoring with simultaneous extraction to the setup, depending on a calibration measurement for the given ion species and energy.
Based on the online beam monitoring capabilities, a Python-based (open-source) software framework (`irrad_control`) has been developed, implementing a purely beam-based on- and offline dosimetry and an beam-driven irradiation routine. It provides a GUI for online data visualization, setup control, interaction with the irradiation routine and DAQ of all raw and processed data. Real-time analysis of the irradiation-related information allows for autonomous execution of the irradiation routine to the target fluence while instantaneously adapting the procedure to varying conditions, resulting in extremely uniform irradiation profiles. The acquired data is stored by the framework and can be analyzed offline via a set of analysis procedures, providing transparency and the foundation for extensive damage studies.
The irradiation infrastructure at the BIC, consisting of diagnostics, setup and software framework, is designed with comparable facilities such as Birmingham [12], CERN [11] or KIT [99] in mind, allowing for easy adaptation with minimal modification to the existing irradiation site.

Characterization of the beam diagnostics confirm their anticipated functionality and operational

characteristics as obtained from simulations. The analog readout board yields a relative uncertainty of approximately 1 % on the transimpedance conversion of the input signals from the diagnostics for the typical mode of operation. The beam monitor calibration constant, required for non-destructive beam monitoring, for 14 MeV protons is demonstrated to be stable over time and typical run-to-run variations of environmental and accelerator parameters with a standard deviation of approximately 2 %. The mean calibration constant is $\lambda = (0.912 \pm 0.020)\ \mathrm{V}^{-1}$ which corresponds to a yield of $\gamma = (21.94 \pm 0.47)$ %, in agreement with the literature value for the carbonized foil surfaces and the given proton energy. Consequently, this enables online beam monitoring with a relative uncertainty of generally ≤ 3 % which can be improved significantly by performing individual calibration measurements per irradiation. The results indicate the robustness of the developed non-destructive beam current measurement setup and build the foundation of the purely beam-based on- and offline dosimetry.
To establish the beam-based approach versus the standard dosimetry via metallic foil activation, dedicated irradiations of titanium foils have been carried out at the BIC. The resulting proton fluences, determined with either method, yield comparable values whereas the beam-based dosimetry consistently provides lower relative uncertainties of ≤ 5 %, dominated by the beam current error. Additionally, these irradiations have been performed with varying parameters of the irradiation routine, verifying the independence of the applied fluence of the routines parametrization. The beam-based dosimetry yields spatial information and facilitates online fluence monitoring, enabling on-the-fly identification and correction of deficiencies in the applied fluence distribution. This results in highly uniform fluence profiles with variations of $\ll 1$ %, significantly smaller than the uncertainties, and allows for versatile irradiation campaigns with custom fluence distributions.
Simulations of the energy degradation and corresponding distributions on transmission into the irradiation setup yield proton energies of (12.28 ± 0.06) MeV at the DUT position for typical accelerator operation. Using these proton energies, electrical characterization of six 150 µm thin *LFoundry* sensors pre- and post-irradiation shows excellent agreement with the expected leakage current increase with fluence and allows for an extraction of the hardness factor $\kappa_p = 3.75 \pm 0.12$. This corresponds to the highest NIEL scaling with the lowest relative uncertainty among the sites in Birmingham, at KIT and at CERN. Considering the non-negligible energy loss within the silicon, the determined hardness factor corresponds to a mean proton energy of (11.75 ± 0.08) MeV. These findings, in combination with the available beam currents at the BIC, allow for irradiation to $\geq 10^{16}\ \mathrm{n_{eq}/cm^2}$ within one day of accelerator operation. In contrast to the aforementioned sites, the comparatively low proton energy at the BIC imposes limits on the maximum DUT thickness to ensure accurate NIEL scaling. A limit of 300 µm is suggested from simulations to maintain an uncertainty of ≤ 10 % on the NIEL scaling, for which an increased hardness factor and respective error of $\kappa_p = 4.0 \pm 0.4$ is assumed.

The developed and characterized infrastructure at the BIC has been used to perform precision radiation hardness tests of the ATLAS ITk pixel detector assembly, consisting of an `ITkPixV1.1` readout chip and *SINTEF* 3D silicon sensor. Using the possibility to power, read out and measure DUTs during the irradiation routine, mixed NIEL and TID irradiations with protons have been conducted, up to the anticipated EOL radiation levels of the corresponding detector component of $10^{16}\ \mathrm{n_{eq}/cm^2}$ and 1 Grad, respectively.
Separated into a low- and high-dose part, the TID-induced gate delay of the readout chips ROs is measured with resolutions and dose rates comparable to typical X-ray studies for the initial few Mrad, followed by irradiation in 128 Mrad as well as $10^{15}\ \mathrm{n_{eq}/cm^2}$ steps. The development of the RO frequencies with dose is in line with the results obtained via X-rays whereas the the absolute values

show significantly smaller gate delay for the same dose with protons. This coincides with observations where the resulting gate delay is approximately a factor of two larger for X-rays compared to to protons for the same dose and RO type, indicating that TID effects due to proton irradiation are considerably less. This is possibly a result of the two to three orders of magnitude higher dose rates when using MeV protons compared to typical X-ray setups. With the maximum RO delay of 30 % at 1.2 Grad, the `ITkPix` chip comfortably meets the requirement (ensuring functionality) of ≤ 200 % gate delay.
Investigation of the sensor IV properties over the course of the irradiation campaign shows the anticipated leakage current increase with fluence, allowing for validation the previously determined proton hardness factor. After the anticipated fluence levels for the ATLAS ITk, the power dissipation up to 150 V stays a factor of three below the imposed limit of 40 mW cm^{-2}.
Characterization of the performance of the `ITkPix` assembly after the combined NIEL and TID damage show only marginal changes, after retuning, in the chip's threshold and noise levels with irradiation, indicating full functionality. A test beam campaign at the DESY II facility allows for hit detection efficiency studies, using the *DURANTA* telescope setup. Here, for bias voltages between 20 – 95 V, efficiencies of up to 91 % are extracted after a NIEL fluence of 10^{16} n_{eq}/cm^2. This result falls short of similar studies using the same sensor and the ATLAS ITk criteria by 6 %. Due to time constraints, further investigations could not be conducted. Nevertheless, these findings show a prominent headroom with regard to power dissipation, allowing for significantly higher bias voltages, above 150 V, for which an achievement of the ATLAS requirement of 97 % efficiency appears possible.

Appendix

A.1 Error Propagation & Calculation

The measurements within this chapter are subject to systematic and/or statistical uncertainties. Wherever feasible, the error propagation within the presented analysis is done programmatically, using the *Python* package *uncertainties* [111]. Here, errors propagation is predominantly done analytically and correlations between erroneous variables are taken into account. Otherwise, the error propagation is performed according to

$$\Delta f(x_0, \ldots, x_n) \approx \sqrt{\sum_{i=0}^{n} \left(\frac{\partial f(x_i)}{\partial x_i} \Delta x_i \right)^2}, \tag{A.1}$$

where $x_0, \ldots, x_n$ are erroneous variables to a given model f, assuming independence between variables. In order to account for statistical uncertainties when deriving the mean value from a data set $x = x_0, \ldots, x_n$, the error is constructed from quadratically adding the uncertainty of the mean calculation as well as the standard deviation of the distribution of values as

$$\Delta\tilde{\mu} = \sqrt{\Delta\mu(x)^2 + \sigma(x)^2} \quad \text{with} \quad \mu(x) = \frac{1}{n} \sum_{i=0}^{n} x_i \,, \quad \sigma(x) = \sqrt{\frac{1}{n} \sum_{i=0}^{n} (x_i - \mu(x))^2} \tag{A.2}$$

where $\Delta\tilde{\mu}$ is the adjusted error on the mean calculation μ. Furthermore, in order to fit expected models to measurement data, the *Python* library *scipy* [88] is used. Here, the *scipy.optimize* sub-module is used in case of solely erroneous observables whereas *scipy.odr* is utilized in case of uncertainties on the observables as well as input variables. To visualize the data and corresponding analysis as well as results, the *Python* graphics library *matplotlib* [112] is used.

A.2 *GEANT4* Energy Simulation for Light Ions

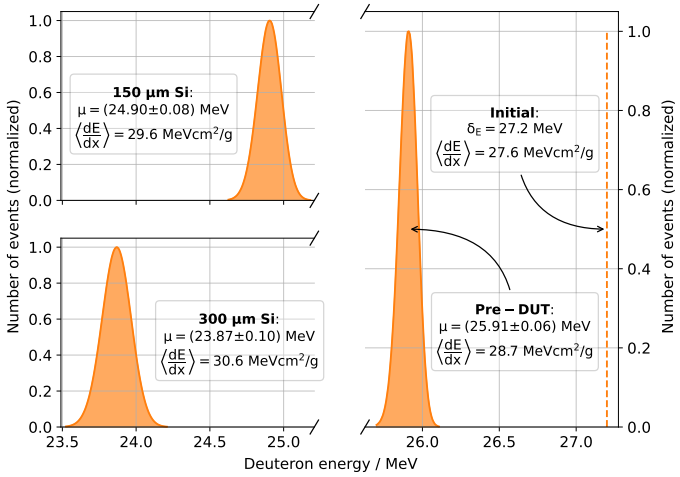

(a) Simulation of deuteron energy distributions

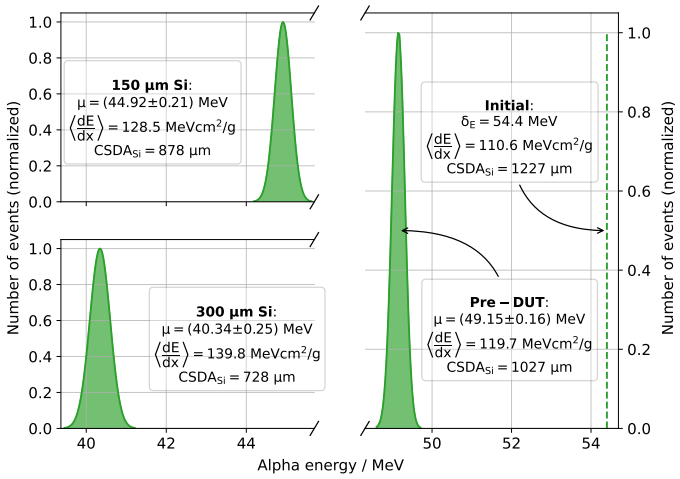

(b) Simulation of alpha energy distributions

Figure A.1: *GEANT4* simulation of pre- (10^8 events) and post- (10^7 events) silicon DUT energy distributions for typical deuterons Fig. A.1(a) and alphas Fig. A.1(b) at the BIC irradiation site. The *stopping power* is calculated according to Eq. (2.1), the projected $\mathrm{CSDA_{Si}}$ range is taken from [19]. The pre-DUT distribution corresponds to the transmission from the accelerator through the configuration shown in Fig. 6.1 onto the DUT (also see Fig. 6.2). Energy distributions after traversing two reference silicon thicknesses, namely 150 µm and 300 µm, are displayed on the left side of the broken axis. 100 % of the light ions are transmitted for all simulations. The initial energy distribution is approximated as a δ function due to the high momentum resolution of up to $\frac{p}{\Delta p} = 30000$ on the *C-way* [62]

A.3 Fluence Determination Method Comparison

$\text{Fluence}_{\text{aim}}$ / p/cm^2		7e13	1e14	3e14	5e14	8e14	10e14	12e14
$\frac{\text{Fluence}_{\text{meas}}}{10^{14}\,\text{p/cm}^2}$	M1(Formula)	0.69 ± 0.02	0.93 ± 0.05	2.99 ± 0.03	4.93 ± 0.05	8.17 ± 0.28	9.47 ± 0.31	12.04 ± 0.01
	M2(Data)	0.69 ± 0.04	0.92 ± 0.05	2.97 ± 0.07	4.92 ± 0.10	8.08 ± 0.11	9.44 ± 0.12	12.04 ± 0.05
	M3(Ti-Foil)	0.73 ± 0.10	1.03 ± 0.13	3.20 ± 0.41	4.99 ± 0.64	7.99 ± 1.03	9.460 ± 1.220	13.86 ± 1.78
Scan speed v_{scan} / mm s^{-1}		90	65	60	70	50	40	35
Row separation Δ_{row} / mm		1.25	0.75	1.50	1.00	0.50	0.25	1.75
Mean beam current $I_{\text{beam}}^{\text{scan}}$ / nA		368	807	661	757	759	950	992
$E_{\text{kin}}^{\text{initial}}\left(E_{\text{kin}}^{\text{DUT}}\right)$ / MeV		13.52(12.19)	13.63(12.31)	13.52(12.19)	13.48(12.15)	13.63(12.31)	13.52(12.19)	13.54(12.21)
Number of rows		24	40	20	30	60	120	26
Number of scans		34	9	65	73	43	16	119
Scan area / mm^2		60.00 × 28.75	60.00 × 29.25	60.00 × 28.5	60.00 × 29.00	60.00 × 29.50	60.00 × 29.75	64.46 × 45.48
Calibration constant λ/ V^{-1}		0.897 ± 0.009	0.906 ± 0.009	0.897 ± 0.009	0.906 ± 0.009	0.906 ± 0.009	0.897 ± 0.009	0.883 ± 0.009
Duration		22 min	11 min	45 min	1 h 1 min	1 h 41 min	1 h 22 min	2 h 58 min
Date		27/09/2022	24/08/2022	27/09/2022	17/08/2022	24/8/2022	28/09/2022	06/09/2023

Table A.1: Overview of irradiation parameters for the comparison of dosimetry via beam-based methods (see Section 5.5) versus the dosimetry via isotope activation (see Section 6.3.1) as depicted in Fig. 6.13. For the irradiations, different combinations of parameters for Eq. (5.13) have been chosen to emphasize the independence of the resulting fluence from the scan parameters. The irradiation to 12×10^{14} protons/c^{2}m was conducted using `irrad_control` version 2.X, where the scan rectangle (see Section 5.4) is constructed programmatically, considering the motorstage as well as beam properties. For all other irradiations `irrad_control` version 1.X was used, where the scan rectangle was chosen manually. The mean scan current $I_{\text{beam}}^{\text{scan}}$ shows the mean beam current while scanning the DUT. The kinetic energy on the DUT is calculated according to the simulation shown in Fig. 6.2.

Sensors ID	S11	S1	S7	S8	S9	S10
Proton fluence / 10^{12} p/cm^2	4.83 ± 0.54	9.67 ± 0.77	19.99 ± 1.01	40.10 ± 1.68	76.16 ± 2.34	160.44 ± 4.59
Scan speed v_{scan} / mm s^{-1}	75	75	62	62	62	70
Row separation Δ_{row} / mm	1.25	1.25	1	1	1	1
Mean beam current $I_{\text{beam}}^{\text{scan}}$ / nA	145 ± 5	146 ± 9	199 ± 1	399 ± 18	398 ± 13	600 ± 16
$E_{\text{kin}}^{\text{initial}}\left(E_{\text{kin}}^{\text{DUT}}\right)$ / MeV	13.510(12.180)	13.500(12.169)	13.571(12.246)	13.571(12.246)	13.482(12.149)	13.482(12.149)
Number of rows	43	43	54	54	54	54
Number of scans	5	10	10	10	19	30
Scan area / mm^2	81.22 × 53.48	81.22 × 53.48	80.51 × 53.48	80.51 × 53.48	80.51 × 53.48	80.93 × 53.48
Calibration constant λ/ V^{-1}	0.897 ± 0.009	0.897 ± 0.009	0.897 ± 0.009	0.897 ± 0.009	0.897 ± 0.009	
Duration	5 minute 49 s	13 minute 13 s	16 minute 2 s	16 minute 35 s	36 minute 54 s	53 minute 3 s
Date	12/09/2023	12/09/2023	13/09/2023	13/09/2023	14/09/2023	14/09/2023

Table A.2: Overview of parameters of LF sensor irradiations for determination of the proton hardness factor. The mean scan current $I_{\text{beam}}^{\text{scan}}$ shows the mean beam current while scanning the DUT. The kinetic energy on the DUT is calculated according to the simulation shown in Fig. 6.2.

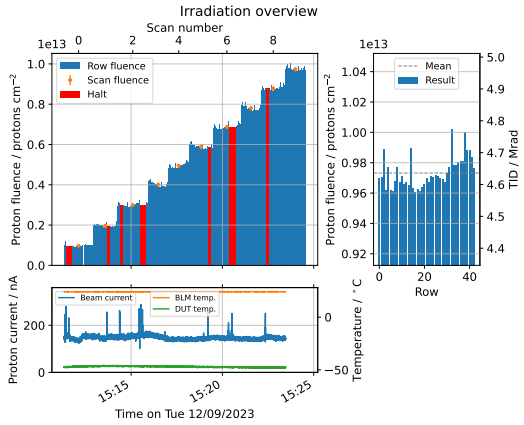

(a) Irradiation overview S1

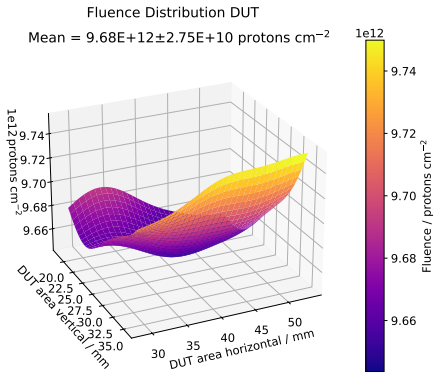

(b) Resulting proton fluence distribution S1

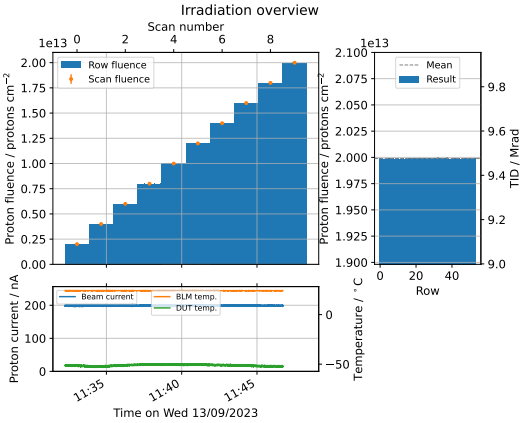

(c) Irradiation overview S7

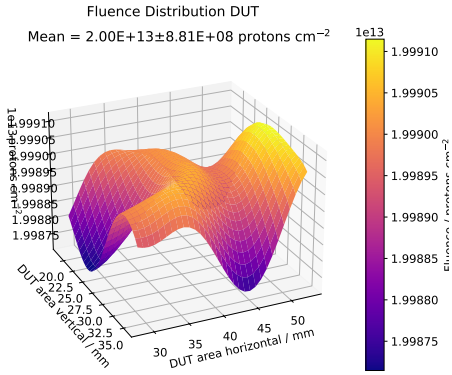

(d) Resulting proton fluence distribution S7

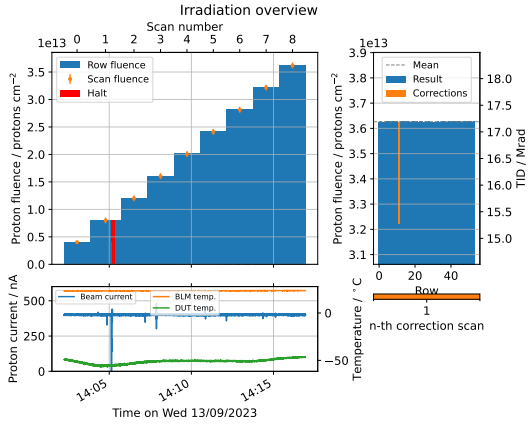

(e) Irradiation overview S8 part one

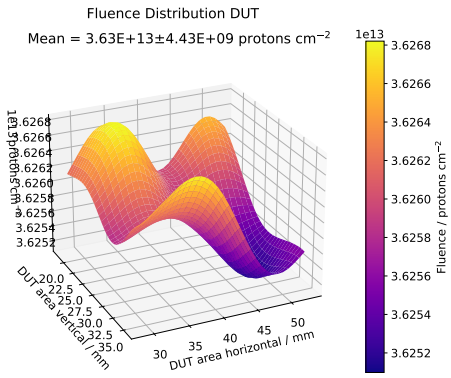

(f) Resulting proton fluence distribution S8 part one

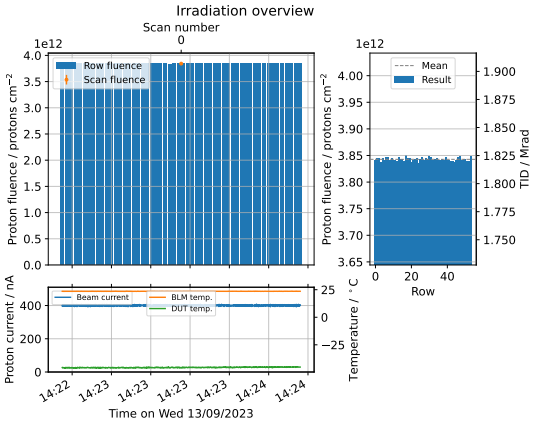

(g) Irradiation overview S8 part two

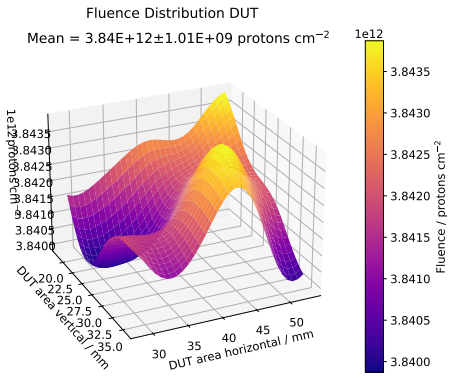

(h) Resulting proton fluence distribution S8 part two

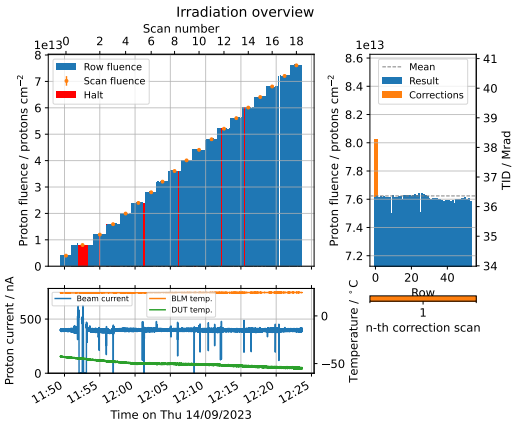

(i) Irradiation overview S9

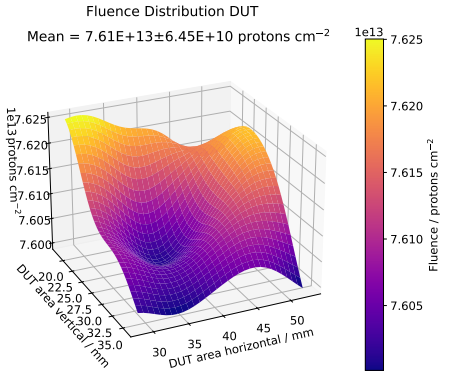

(j) Resulting proton fluence distribution S9

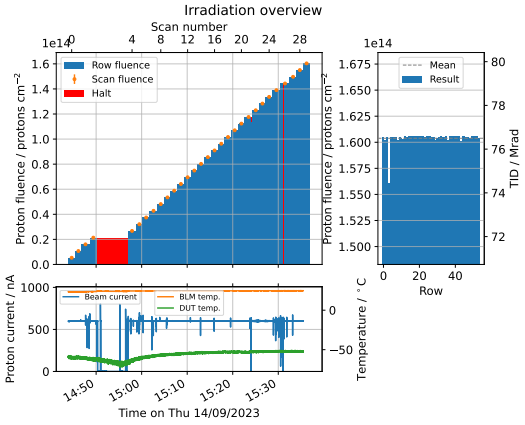

(k) Irradiation overview S10

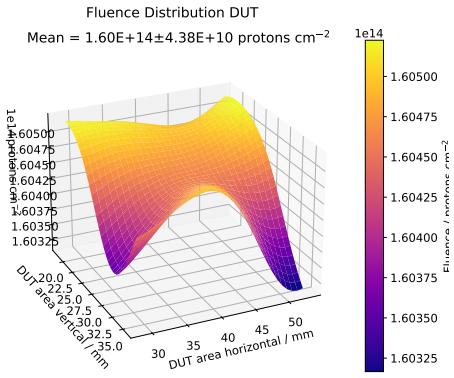

(l) Resulting proton fluence distribution S10

Figure A.2: Overviews and resulting proton fluence distributions of irradiations of LF sensors, performed for extraction of the proton hardness factor at the BIC, generated by `irrad_control`. The irradiation for sensor S8 is split into two parts due to an error during the irradiation routine, requiring a restart of the procedure.

A.5 Gamma Spectroscopy at the HISKP

The HISKP gamma spectroscopy center facilitates spectroscopic analysis of irradiated devices at the BIC. Samples are measured in a lead-shielded container, providing low background, in front of a 16 k channel germanium detector. Using reference radioactive sources with well-distributed gamma lines such as ^{152}Eu, allows for energy as well as activity calibration for a given distance from the detector. Repeating the measurement with the sample under investigation in conjunction with the calibration information, allows for identification of isotopes as well as their activity via the gamma line energies and relative intensities respectively. This functionality is provided by the `irrad_spectroscopy` [78] package, a spectroscopy and dose calculation utility, initially developed during [58] and matured within this work. Using an internal isotope table, `irrad_spectroscopy` identifies isotopes from the respective sample spectrum and provides dose (rate) calculations for different materials. Within the irradiation facility at the BIC, the gamma spectroscopy center in combination with `irrad_spectroscopy` are used to estimate possible return and shipping times.

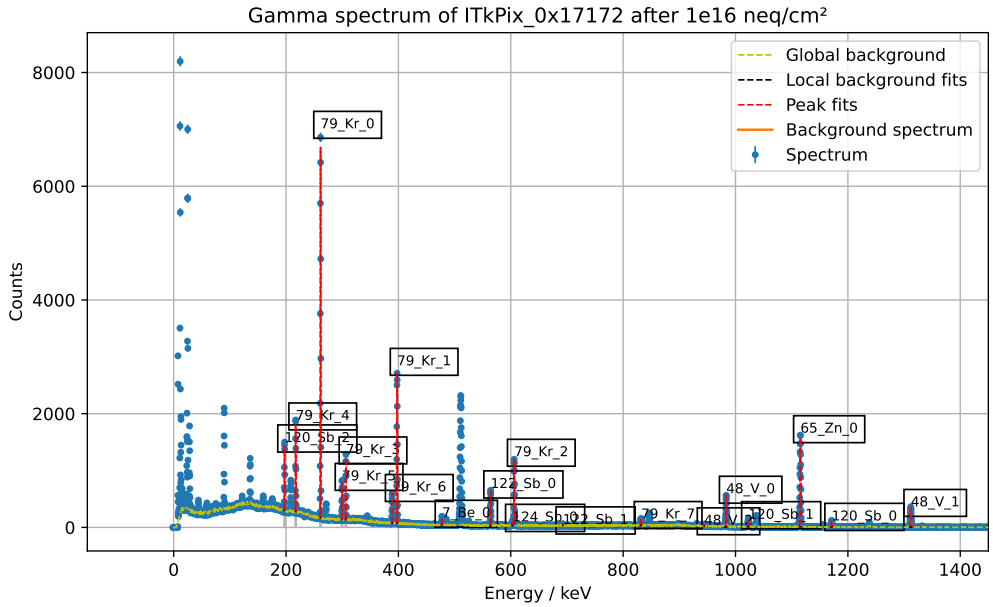

Figure A.3: Gamma spectrum of the `ITkPix` assembly from Chapter 7 after irradiation to a fluence of 10^{16} n_{eq}/cm^2 at BIC. The spectrum was recorded at the HISKP spectroscopy center, approximately three days after the last irradiation step was applied, and analyzed using `irrad_spectroscopy` [78]. The typical isotopes, as listed in Table 5.2, are present.

A.6 ITkPix Irradiations

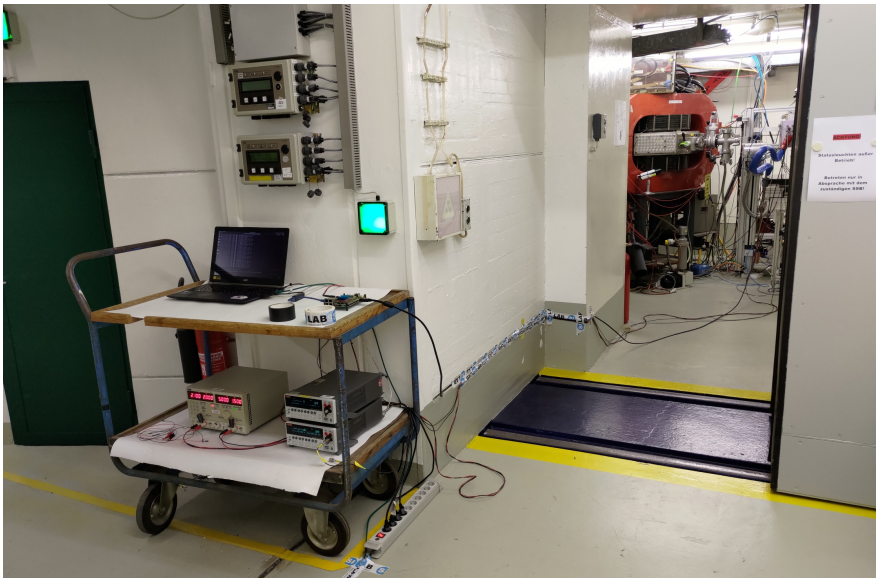

Figure A.4: Measurement setup outside *high-current room* at the BIC (cf. Fig. 5.3) during the irradiation campaign of the `ITkPixV1.1`. A measurement computer, two *Keithley 2410* SMUs, a low voltage power supply as well as the *BDAQ53* board are situated in front of the movable door, on a wagon. The cables are laid along the wall over an approximately 8 m distance, allowing to operate the equipment shielded from radiation as well as access to the setup while the irradiation is in progress.

Proton		Fluence / n_{eq}/cm^2		
energy / MeV	stopping power / MeV cm^2 g^{-1}	Applied	Total	Date
12.17	29.73	$(4.89 \pm 0.15) \times 10^{13}$	$(4.89 \pm 0.15) \times 10^{13}$	29/09/2023
12.18	29.71	$(9.97 \pm 0.36) \times 10^{14}$	$(1.05 \pm 0.04) \times 10^{15}$	17/10/2023
12.16	29.75	$(9.96 \pm 0.36) \times 10^{14}$	$(2.04 \pm 0.05) \times 10^{15}$	17/10/2023
12.15	29.77	$(1.00 \pm 0.04) \times 10^{15}$	$(3.04 \pm 0.06) \times 10^{15}$	18/10/2023
12.15	29.77	$(1.00 \pm 0.04) \times 10^{15}$	$(4.04 \pm 0.07) \times 10^{15}$	18/10/2023
12.15	29.77	$(1.00 \pm 0.04) \times 10^{15}$	$(5.04 \pm 0.08) \times 10^{15}$	18/10/2023
12.16	29.74	$(9.99 \pm 0.36) \times 10^{14}$	$(6.04 \pm 0.09) \times 10^{15}$	19/10/2023
12.16	29.74	$(9.99 \pm 0.36) \times 10^{14}$	$(7.04 \pm 0.09) \times 10^{15}$	19/10/2023
12.16	29.74	$(9.99 \pm 0.36) \times 10^{14}$	$(8.04 \pm 0.10) \times 10^{15}$	19/10/2023
12.15	29.77	$(9.73 \pm 0.35) \times 10^{14}$	$(9.01 \pm 0.11) \times 10^{15}$	20/10/2023
12.15	29.76	$(1.03 \pm 0.04) \times 10^{15}$	$(1.00 \pm 0.01) \times 10^{16}$	20/10/2023

Table A.3: Overview of irradiations of the `ITkPix` assembly at the BIC during September to October 2023. The given proton energies as well as stopping powers correspond to the on-DUT values.

A.7 ITkPix Sensor Temperature Measurement in Irradiation Setup

Throughout the irradiation campaign, described in Section 7.2, several IV curves at different fluence levels were recorded. During these measurements, the `ITkPix` assembly was situated inside the irradiation setup, as shown in Fig. 7.5, and the cooling system was running between −20 – −30 °C. Here, as reference for scaling the IV behavior according to Eq. (2.20), the sensor temperature was approximated by reading of the on-board SCC NTCs.
Due to the configuration of the irradiation setup, specifically the cool box and system, the temperature readings obtained from the on-SCC as well as setup reference NTC lie below the actual DUT temperature. The setup thermistor is located inside the mounting mechanism of the cooling structure, measuring a temperature rather corresponding to the incoming gas. Similarly, the SCC thermistors are situated directly in the stream of the cool gas. Subsequently, both NTCs report lower readings compared to the actual temperature of the DUT. The chip-internal sensors are placed in the digital chip bottom [100], therefore subjected to the chips heat dissipation.

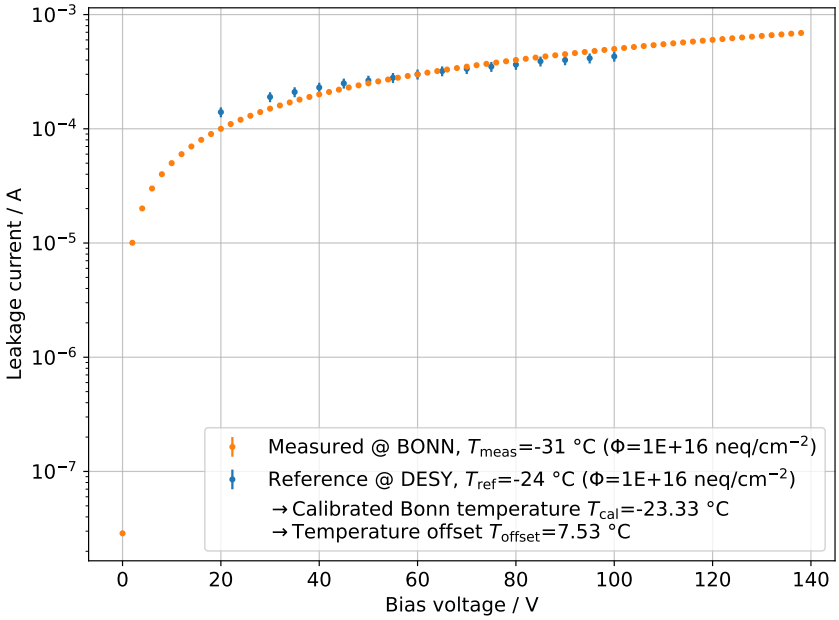

Figure A.5: Temperature calibration for the IV recordings performed inside the irradiation setup at the BIC. A reference measurement at the same sensor fluence is performed inside the test beam cooling setup [106] at DESY. Each entry corresponds to the mean of five measurements, the uncertainty is the respective standard deviation.

To deduce the actual sensor temperature during IV measurements inside the irradiation setup, a calibration was performed where a constant offset between the sensor and NTC temperatures is assumed for a steady cool gas flow. Consequently, the IV curve after 10^{16} n_{eq}/cm^2 was measured inside the test beam cooling setup, as shown in Fig. 7.15(c), which is characterized and optimized in [106]. Here, the sensor as well as the temperature reference, a *Sensirion SHT85*, are not situated directly in the flow of cool gas but are more passively cooled via the surrounding atmosphere. Consequently, the *SHT85* reading is assumed to more-closely resemble the actual sensor temperature in this setup.

Comparison to the IV curve measured inside the irradiation setup after the same fluence level and usage of Eq. (2.20) allow for extraction of the approximate temperature offset. Both measurements are shown Fig. A.5. The reference measurement in the test beam cooling setup is performed at $T_{\text{ref}} = -24\,^{\circ}\text{C}$, the measured temperature during recording the IV behavior in the irradiation cool box is $T_{\text{meas}} = -31\,^{\circ}\text{C}$, both via a *Keithley 2410* SMU. Here, the values represent the mean temperature over the entire measurement. As visible, both IV curves approximately overlap, indicating visibly that the offset lies close to the temperature difference between the reference measurement at DESY and the one in Bonn. Numerical approximating the minimal deviation between the two measurements yields a calibrated temperature of $T_{\text{cal}} = 23.33\,^{\circ}\text{C}$ for IV measurement inside the Bonn irradiation setup, as opposed to the measured $-31\,^{\circ}\text{C}$. Subsequently, the resulting offset of $T_{\text{offset}} = 7.53\,^{\circ}\text{C}$ is added to the temperatures during IV curve measurements inside the irradiation setup at the BIC when scaling via Eq. (2.20).

A.8 Beam Telescope Positions at DESY

Detector	`M26 1`	`M26 2`	`M26 3`	`ITkPix`	`M26 4`	`M26 5`	`M26 6`	`FE-I4`
Position / µm	0	30 250	61 800	148 500	202 550	226 350	250 700	288 150

Table A.4: Measured z-positions of the *DURANTA* telescope setup used during the October 2023 test beam campaign, shown in Fig. 7.15. The z-positions are required for initial alignment and subsequent track reconstruction using the BTA [110] software. The `Mimosa26` telescope planes are denoted as `M26 X` where X corresponds to the index of the sensor. The plane indexing as well as the relative position origin increase downstream with regard to the incoming beam, from right-to-left in Figs. 7.14 and 7.15(a).

Bibliography

[1] X. Llopart et al. “Timepix4, a large area pixel detector readout chip which can be tiled on 4 sides providing sub-200 ps timestamp binning”. In: *Journal of Instrumentation* 17.01 (Jan. 2022), p. C01044. DOI: 10.1088/1748-0221/17/01/C01044. URL: https://dx.doi.org/10.1088/1748-0221/17/01/C01044.

[2] M. K. Gaillard, P. D. Grannis and F. J. Sciulli. “The standard model of particle physics”. In: *Reviews of Modern Physics* 71.2 (Mar. 1999), S96–S111. DOI: 10.1103/revmodphys.71.s96. URL: http://dx.doi.org/10.1103/RevModPhys.71.S96.

[3] G. Aad et al. “Observation of a new particle in the search for the Standard Model Higgs boson with the ATLAS detector at the LHC”. In: *Physics Letters B* 716.1 (2012), pp. 1–29. DOI: https://doi.org/10.1016/j.physletb.2012.08.020. URL: https://www.sciencedirect.com/science/article/pii/S037026931200857X.

[4] S. Chatrchyan et al. “Observation of a new boson at a mass of 125 GeV with the CMS experiment at the LHC”. In: *Physics Letters B* 716.1 (2012), pp. 30–61. DOI: https://doi.org/10.1016/j.physletb.2012.08.021. URL: https://www.sciencedirect.com/science/article/pii/S0370269312008581.

[5] H. E. Haber. *Higgs Boson Physics – The View Ahead*. 2023. arXiv: 2210.00449 [hep-ph]. URL: https://arxiv.org/abs/2210.00449.

[6] P. D. Group et al. “Review of Particle Physics”. In: *Progress of Theoretical and Experimental Physics* 2020.8 (Aug. 2020), p. 083C01. DOI: 10.1093/ptep/ptaa104. eprint: https://academic.oup.com/ptep/article-pdf/2020/8/083C01/34673722/ptaa104.pdf. URL: https://doi.org/10.1093/ptep/ptaa104.

[7] O. Aberle et al. *High-Luminosity Large Hadron Collider (HL-LHC): Technical design report*. CERN Yellow Reports: Monographs. Geneva: CERN, 2020. DOI: 10.23731/CYRM-2020-0010. URL: https://cds.cern.ch/record/2749422.

[8] T. A. Collaboration. *Technical Wiki of Radiation Simulation Public Results*. URL: https://twiki.cern.ch/twiki/bin/view/AtlasPublic/RadiationSimulationPublicResults (visited on 03/09/2024).

[9] *Technical Design Report for the ATLAS Inner Tracker Pixel Detector*. Tech. rep. Geneva: CERN, 2017. DOI: 10.17181/CERN.FOZZ.ZP3Q. URL: https://cds.cern.ch/record/2285585.

[10] The RD53 Collaboration. *RD53 Collaboration Homepage*. homepage. URL: https://rd53.web.cern.ch/ (visited on 03/06/2024).

[11] B. Gkotse et al. “IRRAD: The New 24 GeV/c Proton Irradiation Facility at CERN”. In: *12th International Topical Meeting on Nuclear Applications of Accelerators*. 2015, pp. 182–187.

[12] P. Dervan et al. “The Birmingham Irradiation Facility”. In: *Nucl. Instrum. Methods Phys. Res., A* 730 (2013), pp. 101–104. URL: https://cds.cern.ch/record/1999143.

[13] Dierlamm, Alexander. *Irradiations in Karlsruhe*. Talk given on 16th RD50 workshop in Barcelona, Spain. June 2010. URL: https://indico.cern.ch/event/86625/contributions/2103519/ (visited on 14/03/2024).

[14] R. Diener et al. “The DESY II test beam facility”. In: *Nuclear Instruments and Methods in Physics Research Section A: Accelerators, Spectrometers, Detectors and Associated Equipment* 922 (2019), pp. 265–286. DOI: https://doi.org/10.1016/j.nima.2018.11.133. URL: https://www.sciencedirect.com/science/article/pii/S0168900218317868.

[15] N. Wermes. “Pixel detectors ... where do we stand?” In: *Nuclear Instruments and Methods in Physics Research Section A: Accelerators, Spectrometers, Detectors and Associated Equipment* 924 (2019). 11th International Hiroshima Symposium on Development and Application of Semiconductor Tracking Detectors, pp. 44–50. DOI: https://doi.org/10.1016/j.nima.2018.07.003. URL: https://www.sciencedirect.com/science/article/pii/S016890021830826X.

[16] H. Kolanoski and N. Wermes. *Particle Detectors*. Oxford University Press, June 2020.

[17] D.-L. Pohl. “3D-Silicon and Passive CMOS Sensors for Pixel Detectors in High Radiation Environments”. PhD thesis. Universität Bonn, 2019.

[18] L. Rossi et al. *Pixel Detectors. From Fundamentals to Applications*. Particle Acceleration and Detection. Springer, 2006. DOI: 10.1007/3-540-28333-1.

[19] M. Berger, J. Coursey and M. Zucker. *ESTAR, PSTAR, and ASTAR: Computer Programs for Calculating Stopping-Power and Range Tables for Electrons, Protons, and Helium Ions (version 1.21)*. en. Jan. 1999.

[20] Y. M. Dieter. “Development and Characterisation of Passive CMOS Sensors for Pixel Detectors in High Radiation Environments”. PhD thesis. Universität Bonn, June 2022.

[21] C. Bespin Valero. “Characterization of the TJ-Monopix2 Depleted Monolithic Active Pixel Sensor for High-Energy Physics Experiments”. PhD thesis. Universität Bonn, 2024.

[22] A. Chilingarov. “Temperature dependence of the current generated in Si bulk”. In: *Journal of Instrumentation* 8 (Oct. 2013), P10003–P10003. DOI: 10.1088/1748-0221/8/10/P10003.

[23] S. Mägdefessel et al. “Understanding the Frequency Dependence of Capacitance Measurements of Irradiated Silicon Detectors”. In: (Jan. 2023). arXiv: 2301.09371 [physics.ins-det].

[24] G.-F. Dalla Betta and J. Ye. “Silicon Radiation Detector Technologies: From Planar to 3D”. In: *Chips* 2.2 (2023), pp. 83–101. DOI: 10.3390/chips2020006. URL: https://www.mdpi.com/2674-0729/2/2/6.

[25] H. Pernegger. “The Pixel Detector of the ATLAS experiment for LHC Run-2”. In: *Journal of Instrumentation* 10.06 (June 2015), p. C06012. DOI: 10.1088/1748-0221/10/06/C06012. URL: https://dx.doi.org/10.1088/1748-0221/10/06/C06012.

[26] S. Terzo et al. “Novel 3D Pixel Sensors for the Upgrade of the ATLAS Inner Tracker”. In: *Frontiers in Physics* 9 (2021). DOI: 10.3389/fphy.2021.624668. URL: https://www.frontiersin.org/journals/physics/articles/10.3389/fphy.2021.624668.

[27] C. Bespin et al. “Development and characterization of a DMAPS chip in TowerJazz 180 nm technology for high radiation environments”. In: *Nuclear Instruments and Methods in Physics Research Section A: Accelerators, Spectrometers, Detectors and Associated Equipment* 1040 (July 2022), p. 167189. DOI: 10.1016/j.nima.2022.167189.

[28] I. Caicedo Sierra et al. “Development and testing of a radiation-hard large-electrode DMAPS design in a 150 nm CMOS process”. In: *Nuclear Instruments and Methods in Physics Research Section A: Accelerators, Spectrometers, Detectors and Associated Equipment* 1040 (July 2022), p. 167224. DOI: 10.1016/j.nima.2022.167224.

[29] *Expected tracking and related performance with the updated ATLAS Inner Tracker layout at the High-Luminosity LHC*. Tech. rep. All figures including auxiliary figures are available at https://atlas.web.cern.ch/Atlas/GROUPS/PHYSICS/PUBNOTES/ATL-PHYS-PUB-2021-024. Geneva: CERN, 2021. URL: https://cds.cern.ch/record/2776651.

[30] L. Gonella. “The ATLAS ITk detector system for the Phase-II LHC upgrade”. In: *Nuclear Instruments and Methods in Physics Research Section A: Accelerators, Spectrometers, Detectors and Associated Equipment* 1045 (2023), p. 167597. DOI: https://doi.org/10.1016/j.nima.2022.167597. URL: https://www.sciencedirect.com/science/article/pii/S0168900222008890.

[31] CERN. *The Large Hardon Collider*. Accelerator homepage. URL: https://home.cern/science/accelerators/large-hadron-collider (visited on 01/10/2024).

[32] CERN. *Facts and figures about the LHC*. FAQ page. URL: https://home.cern/resources/faqs/facts-and-figures-about-lhc (visited on 01/10/2024).

[33] CERN. *Longer term LHC schedule*. LHC schdule page. URL: https://lhc-commissioning.web.cern.ch/schedule/LHC-long-term.htm (visited on 01/10/2024).

[34] C. Service graphique. “Overall view of the LHC. Vue d’ensemble du LHC”. In: (2014). General Photo. URL: https://cds.cern.ch/record/1708849.

[35] M. Mironova. “Radiation Tolerance of the ITkPixV1 Pixel Readout Chip”. In: *Search for Higgs Boson Decays to Charm Quarks with the ATLAS Experiment and Development of Novel Silicon Pixel Detectors*. Cham: Springer Nature Switzerland, 2023, pp. 141–178. DOI: 10.1007/978-3-031-36220-0_6. URL: https://doi.org/10.1007/978-3-031-36220-0_6.

[36] T. L. H. W. Group. *Higgs cross sections and decay branching ratios*. TWiki. URL: https://twiki.cern.ch/twiki/bin/view/LHCPhysics/HiggsXSBR (visited on 02/10/2024).

[37] G. Aad et al. “The ATLAS experiment at the CERN Large Hadron Collider: a description of the detector configuration for Run 3”. In: *Journal of Instrumentation* 19.05 (May 2024), P05063. DOI: 10.1088/1748-0221/19/05/p05063. URL: http://dx.doi.org/10.1088/1748-0221/19/05/P05063.

[38] A. Outreach. "ATLAS Fact Sheet : To raise awareness of the ATLAS detector and collaboration on the LHC". 2010. DOI: 10.17181/CERN.1LN2.J772. URL: https://cds.cern.ch/record/1457044.

[39] A. Collaboration. "ATLAS Inner Tracker (ITk) Schematics". General Photo. 2024. URL: https://cds.cern.ch/record/2908925.

[40] *Technical Design Report for the ATLAS Inner Tracker Strip Detector*. Tech. rep. Geneva: CERN, 2017. URL: https://cds.cern.ch/record/2257755.

[41] J. Christiansen. *RD53 Pixel Readout Integrated Circuits for ATLAS and CMS HL-LHC Upgrades*. Tech. rep. Geneva: CERN, 2024. URL: https://cds.cern.ch/record/2898416.

[42] T. Heim. *A bare ITkPixV1 readout chip mounted to single chip carrier card*. Berkeley Lab. 20th Oct. 2023. URL: https://physicalsciences.lbl.gov/2023/10/20/berkeley-lab-develops-next-generation-pixel-detector-and-readout-chip-technology-for-hl-lhc/ (visited on 30/09/2024).

[43] K. Mauer. "Study of TID Radiation Effects and Characterization of the ITkPixV2 Readout Chip for the ATLAS ITk Pixel Detector Upgrade". MA thesis. Universität Bonn, Apr. 2024.

[44] M. Daas et al. "BDAQ53, a versatile pixel detector readout and test system for the ATLAS and CMS HL-LHC upgrades". In: *Nuclear Instruments and Methods in Physics Research Section A: Accelerators, Spectrometers, Detectors and Associated Equipment* 986 (2021), p. 164721. DOI: https://doi.org/10.1016/j.nima.2020.164721. URL: https://www.sciencedirect.com/science/article/pii/S0168900220311189.

[45] P. Ahlburg. "Development of a Laboratory Readout System for DEPFET Pixel Detector Modules and Investigation of Radiation Backgrounds at the SuperKEKB Accelerator". PhD thesis. Universität Bonn, Oct. 2022.

[46] The RD50 Collaboration. *RD53 Collaboration Homepage*. homepage. URL: https://rd50.web.cern.ch/ (visited on 11/10/2024).

[47] M. Moll. "Displacement Damage in Silicon Detectors for High Energy Physics". In: *IEEE Transactions on Nuclear Science* 65.8 (Aug. 2018), pp. 1561–1582. DOI: 10.1109/TNS.2018.2819506.

[48] F. Faccio et al. "Radiation-Induced Short Channel (RISCE) and Narrow Channel (RINCE) Effects in 65 and 130 nm MOSFETs". In: *IEEE Transactions on Nuclear Science* 62.6 (2015), pp. 2933–2940. DOI: 10.1109/TNS.2015.2492778.

[49] G. Borghello et al. "Ionizing radiation damage in 65 nm CMOS technology: Influence of geometry, bias and temperature at ultra-high doses". In: *Microelectronics Reliability* 116 (Jan. 2021), p. 114016. DOI: 10.1016/j.microrel.2020.114016.

[50] L. Gonella et al. "Total Ionizing Dose effects in 130-nm commercial CMOS technologies for HEP experiments". In: *Nuclear Instruments and Methods in Physics Research Section A: Accelerators, Spectrometers, Detectors and Associated Equipment* 582.3 (2007). VERTEX 2006, pp. 750–754. DOI: https://doi.org/10.1016/j.nima.2007.07.068. URL: https://www.sciencedirect.com/science/article/pii/S0168900207015501.

[51] M. Huhtinen. “Simulation of non-ionising energy loss and defect formation in silicon”. In: *Nuclear Instruments and Methods in Physics Research Section A: Accelerators, Spectrometers, Detectors and Associated Equipment* 491.1 (2002), pp. 194–215. DOI: https://doi.org/10.1016/S0168-9002(02)01227-5. URL: https://www.sciencedirect.com/science/article/pii/S0168900202012275.

[52] M. S. Lazo, D. M. Woodall and P. J. McDaniel. *Silicon and Silicon dioxide neutron damage functions*. Tech. rep. SAND–87-0098-Vol1. United States, 1987, pp. 85–104. URL: http://inis.iaea.org/search/search.aspx?orig_q=RN:22038475.

[53] M. Moll. “Radiation damage in silicon particle detectors: Microscopic defects and macroscopic properties”. PhD thesis. Hamburg U., 1999. URL: http://www-library.desy.de/cgi-bin/showprep.pl?desy-thesis99-040.

[54] P. Allport et al. “Experimental determination of proton hardness factors at several irradiation facilities”. In: *Journal of Instrumentation* 14 (Dec. 2019), P12004–P12004. DOI: 10.1088/1748-0221/14/12/P12004.

[55] G. Kramberger et al. “Effective trapping time of electrons and holes in different silicon materials irradiated with neutrons, protons and pions”. In: *Nuclear Instruments & Methods in Physics Research Section A-accelerators Spectrometers Detectors and Associated Equipment* 481 (2002), pp. 297–305. URL: https://api.semanticscholar.org/CorpusID:32775427.

[56] G. Lindström et al. “Radiation hard silicon detectors—developments by the RD48 (ROSE) collaboration”. In: *Nuclear Instruments and Methods in Physics Research Section A: Accelerators, Spectrometers, Detectors and Associated Equipment* 466.2 (2001). 4th Int. Symp. on Development and Application of Semiconductor Tracking Detectors, pp. 308–326. DOI: https://doi.org/10.1016/S0168-9002(01)00560-5. URL: https://www.sciencedirect.com/science/article/pii/S0168900201005605.

[57] G. Ms Jain. “Radiation damage modeling:TCAD simulation”. In: *Proceedings of The 27th International Workshop on Vertex Detectors — PoS(VERTEX2018)*. Vol. 348. 2019, p. 017. DOI: 10.22323/1.348.0017.

[58] P. Wolf. “Development of a Proton Irradiation Site at the Bonn Isochronous Cyclotron”. MA thesis. Universität Bonn, June 2019.

[59] D. Sauerland et al. “Proton Irradiation Site for Si-Detectors at the Bonn Isochronous Cyclotron”. In: *13th Int. Particle Acc. Conf.* (Bangkok, Thailand). International Particle Accelerator Conference 13. JACoW Publishing, June 2022, pp. 130–132. DOI: 10.18429/JACoW-IPAC2022-MOPOST030. URL: https://ipac2022.vrws.de/papers/mopost030.pdf.

[60] D. Sauerland et al. “Proton Irradiation Site for High-Uniformity Radiation Hardness Tests of Silicon Detectors at the Bonn Isochronous Cyclotron”. In: *23rd Int. Conf. on Cyclotrons and their Applications* (Beijing, China). International Conference on Cyclotron and their Applications 23. JACoW Publishing, Dec. 2022.

[61] M. Agena et al. “External Ion Sources and Injection Lines at the Bonn Isochronous Cyclotron”. In: *IEEE Transactions on Nuclear Science* 26.2 (1979), pp. 2156–2159. DOI: 10.1109/TNS.1979.4329826.

[62] F. Hinterberger et al. “The beam handling system at the bonn isochronous cyclotron”. In: *Nuclear Instruments and Methods* 130.2 (1975), pp. 335–346. DOI: https://doi.org/10.1016/0029-554X(75)90033-6. URL: https://www.sciencedirect.com/science/article/pii/0029554X75900336.

[63] D. Sauerland. *Bonn Isochonous Cyclotron Homepage*. 2022. URL: https://www.zyklotron.hiskp.uni-bonn.de/zyklo/bonn_isochronous_cyclotron_EN.html (visited on 28/04/2024).

[64] Zaber Technologies Inc. *Homepage*. URL: https://www.zaber.com (visited on 18/04/2024).

[65] item Industrietechnik GmbH. *Homepage*. URL: https://de.item24.com/en/index.html (visited on 18/04/2024).

[66] Thorlabs. *Homepage*. URL: https://www.thorlabs.com/ (visited on 19/04/2024).

[67] Waveshare. *Raspberry Pi High-Precision AD/DA Expansion Board, Homepage*. URL: https://www.waveshare.com/High-Precision-AD-DA-Board.htm (visited on 12/04/2024).

[68] Wolf, Pascal. *irrad_control: DAQ, Control and Analysis Software for the Proton Irradiation Site at Bonn University*. Github repository. 2024. URL: https://github.com/cyclotron-bonn/irrad_control (visited on 18/03/2024).

[69] H. Garnir, P. Dumont and Y. Baudinet-Robinet. “Secondary electron emission from thin foils under fast ion bombardment”. In: *Nuclear Instruments and Methods in Physics Research* 202.1 (1982), pp. 187–192. DOI: https://doi.org/10.1016/0167-5087(82)90394-5. URL: https://www.sciencedirect.com/science/article/pii/0167508782903945.

[70] H. Beck and R. Langkau. “Die Sekundärelektronen-Ausbeute verschiedener Materialien bei Beschußmit leichten Ionen hoher Energie / Secondary Electron Yield from Various Materials under the Impact of Light Ions at High Energies”. In: *Zeitschrift für Naturforschung A* 30 (June 2014). DOI: 10.1515/zna-1975-0810.

[71] Systèmes Dassault. *Simula CST Studio Suite*. Website. URL: https://www.3ds.com/products/simulia/cst-studio-suite (visited on 14/02/2024).

[72] C. Peterson and R. Laubert. “Carbon Accumulation on Target Surfaces Irradiated by Protons”. In: *IEEE Transactions on Nuclear Science* 24.3 (1977), pp. 1542–1544. DOI: 10.1109/TNS.1977.4329004.

[73] Analog Devices. *Precision, 20 MHz, CMOS, Rail-to-Rail Input/Output Operational Amplifiers AD8615/16/18 data sheet*. Data sheet. URL: https://www.analog.com/media/en/technical-documentation/data-sheets/AD8615_8616_8618.pdf (visited on 19/02/2024).

[74] J. S. Steinhart and S. R. Hart. “Calibration curves for thermistors”. In: *Deep Sea Research and Oceanographic Abstracts* 15.4 (1968), pp. 497–503. DOI: https://doi.org/10.1016/0011-7471(68)90057-0. URL: https://www.sciencedirect.com/science/article/pii/0011747168900570.

[75] Arduino. *Arduino Nano microcontroller overview*. Documentation page. 2024. URL: https://docs.arduino.cc/hardware/nano/ (visited on 20/02/2024).

[76] Knopp, Béla. *nano_util_board: PCB design of the Arduino-Nano-based utility board*. Github repository. 2023. URL: https://github.com/cyclotron-bonn/nano_util_board (visited on 19/02/2024).

[77] P. Wolf et al. "A beam-driven proton irradiation setup for precision radiation damage tests of silicon detectors". In: *Nuclear Inst. and Methods in Physics Research, A (NIMA)* (2024). DOI: 10.1016/j.nima.2024.169358.

[78] Wolf, Pascal. *irrad_spectroscopy: A Python-based Gamma / X-Ray Spectroscopy and Dosimetry Tool*. Github repository. 2024. URL: https://github.com/silab-bonn/irrad_spectroscopy (visited on 18/03/2024).

[79] N. Soppera, M. Bossant and E. Dupont. "JANIS 4: An Improved Version of the NEA Java-based Nuclear Data Information System". In: *Nuclear Data Sheets* 120 (2014), pp. 294–296. DOI: https://doi.org/10.1016/j.nds.2014.07.071. URL: https://www.sciencedirect.com/science/article/pii/S0090375214005237.

[80] National Nuclear Data Center. *NuDat 3.0: Nuclear Database Web Application*. URL: https://www.nndc.bnl.gov/nudat/ (visited on 17/02/2025).

[81] A. Dierlamm. "Untersuchung zur Strahlenhärte von Silizium-Sensoren". URL. PhD thesis. 2003. URL: https://ekp-invenio.physik.uni-karlsruhe.de/record/45039.

[82] T. Senger. "Erweiterung und Charakterisierung der Strahldiagnostik des Bestrahlungsplatzes am Bonner Isochronzyklotron". BA thesis. Universität Bonn, Feb. 2020.

[83] Wikipedia, the free encyclopedia. *Gaussian function*. URL: https://en.wikipedia.org/wiki/Gaussian_function#Two-dimensional_Gaussian_function (visited on 06/05/2024).

[84] The YAML Project. *YAML: a human-friendly data serialization language*. URL: https://yaml.org/ (visited on 14/05/2024).

[85] The HDF Group. *HDF homepage*. URL: https://www.hdfgroup.org/ (visited on 28/04/2024).

[86] C. R. Harris et al. "Array programming with NumPy". In: *Nature* 585.7825 (Sept. 2020), pp. 357–362. DOI: 10.1038/s41586-020-2649-2. URL: https://doi.org/10.1038/s41586-020-2649-2.

[87] S. K. Lam, A. Pitrou and S. Seibert. "Numba: a LLVM-based Python JIT compiler". In: *Proceedings of the Second Workshop on the LLVM Compiler Infrastructure in HPC*. LLVM '15. Austin, Texas: Association for Computing Machinery, 2015. DOI: 10.1145/2833157.2833162. URL: https://doi.org/10.1145/2833157.2833162.

[88] P. Virtanen et al. "SciPy 1.0: Fundamental Algorithms for Scientific Computing in Python". In: *Nature Methods* 17 (2020), pp. 261–272. DOI: 10.1038/s41592-019-0686-2.

[89] S. Agostinelli et al. "Geant4—a simulation toolkit". In: *Nuclear Instruments and Methods in Physics Research Section A: Accelerators, Spectrometers, Detectors and Associated Equipment* 506.3 (2003), pp. 250–303. DOI: https://doi.org/10.1016/S0168-9002(03)01368-8. URL: https://www.sciencedirect.com/science/article/pii/S0168900203013688.

[90] P. Allport et al. “Recent results and experience with the Birmingham MC40 irradiation facility”. In: *Journal of Instrumentation* 12.03 (Mar. 2017), pp. C03075–C03075. DOI: 10.1088/1748-0221/12/03/c03075. URL: https://doi.org/10.1088/1748-0221/12/03/c03075.

[91] Dierlamm, Alexander. private communication. 20th July 2022.

[92] F. Szelecsényi et al. “Excitation function for the natTi(p,x)48V nuclear process: Evaluation and new measurements for practical applications”. In: *Nuclear Instruments and Methods in Physics Research Section B: Beam Interactions with Materials and Atoms* 174 (Mar. 2001), pp. 47–64. DOI: 10.1016/S0168-583X(00)00516-4.

[93] A. V. Himmelreich. “Development of a Capacitance Measurement Setup for Silicon Pixel Sensors”. BA thesis. Universität Bonn, Aug. 2021.

[94] R. Collaboration. *Recommendations towards a standardisation of the macroscopic parameter measurements*. Mar. 2003. URL: https://rd50.web.cern.ch/doc/Internal/rd50_2003_003_version_15-10-2004.doc (visited on 02/04/2024).

[95] F. Ravotti et al. “BPW34 Commercial p-i-n Diodes for High-Level 1-MeV Neutron Equivalent Fluence Monitoring”. In: *IEEE Transactions on Nuclear Science* 55.4 (2008), pp. 2133–2140. DOI: 10.1109/TNS.2008.2000765.

[96] P. Palni et al. “A method for real time monitoring of charged particle beam profile and fluence”. In: *Nuclear Instruments and Methods in Physics Research Section A: Accelerators, Spectrometers, Detectors and Associated Equipment* 735 (2014), pp. 213–217. DOI: https://doi.org/10.1016/j.nima.2013.09.037. URL: https://www.sciencedirect.com/science/article/pii/S0168900213012710.

[97] M. Hoeferkamp et al. “Application of p–i–n photodiodes to charged particle fluence measurements beyond 10^{15} 1-MeV-neutron-equivalent/cm2”. In: *Nuclear Instruments and Methods in Physics Research Section A: Accelerators, Spectrometers, Detectors and Associated Equipment* 890 (2018), pp. 108–111. DOI: https://doi.org/10.1016/j.nima.2018.02.070. URL: https://www.sciencedirect.com/science/article/pii/S0168900218302249.

[98] Osram. *BPF34F Silicon PIN Photodiode with Daylight Blocing Filter Datasheet*. URL: https://look.ams-osram.com/m/2c4b674435bb90e8/original/BPW-34-F.pdf (visited on 08/04/2024).

[99] Karlsruhe Institut für Technologie. *Proton Irradiation: The Cyclotron and the Irradiation Setup, Homepage*. URL: https://www.etp.kit.edu/english/264.php (visited on 11/04/2024).

[100] M. Garcia-Sciveres, F. Loddo and J. Christiansen. *RD53B Manual*. Tech. rep. Geneva: CERN, 2019. URL: https://cds.cern.ch/record/2665301.

[101] D. Bortoletto et al. *Dose rate dependence of TID damage to 65 nm CMOS transistors in X-ray irradiations of the ATLAS ITk Pixel ASIC (ITkPix)*. 2024. arXiv: 2404.10963.

[102] M. H. Standke. “Hybrid Pixel Readout Chip Verification, Characterization and Wafer Level Testing for the ATLAS-ITK Upgrade at the HL-LHC”. PhD thesis. Universität Bonn, Mar. 2023.

[103] M. Mironova. *X-ray irradiations for RD53B*. Version 1.0. Feb. 2021. URL: https://indico.cern.ch/event/993420/contributions/4230896/attachments/2191757/3704514/Xray_irradiation_v1.0.pdf (visited on 25/06/2024).

[104] C. Hu-Guo et al. "First reticule size MAPS with digital output and integrated zero suppression for the EUDET-JRA1 beam telescope". In: *Nuclear Instruments and Methods in Physics Research Section A: Accelerators, Spectrometers, Detectors and Associated Equipment* 623.1 (2010). 1st International Conference on Technology and Instrumentation in Particle Physics, pp. 480–482. DOI: https://doi.org/10.1016/j.nima.2010.03.043. URL: https://www.sciencedirect.com/science/article/pii/S0168900210006078.

[105] M. Garcia-Sciveres et al. "The FE-I4 pixel readout integrated circuit". In: *Nuclear Instruments and Methods in Physics Research Section A: Accelerators, Spectrometers, Detectors and Associated Equipment* 636.1, Supplement (2011). 7th International ""Hiroshima"" Symposium on the Development and Application of Semiconductor Tracking Detectors, S155–S159. DOI: https://doi.org/10.1016/j.nima.2010.04.101. URL: https://www.sciencedirect.com/science/article/pii/S0168900210009551.

[106] H. Lhabil. "Charakterisierung und Optimierung eines Sticktoffkülsystems für Detektortestandwendungen". BA thesis. Universität Bonn, Dec. 2022.

[107] Y. Dieter et al. *pymosa - A readout software for Mimosa26 CMOS pixel sensors*. GitHub project page. URL: https://github.com/SiLab-Bonn/pymosa (visited on 01/12/2024).

[108] J. Janssen, D.-L. Pohl, T. Hemperek et al. *pyBAR - Bonn ATLAS Readout in Python*. GitHub project page. URL: https://github.com/SiLab-Bonn/pyBAR (visited on 24/07/2024).

[109] Y. Dieter et al. *pyTLU - DAQ software and firmware for the EUDAQ Trigger Logic Unit*. GitHub project page. URL: https://github.com/SiLab-Bonn/pytlu (visited on 01/12/2024).

[110] Y. Dieter, J. Janssen and D.-L. Pohl. *Beam Telescope Analysis (BTA) is a testbeam analysis software written in Python (and C++)*. GitHub page. URL: https://github.com/silab-Bonn/beam_telescope_analysis (visited on 15/07/2024).

[111] E. O. Lebigot. *Uncertainties: a Python package for calculations with uncertainties*. URL: http://uncertainties-python-package.readthedocs.io/ (visited on 04/04/2024).

[112] J. D. Hunter. "Matplotlib: A 2D graphics environment". In: *Computing in Science & Engineering* 9.3 (2007), pp. 90–95. DOI: 10.1109/MCSE.2007.55.

List of Figures

List of Tables

Acronyms

ADC Analog-to-Digital Converter. 29, 50, 51, 53, 62, 72, 73, 82, 83

ATLAS A Torodial LHC Apparatus. 1–3, 19–21, 25–29, 31, 33, 34, 36, 40, 42, 43, 109, 113, 122, 126, 127, 129–131, 133–135, 159

BIC Bonn Isochronous Cyclotron. v, 3, 35, 38, 45–48, 50, 53, 54, 63, 68, 70–72, 77–79, 88, 91, 92, 94, 100–106, 109, 110, 113, 115, 120–123, 125, 133, 134, 140, 144–148, 161, 169

BLM Beam Loss Monitor. 58–60, 63, 74, 82–85, 88

BSM Beyond Standard Model. 1, 2, 23

BTA Beam Telescope Analysis. 130, 131, 148

CAD Computer-Aided Design. 49, 53, 54, 56–58, 77, 78, 160, 169

CB conduction band. 12

CCE Charge Collection Efficiency. 129

CERN Conseil Européen pour la Recherche Nucléaire. 1, 3, 21, 22, 31, 91, 107, 131, 133, 134, 159

CMOS Complementary Metal-Oxide-Semiconductor. 20, 28, 32, 33, 94, 110, 113

CMS Compact Muon Solenoid. 1, 20, 21, 28, 29

CSA charge sensitive amplifier. 19

CST Computer Simulation Technology. 56, 57, 59, 60

CV Capacitance-Voltage. 15–17, 94, 96–99, 160

DAC Digital-to-Analog Converter. 29, 114, 161

DAQ Data Acquisition. iv, 29, 45, 50, 70–73, 75, 110, 114, 125, 127, 133

DESY Deutsches Elektronen-Synchrotron. v, 3, 109, 110, 125–128, 130, 131, 135, 148, 161

DMAPS Depleted Monolothic Active Pixel Sensor. 20

DUT Device Under Test. 29, 30, 43, 45, 49, 51–55, 57, 63–68, 70, 73–80, 87–97, 104–106, 109, 114–118, 122, 126–130, 133, 134, 140–142, 146, 147, 160, 161, 163

ECR Electron Cyclotron Resonance. 47

EOL End-Of-Life. 3, 34, 109, 113, 116, 117, 125, 134

FC Faraday Cup. 48–54, 56–64, 81–86, 160

FE front-end. 19, 20, 28

FPGA Field-Programmable Gate Array. 29

FWHM Full-Width Half-Maximum. 59, 63, 64, 69

GPIO General-Purpose Input Output. 60

GUI Graphical User Interface. 71, 72, 74, 133

HEP High Energy Physics. 19, 20, 23, 31, 33, 39, 40

HISKP Helmholtz Institut für Strahlen- und Kernphysik. v, 43, 45, 46, 67, 68, 91, 145, 169, 170

HL-LHC High-Luminosity Large Hadron Collider. 2, 3, 21, 23, 24, 26–29, 34, 109

HS Higgs Sector. 1, 2

HV High-Voltage. iv, 52, 58, 78, 81–84, 96, 115, 160

IBL Insertable B-Layer. 25

ID Inner Detector. 25, 26, 28

IP interaction point. 1–3, 25–27, 34

ITk Inner Tracker. 2, 3, 21, 27–29, 33, 34, 43, 109, 112, 113, 122, 131, 134, 135, 159

IV Current-Voltage. 15, 17, 94, 96, 97, 99, 100, 102–105, 110, 112, 114, 117, 121–123, 129, 135, 147, 148, 160, 161

KIT Karlsruher Institut für Technologie. 71, 106, 107, 133, 134

LAN Local Area Network. 50, 53, 71

LF LFoundry. 94–100, 102, 142, 144, 160, 161, 163

LHC Large Hadron Collider. 1–3, 21–25, 40, 159

MAPS Monolithic Active Pixel Sensor. 20, 126

MIP minimum-ionizing particle. 6, 7, 12, 15, 20, 113

MOS Metal-Oxide-Semiconductor. 32, 33, 159

MPV most probable value. 6

NIEL Non-Ionizing Energy Loss. v, 31, 35–43, 77, 80, 90, 94, 95, 102, 104–109, 112, 113, 115–118, 122, 123, 125, 134, 135, 159

NIST National Institute of Standards and Technology. 104

NUB Nano-Utility-Board. 51, 62, 160

PCB Printed Circuit Board. 28, 29, 53, 54, 68, 81, 94, 110, 120, 159

PIC Particle in Cell. 57, 59

PID particle identification. 7

PKA Primary Knock-on Atom. 34, 35

R/O electronics readout electronics. 51, 60–63, 72, 74, 81–83, 85, 86, 160

RF Radio Frequency. 21, 46, 47

RINCE Radiation-Induced Narrow Channel Effect. 33

RISCE Radiation-Induced Short Channel Effect. 33

RO Ring Oscillator. 110–112, 114–116, 119–121, 125, 134, 135, 161

RPi Raspberry Pi. 50–53, 71

SCC Single-Chip Card. 29, 30, 53, 109, 110, 113, 115, 120, 122, 126, 147, 160

SCT SemiConductor Tracker. 26

SE Secondary Electron. 55–60, 82–84

SEE Secondary Electron Emission. 55–61, 64, 73, 83, 85–87, 160

SEM Secondary Electron Monitor. 58–61, 73, 74, 78, 82–86, 88

SEY Secondary Electron Emission Yield. 55, 56, 58, 73, 83, 85–87, 160

SM Standard Model of particle physics. 1, 24

SMU Source Measure Unit. 81, 82, 96, 97, 112–114, 121, 128, 146, 148

TCAD Technology Computer Aided Design. 43

TCP Transmission Control Protocol. 71

TID Total Ionizing Dose. 28, 29, 33, 34, 41, 70, 72, 73, 75–77, 79, 90, 106, 107, 109, 110, 113–116, 119–121, 124, 125, 131, 134, 135, 160, 161

TLU Trigger Logic Unit. 29, 127, 128

ToT time-over-threshold. 19, 28

TRT Transition Radiation Tracker. 26

VB valence band. 12

Acknowledgments

This thesis is the result of a collection of a few victories, alongside a variety of failures. The achievements are made possible by not only my efforts, but the contributions of many of my colleagues who became dear friends along the way, to whom I want to express my gratitude.

Firstly, I would like to thank Prof. Jochen Dingfelder for giving me the opportunity to continue my work in the Silizum Labor Bonn and allow me to complete the project of a proton irradiation facility at Bonn University.
Furthermore, I would like to express my gratitude towards professor Sebastian Neubert for actively offering to be the second supervisor for this thesis, showing interest in the project and supporting the challenging progress across two (three during the later years) different institutes.
Also, I would like show my appreciation for Prof. Reinhardt Beck and P.D. Paul-Dieter Eversheim, the former specifically for providing the resources at the HISKP, the latter for his passion and deep knowledge around the BIC facility.

I would like to thank Prof. Norbert Wermes for sparking interest in the field of detector physics in the first place, his supervision throughout the entirety of my time at Bonn University and lastly for his leadership and efforts inside every department of the group.

Moreover, I want to acknowledge the contribution of Dr. Dennis Sauerland, Berthold "Bert" Kann and Markus Klümpen of the Bonn Isochronous Cyclotron crew.
Dennis has contributed greatly to the developments at the irradiation site, specifically through (but not limited to) CAD-design of irradiation-related components and accelerator parts. I appreciate his work and, specifically, his way of handling certain aspects of my character, which I know are not always easy to deal with.

Bert sadly passed away in August 2023, during the course of this work. He was passionately supporting the new project at the cyclotron since its beginnings in 2018 and had an exceptional understanding of the machine. His expertise more often than not saved an entire irradiation campaign and configured the accelerator to unmatched levels of performance. He was a major contributor to the success of the project and I will remembered him for his kind, warm and passionate character.
Remarkably, when Markus joined the team in late 2022, the outstanding collaboration between them resulted in a substantial transfer of knowledge within a short time. With his eagerness and talent, Markus was able to continue Berts legacy and provided quality beam times with a great technical understanding, often contributing to solutions outside of the realm of his responsibilities at the

cyclotron.
Naturally, I would also like to express my thanks to the remaining members of the crew for their continuous labor to maintain the accelerator facility: Stefan Birkenbach, Stefan Dernbach, Achim Henny, Eugen Momper and Siegbert Lehmann.
Additionally, I want to thank Dr. Christoph Wendel and Dr. Marcus Grüner, responsible for the radiation protection at the HISKP and cyclotron. They provided support, in- and outside of the project, to help advance the irradiation infrastructure.

In the following, I want to express my heartfelt appreciation for the members (current and former) of the SiLab. I could very likely write more than one abstract about each and every individual in this group and I would still feel that it is not enough. I want to thank these people for their help, support and friendship over all these years. We shared difficulties, beers, vacations and, more often than one would think, beds. Thank you to Jannes Schmitz, Patrick Ahlburg, Tomasz Hemperek, Nikolaus G.G. Owtscharenko, Christian "LJ Chris" Bespin, Bruno Deschamps, Botho "BothoSan" Paschen, Georgios "Schorschi" Giakoustidis, Yannick "ReusenD" Dieter, Lars "Larsi" Schall, David-Leon Pohl, Sinuo "Snow" Zhang, and Ahmed Fouad Qamesh. I am grateful for the times we shared that go far beyond work and created friendships, by coincidence, in a random group of people. To all remaining people that are not explicitly mentioned here: thank you for taking part in this journey.

Also, I would like to thank the people outside of the physics environment: Alexander Braun, who supported me in countless situations with more than you can ask from a friend. He shared valuable insights and talked some sense into me, whenever it was needed. Thanks to him, I find myself in a better place today.
Subsequently, I would like to thank my grandmother, for countless meals and her strength in difficult situations, my mother, my uncle Andre and the Trojan family for their support throughout the years.

Lastly, I would like to acknowledge a person whom I have failed: my brother Simon. Due to differences in character, in dealing with the past and my own deficiencies, I was unable to take part in his life for over a decade. I regret that I could not be there when it was needed and I apologize for the things I know I could have done differently, but was too weak to do so. At the same time, I am grateful and hopeful to see that after all this time, there is still the possibility for a new path to be taken.